

# FINAL TECHNICAL REPORT

ARPA/ONR Grant No.N00014-91-J-1976  
(for the period: 08/01/91 – 01/31/95)

## Development of Ultra-Low Dark Current, High Performance III-V Quantum Well Infrared Photodetectors (QWIPs) for Focal Plane Arrays Staring Imaging Sensor Systems

Submitted to

Max N. Yoder

Office of Naval Research  
Code 3140  
800 North Quincy Street  
Arlington, VA 22217-5000

Prepared by

Sheng S. Li  
Professor

Dept.of Electrical Engineering  
University of Florida  
Gainesville, FL. 32611-6200  
Tel.(904) 392-4937  
Fax (904) 392-8671  
E-mail: Shengli@eng.ufl.edu



DTIC QUALITY INSPECTED 3

February 1, 1995

19950130 103

DISTRIBUTION STATEMENT A

Approved for public release;  
Distribution Unlimited

REPORT DOCUMENTATION PAGE			Form Approved OMB No. 0704-0188
<p>Public reporting burden for this collection of information is estimated to average 1 hour per response, including the time for reviewing instructions, searching existing data sources, gathering and maintaining the data needed, and completing and reviewing the collection of information. Send comments regarding this burden estimate or any other aspect of this collection of information, including suggestions for reducing this burden, to Washington Headquarters Services, Directorate for Information Operations and Reports, 1215 Jefferson Davis Highway, Suite 1204, Arlington, VA 22202-4302, and to the Office of Management and Budget, Paperwork Reduction Project (0704-0188), Washington, DC 20503.</p>			
1. AGENCY USE ONLY (Leave blank)	2. REPORT DATE	3. REPORT TYPE AND DATES COVERED	
	February 1, 95	Final Report: 08/1/91 - 01/31/95	
4. TITLE AND SUBTITLE Development of Ultra-Low Noise, High Sensitivity Planar Metal Grating Coupled III-V Quantum Well Infrared Detectors for Focal Plane Array Staring IR Sensor Systems		5. FUNDING NUMBERS ONR G-N00014-91-J-1976	
6. AUTHOR(S) Sheng S. Li, Professor			
7. PERFORMING ORGANIZATION NAME(S) AND ADDRESS(ES) University of Florida Gainesville, FL 32611-6200		8. PERFORMING ORGANIZATION REPORT NUMBER 92122803	
9. SPONSORING/MONITORING AGENCY NAME(S) AND ADDRESS(ES) US Navy, Office of Naval Research 800 North Quincy Street, Code 1512B:SM Arlington, VA 22217-5000		10. SPONSORING/MONITORING AGENCY REPORT NUMBER	
11. SUPPLEMENTARY NOTES			
12a. DISTRIBUTION / AVAILABILITY STATEMENT Approved for public release, distribution unlimited.		12b. DISTRIBUTION CODE	
13. ABSTRACT (Maximum 200 words)  This final report presents the research findings and accomplishments made on the research project sponsored by ARPA/ONR under grant No. N00014-91-J-1976 for the period of 08/01/91 to 02/01/95. Specific achievements include: (i) development of the first bound-to-miniband (BTM) transition GaAs/GaAlAs QWIP for 8-12 um detection; large area (128/128, 256x256, and 512x512) FPAs based on the BTM QWIP structure have been demonstrated by Martin Marietta with excellent imagery, (ii) development of a normal incidence type-II AlAs/AlGaAs QWIP grown on (110) GaAs substrate for multi-color detection in the 3-5 and 8-14 um spectral windows, (iii) design of 2-D metal grating couplers for efficient coupling of normal incidence IR radiation in n-type QWIPs, and (iv) development of two new normal incidence p-type strained-layer III-V QWIPs for 3-5 and 8-12 um detection. An ultra-low dark current p-type tensile strained-layer (PTSL) $In_{0.3}Ga_{0.7}As/In_{0.52}Al_{0.48}As$ QWIP grown on InP by MBE for 8-12 um detection has been developed with BLIP condition for $T < 100$ K. The BLIP detectivity for this PTSL-QWIP was found to be $5.9 \times 10^{10}$ Jones at 8.1 um, $V_b = 2$ V, and $T = 77$ K. A new p-type compressive strained-layer (PCSL) $In_{0.4}Ga_{0.6}As/GaAs$ QWIP grown on GaAs substrate for 3-5 and 8-14 um was demonstrated for the first time. Detectivity for this PCSL-QWIP was found to be $4.0 \times 10^9$ Jones at 8.9 um, $V_b = 0.3$ V and $T = 75$ K.			
14. SUBJECT TERMS Quantum well infrared photodetectors (QWIPs), GaAs/AlGaAs QWIP, type-II AlAs/GaAlAs QWIP, 2-D grating coupler, p-type strained-layer InGaAs/InAlAs QWIP, p-type strained-layer InGaAs/GaAs QWIP, dark current, responsivity, detectivity, focal plane arrays.		15. NUMBER OF PAGES 16. PRICE CODE	
17. SECURITY CLASSIFICATION OF REPORT Unclassified.	18. SECURITY CLASSIFICATION OF THIS PAGE Unclassified.	19. SECURITY CLASSIFICATION OF ABSTRACT Unclassified.	20. LIMITATION OF ABSTRACT Unlimited

## TABLE OF CONTENTS

	Page	
<b>1</b>	<b>SUMMARY .....</b>	<b>1</b>
<b>2</b>	<b>QUANTUM WELL AND SUPERLATTICE STRUCTURES .....</b>	<b>12</b>
	<b>2.1. Introduction .....</b>	<b>12</b>
	<b>2.2. Methods for Calculating Electronic States .....</b>	<b>12</b>
	<b>2.3. Superlattice and Miniband .....</b>	<b>15</b>
	<b>2.3.1. Dispersion Relations .....</b>	<b>16</b>
	<b>2.3.2. Transmission Probability <math> T \cdot T </math> .....</b>	<b>18</b>
	<b>2.4. Carrier Transports .....</b>	<b>19</b>
	<b>2.4.1. Continuum State Conduction .....</b>	<b>19</b>
	<b>2.4.2. Miniband Conduction .....</b>	<b>19</b>
	<b>2.4.3. Hopping Conduction .....</b>	<b>20</b>
	<b>2.5. Corrections on Subband Energy States .....</b>	<b>21</b>
	<b>2.5.1. Electron-Electron Interaction .....</b>	<b>21</b>
	<b>2.5.2. Depolarization Effects .....</b>	<b>22</b>
	<b>2.5.3. Other Effects .....</b>	<b>23</b>
<b>3</b>	<b>PHYSICS OF QWIPS AND FIGURES OF MERIT .....</b>	<b>27</b>
	<b>3.1. Introduction .....</b>	<b>27</b>
	<b>3.2. Intersubband Transition .....</b>	<b>27</b>
	<b>3.3. PC and PV Detection Modes .....</b>	<b>29</b>
	<b>3.4. Figures of Merit .....</b>	<b>30</b>
	<b>3.4.1. Dark Current <math>I_d</math> .....</b>	<b>30</b>
	<b>3.4.2. Spectral Responsivity <math>R</math> .....</b>	<b>31</b>
	<b>3.4.3. Collection Efficiency <math>\eta_c</math> .....</b>	<b>32</b>
	<b>3.4.4. Noise Characteristics of a QWIP .....</b>	<b>32</b>
	<b>3.4.5. Detectivity <math>D_\lambda^*</math> .....</b>	<b>35</b>
	<b>3.4.6. Background Limited Performance (BLIP) .....</b>	<b>36</b>
<b>4</b>	<b>METAL GRATING COUPLED BOUND-TO-MINIBAND TRANSITION GaAs/AlGaAs QUANTUM WELL SUPERLATTICE INFRARED DETECTOR .....</b>	<b>39</b>
	<b>4.1. Introduction .....</b>	<b>39</b>

Part I DHC QUALITY INSPECTED 3  
N-type QWIPS

4	METAL GRATING COUPLED BOUND-TO-MINIBAND TRANSITION GaAs/AlGaAs QUANTUM WELL SUPERLATTICE INFRARED DETECTOR ...	39
	4.1. Introduction .....	39

4.2. Sample Preparationon .....	40
4.3. Theory, Experiments and Discussion .....	40
4.4. Conclusion .....	43
<b>5 LOW DARK CURRENT STEP-BOUND-TO-MINIBAND TRANSITION InGaAs/GaAs/AlGaAs QUANTUM WELL INFRARED DETECTOR .....</b>	<b>49</b>
5.1. Introduction .....	49
5.2. Theory and Experiments .....	49
5.3. Advantages of Step-bound-to-miniband Transition Structure .....	52
5.4. Conclusion .....	54
<b>6 A VOLTAGE-TUNABLE InGaAs/InAlAs QUANTUM WELL INFRARED PHOTODETECTOR (VT-QWIP) .....</b>	<b>61</b>
6.1. Introduction .....	61
6.2. Design Consideration .....	61
6.3. Experiments .....	62
6.4. Results and Discussion .....	64
6.5. Conclusions .....	65
<b>7 A DUAL-MODE PC AND PV GaAs/AlGaAs QUANTUM WELL INFRARED PHOTODETECTOR (DM-QWIP) WITH TWO-COLOR DETECTION .....</b>	<b>72</b>
7.1. Introduction .....	72
7.2. Design Consideration .....	72
7.3. Experiments .....	74
7.4. Conclusions .....	75
<b>8 A NORMAL INCIDENCE TYPE-II QUANTUM WELL INFRARED PHOTODETECTOR USING AN INDIRECT BANDGAP AlAs/Al<sub>0.5</sub>Ga<sub>0.5</sub>As GROWN ON (110) GaAs SUBSTRATE FOR THE MID- AND LONG-WAVELENGTH MULTICOLOR DETECTION .....</b>	<b>83</b>
8.1. Introduction .....	83
8.2. Theory .....	84
8.3. Coupling between $\Gamma$ - and X-bands .....	86
8.4. Experiments .....	87
8.5. Conclusions .....	89
<b>9 A TWO-COLOR GaAs/AlAs/AlGaAs AND GaAs/AlGaAs STACKED QWIP FOR 3-5 AND 8-14 <math>\mu</math>m DETECTION .....</b>	<b>102</b>
9.1. Introduction .....	102
9.2. Stacked Structure .....	102
9.3. Results and Discussion .....	103
9.4. Conclusions .....	105

**Part II**  
**Metal Grating Couplers**

10 DESIGN OF 2-D REFLECTION SQUARE METAL GRATING COUPLER .....	116
10.1. Introduction .....	116
10.2. Theoretical Consideration .....	117
10.3. Results and Discussion .....	119
11 DESIGN OF 2-D SQUARE MESH METAL GRATING COUPLER .....	127
11.1. Introduction .....	127
11.2. Basic Theory .....	128
11.3. Results and Discussion .....	131
11.4. Grating Pattern Variation Effect .....	133
12 DESIGN OF 2-D CIRCULAR MESH METAL GRATING COUPLER .....	151
12.1. Introduction .....	151
12.2. Basic Formulation .....	152
12.3. Results and Discussion .....	154

**Part III**  
**P-type Strained-layer QWIPs**

13 PHYSICS OF P-TYPE STRAINED-LAYER QUANTUM WELL INFRARED PHOTODETECTORS .....	167
13.1. Introduction .....	167
13.2. Coherent Strained-layers .....	168
13.3. $k \cdot p$ Model .....	169
13.4. Strain Effects .....	170
14 A P-TYPE TENSILE STRAINED-LAYER InGaAs/InAlAs QUANTUM WELL INFRARED PHOTODETECTOR .....	173
14.1. Inversion between Heavy- and Light-hole States .....	173
14.2. Experiments .....	173
14.3. Conclusions .....	175
15 A P-TYPE COMPRESSIVE STRAINED-LAYER InGaAs/GaAs QUANTUM WELL INFRARED PHOTODETECTOR .....	180
15.1. Interaction between Type-I and Type-II States .....	180
15.2. Experiments .....	181
15.3. Conclusions .....	183

16 CONCLUSIONS .....	191
APPENDICES	
A ENERGY DISPERSION EQUATION FOR SUPERLATTICE .....	193
B OPTICAL MATRIX FOR STRAINED-LAYER SUPERLATTICE .....	197
REFERENCES .....	198

Accesion For	
NTIS CRA&I	<input checked="" type="checkbox"/>
DTIC TAB	<input type="checkbox"/>
Unannounced	<input type="checkbox"/>
Justification _____	
By _____	
Distribution / _____	
Availability Codes	
Dist	Avail and / or Special
<b>A-1</b>	

## 1. SUMMARY

The objective of this research project is to develop ultra-low dark current, high performance III-V quantum well infrared photodetectors (QWIPs) for focal plane arrays (FPAs) staring imaging system applications in the  $8\text{-}12 \mu\text{m}$  atmospheric spectral window. Since the inception of this research program in August, 1991, this principal investigator and his students have engaged in the development of a wide variety of novel III-V quantum well infrared photodetectors (QWIPs) for long wavelength focal plane arrays imaging sensor system applications. Seven new QWIPs were developed from this work. Figure 1.1 shows the energy band diagrams for these novel QWIPs and their detection schemes and quantum well parameters. A comparison of the dark current densities for the conventional BTC QWIP and our QWIPs is shown in Fig.1.2. The normalized spectral responsivities for the QWIPs developed in this work are illustrated in Fig.1.3. Table 1.1 summarizes the peak and cutoff wavelengths, responsivities, detectivities, and the BLIP temperatures for these QWIPs. Major accomplishments from this program are summarized as follows:

### A. Research Achievements

- Demonstrated the first bound-to-miniband (BTM) transition GaAs/AlGaAs multiquantum well/superlattice barrier QWIP for  $8\text{-}12 \mu\text{m}$  detection. Large area focal plane arrays (FPAs) with array size of 128x128, 256x256, and 512x512 based on our BTM QWIP structure have been successfully developed by Martin Marietta group in Baltimore Lab. for the  $8\text{-}12 \mu\text{m}$  wavelength IR staring imaging system applications. In addition, two new BTM QWIPs using a lattice matched InGaAs/InAlAs structure grown on InP and a lightly-strained InGaAs/AlGaAs/GaAs structure grown in GaAs substrate have also been developed in this project. The BTM QWIPs developed in this work all exhibit the photovoltaic (PV) and photoconductive (PC) dual-mode operation characteristics. Reduced dark current and improved noise performance are the common features of these BTM QWIPs when compared to the conventional bound-to-continuum (BTC) transition GaAs/AlGaAs QWIPs.
- Demonstrated the first multi-color type-II normal incidence AlAs/AlGaAs QWIP grown on (110) GaAs substrate for the  $3\text{-}5 \mu\text{m}$  mid-wavelength infrared (MWIR) and  $8\text{-}12 \mu\text{m}$  long wavelength (LWIR) two-band detection.

- Designed and fabricated different 2-D metal grating couplers with square mesh and circular mesh grating structures for enhancing the coupling quantum efficiency of the normal IR incidence radiation in n-type QWIPs.
- Demonstrated the first normal incidence p-type tensile-strained layer (PTSL-) InGaAs/InAlAs QWIP grown on InP substrate, with the lowest dark current and highest BLIP temperature ( $\sim 100$  K) for a QWIP.
- Demonstrated a normal incidence p-type compressive-strained layer (PCSL-) InGaAs/GaAs QWIP for MWIR and LWIR two color detection.
- Published 18 journal papers and presented more than 20 invited and contributed papers at the international conferences/workshops on quantum well infrared detectors in the past 3 years. Dr. Li has also delivered several invited talks at government research laboratories and universities.
- Graduated three Ph.D. and three M.S. students who worked on QWIP development project sponsored by this ARPA/ONR grant for the past three and half years.
- Dr. Li is the co-organizer of the *2nd International Symposium on Long Wavelength Infrared Detectors- Physics and Applications*, for the 186th ECS Meeting held in Miami Beach, FL, Oct.9-14, 1994. He is the principal organizer of the *3rd International Symposium on Long Wavelength Infrared Detectors- Physics and Applications* to be held in Chicago, October 8-13, 1995.
- Contributed a book chapter (chapter 4, 60 pages) on “*Metal Grating Coupled Bound-to-Miniband (BTM) Transition Quantum Well Infrared Photodetectors*” for the monograph on *Long Wavelength Quantum Well Infrared Photodetectors* edited by Prof. M. Razeghi, which is scheduled to publish by Artech House in 1995.

#### B. Journal Publications:

1. L. S. Yu and S. S. Li, “A Low Dark Current, High Detectivity Grating Coupled AlGaAs/GaAs Multiple Quantum Well IR Detector Using Bound-to-Miniband Transition for  $10 \mu\text{m}$  Detection,” *Appl. Phys. Letts.*, **59**(11), 1332 (1991).
2. L. S. Yu, S. S. Li, and Pin Ho “Largely Enhanced Bound-to-Miniband Absorption in an InGaAs Multiple Quantum Well with a Short-Period Superlattice InAlAs/InGaAs Barrier” *Applied Phys. Letts.*, **59**(21), 2712 (1991).

3. L. S. Yu, Y. H. Wang, S. S. Li and Pin Ho, "A Low Dark Current Step-Bound-to-Miniband Transition InGaAs/GaAs/AlGaAs Multiquantum Well Infrared Detector," *Appl. Phys. Letts.*, **60**(8), 992 (1992).
4. L. S. Yu, S. S. Li, and P. Ho, "A Normal Incident Type-II Quantum Well Infrared Detector Using an Indirect AlAs/Al<sub>0.5</sub>Ga<sub>0.5</sub>As System Grown on [110] GaAs," *Electronics Letts.*, **28**(15), 1468 (1992).
5. L. S. Yu, S. S. Li, Y. H. Wang, and Y. C. Kao, "A Study of Coupling Efficiency versus Grating Periodicity in A Normal Incident Grating-Coupled GaAs/AlGaAs Quantum Well Infrared Detector," *J. Appl. Phys.*, **72**(6), 2105 (1992).
6. Y. H. Wang, S. S. Li, and P. Ho, "A Photovoltaic and Photoconductive Dual Mode Operation GaAs/AlGaAs Quantum Well Infrared Detector for Two Band Detection," *Appl. Phys. Lett.*, **62**(1), 93 (1993).
7. Y. H. Wang, S. S. Li, and P. Ho, "A Voltage-Tunable Dual Mode Operation InAlAs/InGaAs Bound-to-Miniband Transition QWIP for Narrow and Broad Band Detection at 10 μm," *Appl. Phys. Lett.*, **62**(6), 621 (1993).
8. P. Ho, P. A. Martin, L. S. Yu, and S. S. Li, "Growth of GaAs and AlGaAs on Misoriented (110) GaAs and a Normal Incidence Type-II Quantum Well Infrared Detector," *J. Vacuum Science and Technology B* **11**(3), 935 (1993).
9. S. S. Li, M. Y. Chuang and L. S. Yu, "Current Conduction Mechanisms in Bound-to-Miniband Transition III-V Quantum Well Infrared Photodetectors," *J. Semiconductor Science and Technology*, vol.8, 406 (1993).
10. Y. H. Wang, S. S. Li, P. Ho, and M. O. Manasreh, "A Normal Incidence Type-II Quantum Well Infrared Photodetector Using An Indirect AlAs/AlGaAs System Grown on [110] GaAs for the Mid- and Long-Wavelength Multicolor Detection," *J. Appl. Phys.*, **74**(2), 1382 (1993).
11. Y. C. Wang and S. S. Li, "A Numerical Analysis of Double Periodic Reflection Metal Grating Coupler for Multiquantum Well Infrared Photodetectors," *J. Appl. Phys.*, **74**(4), 2192 (1993).
12. Y. C. Wang and S. S. Li, "Design of A Two-Dimensional Square Mesh Metal Grating Coupler for GaAs/AlGaAs Quantum Well Infrared Photodetectors," *J. Appl. Phys.*, **75**(1), 582 (1994).

13. Y. H. Wang, S. S. Li, J. Chu, and P. Ho, "An Ultra-low Dark Current Normal Incidence P-type Strained Layer InGaAs/InAlAs QWIP with Background Limited Performance at 77 K," *Appl. Phys. Lett.*, **64**(6), 727 (1994).
14. D. Wang, G. Bosman, and S. S. Li, "On the Dark Current Noise of Quantum Well Infrared Photodetectors," *Appl. Phys. Lett.*, **65**(2), 183 (1994).
15. Y. C. Wang and S. S. Li, "A Planar 2-Dimensional Circular Aperture Metal Grating Coupler for Quantum Well Infrared Photodetectors," *J. Appl. Phys.*, **75**(12), 8168 (1994).
16. Y. H. Wang, J. C. Chiang, S. S. Li, and P. Ho, "A GaAs/AlAs/AlGaAs and GaAs/AlGaAs Stacked quantum well infrared photodetector QWIP for 3-5 and 8-14  $\mu\text{m}$  Detection," *J. Appl. Phys.*, **76**(4), 2538 (1994).
17. Y. H. Wang and S. S. Li, and P. Ho, "A Normal Incidence two-color p-type Compressive Strained-Layer InGaAs/GaAs Quantum Well Infrared Photodetector for 3-5  $\mu\text{m}$  and 8-12  $\mu\text{m}$  Detection," *J. Appl. Phys.*, **76**(10), 6009 (1994).
18. D. C. Wang, G. Bosman, Y. H. Wang and S. S. Li, "The Noise Performance of Bound-to-Miniband Transition III-V Quantum Well Infrared Photodetectors," *J. Appl. Phys.* accepted, Nov. 1994.
19. S. S. Li, "Recent Progress in Quantum Well Infrared Photodetectors and Imaging Arrays," **Invited Paper**, Special Issue of *J. of the Chinese Institute of Electrical Engr. on Electronic Devices and Materials*, Feb. issue, 1995.

#### C. Conference/Workshop Presentations/Papers:

1. L. S. Yu, S. S. Li, and Pin Ho, "Largely Enhanced Intra-subband Absorption in a Wide InAlAS/InGaAs Quantum Well with a Short-Period Superlattice Barrier Structure," presented at the *SPIE's Symposium on Quantum Wells and Superlattices*, Somerset, NJ, 23-27 March, 1992. Paper published in the SPIE Conference Proceeding.
2. S. S. Li and L. S. Yu, "Grating Coupled Bound-to-Miniband Transition III-V Quantum Well Infrared Detectors," **Invited Talk**, presented at the *Innovative Long Wavelength Infrared Photodetector Workshop*, Jet Propulsion Lab., Pasadena, CA, April 7-9, 1992.
3. L. S. Yu and S. S. Li, "A Normal Incident Type-II Quantum Well Infrared Detector Using an Indirect AlAs/Al<sub>0.5</sub>Ga<sub>0.5</sub>As System Grown on [110] GaAs, presented at the *Innovative Long*

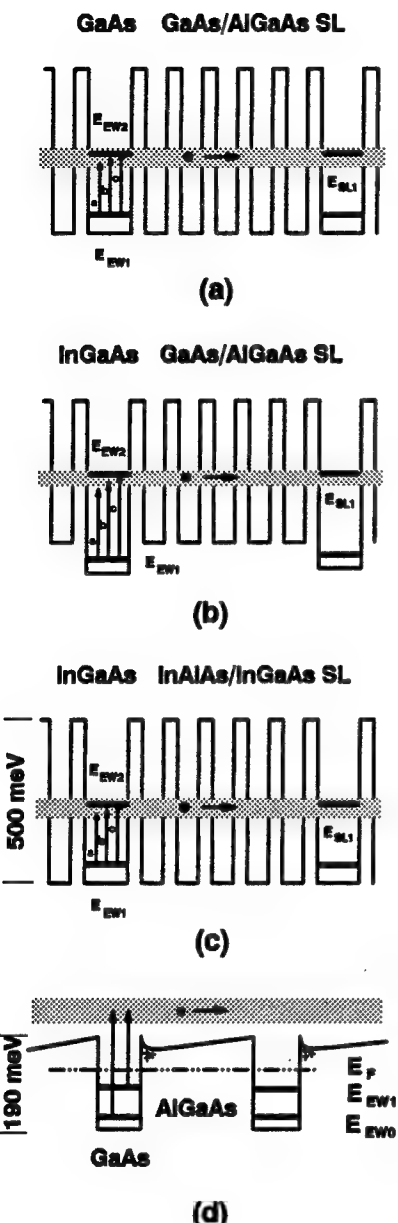
*Wavelength Infrared Photodetector Workshop*, Jet Propulsion Lab., Pasadena, CA, April 7-9, 1992.

4. L. S. Yu, S. S. Li, Y. H. Wang, and P. Ho, "Grating Coupled III-V Quantum Well Infrared Detectors Using Bound-to-Miniband Transition," presented at the *SPIE Conference on Infrared Detectors and Focal Plane Arrays at OE/Aerospace Sensing 92*, Orlando, FL, April 20-24, 1992. Full paper published in the SPIE conference proceeding.
5. S. S. Li, "Grating Coupled Bound-to-Miniband Transition III-V Multiquantum Well Infrared Photodetectors," presented at the DARPA IR Detector Workshop, Washington D.C., June 12, 1992.
6. S. S. Li, M. Y. Chuang and L. S. Yu, "Current Conduction Mechanisms in Bound-to-Miniband Transition III-V Quantum Well Infrared Photodetectors," presented at the *International Conference on Narrow Gap Semiconductors*, University of Southampton, Southampton, UK, July 19-23, 1992. Full paper published in conf. proc.
7. P. Ho, P. A. Martin, L. S. Yu, and S. S. Li, "Growth of GaAs and AlGaAs on Misoriented (110) GaAs and a Normal Incidence Type-II Quantum Well Infrared Detector," presented at the *12th North American Conference on Molecular Beam Epitaxy*, Oct.12-14, 1992.
8. S. S. Li, "Novel Grating Coupled Miniband Transport III-V Multiquantum Well Infrared Photodetectors for Focal Plane Array Applications," presented at the DARPA IR Detector Workshop, Washington D.C., Dec 11, 1992.
9. S. S. Li, Y. H. Wang, M. Y. Chuang, P. Ho, "Photoconductive and Photovoltaic Dual-Mode Operation III-V Quantum Well Infrared Photodetectors for 2 - 14  $\mu\text{m}$  Detection," presented at the Materials Research Society (MRS), Symposium C2 on *Infrared Detectors*, San Francisco, April 12-16, 1993. Full paper published in conf. proc.
10. D. Wang, Y. H. Wang, G. Bosman and S. S. Li, "Noise Characterization of Novel Quantum Well Infrared Photodetectors," Invited Talk presented at the *12th Int. Conf. on Noise in Physical Systems and 1/f Fluctuations - The High Technologies Conference*, St. Louis, MO, August 16-20, 1993.
11. S. S. Li, "Some Novel High Performance III-V Quantum Well Infrared Photodetectors for Focal Plane Array Image Sensor Applications," Invited Talk presented at the *NATO Advanced Research Workshop on Intersubband Transition Physics and Devices*, Whistler, Canada, September 7 - 10, 1993. Full paper published in conf. proc.

12. S. S. Li, "Grating Coupled III-V Quantum Well Infrared Photodetectors for Mid-Wavelength and Long-Wavelength Infrared Detection," **Invited Talk** presented at *the First International Symposium on Long Wavelength Infrared Photodetectors* in conjunction with the Fall Electrochemical Society (ECS) Meeting in New Orleans, LA, October 10 -15, 1993. Full paper to be published in conf. proc.
13. S. S. Li, Y. H. Wang, J. Chu, and P. Ho, "A Normal Incidence P-Type Strained-Layer In-GaAs/InAlAs Quantum Well Infrared Photodetector with Background Limited Performance at 77 K," *1994 SPIE Conference on Infrared Detectors and Focal Plane Arrays III*, Orlando, FL, April 4-6, 1994. Full paper published in conf. proc.
14. Y. H. Wang and S. S. Li, and P. Ho, "A Two-Color Normal Incidence P-type Compressive-Strained-Layer InGaAs/GaAs Quantum Well Infrared Photodetector for Mid- and Long-Wavelength Infrared Detection," *2nd Int. Symp. on 2- 20 μm Long Wavelength Infrared Detectors and Arrays: Physics and Applications*, the 186th ECS Meeting, Miami Beach, FL, Oct. 9-14, 1994. Full paper to be published in conf. proc.
15. D. C. Wang, G. Bosman, Y. H. Wang, and S. S. Li, "Device parameter extraction from noise measurements on bound-to-miniband transition III-V quantum well infrared photodetectors" *2nd Int.Symp. on 2- 20 μm Long Wavelength Infrared Detectors and Arrays: Physics and Applications*, the 186th ECS Meeting, Miami Beach, FL, Oct. 9-14, 1994. Full paper to be published in conf. proc.
16. S. S. Li, Y. H. Wang and P. Ho, "A New Class of P-type Strained-layer III-V Quantum Well Infrared Photodetectors for Long Wavelength Infrared Detection," presented at IEEE LEOS'94, Oct.31-Nov.2, Boston, 1994.
17. S. S. Li, "Recent Development in III-V Quantum Well Infrared Photodetectors for IR Focal Plane Imaging Arrays Applications," **Invited paper**, ICEM'94, National Chiao-Tung University, Hsinchu, Taiwan, Dec.19-21, 1994. Full paper to be published in conf. proc.

Table 1.1. Summary of the peak and cutoff wavelengths, responsivities, detectivities, and BLIP temperature for the developed QWIPs.

QWIP	$\lambda_p$ ( $\mu\text{m}$ )	$\lambda_c$ ( $\mu\text{m}$ )	R (A/W)	$D^*$ ( $\text{cm}\cdot\sqrt{\text{Hz}}/\text{W}$ )	$T_{\text{BLIP}}$ (K)
BTM	8.9 (PC)	9.3	0.23	$1.2\times10^{10}$	55
	8.9 (PV)	9.2	0.15	$7.5\times10^9$	
SBTM	10.5 (PC)	11.3	0.11	$8.1\times10^9$	58
VT	10.3 (PC)	11.7	0.038	$5.8\times10^9$	45
	10 (PV)	10.4	12,000 (V/W)	$5.7\times10^9$	
DM	12 (PC)	13.2	0.48	$2.0\times10^{10}$	70
	7.7 (PV)	8.5	11,000 (V/W)	$1.5\times10^9$	
T-II	2.2 (PC)	2.45	110	$1.1\times10^{12}$	50
	2.2 (PV)	2.45	64,000 (V/W)	$1.4\times10^{10}$	
	3.5 (PC)	4.3	18.3	$3.0\times10^{11}$	
	3.5 (PV)	4.3	58,000 (V/W)	$1.2\times10^{10}$	
	12.5 (PC)	14.8	0.024	$1.1\times10^9$	
PTSL	8.1 (PC)	8.8	0.018	$5.9\times10^{10}$	100
PCSL	8.9 (PC)	10	0.024	$4.0\times10^9$	70
	5.5 (PC)	6.2	0.007		



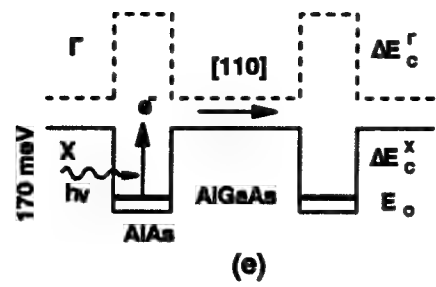
**(a) Energy band diagram for a GaAs (88 Å QW)/GaAs-AlGaAs(29-58 Å SL) BTM-QWIP.**

**(b) Energy band diagram for an InGaAs (106 Å QW)/GaAs-AlGaAs(59-30 Å SL) SBTM-QWIP.**

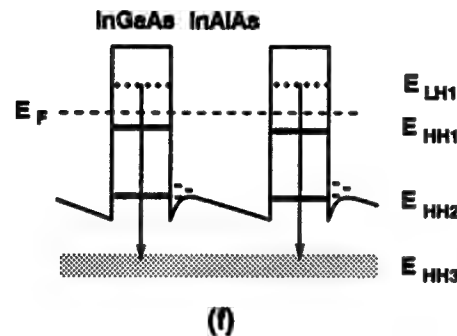
**(c) Energy band diagram for an InGaAs (110 Å QW)/InAlAs-InGaAs(30-46 Å SL) VT-QWIP.**

**(d) Energy band diagram for a GaAs(110 Å QW)/AlGaAs(875 Å BA) DM-QWIP.**

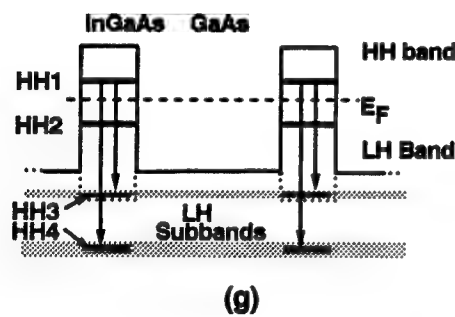
Figure 1.1. Schematic energy-band diagrams for these QWIPs developed in this work.



(e) Energy band diagram for an AlAs(30 Å QW)/AlGaAs(500 Å BA) type-II Normal Incidence QWIP.



(f) Energy band diagram for a p-type tensile strained-layer InGaAs(40 Å QW)/InAlAs(450 Å BA) PTSL-QWIP.



(g) Energy band diagram for a p-type compressive strained-layer InGaAs(40 Å QW)/GaAs(350 Å BA) PCSL-QWIP.

Figure 1.1. Continued.

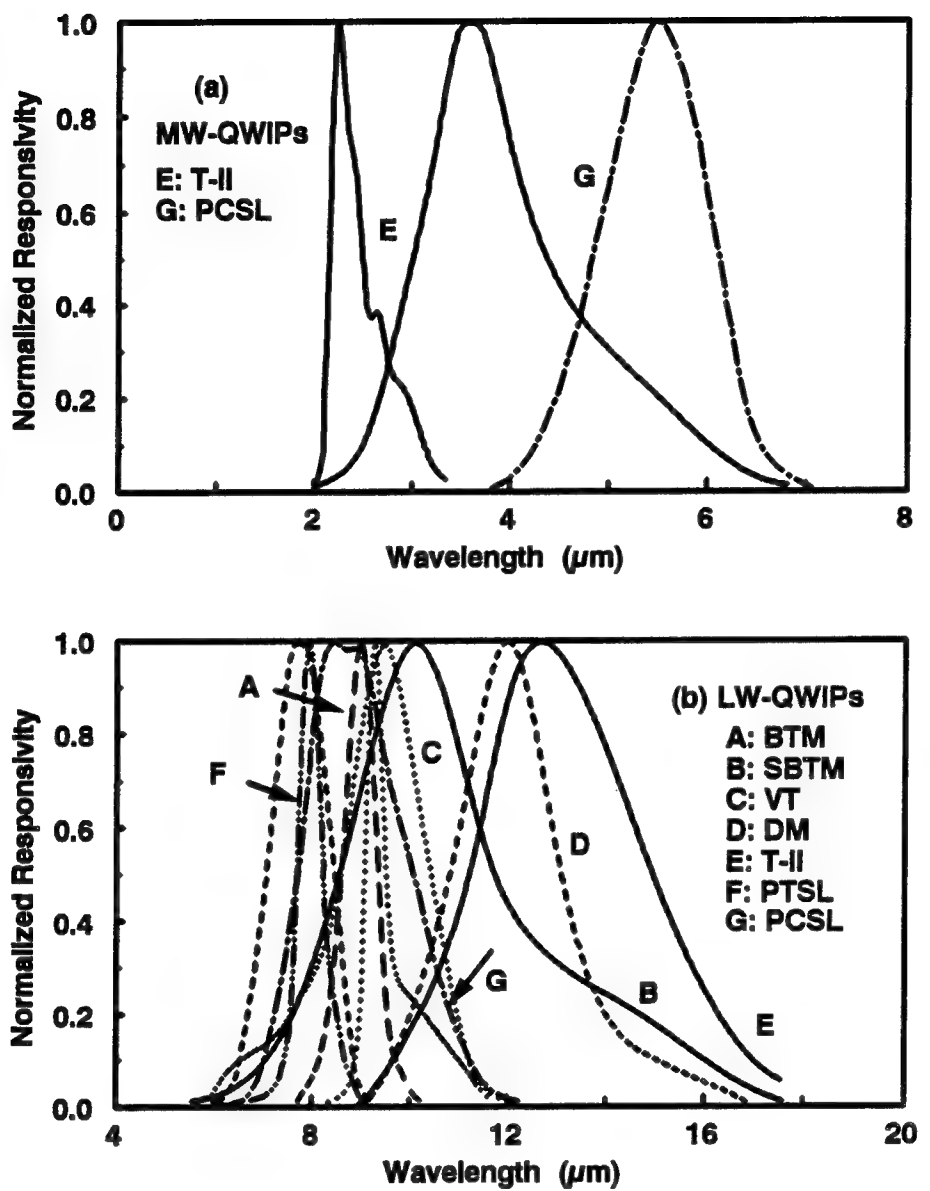


Figure 1.2. Normalized responsivities of (a) the 3-5  $\mu\text{m}$  MWIR and (b) the 8-14  $\mu\text{m}$  LWIR detection bands for these QWIPs developed in this work.

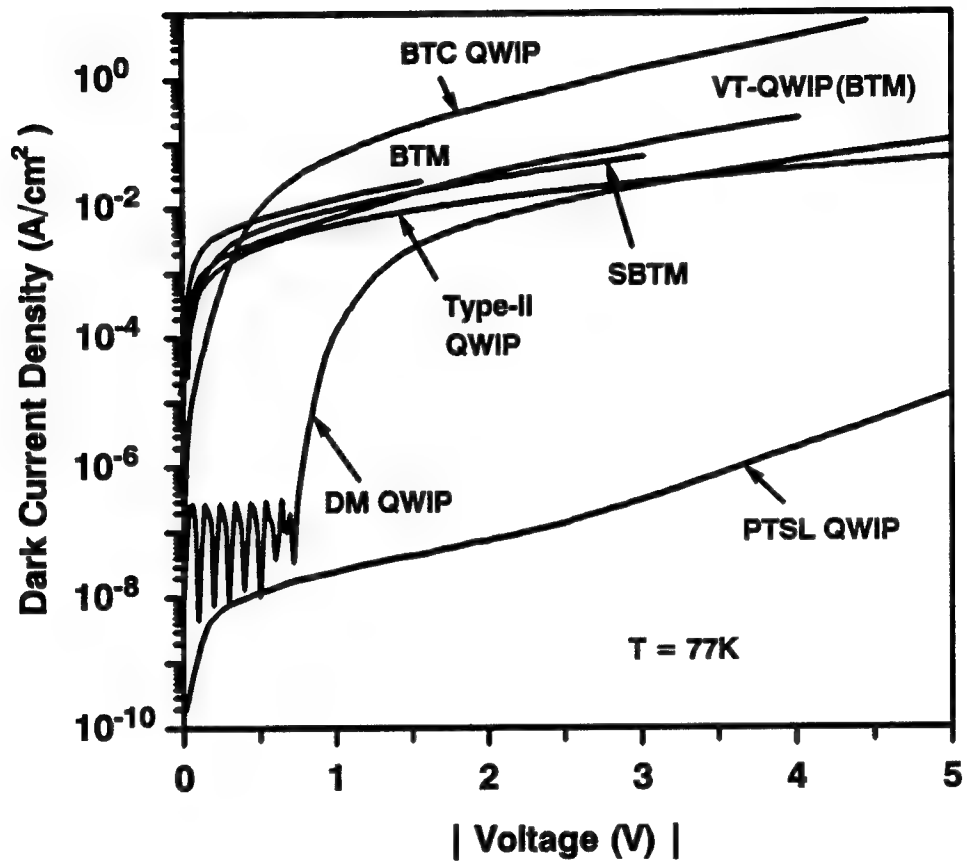


Figure 1.3. Dark current densities for these QWIPs developed in this work.

## 2. QUANTUM WELL AND SUPERLATTICE STRUCTURES

### 2.1. Introduction

The introduction of quantum well (QW) and superlattice structure makes it possible to design and fabricate various novel quantum devices [1-18]. Long wavelength infrared (LWIR) photodetectors using the superlattice and quantum well structures have been extensively investigated based on bound-to-bound [10, 19], bound-to-quasicontinuum [20], bound-to-miniband [13], bound-to-continuum [11, 21], and mini-band-to-miniband [22, 23] intersubband transition mechanisms. In order to understand the optical and electrical properties of quantum well and superlattice structures, it is necessary to study them from both macroscopic and microscopic theories.

### 2.2. Methods for Calculating Electronic States

A crystal is made up of a large number of interacting particles, positive nuclei surrounded by negative electrons. The nuclei form a rigid lattice that is completely frozen at low temperatures. As the temperature is raised, nuclei vibrate about their mean positions, as described by phonons. Consequently, the theoretical treatment of the energy levels and wavefunctions in solids cannot be attempted without a number of simplifying approximations. We can write the total Hamiltonian of the system in the form

$$H_t = T_e + T_N + V_{ee} + V_{eN} + V_{NN}, \quad (2.1)$$

where  $T_e$  and  $T_N$  are the kinetic energy of electrons and nuclei, respectively, and  $V_{ee}$ ,  $V_{eN}$ , and  $V_{NN}$  are the electron-electron, electron-nuclei, and nuclei-nuclei interactions, respectively. Since the strongest force between particles in a solid is due to coulomb interaction, the kinetic (T) and potential (V) energy terms can be expressed as

$$T = - \sum \frac{\hbar^2}{2m^*} \nabla^2 \quad (2.2)$$

$$V = \sum \frac{Ze^2}{4\pi\epsilon_0|r_i - r_j|}, \quad (2.3)$$

where  $Z = 1$  is for the electron, otherwise for the nuclei charges.

The system Schrödinger equation can be written as

$$H_t \Psi(\mathbf{R}, \mathbf{r}) = E \Psi(\mathbf{R}, \mathbf{r}). \quad (2.4)$$

The system wavefunction  $\Psi(\mathbf{R}, \mathbf{r})$  can be expressed as the product of the nuclei wavefunction  $\chi(\mathbf{R})$  and the electron wavefunction  $\psi(\mathbf{R}, \mathbf{r})$ ,

$$\Psi(\mathbf{R}, \mathbf{r}) = \chi(\mathbf{R})\psi(\mathbf{R}, \mathbf{r}) \quad (2.5)$$

where  $\mathbf{R}$  represents the space and spin coordinates of the nuclei and  $\mathbf{r}$  denotes the coordinates for the electrons. This eigenvalue problem can be further simplified for electronic states by using some basic approximations.

Due to the extremely different masses between the electrons and the nuclei, the eigenvalue problem can be split into two separate, though interdependent, eigenvalue problems for electrons and nuclei by using the *adiabatic approximation* [24], which assumes that electrons will adiabatically follow the lattice (or nuclei) vibration. The eigenvalues for electrons and nuclei can be solved from

$$[T_e + V_{ee} + V_{eN}] \psi_n(\mathbf{R}, \mathbf{r}) = E_n(\mathbf{R}) \psi_n(\mathbf{R}, \mathbf{r}); \quad (2.6)$$

$$[T_N + V_{NN} + E_n(\mathbf{R})] \chi(\mathbf{R}) = E_n \chi(\mathbf{R}), \quad (2.7)$$

where subscript  $n$  denotes a quantum number of the coordinates for the electrons. Even though we have the electron eigenvalue expression, this still represents a very complicated many-body problem. However, most of the systems such as the superlattice can be described by using the *one-electron approximation*, which assumes that the motion of a single electron experiences some average force due to vibrating lattice and all other particles. These one-electron wavefunctions satisfy the self-consistent Hartree-Fock equations [25]. The solution of the Hartree-Fock equation is still a very difficult mathematical problem. For this reason, the *band approximation* is often employed, i.e., one solves the Schrödinger equation with an assumed crystal potential  $V(\mathbf{r})$  [26]. The time-independent one electron Schrödinger equation and the potential are given by

$$\left[ -\frac{\hbar^2 \nabla^2}{2m^*} + V(\mathbf{r}) \right] \psi_n(\mathbf{k}, \mathbf{r}) = E_n(\mathbf{k}) \psi_n(\mathbf{k}, \mathbf{r}), \quad (2.8)$$

$$V(\mathbf{r}) = V_L(\mathbf{r}) + V_E(\mathbf{r}) + V_S(\mathbf{r}), \quad (2.9)$$

where  $V_L$  represents the perfect lattice periodic potential,  $V_E$  is the superlattice periodic potential, and  $V_S$  is the random scattering potential. Figure 2.1 schematically shows the three components of  $V(\mathbf{r})$ . The wavefunction of the electron is  $\psi_n(\mathbf{k}, \mathbf{r})$  and the eigenvalue of the electron in the  $\mathbf{k}$ -space

for n-th band is  $E_n(\mathbf{k})$ . For example, near the bottom of the conduction band, the eigenvalues of electrons in a superlattice can be described by

$$E_n(\mathbf{k}) = E_n(k_z) + \frac{\hbar^2}{2m_{x,y}^*}(k_x^2 + k_y^2), \quad (2.10)$$

where  $E_n(k_z)$  is the energy dispersion relation along the superlattice axis (longitudinal) and other terms are the energy dispersion relations within the superlattice plane (transverse).

There are two different but equivalent procedures for obtaining the energy states and wavefunctions with the band approximation, which assumes that potential is invariant for all symmetry operations. These two procedures are (1) expand the crystal states on a complete set of Bloch type function and then determine the expansion coefficients by requiring the states to satisfy the appropriate Schrödinger equation, such as the tight binding method, the orthogonal plane wave (OPW) method, or the pseudopotential method, and (2) expand the states on a complete set of functions that are solutions of the Schrödinger equation within a unit cell and then determine the expansion coefficients by the appropriate boundary conditions, such as the cellular method, the augmented plane wave (APW) method, or the Green's function method. As a practical matter one has to choose, from physical considerations, the method whose set of basis function sufficiently represents the exact eigenfunction within the band approximation. Besides the two basic analytical procedures above, semi-empirical approaches and interpolation schemes (i.e.,  $\mathbf{k.p}$  theory) are also very powerful tools in determining effective masses and densities of states (DOS) near high symmetry points in  $\mathbf{k}$  space such as  $\mathbf{k} = 0$  of Brillouin zone center. Based on the  $\mathbf{k.p}$  method, calculations of the band structure of a superlattice have been carried out by using the Kronig-Penney model and the modifications of the boundary condition [27]. The nonparabolicity effects in the band structures have been taken into account by using the Kane model [5].

By considering only the periodic potential  $V_L(\mathbf{r})$  in  $V(\mathbf{r})$  (ignoring  $V_E$  and  $V_S$ ), the solution of the Schrödinger equation is the Bloch type wavefunction,

$$\psi_{n,\mathbf{k}}(\mathbf{r}) = U_{n,\mathbf{k}}(\mathbf{r}) \exp(i\mathbf{k} \cdot \mathbf{r}), \quad (2.11)$$

where  $U_{n,\mathbf{k}}(\mathbf{r})$  is a periodic function with the same periodicity as  $V_L$  and  $n$  denotes the band index. By considering slow varying potential  $V_E$  and random scattering potential  $V_S$  and using calculated dispersion relation  $E_n(\mathbf{k})$ , the eigenvalues and eigenfunctions can be solved by using the *effective mass envelope function* approach. The effective mass envelope equation for n-th band can be written as

$$[E_n(-i\nabla) + V_E + V_S]\phi_n(\mathbf{r}) = E\phi_n(\mathbf{r}), \quad (2.12)$$

where  $\phi_n(\mathbf{r})$  is the envelope function and  $E$  is the eigenvalues that satisfy the effective mass equation. If the multiband model is incorporated in the effective mass equation, summation over band index  $n$  is required.

If the superlattice growth is along  $z$ -direction ( $x$ - and  $y$ -directions within superlattice plane), then the Bloch function becomes

$$\psi_{n,\mathbf{k}}(\mathbf{r}) = U_{n,\mathbf{k}}(z) \exp(i k_x x + i k_y y) \quad (2.13)$$

and the envelope function  $\phi_n(\mathbf{r})$  becomes a function of coordinate  $z$ , that is,  $\phi_n(z)$ .

### 2.3. Superlattice and Miniband

In conventional quantum wells, carriers are confined within potential barriers that are formed by energy band gap offset between two materials. In order to reduce the tunneling dark current from the ground states in the quantum wells, the use of thicker barrier layers between the wells is very important for high performance of the QWIPs. However, these QWIP structures suffer from the large dark current due to the defect existence in the thicker barrier layers. In order to overcome this problem, very short period superlattice barrier layers are introduced to replace the thicker barrier layers [13]. The superlattice barriers can confine the defects within the thin layer and significantly reduce the dark current. The replacement of the superlattice barrier layer offers several new features over the conventional quantum wells. They are (1) improvement of the roughness at the heterojunction interfaces by superlattice smoothing, (2) reduction of interface recombination, (3) elimination of deep-levels-related phenomena [28], and (4) realization of a coherent conduction with large quantum photocurrent gain [7].

The superlattice barrier quantum wells also involve the confinement of carriers and the determinations of energy eigenvalues and wavefunctions in the heterostructure. When the carrier de Broglie wavelength becomes comparable to the barrier thickness of the superlattice, the wavefunctions of the individual wells tend to overlap due to tunneling, hence the global minibands are formed. The miniband decoupling occurs when the bias voltage across one period of the superlattice becomes larger than the miniband bandwidth. From the carrier transport point of view, the superlattice can have an adjustable effective barrier height by properly selecting superlattice structure parameters. Due to the adjustability of the superlattice, carrier conduction through the superlattice can be tuned and modulated by the miniband intrinsic transport properties, such as coherent tunneling conduction and ballistic resonant conduction.

### 2.3.1. Dispersion Relations

In an A-B type-I (two different materials) superlattice with growth direction along the z-axis, one period of the alternating layers is called the basis of the superlattice, denoting L (= L<sub>a</sub> + L<sub>b</sub>, L<sub>a</sub> for wells and L<sub>b</sub> for barriers). Since the superlattice period L is much longer than the lattice constant, the Brillouin zone is divided into a series of minizones, leading to a narrow subband (or miniband). As a result, the actual wavefunction of a superlattice is the product of the Bloch wavefunction, which is a periodic function of the atomic potential, and the envelope wavefunction, which is a function of the superlattice potential,

$$\psi(\mathbf{k}, \mathbf{r}) = \sum_n \phi_n(z) U_{n,\mathbf{k}}(z) \exp(ik_x x + ik_y y), \quad (2.14)$$

where summation is over the band index n and k<sub>x,y</sub> are the transverse wavevectors in x- and y-direction.

In the effective mass approximation and using the one-band Kronig-Penney model, the envelope wavefunction  $\phi_n(z)$  can be written as [29]

$$\phi_n(z) = \begin{cases} C_1 \cos[k_a(z - L_a/2)] + C_2 \sin[k_a(z - L_a/2)] & \text{in the well} \\ C_3 \cos[k_b(z + L_b/2)] + C_4 \sin[k_b(z + L_b/2)] & \text{in the barrier,} \end{cases} \quad (2.15)$$

where

$$k_a = \frac{[2m_a^*(E - E_a)]^{1/2}}{\hbar} \quad (2.16)$$

$$k_b = \frac{[2m_b^*(E - E_b)]^{1/2}}{\hbar}, \quad (2.17)$$

C<sub>1~4</sub> are constants that depend on boundary conditions and subband index parity, E<sub>a,b</sub> are band minima or maxima for the well and barrier layers.

Bastard [27] has shown that, in the parabolic band approximation, the dispersion relation for the unbound states is

$$\cos[k_z(L_a + L_b)] = \cos(k_a L_a) \cos(k_b L_b) - \frac{1}{2}(1/\xi + \xi) \sin(k_a L_a) \sin(k_b L_b) \quad (2.18)$$

with  $\xi = m_b^* k_a / m_a^* k_b$  and k<sub>z</sub> defines the superlattice wavevector.

The dispersion relation for the bound states is still valid if one substitutes k<sub>b</sub> by iκ<sub>b</sub> and ξ by -iξ' with  $\xi' = m_b^* k_a / m_a^* \kappa_b$ ,

$$\cos[k_z(L_a + L_b)] = \cos(k_a L_a) \cosh(\kappa_b L_b) - \frac{1}{2}(1/\xi' - \xi') \sin(k_a L_a) \sinh(\kappa_b L_b). \quad (2.19)$$

The minibands for the bound and unbound states can be obtained from Eqs. (2.18) and (2.19). The higher minibands could extend above the potential barriers. However, the electron in-plane wavefunction of superlattice experiences only a regular lattice periodicity, and the dispersion relations in transverse direction (i.e.,  $k_x$  and  $k_y$ ) are much like those for unperturbed cases (i.e., Bloch type wavefunction). It is noted that transverse wavevectors ( $k_x$ ,  $k_y$ ) are conserved across the interfaces since the interface potential in the envelope function approximation depends only on the  $z$  coordinate. However, the spatially dependent effective masses are not entirely decoupled and are  $3 \times 3$  tensors, which introduces nonparabolicity to the subbands. The bandwidth of a miniband is an exponential function of the superlattice barrier thickness  $L_b$ ,

$$\Gamma \sim \exp(-CL_b), \quad (2.20)$$

where  $C$  is a constant. The miniband bandwidths and miniband energy levels versus barrier thickness are illustrated in Fig. 2.2. It is noted that the bandwidth becomes wider and wider as the barrier thickness decreases.

Another feature in superlattice is the effective mass modulation. The effective mass  $m_z$  of a miniband can be deduced from the dispersion relation  $E_n(k_z) = E' (\text{reference}) - (1/2)\Gamma \cos[k_z(L_a + L_b)]$ ,

$$m_z^* = \frac{2\hbar^2}{\Gamma L^2} \quad (2.21)$$

$$\sim \frac{\exp(CL_b)}{(L_a + L_b)^2}. \quad (2.22)$$

A smaller effective mass  $m_z^*$  with higher electron mobility for both wells and barriers can be obtained along superlattice axis. The wider the miniband bandwidth is, the smaller the tunneling time constant becomes. When the tunneling time is much smaller than the carrier relaxation time and scattering time, a coherent and ballistic carrier conduction through the miniband can be built up, which is desirable for QWIP applications.

The above results hold for a perfect superlattice with a flat band diagram, ignoring the effects of growth layer fluctuations and roughness, electron-electron interaction, electron-phonon interaction, and depolarization. In reality, all these corrections to energy states and wavefunctions should be incorporated in the calculations of the miniband properties. In order precisely to analyze superlattice miniband dispersion relations, the two-band or three-band model should be used in which interband and intervalley interactions are included (see Appendix A).

### 2.3.2. Transmission Probability $|T \cdot T|$

The transmission probability through a superlattice can be calculated numerically by using the transfer matrix method [30]. The carrier conduction in each layer of the superlattice potential regions consists of superposition of two components propagating in the forward and backward directions, respectively. The total wavefunctions can be written as

$$\psi_i = \psi_i^+ e^{-i\Delta_i} e^{+ik_i} + \psi_i^- e^{+i\Delta_i} e^{-ik_i}; \quad (2.23)$$

where

$$\begin{aligned} \Delta_1 &= \Delta_2 = 0, \\ \Delta_i &= k_i(d_2 + d_3 + \dots + d_i) \\ i &= 3, 4, \dots, N \end{aligned} \quad (2.24)$$

$$k_i = \left[ \frac{2m_i^*}{\hbar^2} (E - E_i) \right]^{1/2}, \quad (2.25)$$

where  $\psi_i^+$  and  $\psi_i^-$  represent the magnitudes of the particle wave functions propagating along the  $+z$  and  $-z$  directions, respectively,  $N$  is the number of the period of a superlattice, and  $d_i$ ,  $m_i^*$ ,  $E_i$  are the thickness, effective mass, and potential energy of  $i$ -th layer in the superlattice, respectively. Since  $\psi$  and  $d\psi/dz$  are continuous at the boundaries, we obtain

$$\psi_i^+ = (e^{-i\delta_i} \psi_{i+1}^+ + r_i e^{-i\delta_i} \psi_{i+1}^-)/t_i \quad (2.26)$$

$$\psi_i^- = (r_i e^{i\delta_i} \psi_{i+1}^+ + e^{i\delta_i} \psi_{i+1}^-)/t_i. \quad (2.27)$$

Here the recurrence relation may be written in matrix form

$$\begin{pmatrix} \psi_i^+ \\ \psi_i^- \end{pmatrix} = \frac{1}{t_i} \begin{pmatrix} e^{-i\delta_i} & r_i e^{-i\delta_i} \\ r_i e^{i\delta_i} & e^{i\delta_i} \end{pmatrix} \begin{pmatrix} \psi_{i+1}^+ \\ \psi_{i+1}^- \end{pmatrix}, \quad (2.28)$$

where (at normal incidence)

$$r_i = \frac{k_i - k_{i+1}}{k_i + k_{i+1}} \quad (2.29)$$

$$t_i = \frac{2k_i}{k_i + k_{i+1}} \quad (2.30)$$

$$\delta_i = k_i d_i. \quad (2.31)$$

Thus, we have

$$\begin{pmatrix} \psi_1^+ \\ \psi_1^- \end{pmatrix} = S_1 \begin{pmatrix} \psi_2^+ \\ \psi_2^- \end{pmatrix} = S_1 S_2 \begin{pmatrix} \psi_3^+ \\ \psi_3^- \end{pmatrix} = \dots = S_1 S_2 \dots S_N \begin{pmatrix} \psi_{N+1}^+ \\ \psi_{N+1}^- \end{pmatrix}. \quad (2.32)$$

Since there is no backward propagating component in the last medium, i.e.,  $\psi_{N+1}^- = 0$ , one can find  $\psi_i^+(i = 2, 3, \dots, N + 1)$  in term of  $E_1^+$ , where  $i$  represents the layer region to be investigated. If we calculate the quantity  $\frac{\psi_i^+}{\psi_1^+}$  as a function of  $E$ , then we can obtain the resonant peaks with Lorentzian distribution. The transmission probability is given by

$$|T \cdot T| = \left| \frac{\psi_i^+}{\psi_1^+} \right|^2. \quad (2.33)$$

## 2.4. Carrier Transports

The carrier transport in the QWIPs plays a key role in the performance of QWIPs. In general, the carrier conduction processes in the quantum well/superlattice structures are quite complicated. Basically, they can be divided into three different conduction processes: the continuum state conduction, the miniband conduction, and the hopping conduction.

### 2.4.1. Continuum State Conduction

When the excited states of a QWIP lie above the quantum well barrier, the states become continuum states, which have 3-dimensional (3-D) conduction properties. Charge carriers (i.e., either dark or photoexcited carriers) that transport through the continuum states generally have high mobility under applied bias conditions. If the electric field is high enough, then hot carrier conduction through the 3-D continuum states is expected. This type of conduction has advantages of high efficiency, high photoconductive gain, and long mean free path. In fact, if the excited state is placed just above the barrier, resonant infrared absorption and maximum oscillator strength can be obtained [31]. This type of the conduction is usually the dominant transport process in a bulk barrier QWIP.

### 2.4.2. Miniband Conduction

The miniband conduction is a coherent resonant tunneling process in which photoexcited carriers are phase-coherent to the incident IR radiation. This coherent conduction can lead to much higher carrier transmission probability through the quantum well and superlattice. Resonant transmission mode builds up in the miniband to the extent that the scattering reflected wave is cancelled out and the conduction transmitted wave is enhanced. The miniband conduction depends strongly on the miniband bandwidth, heterointerface quality, and layer thickness fluctuation. For example, it has been demonstrated that the morphological quality of the heterointerface can be greatly improved by using interruption growth technique for a few tens of seconds [32]. The interruption growth allows one to reduce the density of monolayer terraces in the plane of the

heterointerface. As a result, the interface improvement can enhance the coherence of the interfacing electron wave overlapping and resonant coupling. In the miniband conduction, the effective mass of the photoexcited electrons can be modulated by superlattice structure parameters, given by  $m_z^* = (2\hbar^2)/(\Gamma L^2)$ . An effective mass  $m_z^*$  for the miniband smaller than that of both the wells and barrier may be obtained. As a result, photoexcited electron transport in the miniband will have a higher electron mobility, which leads to a large oscillator absorption strength, high quantum efficiency, and high response speed. Furthermore, increasing the miniband bandwidth will reduce the tunneling time constant (i.e.,  $\tau_0 = \hbar/\Gamma = 6.6 \times 10^{-16}/\Gamma$  (in eV)). The value of  $\tau_0$  in a QWIP is estimated to be about 20 fs (for  $\Gamma = 30 \sim 70$  meV), while a scattering time constant  $\tau_S$  typically is about 0.1 ps. Thus, for  $\tau_0 \ll \tau_S$ , the coherent resonant tunneling can be built up in the miniband conduction process. The photocurrent strongly depends on the tunneling time constant  $\tau_0$ , while the intersubband relaxation time constant  $\tau_R$  is about 0.4 ps. From the theoretical calculation,  $\tau_0$  is found to be about 20 to 100 fs, hence  $\tau_0 \ll \tau_R$ . Thus, the photoexcited electrons can tunnel resonantly out of the quantum well/superlattice barrier via global miniband states.

In the miniband conduction, charge carrier transport through miniband states inside the quantum well has an average wavevector  $k_z = eF\tau_R/\hbar$ , where  $F$  is the applied electric field. The drift velocity  $v_d$  along the superlattice axis can be expressed as

$$v_d = \frac{\Gamma L}{2\hbar} \sin \left( \frac{eF\tau_R L}{\hbar} \right). \quad (2.34)$$

At low electric field, the carrier mobility along the superlattice axis is given by

$$\mu_z = \frac{e\Gamma L^2 \tau_R}{2\hbar^2}. \quad (2.35)$$

It is noted that the mobility is proportional to the miniband bandwidth  $\Gamma$  and the relaxation time  $\tau_R$  if the superlattice basis  $L$  is kept constant. Since the miniband bandwidth is an exponential function of the superlattice barrier thickness, the carrier mobility is also sensitive to the thickness of the superlattice barrier layer. A similar conclusion can also be drawn from the Boltzmann equation using the relaxation time approximation.

#### 2.4.3. Hopping Conduction

When the miniband conduction fails to form coherent conduction at higher electric field, the incoherent conduction becomes the dominant mechanism, which is referred to as the sequential resonant tunneling with a random wave phase. In the incoherent conduction, the states in the quantum wells (i.e., Kane state) become localized within the individual well, and the carriers will

transport via phonon-assisted tunneling (hopping) with a frequency of  $eFL/\hbar$ . A better approach for analysis of the incoherent hopping conduction is to utilize the carrier scattering mechanism. Carrier scattering tends to destroy the coherency of the wavefunctions, hence the fully resonant threshold value will never be built-up. The mobility of the hopping conduction is usually much lower than that of the miniband conduction. As the barrier layer thickness or the thickness fluctuation increases, the maximum velocity  $v_{max}$  ( $= \Gamma L/2\hbar$ ) and the carrier mobility decrease. This is due to the fact that the relaxation time is nearly independent of superlattice period  $L$ . The mobility for the hopping conduction can be expressed as [33]

$$\mu_z \approx \frac{eL^2A}{k_B T} \exp\left[-\left(\frac{8m^*}{\hbar^2}(\Delta E - E_1)\right)^{1/2} L_b\right]. \quad (2.36)$$

It is worth noting that the product of  $v_{max} \cdot \tau_R$  is always greater than the mean free path  $L_p$  in the miniband conduction. However, it will reduce to even smaller than the superlattice period  $L$  in the hopping conduction limit. When the QWIPs are operating at cryogenic temperature, phonon-assisted tunneling is suppressed, and other scattering sources such as ionized impurities, intersubband levels, and interface roughness can also play an important role in the tunneling conduction.

## 2.5. Corrections on Subband Energy States

### 2.5.1. Electron-Electron Interaction

In the calculations of electronic states in quantum well/superlattice structures, electron-electron interactions should be taken into consideration when the quantum well is doped to  $10^{18} \text{ cm}^{-3}$  or higher. The interaction includes two components, direct Coulomb force and quantum exchange interaction, which shift energy states in opposite directions. The Coulomb interaction shifts the subband up while the exchange interaction shifts down. In type-I quantum wells, the doping in the quantum well can give rise to charge neutrality within the well, and the exchange energy is more significant than that of Coulomb interaction.

In the one-electron approximation, the solution of the Hartree-Fock equation gives the self-consistent eigenfunctions  $\psi_n$  and eigenvalues  $E_n$ . The Hartree-Fock equation can be written as

$$\begin{aligned} -\frac{\hbar^2}{2m_a^*} \nabla^2 \psi_n(\mathbf{r}) + V(\mathbf{r})\psi_n(\mathbf{r}) + \sum_m \int d\mathbf{r}' \frac{e^2}{4\pi\epsilon|\mathbf{r}-\mathbf{r}'|} |\psi_m(\mathbf{r}')|^2 \psi_n(\mathbf{r}) \\ - \sum_m \int d\mathbf{r}' \frac{e^2}{4\pi\epsilon|\mathbf{r}-\mathbf{r}'|} \psi_m^*(\mathbf{r}') \psi_n(\mathbf{r}') \psi_m(\mathbf{r}) \delta_{s_n, s_m} = E_n \psi_n(\mathbf{r}). \end{aligned} \quad (2.37)$$

The third and fourth terms on the left-hand side of the above equation are the direct Coulomb and exchange interaction terms, respectively.

The exchange interaction energy term associated with electrons in the bound ground state is approximately given by [34]

$$E_{exch}(k = 0) \approx -\frac{e^2 k_F}{4\pi\epsilon} \left[ 1 - 0.32 \frac{k_F}{k_1} \right], \quad (2.38)$$

$$E_{exch}(k_F) \approx -\frac{e^2 k_F}{4\pi\epsilon} \left[ \frac{2}{\pi} - 0.32 \frac{k_F}{k_1} \right], \quad (2.39)$$

where  $k_1 = \pi/L_a$ ,  $k_F = (2\pi\sigma)^{1/2}$ , and  $\sigma = L_a N_D$  is the two-dimensional electron density in the quantum well. For the unpopulated excited states, the exchange-induced energy shift is very small, hence the dominant contribution to the energy shift is due to the electron-electron interaction in the highly populated ground bound state. Figure 2.3 shows a typical exchange-induced energy shift for  $N_D = 10^{18} \text{ cm}^{-3}$  and  $L_a = 100 \text{ \AA}$ .

The energy shift in the ground bound state due to the direct coulomb interaction is given by [35]

$$E_{direct} = \frac{3\sigma e^2}{8\epsilon k_1^2 L_a}. \quad (2.40)$$

This term has a small contribution to the energy shift compared to the exchange-induced energy shift (seen in Fig. 2.3).

### 2.5.2. Depolarization Effects

When IR radiation is impinging on a QWIP, resonant screening of the infrared field by electrons in the quantum well generates a depolarization field effect, which can cause the subband energy shift (also called the plasmon shift). The depolarization effect arises when the external field is screened by the mean Hartree field, which is caused by the other electrons polarized by the external field. The energy shift between subband  $E_0$  and  $E_1$  due to depolarization field effect is given by [36]

$$E_{dep} = \sqrt{\frac{2\sigma e^2(E_0 - E_1)S_{01}}{\epsilon L_a}}, \quad (2.41)$$

where  $S_{01}$  is the Coulomb matrix element given by

$$S_{01} = \int_0^\infty dz \left[ \int_0^z \phi_0(z') \phi_1(z') dz' \right]^2. \quad (2.42)$$

It is noted that the depolarization effect increases as dopant density increases (see Fig. 2.3).

### **2.5.3. Other Effects**

Besides the corrections discussed above on energy states, the temperature shift [37], band nonparabolicity [38], and band bending effect [39] due to dopant migration can also alter the energy states in the wells, which make the deviation from the effective mass approximation. However, compared with the correction from the exchange energy and depolarization effect, these effects give only a small correction on subband energy states.

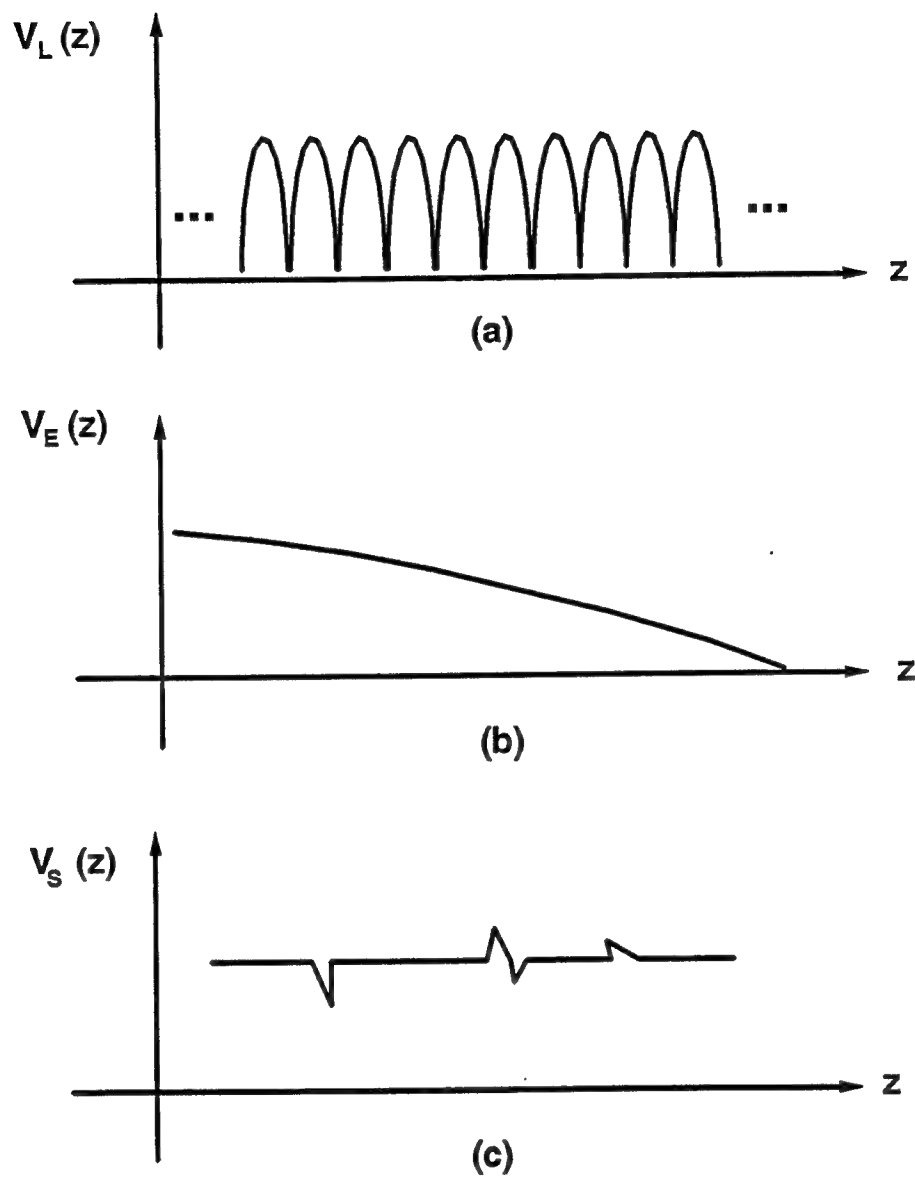


**Figure 2.1.** Three components of the potential energy  $V(\mathbf{r})$  of electrons:  
 $V = V_L + V_E + V_S$ , (a) perfect lattice periodic potential  $V_L$ , (b) superlattice periodic potential  $V_E$ , and (c) random scattering potential  $V_S$ .

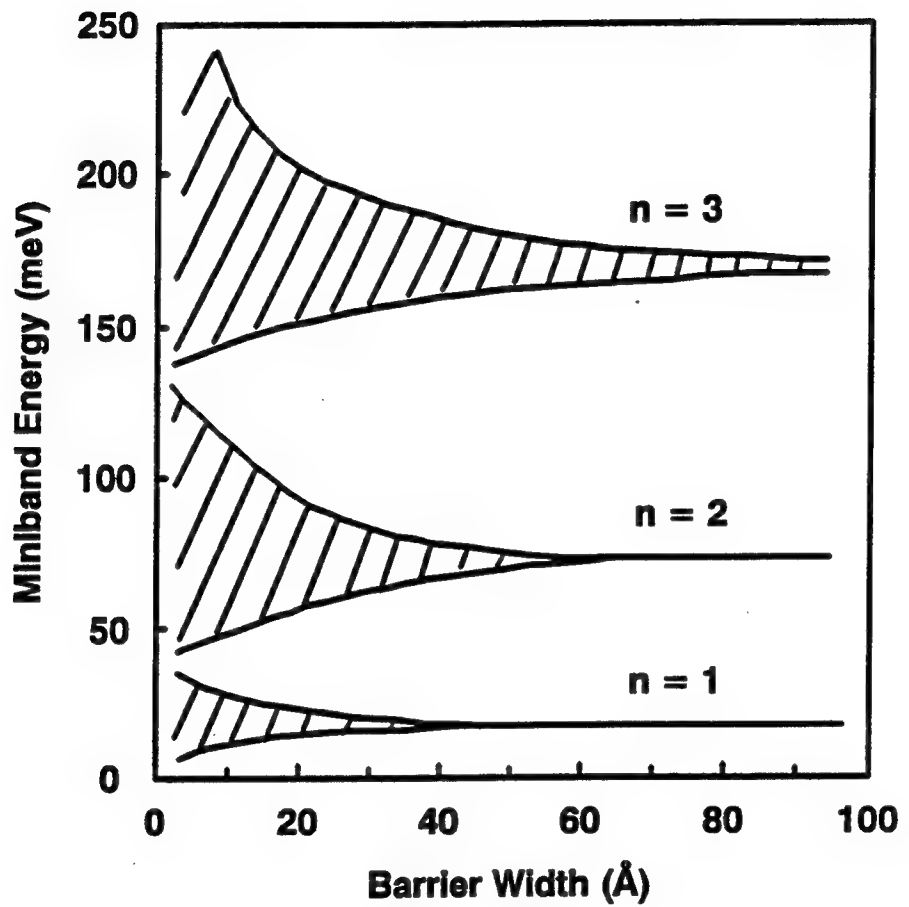


Figure 2.2. Illustration of miniband energy levels and their bandwidths as a function of the superlattice barrier width.

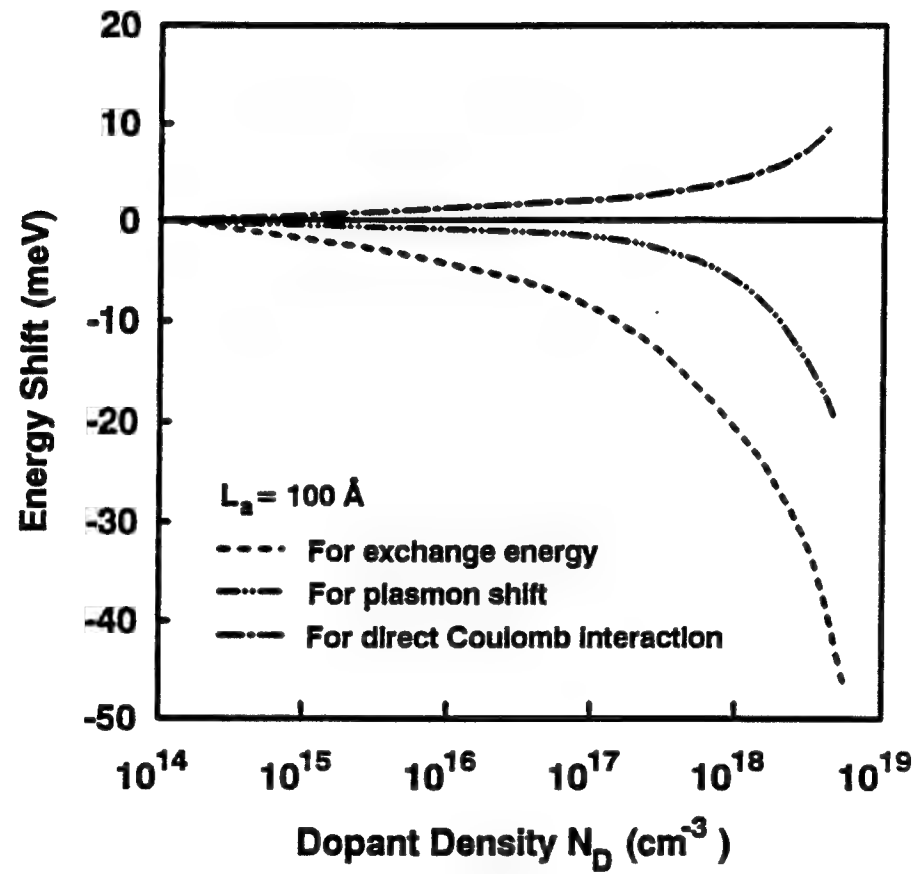


Figure 2.3. Calculated energy shifts due to the direct Coulomb interaction, the electron-electron interaction, and the depolarization effect for  $N_D = 10^{18} \text{ cm}^{-3}$  and  $L_a = 100 \text{ \AA}$ .

### 3. PHYSICS OF QWIPS AND FIGURES OF MERIT

#### 3.1. Introduction

Recently, rapid progress has been made in the development of high performance quantum well infrared photodetectors (QWIPs) [11-23]. The  $128 \times 128$  imaging sensor arrays using GaAs/AlGaAs QWIPs for 8 to  $14 \mu\text{m}$  LWIR detection have been demonstrated by using hybrid technology [14, 15]. The detectivity of the LWIR QWIPs has been improved dramatically in recent years and is now high enough to allow fabrication of large two-dimensional (2-D) staring focal plane arrays (FPAs) with performance comparable to the state-of-the-art MCT IR FPAs.

QWIPs fabricated from III-V material systems such as GaAs/AlGaAs and InGaAs/InAlAs offer a number of potential advantages over MCT material. These include (1) III-V material growth by using MBE or MOCVD is more matured than MCT, (2) monolithic integration of III-V QWIPs with GaAs readout circuits on the same chip is possible, (3) GaAs substrates are larger, cheaper, and higher quality than MCT, (4) III-V materials are more thermal stable than MCT, (5) higher yield, lower cost, and higher reliability is expected in III-V QWIPs than in MCT devices, and (6) III-V QWIPs have inherent advantages in both transient and total dose radiation hardness compared to MCT detectors.

#### 3.2. Intersubband Transition

The intersubband transition in a QWIP takes place between the subband levels of either the conduction band or the valence band. It has some unique features, which include (1) large absorption coefficient [9], (2) narrow absorption bandwidth [40], (3) large optical nonlinearity [41], (4) fast intersubband relaxation [42], (5) reduced Auger effect [43], (6) wavelength tunability [44], and (7) large photocurrent gain. The intersubband transition process can be analyzed by using the *dipole transition model* [45]. The transition rate  $W$  from the initial state  $\psi_i$  to the final state  $\psi_f$  can be described by

$$W_{i \rightarrow f} = \frac{2\pi}{\hbar} \sum_f | \langle \psi_f | V_p | \psi_i \rangle |^2 \delta(E_f - E_i - \hbar\omega), \quad (3.1)$$

where  $\omega$  is the incident photon frequency and  $V_p$  is the interaction potential between the incident

IR radiation and the electrons, which is given by [46]

$$V_p = \frac{eA_o}{m_o c} \hat{\epsilon} \cdot \mathbf{P}, \quad (3.2)$$

where  $A_o$  is the vector potential,  $c$  is the speed of light in vacuum,  $m_o$  is the free-electron mass,  $\mathbf{P}$  is the momentum operator of electron, and  $\hat{\epsilon}$  is the unit polarization vector of the incident photons.

Since the electron wavefunction  $\psi_n(\mathbf{k}, \mathbf{r})$  in the quantum well is the product of Bloch function  $\psi_{n,\mathbf{k}}(\mathbf{r}) (= U_{n,\mathbf{k}}(z) \exp(ik_x x + ik_y y))$  and the envelope function  $\phi_n(z)$ , the transition matrix element can be approximated by

$$\begin{aligned} M_{if} &= \langle (\psi_{n,\mathbf{k}}\phi_n)_f | V_p | (\psi_{n,\mathbf{k}}\phi_n)_i \rangle \\ &\sim \langle (\psi_{n,\mathbf{k}})_f | V_p | (\psi_{n,\mathbf{k}})_i \rangle_{cell} \langle \phi_{nf} | \phi_{ni} \rangle + \\ &\quad \langle (\psi_{n,\mathbf{k}})_f | (\psi_{n,\mathbf{k}})_i \rangle_{cell} \langle \phi_{nf} | V_p | \phi_{ni} \rangle. \end{aligned} \quad (3.3)$$

In the interband transition scheme, the dipole transition occurs between the Bloch states while the envelope states (or momentum vectors) holds constant, hence the second term on the right-hand side of Eq. (3.3) tends to vanish. However, in the intersubband transition scheme such as QWIPs, the dipole transition is between the envelope states while the Bloch states remain *nearly* constant, thus the first term on the right-hand side of Eq. (3.3) becomes zero. From the calculation of the transition matrix element  $M_{if} = \langle \psi_f | V_p | \psi_i \rangle$ , the transition selection rules and the incident polarization requirement for the intersubband transition can be determined.

Finally, the absorption coefficient  $\alpha$  can be calculated by using the expression [46]

$$\alpha_{i \rightarrow f} = \frac{2\pi\hbar c W_{i \rightarrow f}}{n_r A_o^2 \omega}, \quad (3.4)$$

where  $n_r$  is the refractive index of the medium. This absorption coefficient curve can be fitted by the Lorentzian function. The integrated absorption strength  $I_A$  for the polarized incidence radiation at the Brewster angle is given by

$$I_A = \sigma N S \frac{e^2 h}{4\epsilon_o m^* c} \frac{f_{os}}{n_r^2 \sqrt{n_r^2 + 1}}, \quad (3.5)$$

where  $N$  is the number of quantum wells,  $S$  is the quantum well structure factor, and  $f_{os}$  is the dipole oscillator strength given by

$$f_{os} = \frac{4\pi m^* c}{\hbar \lambda} \left( \int_{-L_a/2}^{L_a/2} \psi_f z \psi_i dz \right)^2. \quad (3.6)$$

When the incident radiation is perpendicular to the quantum well surface, transition matrix element  $M_{if}$  is zero if the shape of constant energy surface of the material is spherical. A nonzero transition rate can be obtained by using either a 45° polished facet illumination or a grating coupler [47] for the spherical constant energy surface materials. For a transmission grating coupler, the grating equation is given by

$$n_r \sin\theta_m - \sin\theta_i = m\lambda_p/\Lambda, \quad (3.7)$$

where  $\lambda_p$  is the resonant incident wavelength,  $\Lambda$  is the grating period,  $\theta_{i,m}$  denote the incident and the m-th order diffracted angle with respect to the superlattice axis, respectively. In a grating coupled QWIP, the integrated absorption strength  $I_A$  in Eq. (3.5) should be multiplied by a factor of  $\sin^2 \theta_m / \cos\theta_m$ .

### 3.3. PC and PV Detection Modes

A photodetector may be operated in either the photoconductive (PC) mode or the photovoltaic (PV) mode. In the BTC QWIPs, most of them are operated in the photoconductive (PC) mode and a few are operated in the photovoltaic (PV) mode. However, in the BTM QWIPs, they may be operated in the PC and PV dual-mode detection because of the bandwidth modulation effect in the miniband conduction QWIPs.

A photoconductor exhibits a change in resistance  $\Delta R_d$  when IR radiation is impinging on it. This change of the resistance is due to the generation of the mobile carriers in the photoconductor. The photogenerated carriers  $\Delta n$  can be written as

$$\Delta n = \frac{\eta \Delta \Phi_o \tau_L}{V'} \quad (3.8)$$

where  $\eta$  is the quantum efficiency,  $\Delta \Phi_o$  is the incident photon flux,  $\tau_L$  is the excess carrier lifetime,  $V'$  is the volume of the detector. The photogenerated carriers will transport in the detector under applied bias, thus resulting photovoltage signal. The change in output photovoltage  $\Delta V_o$  due to the resistance change is given by

$$\Delta V_o = - \frac{V_a R_L \Delta R_d}{(R_L + R_d)^2}, \quad (3.9)$$

where  $R_L$  is the load resistance and its value is chosen to be about equal to  $R_d$  in order to give optimized output signal.

When a QWIP operates in the photovoltaic detection mode, the photogenerated carriers can be transported in the detector without using externally applied bias. An internal built-in potential,  $V_{bi}$ , can be created in the bound-to-miniband intersubband transition, which is due to the

growth asymmetry and effective mass filtering effect through the global miniband. In the PV mode detection, the QWIP has an extremely low dark current, and the detector noise is dominated by Johnson noise which is much lower than that of the PC mode detection. The PV mode detector performance can be evaluated by  $R_d A_d$  product, where  $A_d$  is the active area of the detector.

### 3.4. Figures of Merit

In designing a quantum well infrared photodetector, it is important to understand the key parameters that determine the performance of a QWIP. They include: the dark current  $I_d$ , noise equivalent power (NEP), responsivity ( $R$ ), and detectivity  $D_\lambda^*$ . The QWIP performance can be evaluated by these parameters, which are often called the figures of merit.

#### 3.4.1. Dark Current $I_d$

In a quantum well infrared photodetector, the dark current is due to both the thermionic emission and tunneling conduction. In a conventional QWIP, thermionic emission conduction is dominant, whereas in a BTM QWIP thermionic-assisted tunneling conduction through the miniband is dominant. In order to achieve a background limited performance (BLIP) in a QWIP, the dark current must be kept below the background photocurrent (also called window current).

In the low-field regime, the thermionic emission current is related to the density of mobile carriers  $n_t$  and the average drift velocity  $v_d$ . It can be expressed as [48]

$$I_{th} = A_d e v_d n_t, \quad (3.10)$$

where  $A_d$  is the detector active area, and

$$v_d = \frac{\mu F}{[1 + (\mu F/v_s)^2]^{1/2}}, \quad (3.11)$$

$$n_t = (m^* k_B T / \pi \hbar^2 L) \exp[-(E_{cut} - E_F)/(k_B T)]. \quad (3.12)$$

Here  $v_s$  is the saturation drift velocity,  $E_{cut}$  is the cutoff energy related to the cutoff wavelength  $\lambda_c$ , and  $m^* / \pi \hbar^2$  is the 2-dimensional density of states. The Fermi level  $E_F$  can be obtained from

$$N_D = \frac{m^* k_B T}{\pi \hbar^2 L_a} \sum_n \ln \left[ 1 + \exp \left( \frac{E_F - E_n}{k_B T} \right) \right] \quad (3.13)$$

$$\approx \frac{m^*}{\pi \hbar^2 L_a} \sum_n (E_F - E_n). \quad (3.14)$$

It is noted that  $N_D$  expression is valid for summation over subband levels  $E_n$  below the Fermi level  $E_F$  and the approximate expression for  $N_D$  is only true for cryogenic temperature.

As a result, in the cryogenic temperature range, the dark current from thermionic emission conduction is exponentially proportional to the doping concentration in the quantum well,

$$I_{th} \propto e^{E_F/(k_B T)} \propto e^{CN_D/(k_B T)} \quad (3.15)$$

where C is a constant. It is noted that the dark current is a strong function of the quantum well doping concentration. On the other hand, the intersubband absorption is proportional to the well doping concentration. Therefore, the optimized QWIP performance is the tradeoff between the high intersubband transition and the low dark current operation.

In the miniband conduction, the coherent tunneling current component is dominant compared to the thermionic emission current component and other components such as sequential tunneling, phonon-assisted tunneling, and defect-assisted tunneling. The coherent tunneling current along the superlattice axis can be expressed by [49, 50]

$$I_{tun} = A_d \int_0^{\infty} |T \cdot T| g(E_z, V_b) dE_z \quad (3.16)$$

where  $|T \cdot T|$  is the transmission probability (see Chapter 2.3.2) and  $g(E_z, V_b)$  is the energy distribution function along superlattice axis at bias voltage  $V_b$ , which can be expressed as

$$g(E_z, V_b) = \frac{4\pi e m_z^* k_B T}{h^3} \ln \left( \frac{1 + \exp[(E_F - E_z)/(k_B T)]}{1 + \exp[(E_F - E_z - eV_b)/(k_B T)]} \right). \quad (3.17)$$

Modified Fermi level  $E_F$  resulting from the correction due to exchange energy, cryogenic temperature, depolarization effect should be used in the calculation of both  $I_{th}$  and  $I_{tun}$ .

### 3.4.2. Spectral Responsivity R

Spectral responsivity  $R_A$  for the PC mode QWIP is defined by the photocurrent output (in ampere) under IR radiation power (in watt) at a specific wavelength. The responsivity depends on the detector quantum efficiency  $\eta$  and the photoconductive gain  $g$ , and can be written as

$$R_A = \frac{e}{h\nu} (\eta \cdot g) = \frac{e}{h\nu} \eta_c \quad (3.18)$$

$$= \frac{\lambda}{1.24} \eta_c, \quad (3.19)$$

where

$$\eta = \kappa(1 - R_f)(1 - e^{-m\alpha l}). \quad (3.20)$$

Here  $R_f$  is the reflection coefficient (typical 0.3 for GaAs),  $\kappa$  is the polarization correction factor ( $\kappa = 0.5$  for n-type QWIP and  $\kappa = 1$  for p-type QWIP),  $m$  is the number of absorption pass,  $\alpha$  is the absorption coefficient for the superlattice, and  $l$  is the total superlattice thickness.

The spectral responsivity (V/W) for the PV mode QWIP can be obtained from the relationship  $R_V = R_A \cdot R_d$ , where  $R_d$  is differential resistance of a QWIP.

### 3.4.3. Collection Efficiency $\eta_c$

The QWIP collection efficiency  $\eta_c$  describes the converting efficiency from incident radiation photons to net carriers that are collected at the output of the QWIP, and is defined as the product of the quantum efficiency  $\eta$  to photoconductive gain  $g$ , namely,  $\eta_c = \eta \cdot g$ .

Photoconductive gain  $g$  is expressed as the ratio of the carrier transport lifetime  $\tau_L$  to the transit time  $\tau_T$  through a QWIP. From the empirical point of view, the photoconductive gain can be described in terms of the capture or trapping probability  $p_c$  [51, 52],

$$g = \frac{1 - p_c}{N p_c}. \quad (3.21)$$

The trapping probability  $p_c$  is defined as the ratio of the escaping time in the well region to the lifetime of the excited carriers from the confined ground state. If the excited states are resonantly lined up with the top of the barrier, the escaping time will be greatly reduced, thus minimizing trapping probability and maximizing the photoconductive gain.

The final expression for  $\eta_c$  can be given by

$$\eta_c = \kappa(1 - R_f)(1 - e^{-m\alpha l}) \frac{1 - p_c}{N p_c} \quad (3.22)$$

$$\approx \kappa(1 - R_f) \frac{m\alpha l}{N p_c}. \quad (3.23)$$

It is noted that the approximate expression is only true for  $m\alpha l \ll 1$  and  $p_c \ll 1$ .

### 3.4.4. Noise Characteristics of a QWIP

The common sources of noise in a QWIP are the thermal noise, generation-recombination (g-r) noise, and the flicker noise. The thermal noise in a QWIP may be attributed to the random motion of the charge carriers. It produces a fluctuating emf across its terminals and is related directly to the detector temperature. In semiconductors, the number of carriers fluctuate because of generation and recombination via donors, traps, recombination centers, or band-to-band transitions. Therefore, the resistance,  $R$ , fluctuates. If  $\delta R(t)$  represents this fluctuation and a dc current  $I$  flows through the sample, then a fluctuating emf  $\delta V(t) = I\delta R(t)$  will be developed across the terminals. This noise is called the generation-recombination noise, or g-r noise. Most of the noise sources has a frequency-independent spectrum at low frequencies, whereas the spectral intensity decreases at

higher frequencies. The only exception is the flicker noise, which usually has a  $1/f$  spectrum throughout the entire frequency range. As a result, the flicker noise is often called the  $1/f$  noise. We shall briefly discuss each of these noise sources as follows.

(i) Thermal Noise: Thermal noise theory was first reported by Nyquist in 1928 [53]. The thermal noise, also known as Johnson noise [54], is the dominant noise source at very low bias in a QWIP. From the Nyquist equation, the current spectral density for a QWIP with resistance  $R$  and temperature  $T$  can be expressed by

$$S_i(f) = \frac{4kT}{R} \quad (3.24)$$

(ii) Generation-Recombination (g-r) Noise: The general expression for the fluctuation of free carrier density  $N$  in a QWIP can be expressed as

$$\frac{dN}{dt} = g(N) - r(N) + \Delta g(t) - \Delta r(t) \quad (3.25)$$

where  $g(N)$  and  $r(N)$  denote the generation and recombination rates of carriers, respectively, and  $\Delta g(t)$  and  $\Delta r(t)$  describe the randomness in these rates. With  $N = N_o + \Delta N$ ,  $g(N_o) = r(N_o)$ , and Poisson statistics,  $\overline{\Delta N^2} = \overline{N}$ , the g-r spectrum density can be written as

$$S_N(f) = 4\overline{\Delta N^2} \frac{\tau}{1 + \omega^2 \tau^2} \quad (3.26)$$

This equation is valid for all the g-r processes described by fluctuations in carrier density  $N$ .

(iii) Flicker Noise: Flicker noise was discovered in vacuum tubes by Johnson [54] in 1925 and interpreted by Schottky in 1926 [55]. The main characteristic of the flicker noise is that it has a  $1/f^\alpha$  spectrum with  $\alpha$  close to unity. For that reason, the flicker noise is also referred to as the  $1/f$  noise.

One popular explanation for the  $1/f$  noise is the so-called McWhorter model [56] which interprets the  $1/f$  spectrum as a superposition of a large number of Lorentzian spectra,  $4A_i \tau_i / (1 + \omega^2 \tau_i^2)$ . Another possible explanation for the  $1/f$  noise is given in terms of mobility fluctuations caused by lattice scattering and Brehm strahlung effect, which produce true  $1/f$  noise. However, the observed excess noise in QWIPs at low frequencies does not exactly show a  $-1$  frequency slope, and hence the McWhorter model appears to be more adequate for the QWIP devices.

(iv) Noise Gain: In a QWIP, the number of conduction electrons is equal to the total number of electrons  $N_c$  excited from the bound ground state to the miniband states. For an average current

$\overline{I_d} = N_c i_e$ , the noise current spectral density is given by

$$S_i(f) = i_e^2 S_N(f) = 4\overline{I_d}^2 \frac{\overline{\Delta N^2}}{N_c^2} \frac{\tau}{1 + \omega^2 \tau^2} \quad (3.27)$$

For a QWIP that satisfies the Poisson statistics, the variance  $\overline{\Delta N^2}$  is equal to  $N_c$ . Using  $\overline{I_d} = qN_c/\tau_d$ , Eq. (3.27) becomes

$$S_i(f) = 4q\overline{I_d}g \frac{1}{1 + \omega^2 \tau^2} \quad (3.28)$$

where  $g = \frac{\tau}{\tau_d}$  is defined as the “noise current gain”;  $\tau$  is the carrier lifetime and  $\tau_d$  is the carrier transit time across the QWIP. For most QWIPs with  $\omega\tau \ll 1$ , the g-r noise current spectral density can be simplified to

$$S_i(f) \approx 4q\overline{I_d}g \quad (3.29)$$

#### (v) Electron Trapping Probability:

To derive the electron trapping probability expression for a QWIP, three assumptions are made in the model: (a) the photon flux is independent of the position; (b) the dark current is limited by thermal effects and the interwell tunneling is negligible, and (c) perfect ohmic contacts.

Let us consider a QWIP with  $N$  quantum wells. If  $p$  denotes the electron trapping probability for the excited carriers in the extended states to be trapped into the bound ground state of the quantum well, then  $(1 - p_c)$  is the probability that electrons will escape from the well region. Applying the current continuity condition, the photocurrent flows through the  $N$  quantum wells of the QWIP can be expressed by [51]

$$i_{photo} = q\phi\eta' \frac{(1 - p_c)}{p_c} = q\phi\eta \frac{(1 - p_c)}{Np_c} \quad (3.30)$$

where the quantum efficiency  $\eta \approx N\eta'$ , and  $\eta'$  is the quantum efficiency of the single quantum well. The photocurrent gain  $g$  is related to the capture probability  $p$  by

$$g = \frac{(1 - p_c)}{Np_c} \quad (3.31)$$

Since the current gain of a QWIP is independent of the excitation methods, the photocurrent gain given in Eq. (3.31) should be the same as the noise gain.

### 3.4.5. Detectivity $D_\lambda^*$

The detectivity of a QWIP is a very important figure of merit, which measures the QWIP sensitivity and the normalized QWIP noise equivalent power (NEP) with respect to the detector area and noise bandwidth. It can be calculated by

$$D_\lambda^* = \frac{R_A \sqrt{A_d \Delta f}}{i_n}, \quad (3.32)$$

where  $\Delta f$  is the noise spectral bandwidth, and  $i_n$  is the overall root-mean-square noise current (in unit of A) for a QWIP. In general, the noise current for the QWIP includes two components, one is QWIP's dark current noise  $i_{nd}$  and the other is 300 K background photon noise current  $i_{nb}$ .

The dark current noise  $i_{nd}^2$  is given by

$$i_{nd}^2 = \begin{cases} 4eI_{dg}\Delta f & \text{for G-R noise} \\ \frac{4k_B T}{R_d} \Delta f & \text{for Johnson noise.} \end{cases} \quad (3.33)$$

The G-R noise is associated with random thermal excitation and decay of the carriers, thus resulting in the fluctuation in the number of the carriers in the QWIP. The G-R noise is the dominant noise current source in the PC mode detection QWIP. However, the Johnson noise is associated with the fluctuation in the velocity of the carriers, which is the dominant noise current source in the PV mode detection QWIP.

The background photon noise is caused by the fluctuations in the number of background photons absorbed by a QWIP, which can be calculated based on the arrival statistics of the incoherent photons. The background photon noise current  $i_{nb}^2$  is given by [57, 58]

$$i_{nb}^2 = 4e^2 g^2 \left( \eta \kappa \frac{P_b}{h\nu} \right) B, \quad (3.34)$$

where  $P_b$  is the incident background optical power for unit time,  $B$  is the QWIP bandwidth,  $\eta$  is the absorption quantum efficiency,  $\kappa$  is the polarization correction factor,  $\nu$  is the incident photon frequency, and  $g$  is the photoconductive gain.

The overall noise current for the QWIP is expressed by

$$i_n^2 = i_{nd}^2 + i_{nb}^2 \quad (3.35)$$

$$= 4eg \left[ I_d + eg \left( \eta \kappa \frac{P_b}{h\nu} \right) \right] \Delta f \quad (3.36)$$

$$= 4eg(I_d + I_b)\Delta f, \quad (3.37)$$

where  $I_b = eg\eta\kappa[P_b/(h\nu)]$  is the background photocurrent detected by the QWIP. When  $I_d < I_b$ , the overall noise current  $i_n \sim i_{nb}$ , and the QWIP is operated under the background photon noise

limitation. When  $I_d > I_b$ , the overall noise current  $i_n \sim i_{nd}$  and the QWIP is operated under the operation of G-R noise or Johnson noise limitation. The detectivity  $D_\lambda^*$  for each noise source limitation can be calculated by

$$D_\lambda^* = \begin{cases} \frac{\kappa R_A \sqrt{A_d \Delta f}}{i_{nb}} & \text{for background photon noise limitation} \\ \frac{R_A \sqrt{A_d \Delta f}}{i_{nd}} & \text{for dark current noise limitation.} \end{cases} \quad (3.38)$$

### 3.4.6. Background Limited Performance (BLIP)

A mid-wavelength or long-wavelength QWIP has two kinds of backgrounds: (1) high temperature ambient background ( $T = 300$  K) and (2) low temperature cold background ( $T = 77$  or  $195$  K). Under the normal thermal imaging condition, the total current feeding to the following readout circuits in a QWIP includes both the dark current  $I_d$  and  $300$  K background photocurrent  $I_b$  (i.e.,  $I_d + I_b$ ). Due to the limitation on the charge handling capacity in the following readout circuits, the total current level of a QWIP under proper operation must be below this limited charge capacity for a given integration time of the imaging arrays. In addition, in order to achieve the stable and clear imaging patterns, it is highly desirable to operate QWIPs under the background photon noise limitation, that is the background limited performance (BLIP).

The BLIP operation requires that  $I_b > I_d$ . In order to reduce  $I_d$  down to less than  $I_b$ , QWIP has to be operated at a low temperature  $T \sim 77$  K for LWIR ( $8 \sim 14$   $\mu\text{m}$ ) detection and  $T \sim 195$  K for MWIR ( $3 \sim 5$   $\mu\text{m}$ ) detection. BLIP temperature  $T_{\text{BLIP}}$  can be found from

$$I_d(T = T_{\text{BLIP}}) = I_b \quad (3.39)$$

$$= eg\eta\kappa \left( \frac{P_b}{h\nu} \right) \quad (3.40)$$

$$= A_d e g \eta \kappa Q_b \quad (3.41)$$

where  $Q_b = P_b / (A_d h\nu)$  is the incident photon flux density from the background for a given spectral bandwidth  $\Delta\nu$  at peak wavelength  $\lambda_p$ .  $Q_b$  is given by

$$Q_b = \frac{2\pi}{c^2} \frac{\nu^2 \Delta\nu}{e^{h\nu/k_B T_B} - 1} \sin^2 \left( \frac{\theta}{2} \right), \quad (3.42)$$

where  $\theta$  is the field of view (FOV) and  $T_B$  is the background temperature of the QWIPs ( $T_B = 300$  K for ambient temperature). On the other hand, the background photocurrent  $I_b$  can be modified by using different FOV. As a result,  $T_{\text{BLIP}}$  for a QWIP can also be changed by using different FOV optical configuration.

In a BLIP QWIP, the dominant noise source is the background photon noise while other noise sources such as G-R noise and Johnson noise are negligible in comparison. Under normal imaging

conditions, the photosignal current  $I_{ph}$  can be approximated by

$$I_{ph} = (e/h\nu)\eta\kappa g P_{ph}, \quad (3.43)$$

where  $P_{ph}$  is the incident optical signal power for the unit time. By setting the signal-to-noise power ratio equal to unity (i.e.,  $I_{ph} = i_{nb}$ ), the background-limited noise equivalent power ( $NEP$ )<sub>BLIP</sub> and the detectivity  $D^*_{BLIP}$  for the QWIPs can be expressed by

$$(NEP)_{BLIP} = 2\sqrt{h\nu B P_b / (\eta\kappa)}, \quad (3.44)$$

$$D^*_{BLIP} = \sqrt{A_d B} / (NEP)_{BLIP} = \frac{\lambda}{2hc} \left( \frac{\eta\kappa}{Q_b} \right)^{1/2}. \quad (3.45)$$

It is noted that the detectivity  $D^*_{BLIP}$  for the BLIP QWIP is independent of both photoconductive gain  $g$  and dark current  $I_d$ , while the detectivity for the non-BLIP QWIP is dependent of both the  $g$  and the  $I_d$ .

When the readout circuit noise is ignored, %BLIP for a QWIP can be evaluated by using

$$\%BLIP \approx \frac{i_{nb}}{(i_{nb}^2 + i_{nd}^2)^{1/2}} \quad (3.46)$$

where  $i_{nb}$  and  $i_{nd}$  are the 300 K background photocurrent noise and dark current noise, respectively.

## **Part I**

### **N-type QWIPs**

## 4. METAL GRATING-COUPLED BOUND-TO-MINIBAND TRANSITION GaAs/AlGaAs QUANTUM WELL SUPERLATTICE INFRARED DETECTOR

### 4.1 Introduction

A principal concern with quantum well infrared photodetectors is obtaining high detectivity at high operating temperature. At high temperatures (77 K or higher), the detectivity is significantly reduced because of the existence of large dark current and its associated thermal noises. In the bound-to-continuum transition detector, the major dark current consists of thermionic emission contribution arising from the Maxwell-Boltzmann tail of Fermi-Dirac distribution above the AlGaAs barrier. To reduce the dark current, a higher barrier potential is needed to suppress the thermionic emission contribution.

The introduction of superlattice and quantum well technology makes it possible to design and construct various novel quantum devices which were impossible to make earlier. Several long wavelength infrared (LWIR) detectors based on bound-to-bound [19, 10], bound-to-virtual excited state [20], and bound-to-continuum [21, 11] state transition in the multiple quantum well structures have been extensively explored. A large photoconductive gain [59] has also been observed in the quantum-well infrared photodetector (QWIP's).

Here we focus on a class of long wave infrared (LWIR) detectors using the enlarged quantum well and short-period superlattice barrier structures. The infrared detection mechanism is based on the bound-to-miniband (BTM) transition and superlattice miniband transport. A high superlattice barrier potential is used to suppress the thermionic emission contribution to the dark current.

The creation of enlarged quantum wells and resonant miniband transport structure offers a great deal of design flexibility and improved device performance. Figure 4.1 shows the schematic conduction band energy diagram of the BTM transition GaAs/AlGaAs QWIP. The intersubband transition takes place from the localized bound ground state  $E_{EW_1}$  in the enlarged wells (EWs) to the resonant-coupled miniband state  $E_{SL}$  of the superlattice (SL) barrier. The absorption region of the detector consists of GaAs EWs cladded by the AlGaAs/GaAs superlattice (SL) barriers at both sides. The physical parameters of the quantum wells and superlattices are chosen so that

there are only two levels in the EW region, and the first excited level  $E_{EW_1}$  of the EW is merged and lined up with the ground level miniband  $E_{SL}$  of the SL on both sides of the GaAs quantum well to achieve a large oscillation strength  $f$  and intersubband absorption coefficient  $\alpha$ . Since the superlattice has a relatively thin barrier, the photoexcited electrons can easily tunnel through the superlattice and transport along the aligned miniband, which are then collected by the external ohmic contacts.

#### 4.2 Sample Preparation

The AlGaAs/GaAs multiple quantum well (MQW)/superlattice (SL) layer structure was grown on a semi-insulating (S.I.) GaAs substrate by using the molecular beam epitaxy (MBE) technique. A  $1\text{ }\mu\text{m}$  thick GaAs buffer layer of  $2.0 \times 10^{18}\text{ cm}^{-3}$  was first grown on a S.I. GaAs substrate, followed by the growth of a 40-period of GaAs quantum wells with a well width of  $88\text{ \AA}$  and a dopant density of  $2.0 \times 10^{18}\text{ cm}^{-3}$ . The barrier layer on each side of the GaAs quantum well consists of a 5-period of undoped  $\text{Al}_{0.4}\text{Ga}_{0.6}\text{As}$  ( $58\text{ \AA}$ ) /GaAs ( $29\text{ \AA}$ ) superlattice layers which were grown alternatively with the GaAs quantum wells. Finally, an  $n^+$ -GaAs cap layer of  $0.45\text{ }\mu\text{m}$  thick and dopant density of  $2.0 \times 10^{18}\text{ cm}^{-3}$  was grown on top of the MQW layer structure to facilitate ohmic contact.

#### 4.3 Theory, Experiments, and Discussions

In order to understand the mechanism of bound-to-miniband transition, a numerical calculation of the relative density of states  $D(E) = C |\psi(E)|^2$ , where  $C$  is a constant, for different potential energy  $E$  was performed for the multiple quantum well/superlattice layers by the matrix method [30]. For simplicity, the parabolic energy band relation and an effective mass  $m^* = 0.0665m_0$  were assumed in the calculation. Results are shown in Fig. 4.2. From the figure, one finds that a broad miniband  $E_{SL}$  structure was formed in the quantum well and the first excited state  $E_{EW_1} = 163\text{ meV}$  is merged with the superlattice miniband  $E_{SL}$ . The ground state is at  $E_{EW_0} = 42\text{ meV}$ . The Fermi level  $E_f$  was found to be  $68\text{ meV}$  above the ground state  $E_{EW_0}$ . The exchange energy shift [34] due to the doping concentration is estimated to be  $E_{xch} = 5\text{ meV}$  at  $T = 300\text{ K}$ , and  $18\text{ meV}$  at  $T = 20\text{ K}$ , respectively. Outside the quantum wells, the first continuum state is about  $4\text{ meV}$  above the barrier ( $E_{cn_1} = 326\text{ meV}$ ), and the second continuum state  $E_{cn_2}$  is  $48\text{ meV}$  higher than the first continuum state. A large energy separation  $E_{cn_1} - E_{EW_0} - E_{xch} = 300\text{ meV}$  is used to suppress the thermionic emission [40, 60].

Figure 4.3 shows the absorption spectral curve of the sample measured at  $T = 300\text{ K}$  by using a Perkin-Elmer Fourier transform infrared (FTIR) spectroscopy at the Brewster's angle.

The absorption peak is centered at  $\lambda_p = 9.6 \mu\text{m}$ . The measured peak absorbance  $A = -\log_{10}$  (transmission) was found to be about  $7 \times 10^{-2}$ . The bandwidth broadening, slightly larger than the expected value of 16 meV, might be attributed to the result of interface roughness and spatial inhomogeneities in the well and superlattice widths [9], high temperature influence, and higher subband lifetime broadening effect. Considering the peak wavelength position  $\lambda_p$  as well as the uncertainties such as band gap discontinuity, actual electron density distribution, true well shape, interactions between the electrons and phonons (phonon scattering), electrons and holes, the experimental results are in good agreement with the theoretical prediction.

Device characterization was carried out in a liquid-helium cryogenic dewar. An HP4140B semiconductor parameter analyzer was used to measure the dark current vs. voltage (I-V) curves. Figure 4.4 displays a semi-log scale plot of the I-V curves obtained for temperatures between 42 and 85 K. Under dark conditions, electrons can transfer out of the wells and produce the observed current mainly via two mechanisms. One is the thermionic emission out of the quantum wells, which is the dominant component of the dark current for the low barrier structure detectors at low bias, especially at higher temperatures. The other is the thermally generated carriers tunneling through the superlattice miniband. In the bound-to-miniband transition structure, we chose a high value of 'Al' composition,  $x = 0.4$ , which gave the barrier potential as high as  $\Delta E_c = 322 \text{ meV}$  ( $\sim 65\% \Delta E_g$ ). The highly localized and heavily populated ground state  $E_{EW_0}$  resides deep in the enlarged quantum well sandwiched between the large potential superlattice barrier regions, and far from the continuum states above the barrier. Therefore, carriers due to thermionic emission out of the quantum wells in the new QWIP's can be greatly reduced. On the other hand, the thermally generated carriers tunneling through the  $E_{EW_1}$  and the miniband can also be reduced by adjusting the bandwidth [61, 62] of the miniband  $E_{SL}$ . For our quantum well device with an area  $A = 4 \times 10^{-4} \text{ cm}^2$  and a doping concentration  $n_d = 2.0 \times 10^{18}$ , the dark current  $I_d$  was found to be around  $8 \times 10^{-9} \text{ A}$  at  $V_b = 0.2 \text{ V}$  and  $T = 68 \text{ K}$ , and  $9 \times 10^{-8} \text{ cm}^{-3} \text{ A}$  at  $T = 77 \text{ K}$ , respectively.

To enhance the light coupling efficiency to the quantum wells, we developed a planar transmission metal grating coupler for the top illumination, which consists of regularly spaced metal grating fingers. Its periodicity  $\Lambda$  is chosen so that the phase matches the peak wavelength of the spectral response (blazing wavelength  $\lambda_B$ ) of the detector. The metal grating was deposited by using E-beam evaporation of AuGe-Ni-Au materials. A high efficient grating pattern deposited on the top surface of the detector mesa structure for the front surface illumination was obtained by using a new planar grating with a periodicity  $\Lambda = 5 \mu\text{m}$  and ratio factor  $t/\Lambda = 0.4$ , where  $t$  is the metal strip width. The photocurrent was measured as a function of temperature, polarization

direction, radiation wavelength, using a CVI Laser Digikrom 240 monochromator and an ORIEL ceramic element infrared source. Due to the very large device resistance ( $\geq 500K\Omega$  in the temperature range from 6 K to 77 K) and the small values of dark current  $I_d$  present in the device , the short-circuit measurements were used to determine the photocurrent  $I_{ph}$ . Figure 4.5 (a) shows the normalized measured responsivity curve versus wavelength for the detector, which shows a peak spectral response at  $8.9 \mu m$  at  $T = 20$  K. In the inset of Fig. 4.5 (a), we also show the cross sectional view of a top illuminated metal grating coupled QWIP's used in this study with a periodicity of 5  $\mu m$ . Figure 4.5 (b) shows the measured responsivity  $R_\lambda$  as a function of the applied bias voltage  $V_b$  using  $8.9 \mu m$  radiation at  $T = 20$  K; a maximum responsivity  $R_\lambda = 0.54$  A/W was obtained at  $V_b = 1.2$  V. As expected, the device responsivity  $R_\lambda$  increases with the applied bias voltage from  $V_b = 0$  to  $V_b = 0.6$  V. For  $V_b > 0.6$  V, the photocurrent becomes saturated. A maximum operation bias at 1.8 V was obtained, and the photocurrent was found to decrease rapidly beyond 1.8 V, corresponding to the onset of the misalignment between the quasi-bound state levels and the superlattice miniband. The conduction mechanism for  $V_b \geq 1.8V$  is due to phonon assisted tunneling (or hopping conduction). Further increase in the applied bias voltage will result in a strong decrease of the detector responsivity, which is consistent with the fact of a total misalignment of the minibands in the EWs and the superlattice barrier layers. We also measured the temperature dependence of the responsivity, and found that the responsivity was slightly decreased as the temperature increased. However, the change was small, and the responsivity still retained a peak value of  $R_\lambda = 0.38$  A/W at  $V_b = 1.2$  V, and  $R_\lambda = 0.23$  A/W at  $V_b = 0.2$  V and at  $T = 77$  K.

It is worthwhile mentioning that a relatively large photocurrent was observed even at zero bias. One reason for this may be resulted from the space charges built up inside the superlattice layers. Another important mechanism could be due to the strongly coupled coherent states (miniband) transport in the superlattice structure. Since a large portion of the electron wave functions in the superlattice region is overlapped and the discrete quantum levels of the different superlattice layers are so closely packed, a strongly degenerate miniband is formed in the superlattice. There exists large coupling effects among these states. In other words, the excited electrons in the miniband are co-governed and shared by different quantum wells in the superlattice region, and the resonant tunneling can easily take place along the miniband. Therefore, the low bias operation, or the zero bias (dual-mode) condition can be realized in such a short period superlattice composed photoconductive detector. Similar phenomena were also observed in the different superlattice devices [7, 22, 23], even without grading layer.

From the measured responsivity and dark current, we can calculate the detectivity  $D^*$  of the

detector using the expression

$$D^* = R_\lambda (A\Delta f)^{1/2} / (4eI_dG\Delta f)^{1/2} \quad (4.1)$$

where A is the effective area of the detector, G is the optical gain, which can be evaluated from  $R_\lambda = \eta(\lambda/1.24)G$  and  $\eta = (1/2)(1 - e^{-2\alpha l})$ , and  $\Delta f$  is the bandwidth. For  $V_b = 0.2$  V, we found  $D^* = 1.6 \times 10^{10}$  cm $\sqrt{\text{Hz}}/\text{W}$  at  $\lambda = 8.9$   $\mu\text{m}$  and  $T = 77$  K. By optimizing the device parameters further improvements in detector performance can be realized in a GaAs/AlGaAs MQW IR detector.

The bound-to-miniband (BTM) transition detection scheme offers a great deal of flexibility in detector design and manufacture. It has received a lot of industrial attention for its potential infrared imaging applications. Extensive work has been conducted at Martin Marietta Laboratories in developing high quality  $128 \times 128$  long wavelength infrared (LWIR) detector array systems by using the BTM transition scheme. The arrays consist of 30 periods of enlarged wells and superlattice barriers. Pixels were  $40 \times 40$   $\mu\text{m}$  on  $50$   $\mu\text{m}$  centers. The peak wavelength is at  $\lambda_p = 9.5$   $\mu\text{m}$ , with a full width at half maximum (FWHM) of  $1.5$   $\mu\text{m}$ . At a bias of  $-3.0$  V the peak responsivity was  $50$  mA/W, yielding a peak  $D^* = 4 \times 10^9$  cm Hz $^{1/2}/\text{W}$  at  $T = 80$  K.

The hybridized focal plane array (FPA) had an uncorrected response non-uniformity of 18% and dark current non-uniformity of 20 - 30%. The pixel operability was greater than 99%. The noise-equivalent temperature difference of the array was about  $\text{NE}\Delta T = 0.1$  K, at  $T = 60$  K. With the improvement of readout electronics, a single pixel limited  $\text{NE}\Delta T \leq 0.01$  K is achievable.

#### 4.4 Conclusion

In conclusion, we have demonstrated a novel GaAs/AlGaAs multiple quantum well infrared photodetector (QWIP) using the bound-to-miniband transition, resonant tunneling and effective mass filtering mechanisms. The new structure also shows the advantages of large intersubband absorption and dual mode operation. With high detectivity, low bias operation, and grating coupled surface illumination, the GaAs QWIPs can be used for high quality detector arrays and infrared imaging sensors.

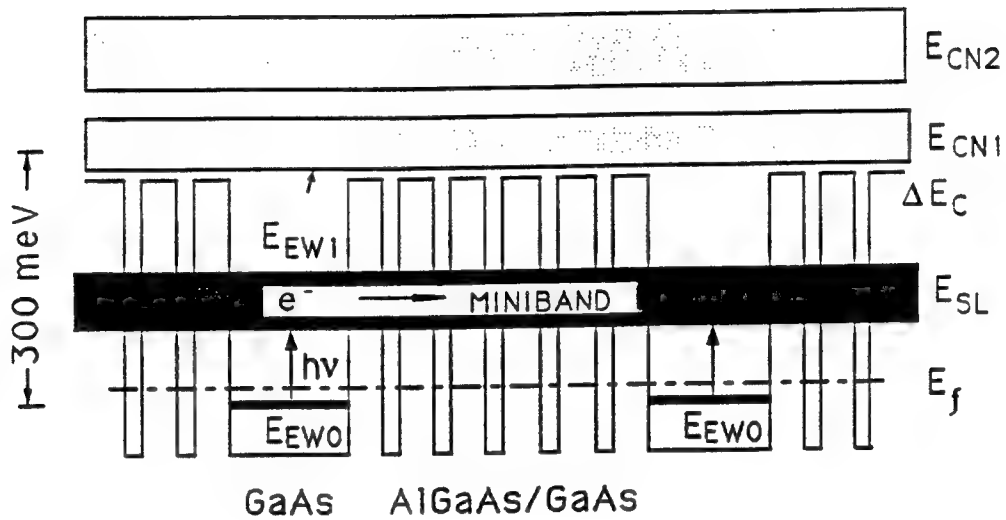


Figure 4.1 The energy band diagram for the bound-to-miniband transition followed by coherent superlattice miniband transport. The first excited level  $E_{EW1}$  of quantum well is aligned with the miniband  $E_{SL}$  of the superlattice to achieve a large absorption. The continuum states  $E_{cn_i}$  ( $i = 1, 2, \dots$ ) are “lifted” up away from the heavily populated ground state  $E_{EW0}$  to reduce the thermionic emission.

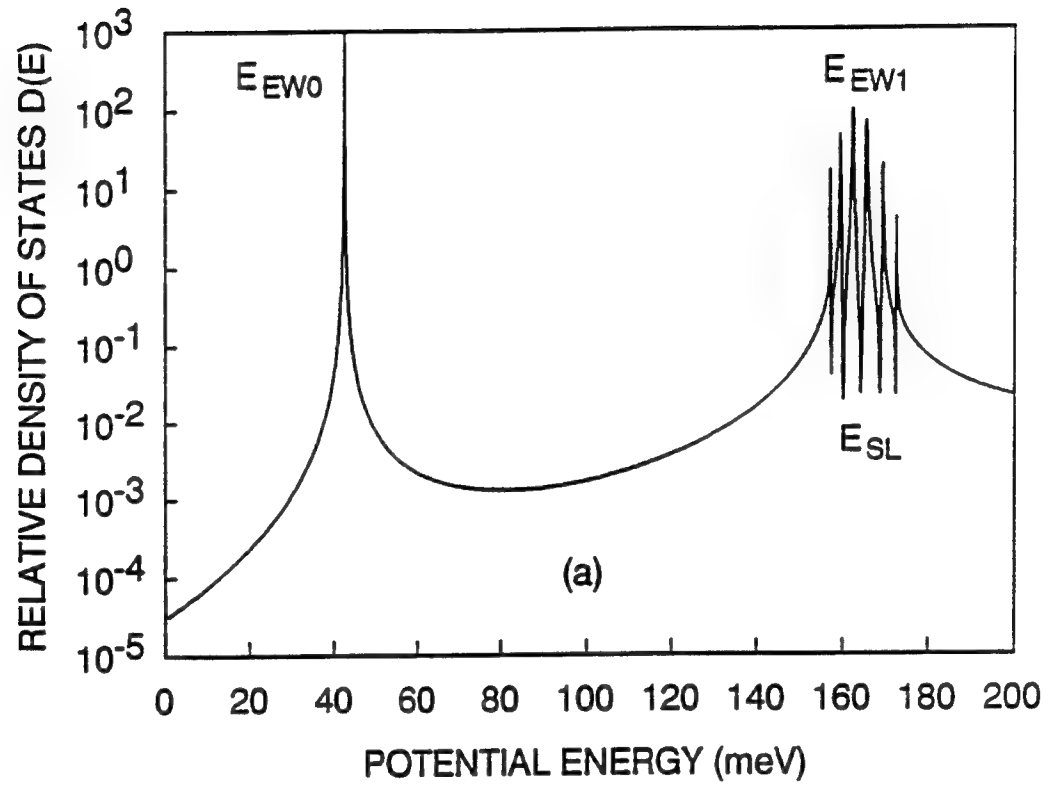


Figure 4.2 Calculated energy eigenvalues and relative density of states  $D(E)$  vs. electron potential energy  $E$  in the enlarged quantum well (EW). A broad miniband  $E_{SL}$  was formed in the quantum layer structure by using the superlattice barriers.

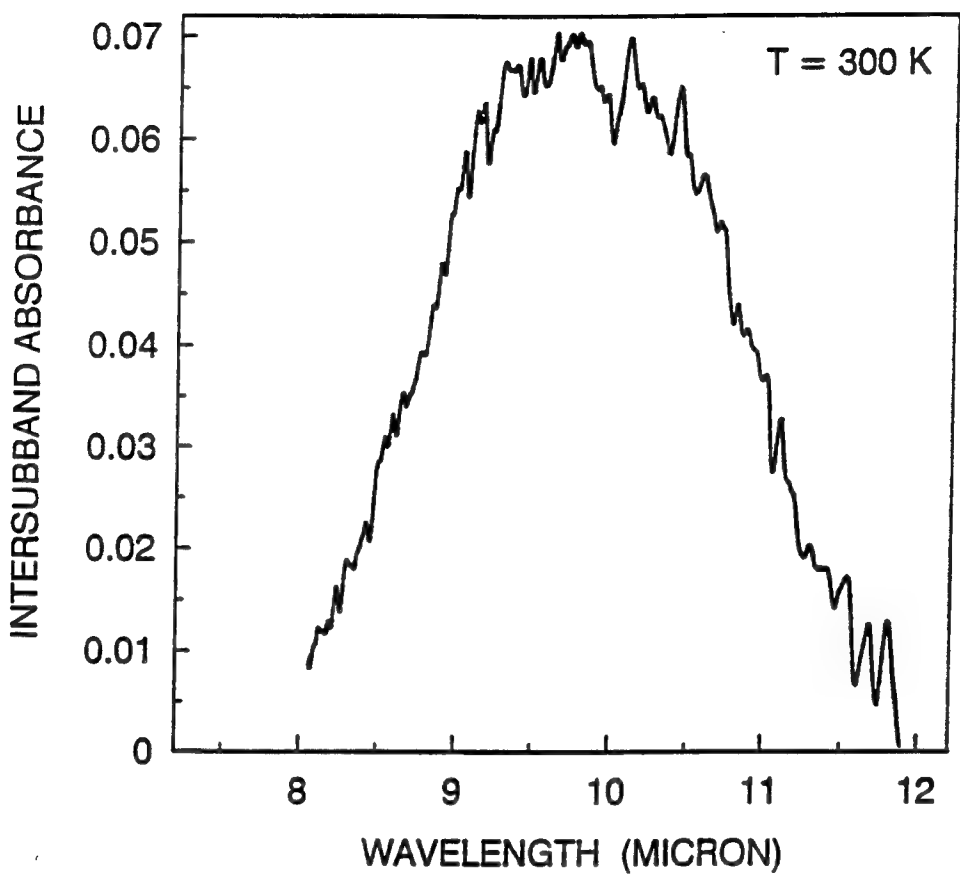


Figure 4.3 Measured room temperature ( $T = 300\text{ K}$ ) intersubband absorbance vs. wavelength by the Fourier transform infrared (FTIR) spectroscopy at the Brewster's angle.

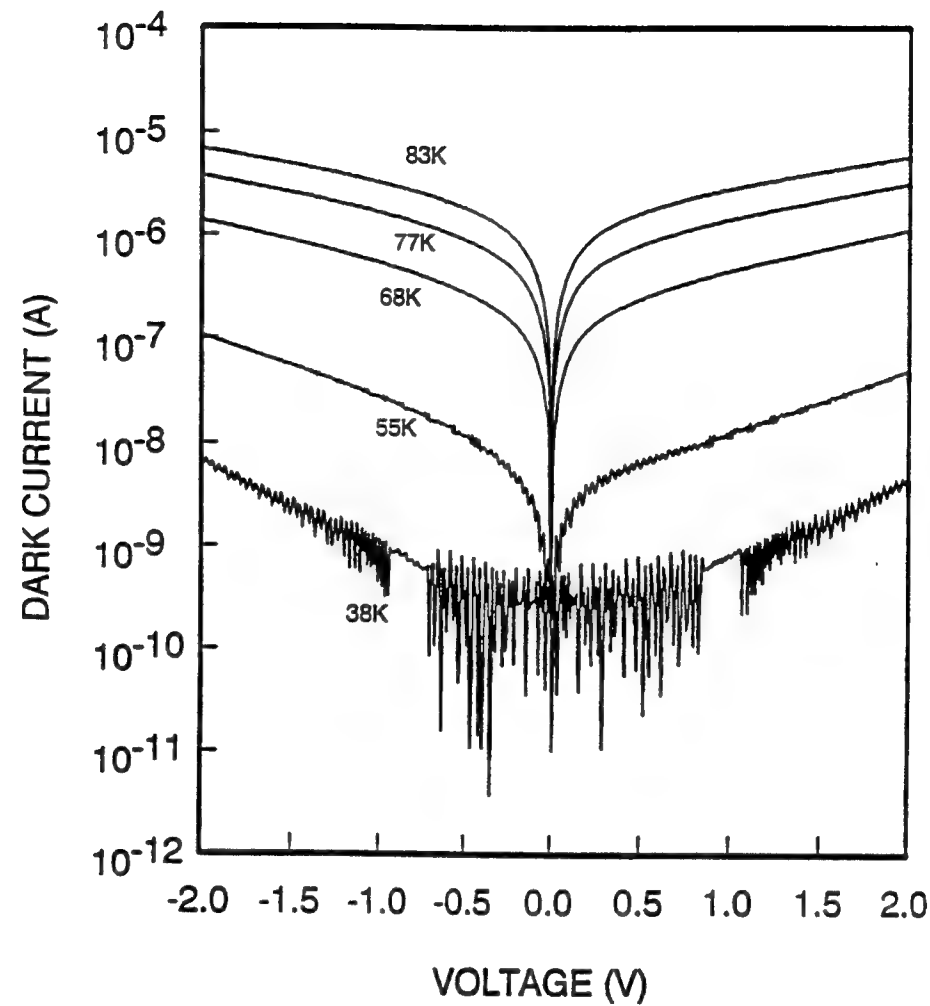


Figure 4.4 Plot of dark current vs. applied bias at different temperatures. A strong negative differential resistance (NDR) was obtained at a low temperature, confirming the existence of coherent miniband transport and resonant tunneling

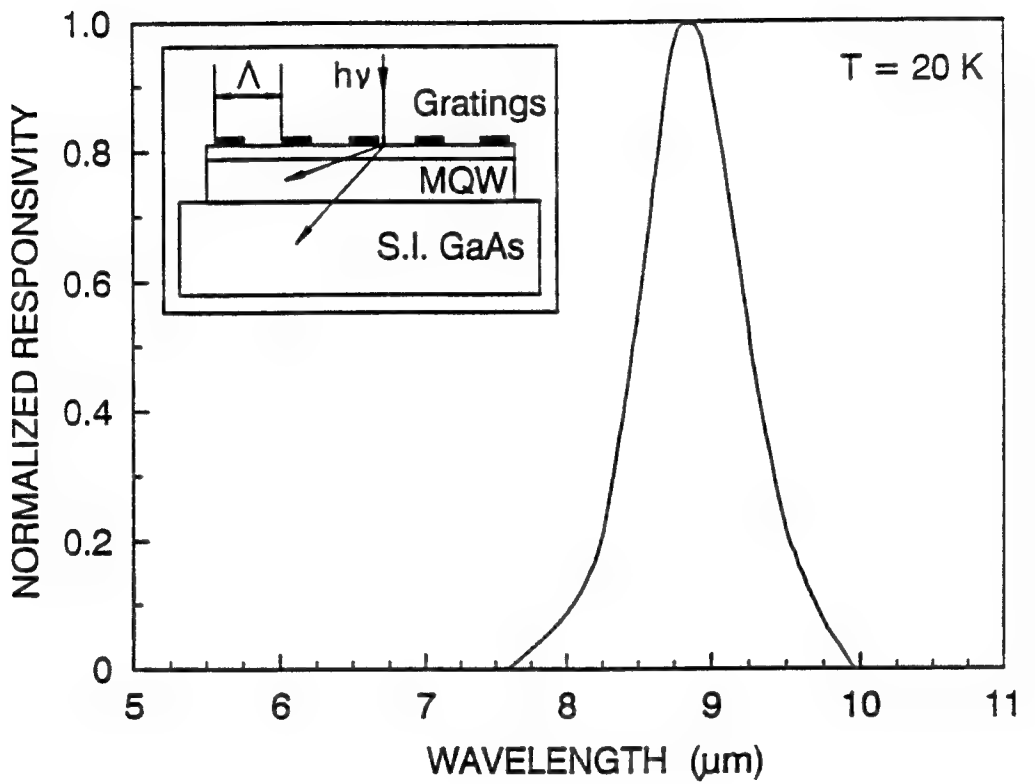


Figure 4.5 Measured spectral responsivity of the QWIP with a planar metal grating coupled top illumination at  $T = 20$  K. The peak wavelength is at  $\lambda_p = 8.9\mu\text{m}$ . A grating periodicity  $\Lambda = 5\mu\text{m}$  and ohmic contact material AuGe-Ni-Au was used for the study.

## 5. LOW DARK CURRENT STEP-BOUND-TO-MINIBAND TRANSITION InGaAs/GaAs/AlGaAs QUANTUM WELL INFRARED DETECTOR

### 5.1 Introduction

The possibility of realizing novel high-speed quantum well devices such as lasers, photodetectors, and modulators has spurred extensive investigations on the intersubband absorption in quantum wells and superlattices. A great deal of work has been reported on the lattice-matched GaAs/AlGaAs [11, 63, 13] and InGaAs/InAlAs/InP [64, 65] quantum well systems. Recent study [13] revealed that  $8 - 12 \mu\text{m}$  infrared detectors may be obtained by using a multiquantum well(MQW) or superlattice (SL) barrier structure and resonant tunneling mechanism. A significant improvement in intersubband absorption and thermionic emission has been successfully demonstrated using a GaAs/AlGaAs superlattice reinforced bound-to-miniband (BTM) transition [13] structure. The replacement of the bulk barrier region with a very short period superlattice barrier layer offers several new properties such as reduction of interface recombination, elimination of deep level related phenomena [28], realization of a new type of quantum photocurrent gain ( $\sim 10^4$ ) [7], and a significant enhancement of intersubband absorption.

### 5.2 Theory and Experiments

Here we describe a low dark current lightly-strained InGaAs/GaAs/AlGaAs QWIP based on the step-bound-to-miniband (SBTM) transition, superlattice miniband resonant tunneling and coherent transport mechanism. As illustrated in Figure 5.1, the transition scheme of our QWIP's is from the localized bound ground state in the enlarged  $In_{0.07}Ga_{0.93}As$  quantum wells to the resonant-coupled miniband of GaAs/  $Al_{0.4}Ga_{0.6}As$  superlattice (SL) barrier. This new structure created a potential 'step' in the superlattice barrier region to block the undesirable tunneling dark current from the heavily doped ground state  $E_{EW}$  in the quantum well. The physical parameters of the quantum wells and superlattices are chosen so that the ground bound state in the enlarged (EW) InGaAs well is pushed below the step barrier, and the first excited level  $E_{EW_1}$  of the quantum well is merged and lined up with the ground level of the miniband  $E_{SL}$  in the superlattice barrier layer to achieve a large oscillation strength  $f$  and intersubband absorption coefficient  $\alpha$ . Since the superlattice has a relatively thin barrier, the photoexcited electrons can easily transport through

the superlattice barrier layers along the aligned miniband, and are then collected at the external ohmic contacts.

To characterize the SBTM transition we performed theoretical calculations of the energy states  $E_{EW}$ ,  $E_{SL}$  and the transmission coefficient  $T^*T$  on our LWIP's by using the multiple-layer transfer matrix method, and the results are shown in Figure 5.2. It is noted that a broad and strongly degenerated miniband  $E_{SL}$  was formed inside the enlarged well by using the superlattice barrier structure. The ground state of the enlarged InGaAs well is confined much below the step barrier height so as to reduce the sequential tunneling and hopping currents. As a comparison, in the inset of Figure 5.2, we calculated the transmission coefficient of the superlattice for both the step-bound-to-miniband (SBTM) transition structure and the normal bound-to-miniband (BTM) transition structure without the potential step. Many orders of magnitude reduction in  $T^*T$  were observed in the present SBTM structure.

The SBTM detector structure was grown on a semi-insulating (S.I.) GaAs substrate by using the molecular beam epitaxy (MBE) technique. A 1  $\mu\text{m}$  thick GaAs buffer layer of  $1.4 \times 10^{18} \text{ cm}^{-3}$  was first grown on a S.I. GaAs substrate, followed by the growth of a 40-period of  $In_{0.07}Ga_{0.93}As$  quantum wells with a well width of 106 Å and a dopant density of  $1.4 \times 10^{18} \text{ cm}^{-3}$ . The barrier layer on each side of the quantum well consists of a 5-period of undoped  $Al_{0.4}Ga_{0.6}As$  (30 Å)/GaAs (59 Å) superlattice layers which were grown alternatively with the InGaAs quantum wells. Finally, a 0.4- $\mu\text{m}$ -thick n<sup>+</sup>-GaAs cap layer with dopant density  $1.4 \times 10^{18} \text{ cm}^{-3}$  was grown on top of the MQW/SL layer structure to facilitate ohmic contacts. An array of  $200 \times 200 \mu\text{m}^2$  mesas were chemically etched down to the n<sup>+</sup>-GaAs buffer contact layer on the GaAs substrate. Finally, AuGe/Ni/Au ohmic contacts were evaporated onto the top and bottom of n<sup>+</sup>-GaAs contact layers by using E-beam evaporation.

Device characterization was performed in a liquid-helium cryogenic dewar. An HP4140B semiconductor parameter analyzer was used to measure the dark current vs. voltage (I-V) curves. Under dark conditions, electrons can transfer out of the quantum wells and produce the observed current mainly via two mechanisms. One is attributed to the thermionic emission out of the quantum wells, which is the dominant current component at higher temperatures (i.e., for  $T \geq 77 \text{ K}$ ). The other is the thermally generated carriers tunneling through the superlattice miniband. In the present SBTM transition structure, we created a levitated potential step in the superlattice to block much of the tunneling current component due to electron tunneling from the heavily populated ground state at low temperatures. We also chose a high value of 'Al' composition,  $x = 0.4$ , which gave rise

to a barrier potential as high as  $\Delta E_c \simeq 388$  meV ( $\sim 65\% \Delta E_g$ ), to suppress the thermionic emission out of the quantum wells. Figure 5.3 shows the measured dark I-V curves for temperatures between 35 and 92 K. Substantial reduction in device dark current was achieved in the present step-potential reinforced InGaAs multiquantum well/GaAs/AlGaAs superlattice barrier structure.

To identify the origins of the dark currents flow in the detector we performed the numerical calculation of the dark currents using the expression [2, 11]

$$I_d = \frac{4\pi q A v(\mathcal{E}) m^* k T}{h^2 L} \int_0^\infty |T(E, \mathcal{E})|^2 \{ \ln[1 + e^{-(E-E_f)/kT}] - \ln[1 + e^{-(E-qV-E_f)/kT}] \} dE; \quad (5.1)$$

where  $v(\mathcal{E})$  is the electron velocity in GaAs which is given by [67]

$$v(\mathcal{E}) = \frac{\mu \mathcal{E} + v_s (\mathcal{E}/\mathcal{E}_0)^4}{1 + (\mathcal{E}/\mathcal{E}_0)^4} \quad (5.2)$$

where  $q$  is the electron charge,  $A$  is the device area,  $m^*$  is the electron effective mass,  $L$  is the multiquantum well period,  $E_f$  is the Fermi level, and  $\mathcal{E}_0$  is the critical field, which is equal to  $4 \times 10^3$  V/cm for GaAs. As previously described (chapter 3), the parameter  $|T(E, \mathcal{E})|^2$  is the field-dependent transmission coefficient which can be calculated by using the multi-layer matrix method, assuming the potential energy variation of  $V(x) = V_0 + q\mathcal{E}x$ . The calculated current values are in good agreement with the observed results, which shows that the levitated step potential barrier is indeed very effective in suppressing the device dark current. Another interesting result observed in this SBTM LWIP's (as shown in Figure 5.3) is the negative resistance exhibited by the sequential resonant tunneling through an expanding high-field superlattice domain [68] at a low temperature. A detailed study of the device conductance was also performed at  $T = 77$  K (Figure 5.4). The high-frequency oscillations of the measured conductance confirms the existence of the resonant tunneling (RT) and negative differential resistance (NDR).

Measurement of the intersubband absorption for the present detector was performed at 300 K using a Perkin-Elmer Fourier transform infrared (FTIR) spectroscopy. Figure 5.5 shows the room temperature absorption spectra at the Brewster's angle ( $\theta_B = 73^\circ$ ). The measured peak absorbance  $A = -\log_{10}$  [transmission] was found to be about 40 mAbs. The absorption peak is centered at 11.4  $\mu\text{m}$ . The full width at half-maximum (FWHM) of the absorption peak is about  $220 \text{ cm}^{-1}$ . To determine the spectral responsivity, the edge of the sample was polished into  $50^\circ$  to facilitate light illumination. The photocurrent was measured using a CVI Laser Digikrom 240 monochromator and an ORIEL ceramic element infrared source. The responsivity  $R_\lambda = 0.38 \text{ A/W}$  was obtained at  $V_b = 5 \text{ V}$  and  $T = 77 \text{ K}$ . Figure 5.6 shows the normalized responsivity versus wavelength measured at 77 K. From the measured responsivity and dark current, we can calculate the detectivity  $D^*$  of

the detector using the relation

$$D^* = R_\lambda (A_d \Delta f)^{1/2} / (4qI_d G \Delta f)^{1/2} \quad (5.3)$$

where  $A_d = 4 \times 10^{-4} \text{ cm}^2$  is the effective area of the detector,  $G$  is the optical gain which is taken as 0.5. At  $V_b = 5 \text{ V}$ , we found that values of the peak detectivity at  $\lambda_p = 10.5 \mu\text{m}$  are  $D^* = 0.81 \times 10^{10}$  and  $2.1 \times 10^{10} \text{ cm}\sqrt{\text{Hz}}/\text{W}$  for  $T = 77$  and  $63 \text{ K}$ , respectively.

### 5.3 Advantages of Step-Bound-to-Miniband transition Structure

There are many unique features about the newly developed InGaAs/GaAs/AlGaAs SBTM QWIP [73]. Some of them are listed in the followings:

- **High Operation Temperature and Low Dark Current:** Dark current is a key device parameter for the background limited QWIPs, especially for temperatures  $T \geq 77 \text{ K}$ . Under a dark condition, electrons can transfer out of the quantum wells and produce the observed dark current mainly via two mechanisms. One is the thermionic emission out of the quantum wells, and the other is the carrier tunneling through the superlattice along the miniband. Based on our calculation, it can be shown that the former mechanism is the dominant component of the dark current at low bias and at higher temperatures. With the new bound-to-miniband device structure and the adoption of a much larger barrier height  $V_0$ , the  $E_3$  and other closely spaced higher continuum states could be lifted far away from  $E_2$  and miniband of the SL. Meanwhile the bound states of the quantum wells are deeply “positioned” inside the superlattice and far from the quasi 3-D continuum states above the barrier. Due to relatively large barrier height, the thermionic emission current out of the quantum wells is expected to be effectively suppressed. The introduction of a step bulk barrier in the new step-bound-to-miniband transition (SBMT) structure allows the ground state level of the enlarged quantum well to be located below the step bulk barrier in the superlattice, and the tunneling current can also be further suppressed. Therefore, significant reduction in the detector dark current can be expected from this new structure.
- **Dual-mode Operation:** Low bias operation is always preferred in many infrared applications. Due to the strongly coupled coherent states (miniband) transport in the SBMT structure, a large portion of the electron wave functions in the superlattice region overlaps. The discrete quantum levels of the different superlattice layers are so closely packed, a strongly degenerate miniband is formed in the superlattice barrier region. There exist large coupling

effects among these states. In other words, the excited electrons in the miniband are co-governed and shared by different quantum wells in the superlattice region, and the resonant tunneling can easily take place along the miniband even with a small perturbation or an externally applied electric field. It is interesting to note that we have observed a relatively large photocurrent in such a detector even at zero bias. Therefore, the low bias operation, or zero bias condition (dual-mode operation) could be realized in the proposed SBMT MQW IR detector using a short period of superlattice barrier.

- **High Optical Gain:** A large optical gain can be achieved in the proposed SBMT MQW IR detector. Unlike the conventional GaAs QWIP's, the carrier transport in this SBMT MQW IR detector structure is via the lowest miniband (the ground state) of the SL. The photocarriers in the ground state miniband have a longer lifetime than those in the higher order minibands, and the re-capture rate by the quantum wells is also much lower in the ground level miniband. With a proper design, it is possible to realize a higher photocurrent gain, given by  $G = \tau_e/t_e$ , in the QWIP based on the miniband transport and effective mass filtering effect [7], where  $\tau_e$  is the electron lifetime in the superlattice and  $t_e$  is the electron transit time. Since the tunneling probability increases exponentially with the reduction of barrier width in the superlattice and the tunneling time decreases with the reduction of the barrier width, by adjusting the superlattice structure parameters, an optical gain much greater than unity can be obtained in this proposed IR detector.
- **High Speed:** Due to the effective mass filtering effect in the step-bound-to-miniband transition (SBMT) structure, the holes are relatively confined in the superlattice region, and the electron transport is via the lowest miniband (the ground state) of the SL. The resonant tunneling time along the aligned miniband can be very short and hence a high response speed at  $10\mu\text{m}$  wavelength can be expected in this detector.
- **Adjustable Spectral Bandwidth:** In our proposed SBMT MQW IR detector structure, the bandwidth of the spectral response of the detector is mainly determined by the aligned coherent miniband, which highly depends on the superlattice barrier width. A thin barrier will give a broad photoresponse bandwidth, and a thick barrier will result in a very narrow photoresponse bandwidth. Furthermore, with a hybrid combination of varying the widths of the superlattice barrier and the quantum well, we can select an optimum barrier width which will enable us to cover a broad uniform spectral bandwidth from 8 to  $12\mu\text{m}$  with high quantum efficiency and high responsivity.

#### 5.4 Conclusion

In conclusion, we have demonstrated a new step-bound-to-miniband (SBTM) transition LWIP's using a lightly-strained InGaAs multiquantum well and a GaAs/AlGaAs superlattice barrier layer structure and resonant tunneling mechanisms. The new structure provided a levitated potential step in the superlattice barrier to block much of the tunneling current component from the heavily populated ground state in the quantum wells, which resulted in a significant reduction of the device dark current. The peak detectivity was found to be  $D^* = 2.1 \times 10^{10} \text{ cm}\sqrt{\text{Hz}}/\text{W}$  at  $\lambda = 10.5 \mu\text{m}$  and  $T = 63 \text{ K}$ . With high detectivity and uniformity, this new SBTM LWIP's can be used for a wide variety of long wavelength (e.g., 8 – 12  $\mu\text{m}$ ) infrared applications.

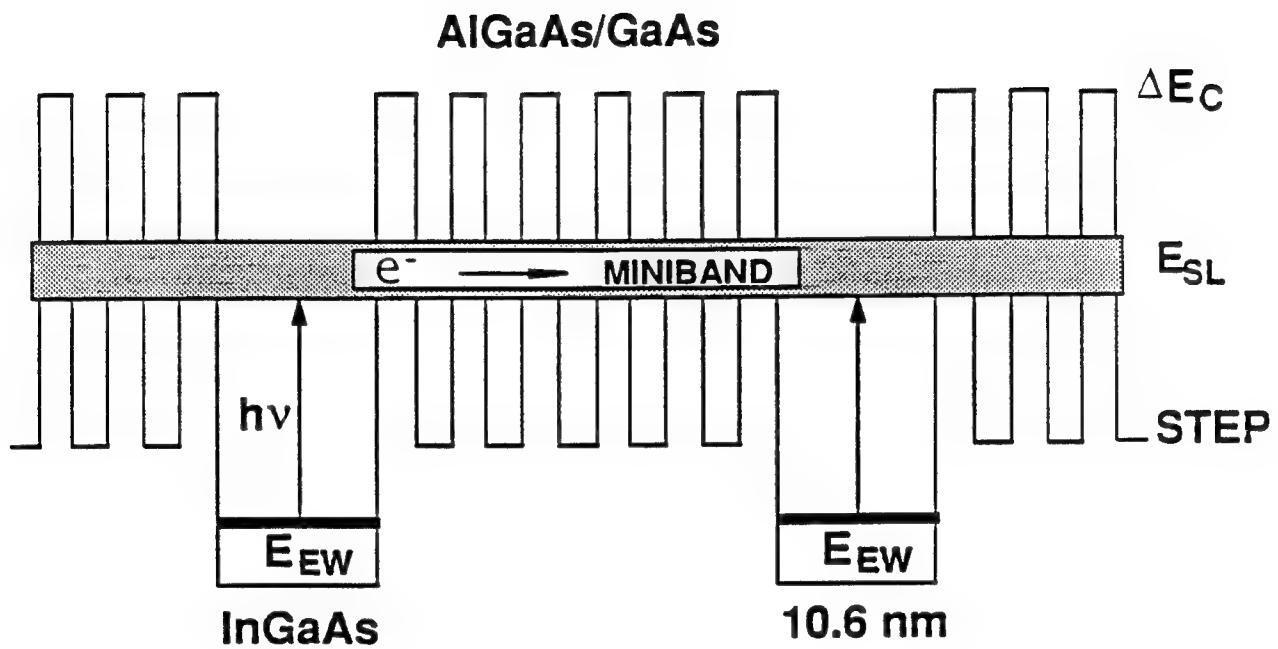


**Figure 5.1** The schematic energy band diagram for the step-bound-to-miniband (SBTM) transition in a new LWIP's structure by using lightly strained InGaAs (106 Å) material. A potential 'step' is created in the GaAs/AlGaAs superlattice barrier layer to suppress the tunneling current from the heavily populated ground state in the InGaAs quantum well.

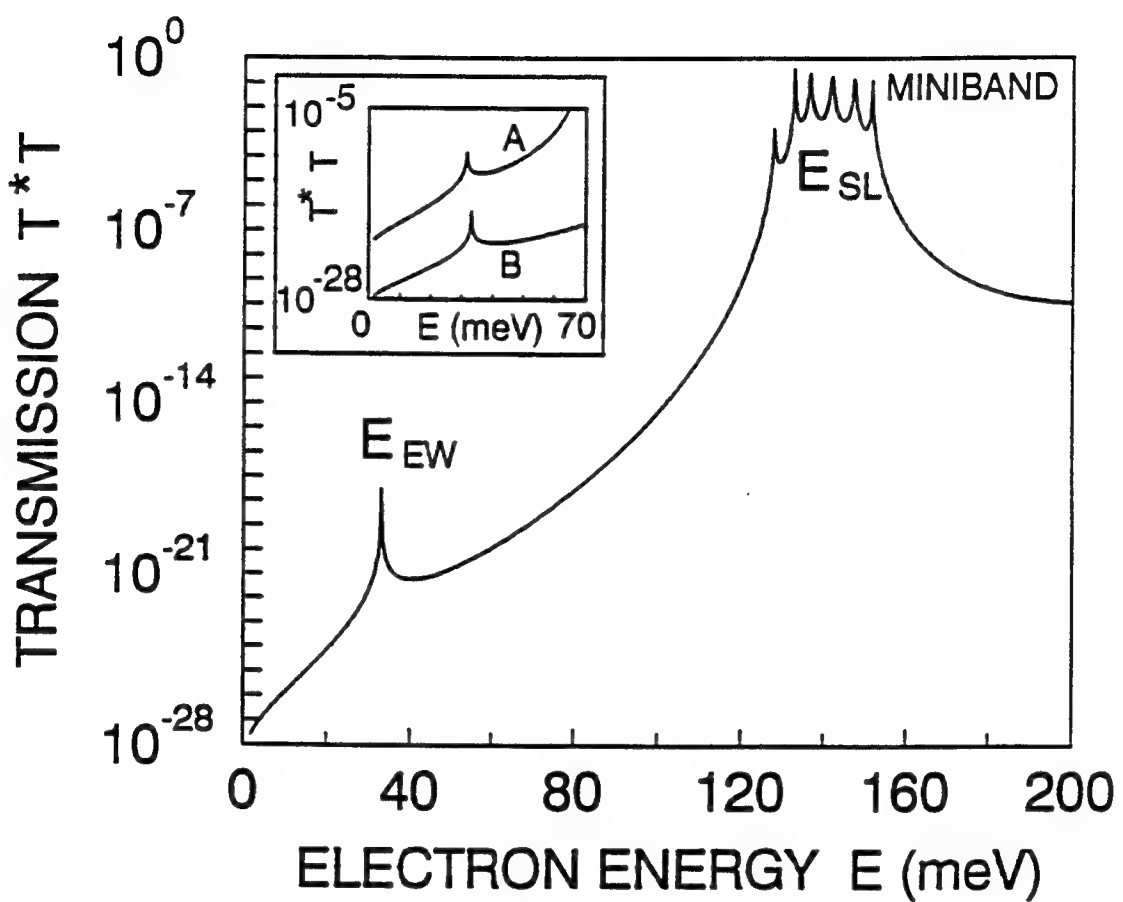


Figure 5.2 The calculated quantized energy states and transmission coefficient  $T^*T$  for the present SBTM transition structure. Inset: The calculated  $T^*T$  for a SBTM (curve B) and a BTM (curve A) LWIP's.

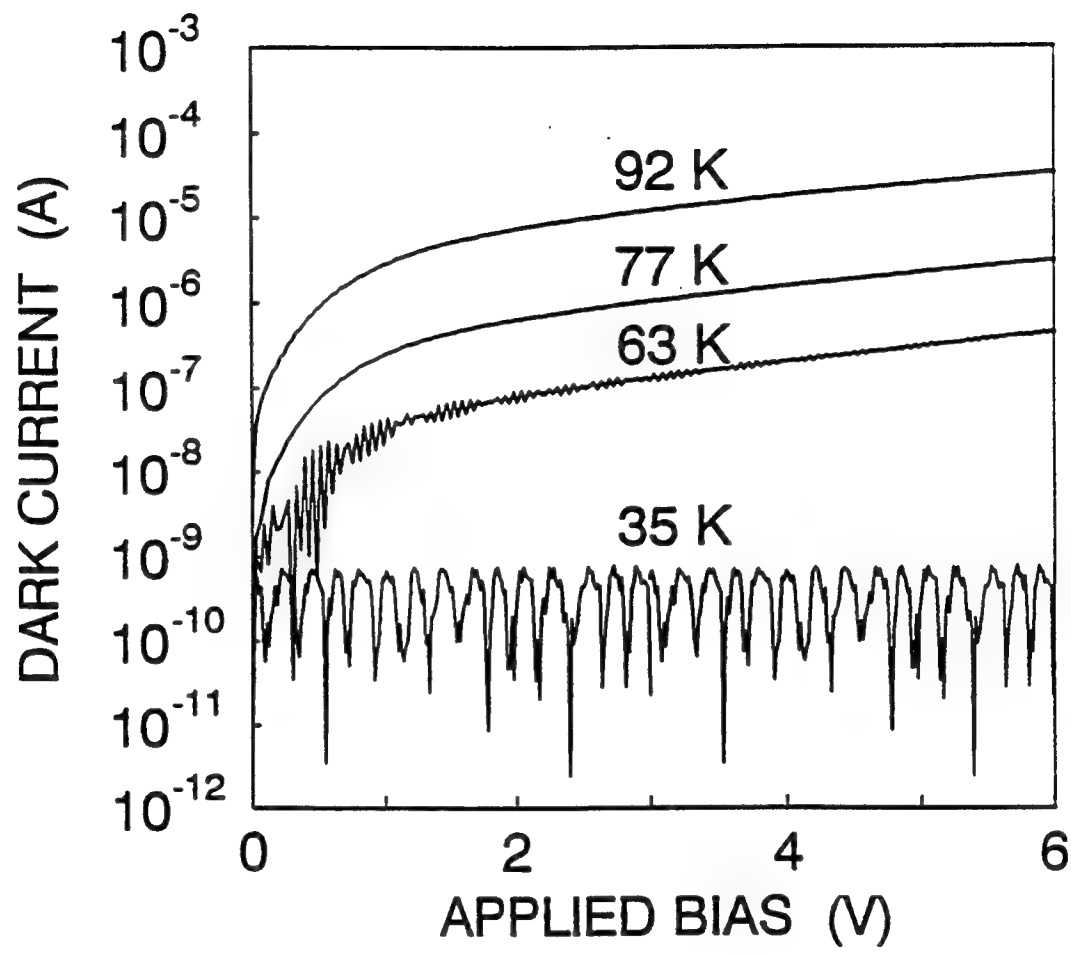


Figure 5.3 Measured dark current vs. applied bias for a SBTM LWIP's for  $35 < T < 92$  K. Note that the dark current is dominated by thermionic emission for  $T \geq 77$  K and by sequential tunneling and hopping for  $T \leq 50$  K.

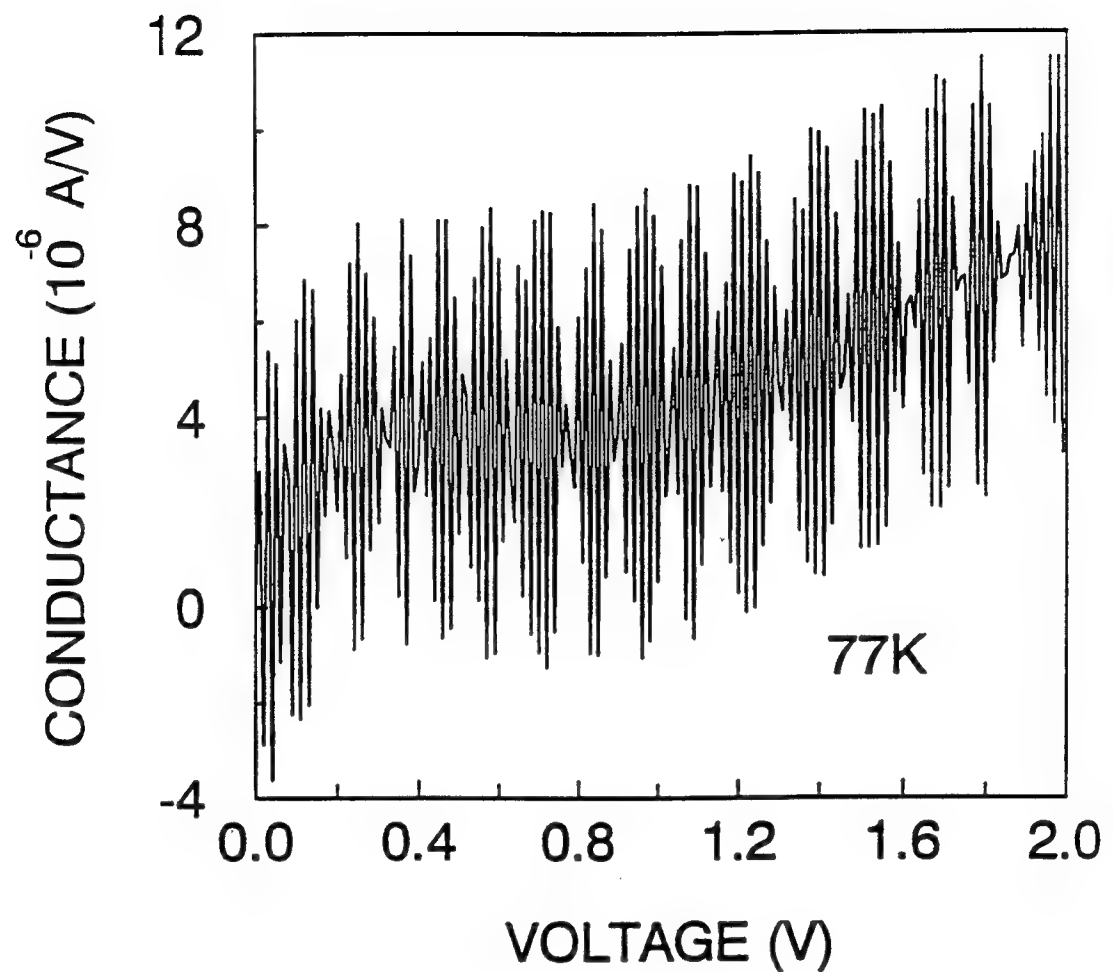


Figure 5.4 A detailed study of negative differential conductance and miniband transport.

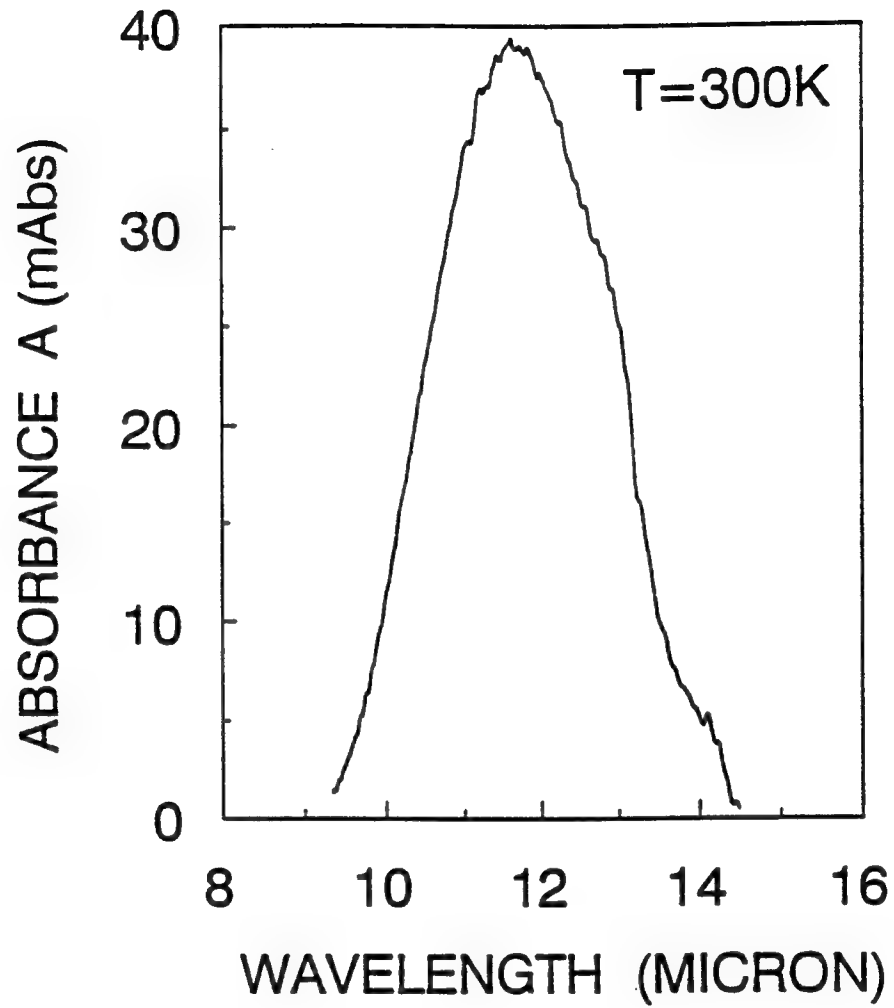


Figure 5.5 Measured room temperature ( $T = 300$  K) intersubband absorbance versus wavelength for the SBTM LWIP's by FTIR spectroscopy at Brewster's angle.

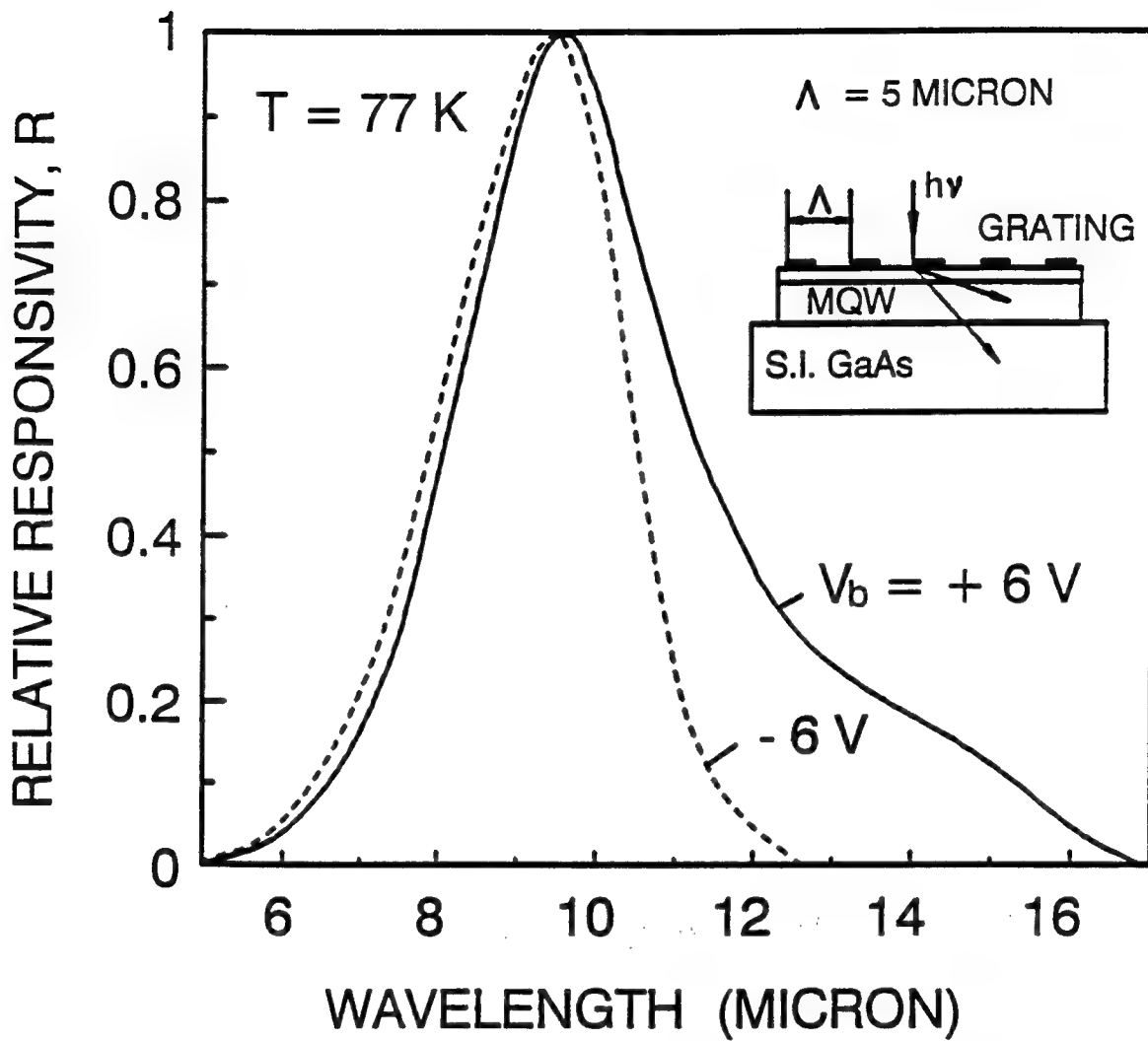


Figure 5.6 Relative responsivity versus wavelength for a SBTM LWIP's measured at 77 K. A broad spectral sensing range is obtained. As noticed by changing the bias direction, the miniband reinforced infrared detector has the capability of tunable band width.

## 6. A VOLTAGE-TUNABLE InGaAs/InAlAs QUANTUM WELL INFRARED PHOTODETECTOR (VT-QWIP)

### 6.1. Introduction

Long-wavelength quantum well infrared photodetectors (QWIPs) based on intersubband transitions for detection in the 8-14  $\mu\text{m}$  atmospheric spectral window have been extensively investigated in recent years. Studies of the intersubband absorption in the InGaAs/InAlAs system for 3 to 5  $\mu\text{m}$  and 8 to 14  $\mu\text{m}$  detection have also been reported [17, 72]. Since the InGaAs/InAlAs heterostructure has a large conduction band offset ( $\Delta E_c \sim 500$  meV) compared to GaAs/AlGaAs system, it is a promising candidate for both the mid-wavelength infrared (MWIR) and the long-wavelength infrared (LWIR) applications. Recently, we have reported the observation of a largely enhanced intersubband absorption in the InAlAs/InGaAs system using intersubband transition for 8-14  $\mu\text{m}$  [72] wavelength detection. The result showed multi-color infrared detection can be realized in the InGaAs/InAlAs QWIP due to a much large potential barrier created by using a short period superlattice barrier structure and resonant miniband conduction mechanism.

### 6.2. Design Consideration

A dual-mode (PV and PC) operation InGaAs/InAlAs QWIP [44] based on the voltage-tuned (VT) bound-to-miniband (BTM) transition mechanism was designed and fabricated. The VT-QWIP layer structure was grown on a semi-insulating (SI) InP substrate by using the molecular beam epitaxy (MBE) technique. A 1- $\mu\text{m}$   $\text{In}_{0.53}\text{Ga}_{0.47}\text{As}$  buffer layer with dopant density of  $2 \times 10^{18} \text{ cm}^{-3}$  was first grown on the SI InP substrate, followed by the growth of 20 periods of enlarged  $\text{In}_{0.53}\text{Ga}_{0.47}\text{As}$  quantum wells with a well width of 110 Å and a dopant density of  $5 \times 10^{17} \text{ cm}^{-3}$ . The barrier layers on each side of the quantum well consist of 6 periods of undoped  $\text{In}_{0.52}\text{Al}_{0.48}\text{As}$  (35 Å)/ $\text{In}_{0.53}\text{Ga}_{0.47}\text{As}$  (50 Å) superlattice layers. A 0.3- $\mu\text{m}$ -thick  $n^+$ - $\text{In}_{0.53}\text{Ga}_{0.47}\text{As}$  cap layer with a dopant density of  $2 \times 10^{18} \text{ cm}^{-3}$  was grown on top of the VT-QWIP layer structure to facilitate the ohmic contact. Figure 6.1 shows the energy band diagram for this VT-QWIP. The transition scheme is from the localized ground state level  $E_{EW1}$  of the enlarged well (EW) to the global resonant-coupled miniband  $E_{SL1}$  in the superlattice (SL) barrier. The physical parameters of the quantum well and superlattices are chosen so that the first excited level  $E_{EW2}$  of the EW is merged

and lined up with the ground miniband  $E_{SL1}$  of the SL on both sides of the quantum well to obtain a maximum intersubband absorption strength.

To analyze these bound-to-miniband transition schemes, theoretical calculations of the energy states  $E_{EWn}$ ,  $E_{SLn}$  ( $n = 1, 2, \dots$ ) and the transmission probability  $|T \cdot T|$  for the VT-QWIP were carried out by using the multi-layer transfer matrix method. In this design, a broad and highly degenerated miniband was formed by using the superlattice barrier structure. The center energy position of the first miniband is located at 163 meV above the conduction band edge of InGaAs EW with a bandwidth of  $\Gamma \sim 60$  meV. In order to precisely determine the intersubband transition levels, we have considered both the electron-electron interaction (exchange energy)  $E_{exch}$  and depolarization  $E_{dep}$  effects. The results show a lowering of  $\sim 5$  meV for the heavily populated bound states  $E_{EW1}$  in the quantum well. The peak absorption wavelength can be found from the relation,

$$\lambda_p = \frac{1.24}{E_{SL1} - E_{EW1} + E_{exch} - E_{dep}} (\mu m). \quad (6.1)$$

Now, substituting values of  $E_{SL1} = 163$  meV,  $E_{EW1} = 51$  meV, and  $E_{exch} - E_{dep} \sim 5$  meV into the above equation, we obtain  $\lambda_p = 10.6 \mu m$ . The infrared intersubband absorption versus wavelength for the VT-QWIP was measured at the Brewster angle ( $\theta_B \sim 73^\circ$ ) by using a Perkin-Elmer Fourier transform interferometer (FTIR) at room temperature [72]. The results showed a main absorption peak centered at  $\lambda_p = 10.7 \mu m$  with a spectral linewidth of  $\Delta\nu = 500 \text{ cm}^{-1}$ .

### 6.3. Experiments

The mesa structure for the VT-QWIP was formed by chemical etching through the QWIP active layers and stopped at the  $n^+$  InGaAs buffer layer for ohmic contact. The active area of the detector is  $200 \times 200 \mu m^2$ . To enhance coupling efficiency for normal illumination and angular-independent radiation polarization, a planar two-dimensional (2-D) metal grating coupler was formed on the VT-QWIP by using electron beam (E-beam) evaporation of  $0.2 \mu m$  gold films. The metal grating coupler consists of equally spaced square shape metal grating with a grating periodicity of  $\Lambda = 10 \mu m$  and a geometrical ratio factor  $d/\Lambda = 0.5$ , where  $d$  is the width of the square metal grating.

Figure 6.2 shows the dark current-voltage (I-V) and the differential resistance ( $R_d$ ) curves for the QWIP measured at  $T = 67$  K. Asymmetric dark current characteristics was observed in the QWIP (mesa top as positive bias). The photocurrent was measured as a function of temperature, bias voltage, polarization direction, and wavelength using an ORIEL 77250 single grating

monochromator and ceramic element infrared source. Figure 6.3 shows the normalized responsivity versus wavelength measured at  $V_b = 0$ , - 0.5 V and  $T = 67$  K. In the PV mode operation ( $V_b = 0$  V), the detector has a peak wavelength response at  $\lambda_p = 10 \mu\text{m}$  with a cutoff wavelength  $\lambda_c = 10.4 \mu\text{m}$ . When a negative voltage is applied to the QWIP, the PC mode conduction becomes the dominant conduction mechanism. The peak wavelength  $\lambda_p$  for the PC mode detection was found to be at  $\lambda_p = 10.3 \mu\text{m}$ , while a full width at half maximum of  $\Delta\nu = 232 \text{ cm}^{-1}$  ( $\sim 29 \text{ meV}$ ) was obtained from Fig. 6.3. The bandwidth  $\Delta\lambda/\lambda_p = 24 \%$  from PC mode response curve was found to be much narrower than the room temperature FTIR absorption curve [72]. The intersubband transitions of both the PC mode and PV mode are attributed to the energy resonant transition from the ground state  $E_{EW1}$  to the global miniband  $E_{SL1}$  states which are aligned with the first excited state  $E_{EW2}$  in the quantum well. The intersubband resonant transition (maximum absorption strength or maximum wavefunction overlap) depends strongly on the location of the first excited state  $E_{EW2}$  of the quantum well relative to the miniband edges,  $E_{SL1}$  [15]. In the VT-QWIP structure, the  $E_{EW2}$  lies near the top of the miniband edges  $E_{SL1}$ , which results in a strong, blueshift ( $0.7 \mu\text{m}$  compared with room temperature FTIR peak wavelength  $10.7 \mu\text{m}$ ), and narrow-band spectral response in the PV mode detection with a linewidth of  $\Delta\lambda = 0.7 \mu\text{m}$  at a half maximum. The bound-to-miniband transition QWIP operated in the PV mode offers a unique feature of ultra-narrow bandwidth ( $\Delta\lambda/\lambda_p = 7 \%$ ) infrared detection, which is not attainable in a conventional bound-to-continuum QWIP. As the negative bias increases, relative position between the “embedding” state  $E_{EW2}$  and the “framing” state  $E_{SL1}$  can be adjusted by the “controlling bias” due to the different dependence of  $E_{EW2}$  and  $E_{SL1}$  on the bias voltage. A peak wavelength blueshift of about  $0.4 \mu\text{m}$  (compared with the FTIR peak wavelength) was observed at  $V_b = -0.5 \text{ V}$  and  $T = 67\text{K}$ . As expected, a broad-band spectral linewidth of  $\Delta\lambda/\lambda_p = 24 \%$  at  $V_b = -0.5 \text{ V}$  was obtained in the PC mode as shown in Fig. 6.3. It is notice that  $0.3 \mu\text{m}$  peak wavelength shift between the PC mode and PV mode operation was obtained by the applied bias. In the bias-tuned QWIP structure, not only can the spectral bandwidth be tailored to the desired width (from 7 % to 24 %), but the spectral response peak can also be tuned as well. This tunability can be obtained by modulating the relative position of the first excited bound state in the quantum well within miniband states. For example, if the first bound excited state lies at the bottom edge of the miniband, then the spectral response will produce a redshift with a longer short-wavelength tail and narrow bandwidth. On the other hand, if the first bound excited state lies at the top of the miniband, then a blueshift results with a longer long-wavelength tail and narrow bandwidth. However, if the first excited state is in the middle of the miniband, then a broader photoresponse curve is expected. This tunability is illustrated in Fig. 6.4.

The photocurrent responsivities  $R_A$  of the PC mode and PV mode operation were measured at  $T = 67$  K,  $\lambda_p = 10.3 \mu\text{m}$  and  $10 \mu\text{m}$ , respectively, and results are shown in Fig. 6.5. The peak responsivity for PV mode was found to be  $12,000 \text{ V/W}$  at  $10 \mu\text{m}$ . The photocurrent responsivity  $R_A$  for the PC mode, measured at  $V_b = -0.5, -1.5 \text{ V}$ , was found to be  $38 \text{ mA/W}$ ,  $145 \text{ mA/W}$ , respectively.

#### 6.4. Results and Discussion

The detectivity  $D_\lambda^*$  can be calculated from the measured responsivity and dark current. Photoconductive gain can be also derived from the noise measurement. The results yielded a peak detectivity  $D_\lambda^* = 5.8 \times 10^9 \text{ cm}\cdot\sqrt{\text{Hz}}/\text{W}$  at  $\lambda_p = 10.3 \mu\text{m}$ ,  $V_b = -0.5 \text{ V}$ , and  $T = 67 \text{ K}$  for the PC mode operation. As shown in Fig. 6.5, the value of  $D_\lambda^*$  decreases with increasing negative bias  $V_b$  due to the increase of dark current with increasing the bias voltage. The zero bias differential resistance  $R_d$  was found to be about  $450 \text{ K}\Omega$  at  $T = 67 \text{ K}$ . Since the detector operating in the PV mode is limited by Johnson noise, the detectivity  $D_\lambda^*$  for the PV mode was found to be  $5.7 \times 10^9 \text{ cm}\cdot\sqrt{\text{Hz}}/\text{W}$ . In order to verify the zero bias noise, we also measured the noise current by using a lock-in amplifier, which yielded a value of  $i_n = 9.0 \times 10^{-14} \text{ A}$ , in good agreement with the calculated value from the Johnson noise expression.

Due to the dopant migration into superlattice barriers from the doped quantum wells, an internal built-in electric field  $E_{bi}$  is generated with the direction opposite to the QWIP layer growth direction. Schematic energy band diagram of considering the dopant migration effect is illustrated in the Fig. 6.6. The miniband bandwidth on two side of each quantum well was modified by the existence of the  $E_{bi}$  (so called miniband bandwidth modulation (MBM)). As a result, bandwidth of the global miniband becomes spatially nonuniform with broadening on the well right-hand side and narrowing on the left-hand side as shown in the Fig. 6.6. The 15 meV wider miniband bandwidth on the side of toward-growth-direction of each InGaAs well than that on the side of backward-growth-direction can be identified and confirmed by temperature-dependent dark I-V and photocurrent measurements. For  $V_b < -0.15 \text{ V}$ , the photoresponse at  $\lambda_p = 10.3 \mu\text{m}$  decreases with increasing bias voltage, indicating that the internal photovoltage is offset by the applied bias voltage in this bias range. For  $V_b > -0.15 \text{ V}$ , the response starts to increase again, which implies that the PC mode conduction will take over when applied bias exceeds the built-in potential  $V_{bi} \sim +0.15 \text{ V}$  resulting from miniband bandwidth modulation. The built-in electric field  $E_{bi}$  is estimated to be about  $2.0 \times 10^3 \text{ V/cm}$ , which is slightly below the electric field  $E_p = 3 \times 10^3 \text{ V/cm}$  for the peak value of electron drift velocity  $v_d$ . Since tunneling time constant  $\tau_o$  is inversely proportional to the

miniband bandwidth  $\Gamma$  ( $\tau_0 = \hbar/\Gamma$ ), the tunneling probability of the photoexcited carriers is 40 % higher toward growth direction than backward growth direction. This different carrier tunneling probability resulting from the MBM gives rise to the PV mode detection.

### 6.5. Conclusions

In conclusion, we have demonstrated a new high performance PV and PC dual-mode operation InGaAs/InAlAs QWIP using voltage-tuned bound-to-miniband transition mechanism. Both the narrow-band PV mode and broad-band PC mode detection at  $\lambda_p \sim 10 \mu\text{m}$  peak wavelength have been achieved. Using the dual-mode operation and bound-to-miniband transition InGaAs/InAlAs QWIP structure grown on the InP substrate, it is possible to design high performance two-color staring focal plane arrays and infrared imaging sensor for use in the 3-5  $\mu\text{m}$  and 8-14  $\mu\text{m}$  detection.

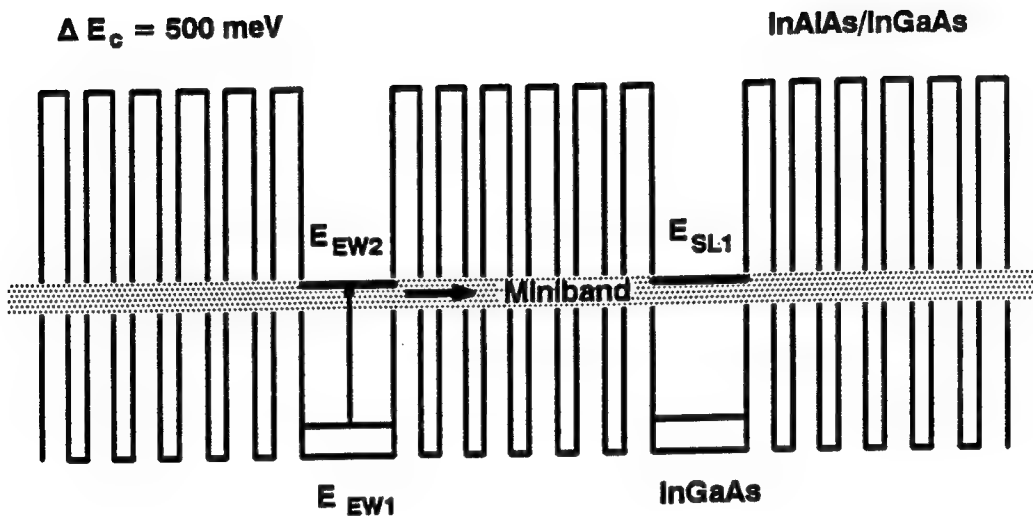


Figure 6.1. Schematic energy band diagram showing the intersubband transitions from the ground state  $E_{EW1}$  to the miniband states  $E_{SL1}$ . The relative position of the first excited state  $E_{EW2}$  to miniband edges strongly influences the resonant intersubband transition [16].

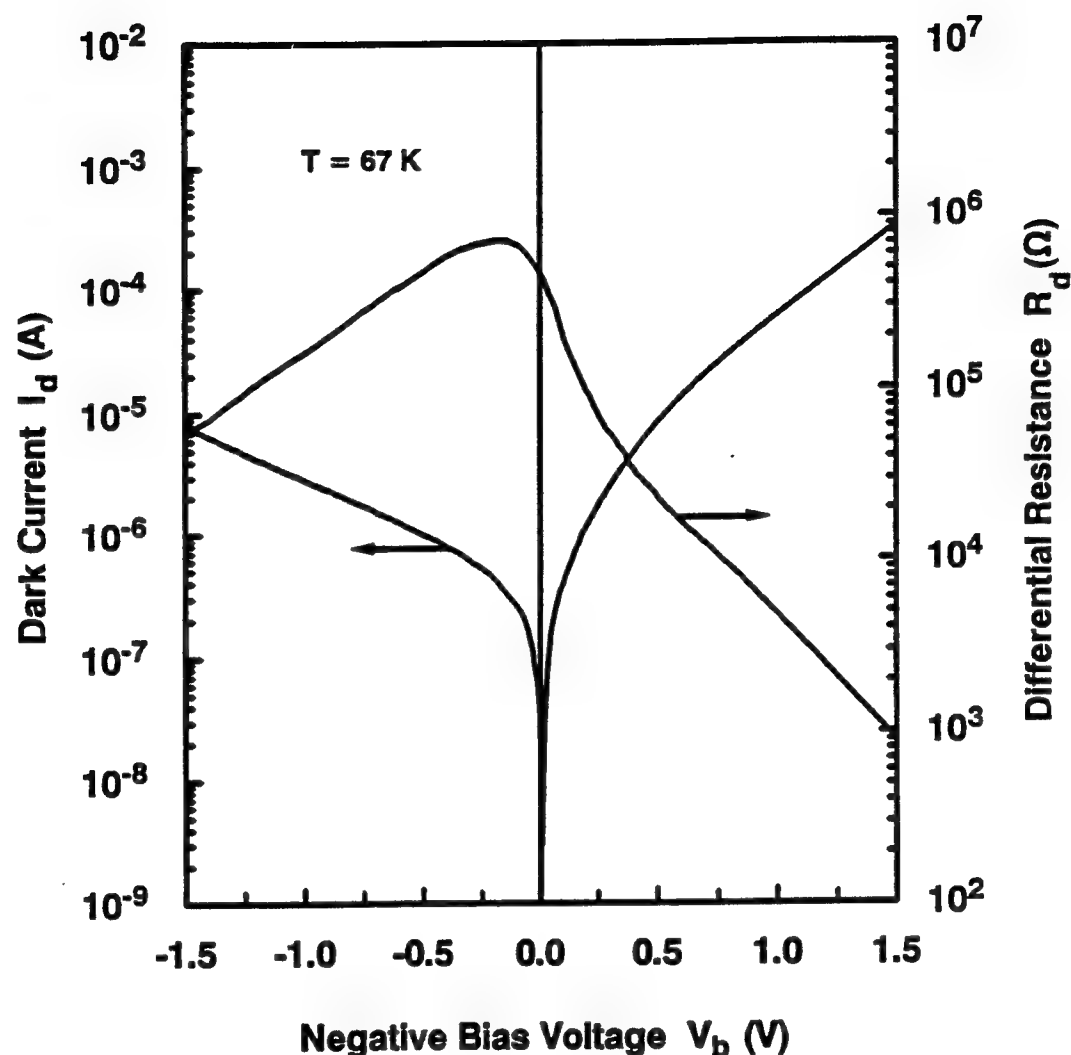


Figure 6.2. Dark current and differential resistance versus applied bias for the InGaAs/InAlAs QWIP measured at  $T = 67$  K.

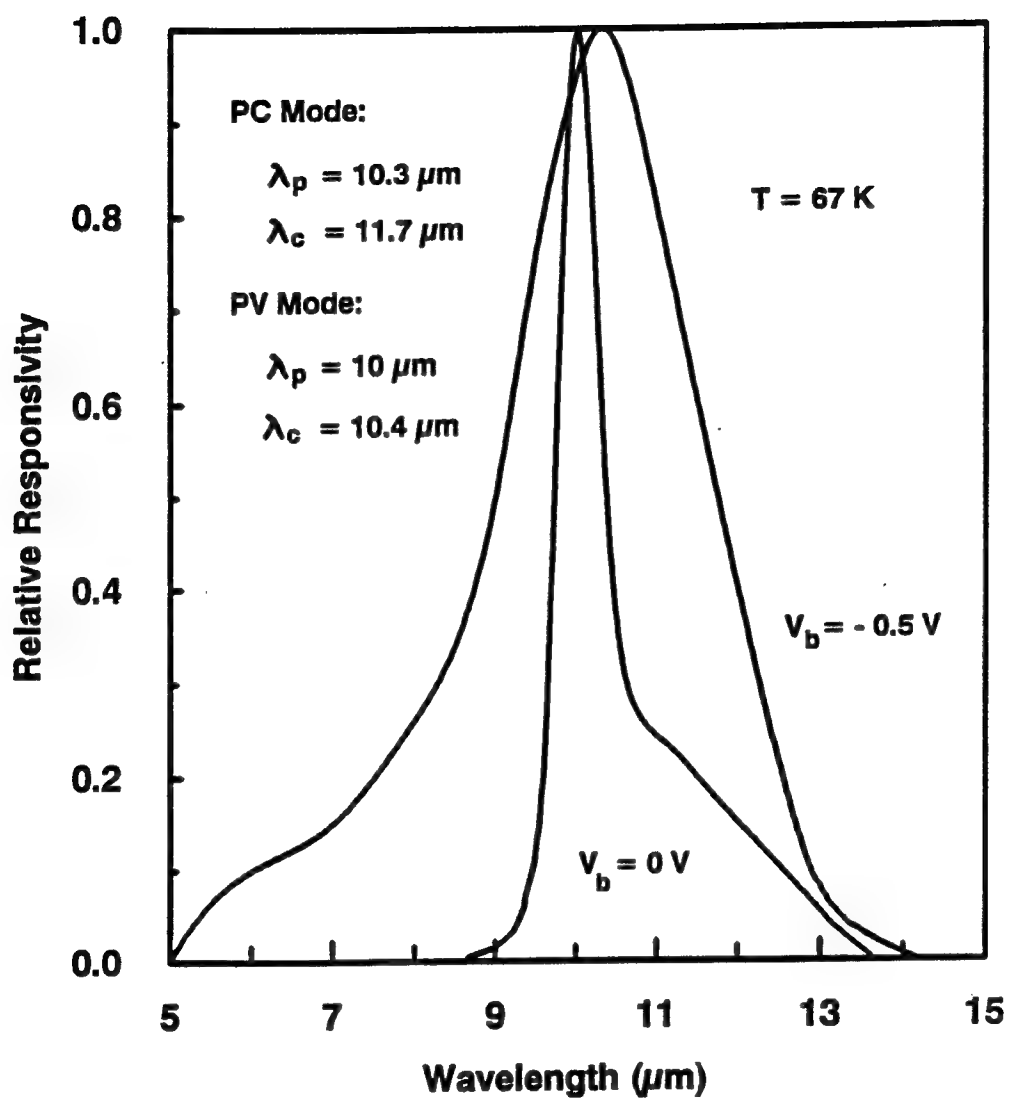
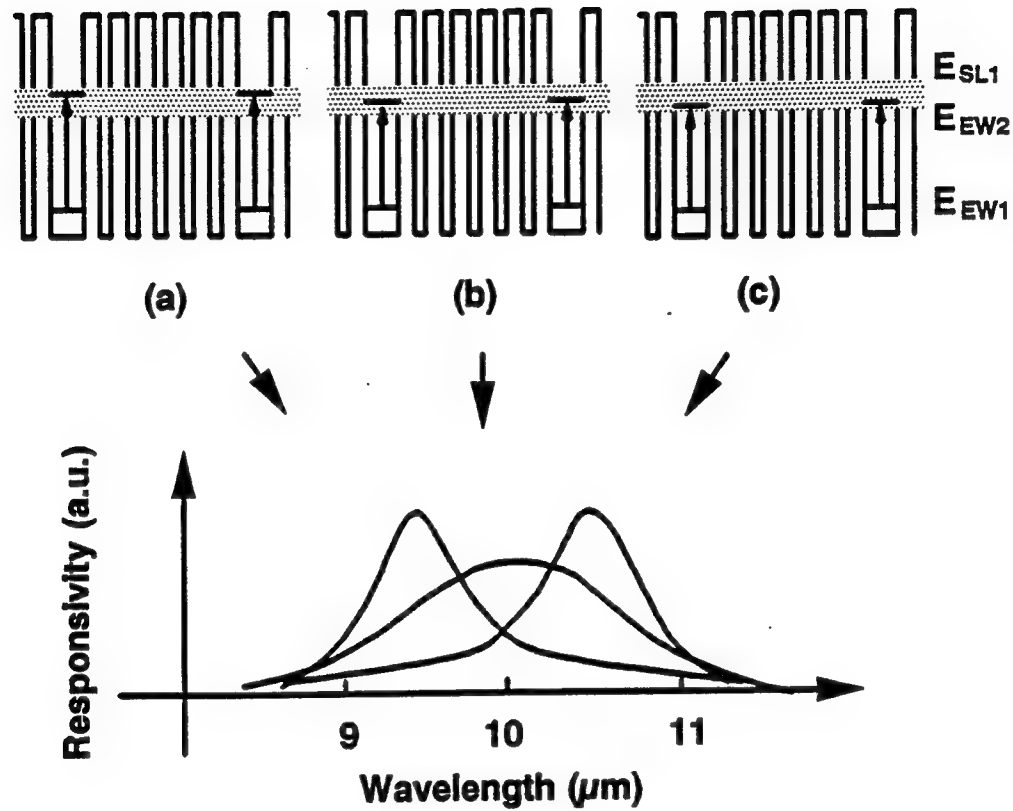


Figure 6.3. Relative responsivity versus wavelength for the InGaAs/InAlAs QWIP measured at  $T = 67 \text{ K}$ .



**Figure 6.4.** Relative spectral response versus wavelength for VT-QWIP  
 (a)  $E_{EW2}$  lined up at the top of the  $E_{SL1}$  miniband states (blueshift), (b)  $E_{EW2}$  in the center of the  $E_{SL1}$  miniband states (broad bandwidth), and (c)  $E_{EW2}$  at the bottom of the  $E_{SL1}$  (redshift).

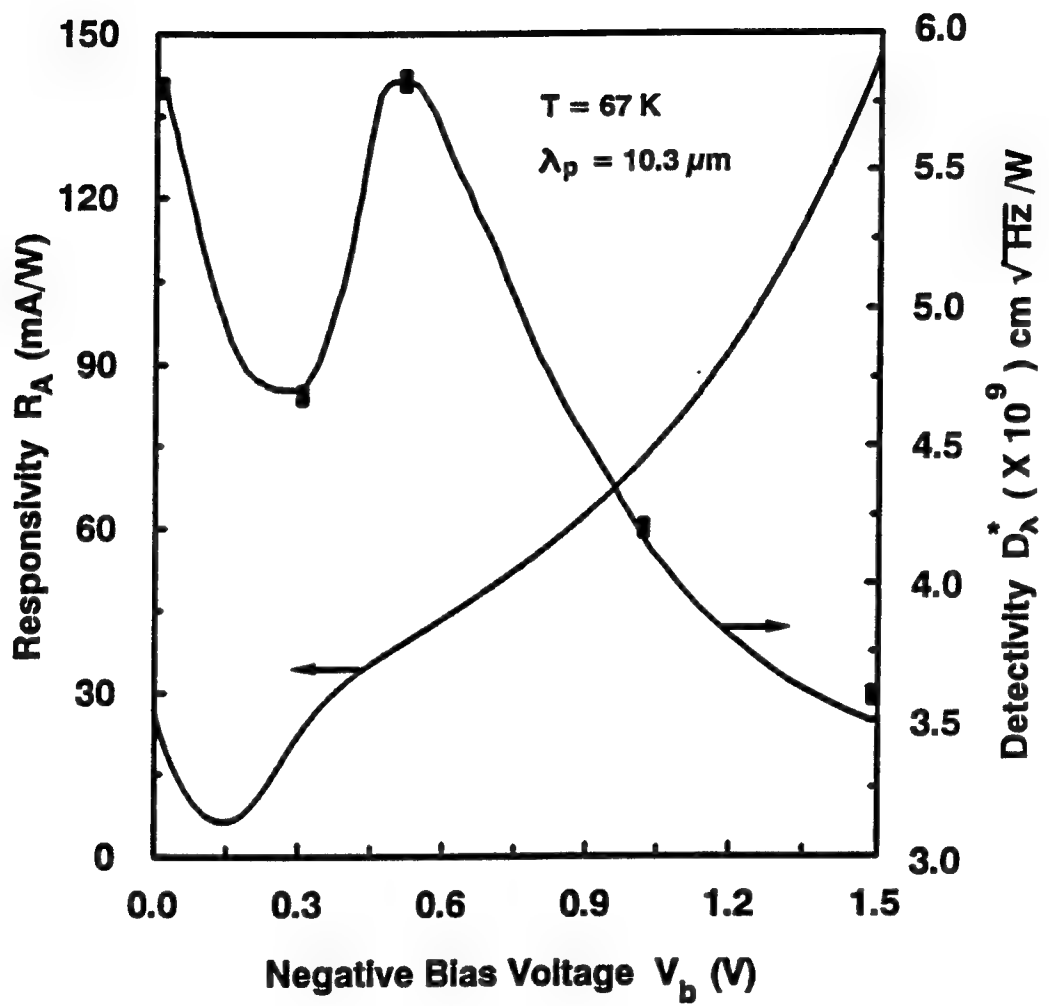


Figure 6.5. Responsivity and detectivity versus applied bias  $V_b$  at  $\lambda_p = 10.3 \mu\text{m}$  and  $T = 67 \text{ K}$ .

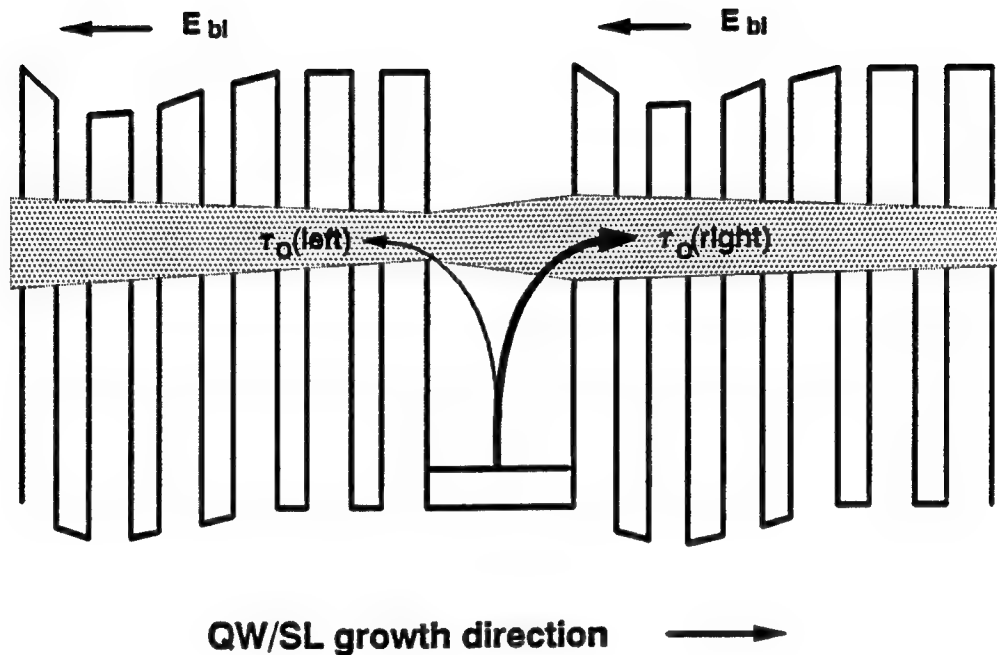


Figure 6.6. Modified energy band diagram at zero bias. An internal electric field  $E_{bl}$  is generated in the VT-QWIP, and a modulation miniband bandwidth is formed with tunneling time constant to the left-hand side larger than that to the right-hand side,  $\tau_o(\text{left}) > \tau_o(\text{right})$ .

## 7. A DUAL-MODE PC AND PV GaAs/AlGaAs QUANTUM WELL INFRARED PHOTODETECTOR (DM-QWIP) WITH TWO-COLOR DETECTION

### 7.1. Introduction

Recently, there has been considerable interest in the study of long-wavelength intersubband quantum well infrared photodetectors (QWIPs). A great deal of work has been reported on the lattice-matched GaAs/AlGaAs and InGaAs/InAlAs multiple quantum well and superlattice systems using bound-to-bound [19], bound-to-miniband (BTM) [13], and bound-to-continuum [11] intersubband transitions. Although a majority of the study on intersubband absorption has been based on the photoconductive (PC) mode operation [69], studies of the photovoltaic (PV) mode operation have also been reported in the literatures [16, 18, 22, 70]. However, due to the relatively low detectivity in these PV mode QWIPs, they have to be operated below 77 K to reduce the Johnson noise. Therefore, improvement of the performance in PV mode QWIPs is highly desirable for large area focal plane array (FPA) image sensor applications.

### 7.2. Design Consideration

A new GaAs/AlGaAs dual-mode (PC and PV) quantum well infrared photodetectors (DM-QWIP) based on bound-to-continuum state transition mechanism was designed and fabricated [71]. Both PC and PV detection modes for this QWIP can be operated at 77 K with excellent characteristics. By properly selecting the detector parameters, we tuned the PV and PC mode operations to the different response peak wavelengths. The DM-QWIP layer structure was grown on a semi-insulating (SI) GaAs substrate by using the molecular beam epitaxy (MBE) technique. A  $1\text{-}\mu\text{m}$ -thick GaAs buffer layer with dopant density of  $2\times 10^{18} \text{ cm}^{-3}$  was first grown on the SI GaAs substrate as an ohmic contact layer, followed by the growth of 40 periods of enlarged GaAs quantum well with well width of  $110 \text{ \AA}$  and a dopant density of  $5\times 10^{18} \text{ cm}^{-3}$ . The enlarged barrier layer on each side of the GaAs quantum well consists of an undoped  $\text{Al}_{0.25}\text{Ga}_{0.75}\text{As}$  ( $875 \text{ \AA}$ ) layers. Finally, a  $n^+$ -GaAs cap layer of  $0.45 \mu\text{m}$  and a dopant density of  $2\times 10^{18} \text{ cm}^{-3}$  was grown on top of the QWIP layer structure to facilitate ohmic contact. The physical parameters of the device structure are chosen so that there are two bound states inside the enlarged well (i.e.  $E_{EW0}$  and  $E_{EW1}$ ), and the continuum states  $E_{CN}$  are just slightly above the top of the barrier. A high dopant

density of  $5 \times 10^{18} \text{ cm}^{-3}$  was used in the enlarged GaAs quantum well so that the ground state  $E_{EW0}$  and the first excited state  $E_{EW1}$  are heavily populated by electrons to enhance absorption of infrared radiation in the quantum well. In order to minimize the undesirable tunneling current through the barrier layers, a thick (875 Å) undoped  $\text{Al}_{0.25}\text{Ga}_{0.75}\text{As}$  barrier layer was used in this QWIP structure to suppress the tunneling current from the ground state  $E_{EW0}$  and the first excited state  $E_{EW1}$ .

Figure 7.1 (a) shows the energy band diagram of the DM-QWIP, which illustrates the Fermi-level and two possible intersubband transition schemes. The first transition scheme is from the localized ground state  $E_{EW0}$  in the GaAs quantum well to the first continuum band states  $E_{CN}$  above the AlGaAs barrier. The second transition scheme takes place from the first excited state  $E_{EW1}$  to the continuum states  $E_{CN}$ . Due to the dopant migration into the enlarged AlGaAs barriers from the heavily doped GaAs quantum well during the layer growth, the actual conduction band diagram in the DM-QWIP is shown in Fig. 7.1 (b). The asymmetric band bending between two side of the quantum wells induces the internal electric field  $E_{bi}$ , which is opposite to the direction of the quantum well layer growth. To analyze these transition schemes, we performed theoretical calculations of the energy levels of the bound states and continuum states and transmission probability  $|T \cdot T|$  for this QWIP using a multilayer transfer matrix method [13] and the results are shown in Fig. 7.2. It is noted that the tunneling probability from the ground states and first excited state through the barrier layers are dramatically reduced so that the tunneling current is virtually eliminated. In order to precisely determine the intersubband transition levels, a complex calculation of the energy difference between the subband levels in the DM-QWIP should be performed. These include considerations of band nonparabolicity [38], electron-electron interaction [34], electron plasma [36], and energy band bending effect [39]. For simplicity, we have only considered the effects due to energy bending, depolarization, and electron-electron interaction in heavily doped bound states in the quantum well. By taking these effects into account, both bound states  $E_{EW0}$  and  $E_{EW1}$  are lowered by about  $\sim 5$  meV. Thus two intersubband transition peaks should be observed in the DM-QWIP, which corresponds to infrared wavelengths of  $7.7 \mu\text{m}$  and  $12 \mu\text{m}$ . Due to the thick barrier layers used in this QWIP, only thermal- and photoexcited electrons can be transported through the continuum states above the barrier and collected by the external ohmic contacts. As a result, charges separation occurs under the internal electric field  $E_{bi}$ , which leads to the creation of a potential difference between the two ohmic contacts of the detector. Furthermore, an asymmetrical energy band bending due to heavy doping effect can also promote the creation of internal photovoltage under IR illumination.

### **7.3. Experiments**

The DM-QWIP mesa structure was created by chemical etching through the quantum well active layers and stopped at the 1- $\mu\text{m}$ -thick heavily doped GaAs buffer layer for ohmic contact. The active area of the detector is  $200 \times 200 \mu\text{m}^2$ . To enhance the normal incidence coupling efficiency in the quantum well, we apply a planar metal grating coupler on the top of detector for normal illumination. The planar metal grating coupler consists of regularly spaced metal grating strips of  $0.2 \mu\text{m}$  thickness and was deposited by using electron beam (E-beam) evaporation of AuGe/Ni/Au materials. To achieve high coupling efficiency, the metal grating strips with a grating periodicity of  $\Lambda=5 \mu\text{m}$  and ratio factor  $d/\Lambda = 0.5$  ( $d$ : the metal strip width) were used in this DM-QWIP.

The infrared intersubband absorption spectra of the sample were measured at the Brewster angle ( $\theta_B = \sim 73^\circ$ ) by using a Bruker Fourier transform interferometer (FTIR) at room temperature. The directly measured quantity is the absorbance  $A = -\log_{10}(\text{transmission})$ , which can be converted to the absorption coefficient  $\alpha$  for  $45^\circ$  incident value. The main lobe of absorption coefficient for incident of  $45^\circ$  is shown in Fig. 7.3. It is noted that main absorption peak is centered at  $\lambda_p = 12.3 \mu\text{m}$ .

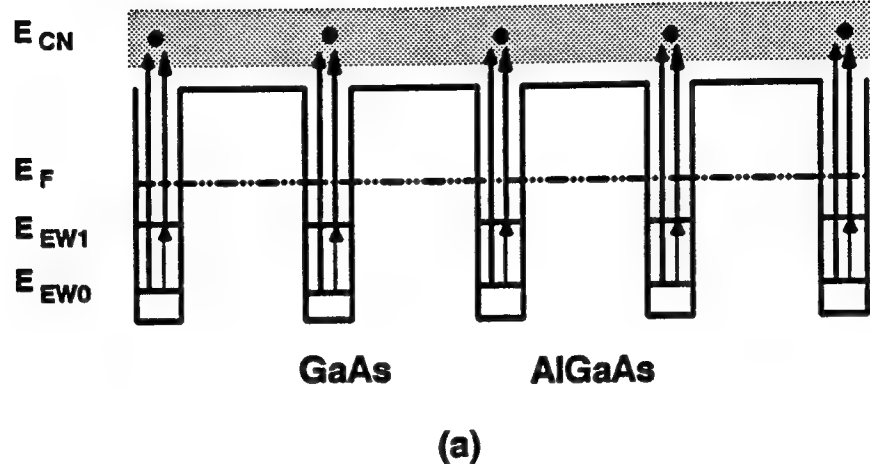
Figure 7.4 shows the current-voltage (I-V) curves and the differential resistance  $R_d$  values for the DM-QWIP measured at negative bias and  $T = 77\text{K}$  (mesa top as positive bias). It is noted that the dark current for bias voltage between - 1 and - 2 V is extremely low, which is attributed to the dramatically reduced tunneling current resulting from the increase of barrier layer thickness. Asymmetric dark current characteristics was observed in the DM-QWIP with a higher current in positive bias than that in negative bias, which results from the asymmetric effective barrier height at different polarity of applied bias as shown in Fig. 7.5. The photocurrent was measured as a function of temperature, bias voltage, polarization direction, and wavelength, using an ORIEL 77250 single grating monochromator and ceramic element infrared source. Figure 7.6 shows a plot of the normalized responsivity versus wavelength for the QWIP measured at  $T = 77 \text{ K}$ . Two responsivity peaks were observed: one at  $\lambda_p = 7.7 \mu\text{m}$  and  $V_b = 0 \text{ V}$ , and the other at  $\lambda_p = 12 \mu\text{m}$  and  $V_b > - 1 \text{ V}$ . At zero bias condition, the detector operates in the PV detection mode with a peak photovoltage responsivity  $R_V = 11,000 \text{ V/W}$  at  $\lambda_p = 7.7 \mu\text{m}$ , which is attributed to the ground state  $E_{EW0}$  to the first continuum state  $E_{CN}$  transition above the barrier. The photoexcited carriers are driven by the internal  $V_{bi}$  (or  $E_{bi}$ ) to generate a PV response current from the top of mesa to the bottom. At  $T = 77 \text{ K}$ , the zero bias differential resistance was found to be  $R_d = 5.5 \text{ M}\Omega$  at  $T = 77 \text{ K}$ . Since the detector operating in the PV mode is limited by Johnson

noise (i.e.  $i_n = \sqrt{4k_B T \Delta f / R_d}$ ), the detectivity  $D_\lambda^*$  for the PV mode was found to be  $1.5 \times 10^9$  cm- $\sqrt{\text{Hz}}/\text{W}$ . In order to verify the zero bias noise, we also measured the noise current by using a lock-in amplifier, which yielded a value of  $i_n = 3.0 \times 10^{-14}$  A, in good agreement with the calculated value from Johnson noise expression. When a negative bias voltage  $V_b$  is applied to the detector that is opposite to the  $V_{bi}$ , the PV response vanishes, and the PC mode conduction becomes the dominant detection mechanism with a PC response current from the bottom of the mesa to the top. The bias dependence of the photocurrent responsivity  $R_A$  was measured using a  $12 \mu\text{m}$  IR radiation at  $T = 77\text{K}$ , and the result is shown Fig. 7.7. The maximum responsivity  $R_A$  was found to be  $0.48 \text{ A/W}$  at  $V_b = -2 \text{ V}$  and  $T = 77 \text{ K}$ . As expected, the detector responsivity  $R_A$  increases with the applied bias voltage from  $V_b = -1 \text{ V}$  to  $V_b = -2 \text{ V}$ . For  $V_b > -2 \text{ V}$ , the photocurrent becomes saturated. The cutoff wavelength for this detector was found to be  $\lambda_c = 13.2 \mu\text{m}$  with a spectral bandwidth  $\Delta\lambda/\lambda_p$  of 18.3 %.

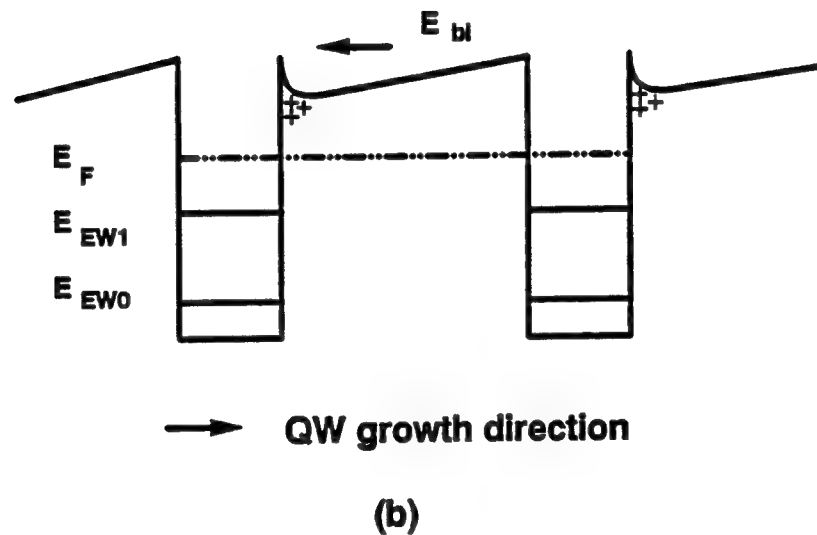
From the measured responsivity and dark current, we can calculate the detectivity  $D_\lambda^*$  of the detector using formula,  $D_\lambda^* = R_A (A_d \Delta f)^{1/2} / i_n$ , where  $A_d$  is the effective area of the detector and  $\Delta f$  is the noise bandwidth. The dark current G-R noise  $i_n$  is given by  $i_n = \sqrt{4eI_{dg}\Delta f}$  and may be evaluated from the measured responsivity  $R_A = (\lambda/1.24)(\eta g)$  and the unpolarized quantum efficiency expression  $\eta = (1/2)(1-e^{-2\alpha l})$ . The photoconductive gain,  $g$ , can be also derived from noise measurement. The results yielded a peak detectivity  $D_\lambda^* = 2 \times 10^{10} \text{ cm-}\sqrt{\text{Hz}}/\text{W}$  at  $\lambda_p = 12 \mu\text{m}$  and  $T = 77 \text{ K}$  for the PC mode operation. As shown in Fig. 7.7, the value of  $D_\lambda^*$  decreases with increasing negative bias voltage.

#### 7.4. Conclusions

In conclusion, we have demonstrated a new high performance PC and PV dual-mode operation GaAs QWIP using transition from the highly populated ground state and first excited state in the enlarged GaAs quantum well to the continuum band states above the AlGaAs barrier. The two bound states confined in the quantum well are a result of using the enlarged quantum well structure in the GaAs/AlGaAs DM-QWIP. With high detectivity and low dark current for both the PC and PV mode IR detection, the GaAs/AlGaAs DM-QWIP can be used for high performance two-color and dual-mode operation staring planar arrays and infrared imaging sensor applications.



(a)



(b)

Figure 7.1. Schematic energy-band diagram for a GaAs/AlGaAs DM-QWIP structure, (a) ideal case and (b) asymmetric energy-band bending which is a result of dopant migration effect in the quantum well. An internal electric field  $E_{bi}$  is generated within the QWIP structure, which is opposite to the growth direction of the QWIP.

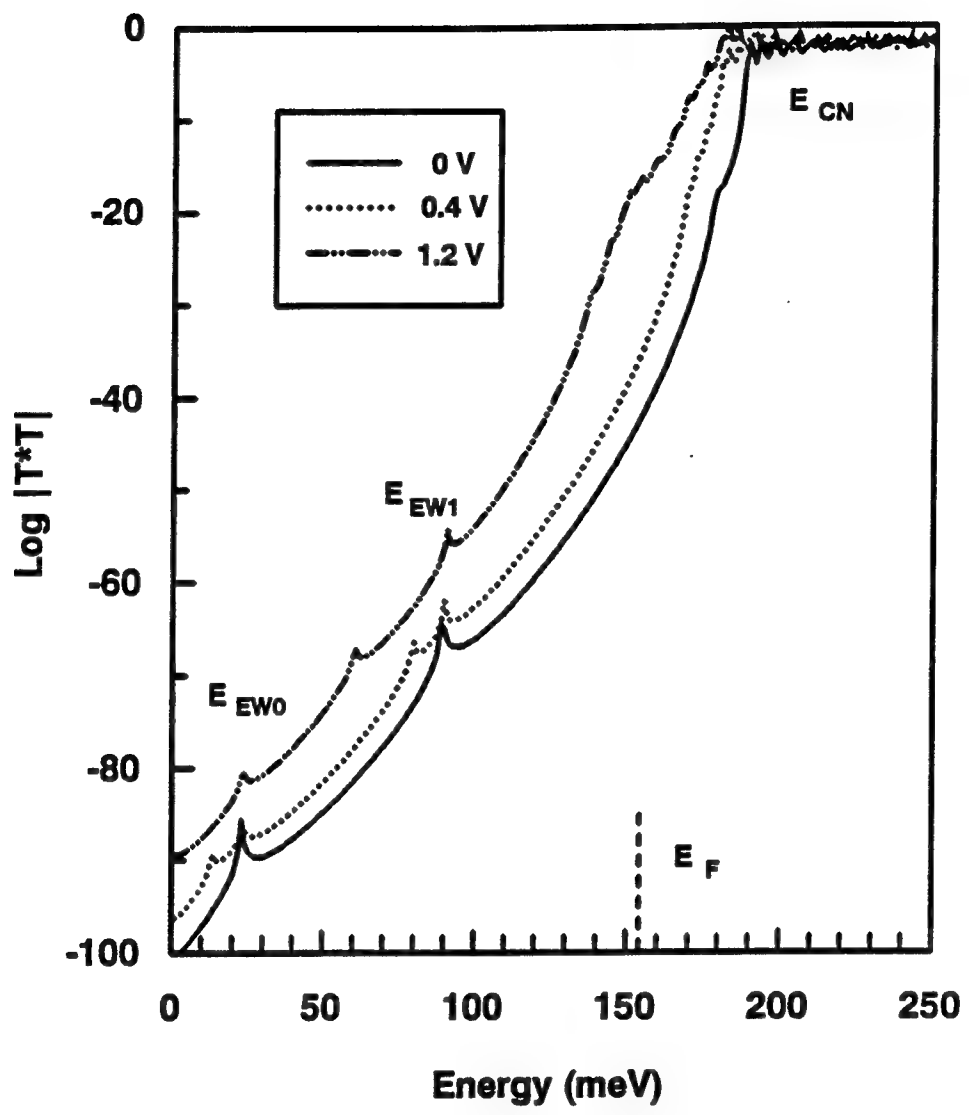


Figure 7.2. Calculated energy states and transmission coefficient  $|T \cdot T^*|$  for the GaAs/AlGaAs DM-QWIP structure by using a multiple-layer transfer matrix method.

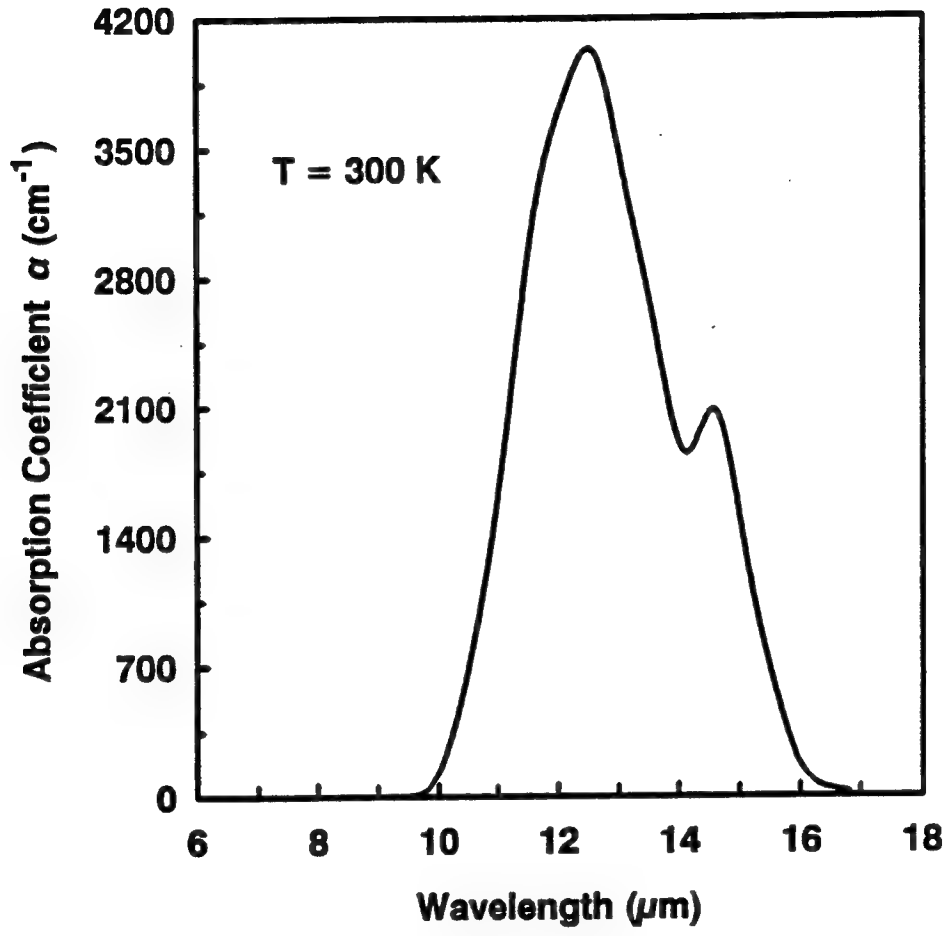


Figure 7.3. Measured intersubband absorption coefficient (converted to 45° incident values) by Bruker FTIR at the Brewster angle and  $T = 300 \text{ K}$ .

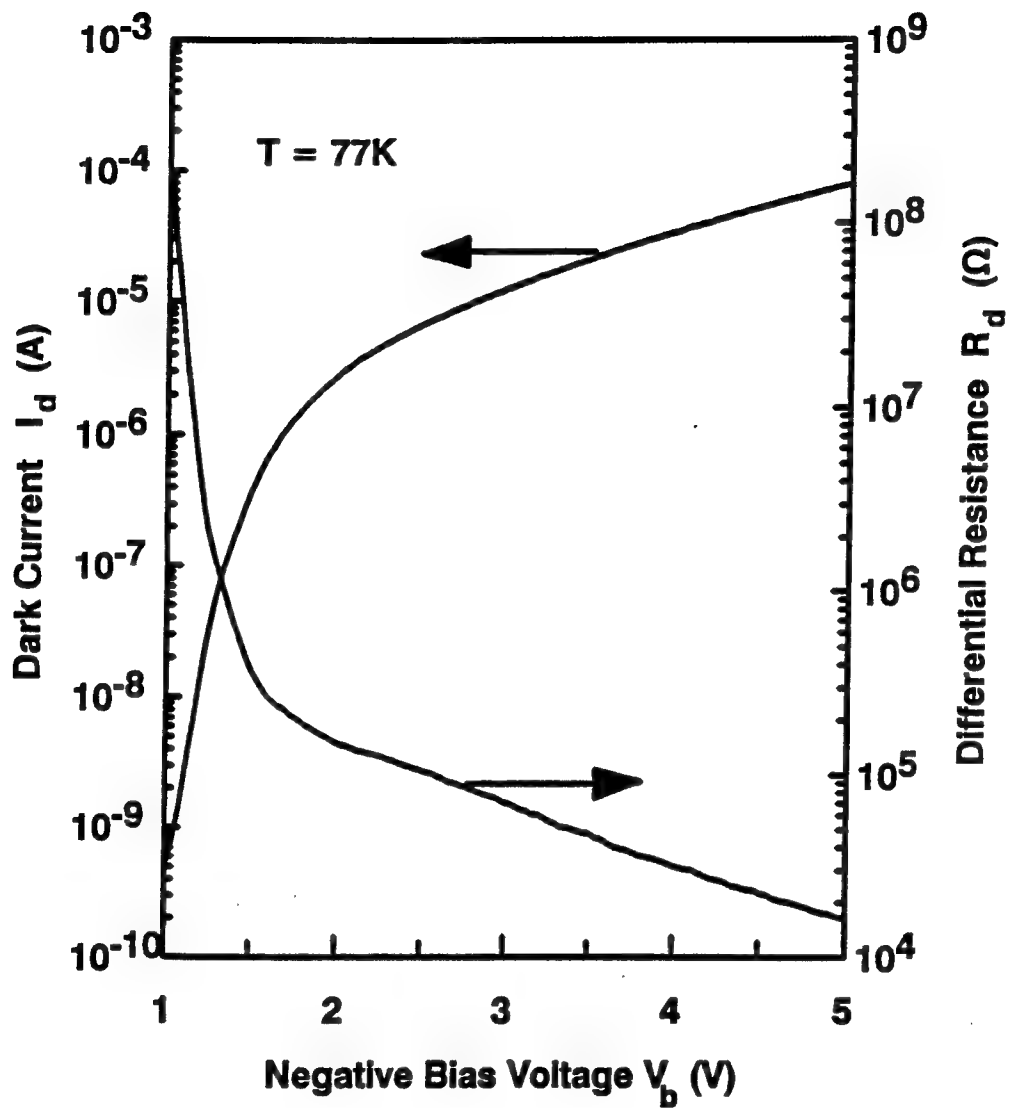


Figure 7.4. Dark current and differential resistance versus applied bias for the GaAs/AlGaAs DM-QWIP at  $T = 77\text{ K}$ .

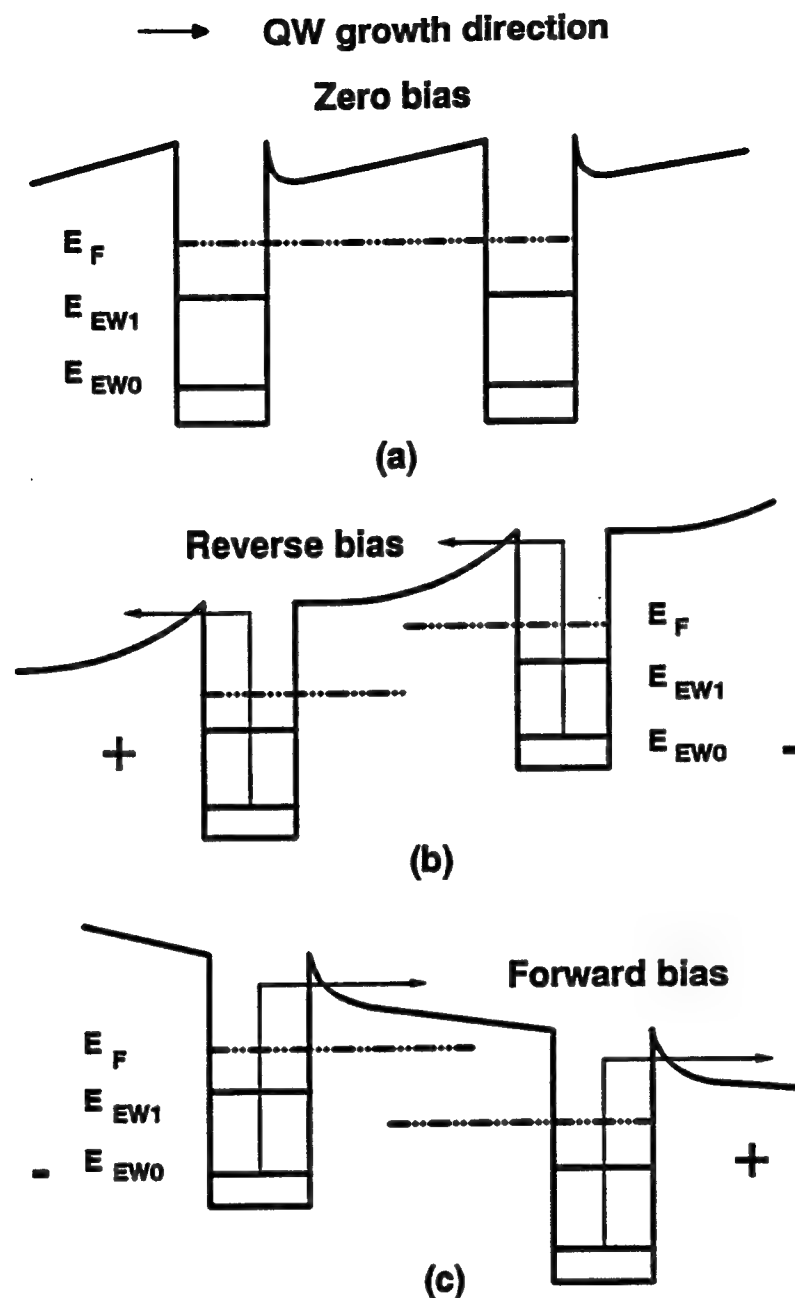


Figure 7.5. Effective barrier height seen by excited carriers for (a) zero bias, (b) reverse bias, and (c) forward bias. It is noticed that the effective barrier height is higher in reverse bias than in forward bias.

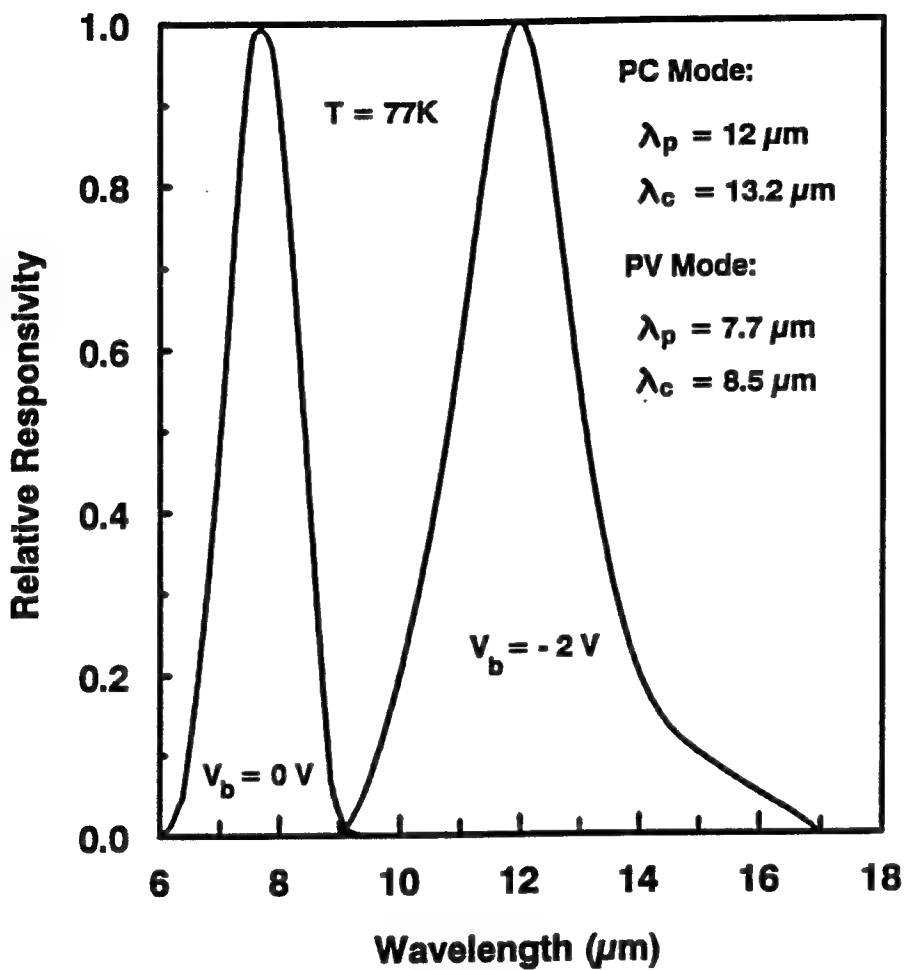


Figure 7.6. Relative responsivity versus wavelength for the GaAs/AlGaAs DM-QWIP at  $T = 77\text{ K}$ .

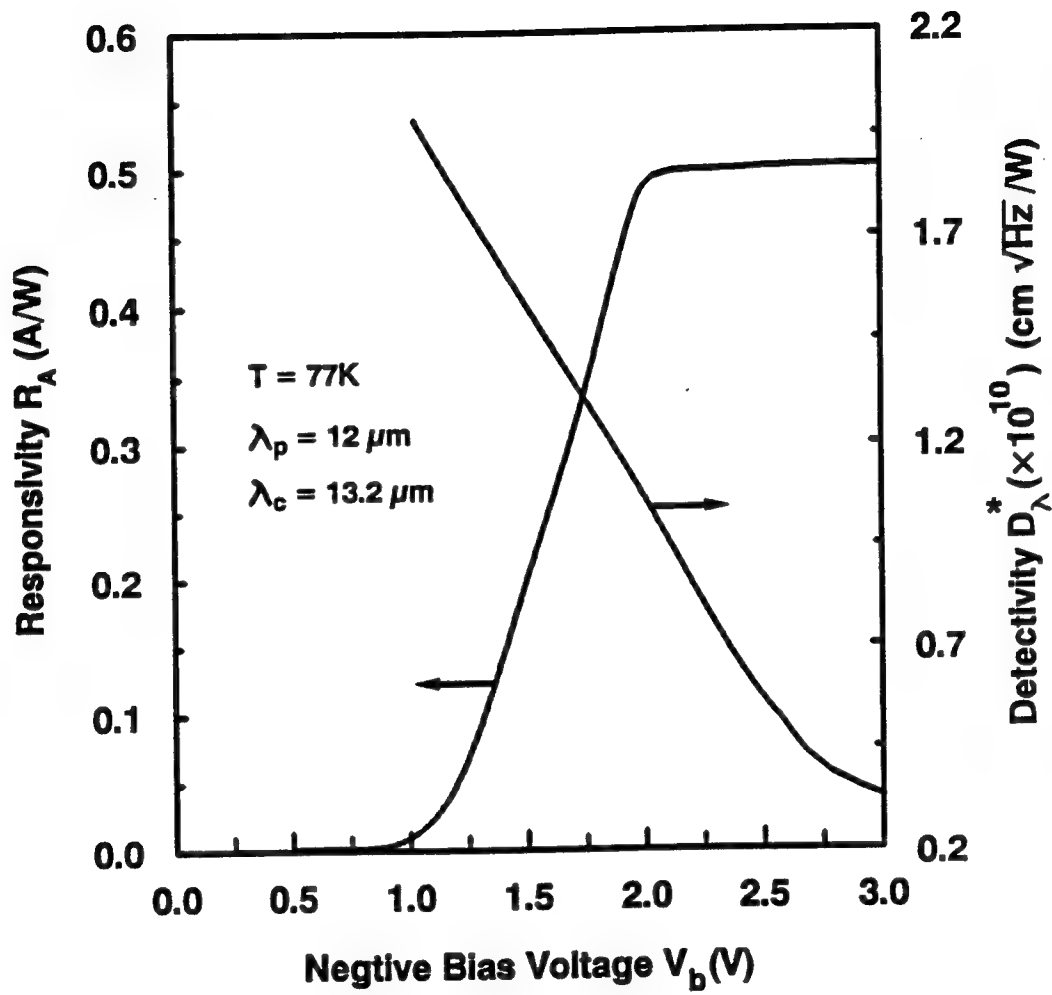


Figure 7.7. Responsivity and detectivity versus applied bias at  $\lambda_p = 12\text{ }\mu\text{m}$  and  $T = 77\text{ K}$  for the GaAs/AlGaAs DM-QWIP.

## 8. A NORMAL INCIDENCE TYPE-II QUANTUM WELL INFRARED PHOTODETECTOR USING AN INDIRECT BANDGAP AlAs/Al<sub>0.5</sub>Ga<sub>0.5</sub>As GROWN ON (110) GaAs SUBSTRATE FOR MID- AND LONG-WAVELENGTH MULTICOLOR DETECTION

### 8.1. Introduction

A normal incidence n-doped type-II indirect AlAs/Al<sub>0.5</sub>Ga<sub>0.5</sub>As quantum well infrared photodetector (QWIP) grown on (110) semi-insulating (SI) GaAs substrate with MBE technique has been developed for mid- and long-wavelength multicolor detection. The normal IR absorption for the n-doped quantum wells (QWs) was achieved in the X-band confined AlAs quantum wells. Six absorption peaks including four from X-band to  $\Gamma$ -band intersubband resonant transitions were observed at  $\lambda_{p1\sim 6} = 2.2, 2.7, 3.5, 4.8, 6.5$  and  $12.5 \mu\text{m}$ . The resonant transport from X-band to  $\Gamma$ -band gives rise to high photoconductive gain and large photoresponsivity, which are highly desirable for multicolor image sensor applications.

Quantum well infrared photodetectors (QWIPs) using type-I structures have been investigated extensively in recent years [74–82]. In type-I quantum well structure, the direct bandgap material systems are usually used, hence the shape of constant energy surfaces is spherical. As a result, only the component of IR radiation with electric field perpendicular to the quantum well layers will give rise to intersubband transition. Therefore, there is no intersubband absorption for normal IR incidence in the n-doped quantum wells. In order to achieve strong absorption for normal IR radiation in the quantum wells, grating couplers [83, 84] are required to induce absorbable component from the normal IR radiation. On the other hand, the intersubband absorption for normal IR incidence from indirect bandgap semiconductors such as SiGe/Si was observed [85, 86]. In indirect bandgap materials, conduction electrons occupy indirect valleys with ellipsoidal constant energy surfaces. The effective-mass anisotropy (mass tensor) of electrons in the ellipsoidal valleys can provide coupling between the parallel and perpendicular motions of the electrons when the principal axes of one of the ellipsoids are tilted with respect to the growth direction. As a result of the coupling, intersubband transitions at normal incidence in an indirect bandgap QWIP structure are allowed.

Since the AlAs/Al<sub>0.5</sub>Ga<sub>0.5</sub>As system is an indirect bandgap material, the conduction band

minima for the AlAs quantum wells are located at the X-point of the Brillouin zone (BZ). The constant energy surface will also undergo change from a typical sphere at the zone center for a direct bandgap material (i.e. GaAs) to off-center ellipsoids of an indirect bandgap material (i.e. AlAs). For AlAs, there are six ellipsoids along [100] axes with the centers of the ellipsoids located at about three-fourth of the distance from the BZ center. By choosing a proper growth direction such as [110], [111], [113], or [115] direction [80, 81], due to the anisotropic band structures and the tilted growth direction with respect to principal axes of ellipsoidal valley, it is possible to realize large area normal incidence IR detection in AlAs/AlGaAs QWIPs.

## 8.2. Theory

The normal incidence type-II QWIP using an indirect bandgap AlAs/AlGaAs material system [80, 82] was grown on (110) SI GaAs substrate by using molecular beam epitaxy (MBE) technique. A  $1.0\text{-}\mu\text{m}$ -thick n-doped GaAs buffer layer with  $N_D = 2 \times 10^{18} \text{ cm}^{-3}$  was first grown on the [110] oriented SI GaAs substrate, followed by the growth of 20 periods of AlAs/Al<sub>0.5</sub>Ga<sub>0.5</sub>As quantum wells with a well width of 30 Å and dopant density of  $2 \times 10^{18} \text{ cm}^{-3}$ . The barrier layers on either side of the quantum well consist of an undoped Al<sub>0.5</sub>Ga<sub>0.5</sub>As (500 Å) barrier layer. Finally, a  $0.3 \mu\text{m}$  thick  $n^+$ -GaAs cap layer with a dopant density of  $2 \times 10^{18} \text{ cm}^{-3}$  was grown on top of the quantum well layers for ohmic contacts. The dopant density of  $2 \times 10^{18} \text{ cm}^{-3}$  in the quantum well is chosen so that only the ground state is populated, and tradeoff between the low dark current and strong absorption strength is considered. We use the indirect bandgap AlAs for the quantum well layer and Al<sub>0.5</sub>Ga<sub>0.5</sub>As for the barrier layer. Since Al<sub>x</sub>Ga<sub>1-x</sub>As becomes an indirect bandgap material for  $x > 0.45$ , the conduction-band minimum shifts from the  $\Gamma$ -band to the X-band. Analyzing band ordering in the AlAs/Al<sub>0.5</sub>Ga<sub>0.5</sub>As MQW is a complicated subject in photonic device engineering [87]. We have used large enough quantum well and barrier layer thicknesses ( $> 10$  monolayers) so that the QWIP under study has a type-II band structure. The conduction band offset of Al<sub>0.5</sub>Ga<sub>0.5</sub>As relative to AlAs is about 170 meV. Figure 7.1 shows a schematic conduction-band ( $\Gamma$ - and X-band) diagram for the type-II indirect AlAs/Al<sub>0.5</sub>Ga<sub>0.5</sub>As quantum well structure, in which electrons are confined inside the AlAs QW layer. The intersubband transition energy levels between the ground bound state ( $E_0$ ) in the AlAs quantum well and the first excited state ( $E_1$ ) in the well or the continuum states ( $E_2 \dots E_6$ ) above the Al<sub>0.5</sub>Ga<sub>0.5</sub>As barrier layers are also shown in Fig. 8.1 (a). It is noted that band splitting between the  $\Gamma$ -band and the X-band edge is about 50 meV in the AlGaAs layer, and the conduction band offset in the  $\Gamma$ -band is found to be 630 meV.

To derive the basic equations for the normal induced intersubband transitions and the corre-

sponding indirect type-II QWIPs, we start with the Hamiltonian description of quantum mechanics for an electron [5]

$$H_0 = \frac{\mathbf{p}^2}{2m^*} + V(\mathbf{r}) + \frac{\hbar}{4m^{*2}c^2}\boldsymbol{\sigma} \cdot (\nabla V(\mathbf{r}) \times \mathbf{p}), \quad (8.1)$$

where  $m^*$ ,  $\mathbf{p}$ , and  $\boldsymbol{\sigma}$  are the effective mass, momentum, and spin operators of an electron, respectively.  $V(\mathbf{r})$  is a periodic potential function. The system under consideration consists of an assembly of electrons and the infrared radiation field. The Hamiltonian of this system,  $H$ , may be written as the sum of the unperturbed Hamiltonian  $H_0$  and the perturbing Hamiltonian  $H'_{rad}$  which represents the interaction between the electrons and the incident infrared photon and is given by [88]

$$H'_{rad} = -\frac{e}{m^*c} \mathbf{A} \cdot \left[ \mathbf{P} + \left( \frac{\hbar}{4m^*c^2} \right) \boldsymbol{\sigma} \times \nabla V(\mathbf{r}) \right], \quad (8.2)$$

where  $\mathbf{A}$  is the vector potential of the IR radiation field and  $\mathbf{P}$  is the canonical momentum.

The matrix element of intersubband transition in the quantum well is given by [89, 90]

$$M_{if} = \int \psi_{kf} H'_{rad} \psi_{ki} d\mathbf{r} = -e \left( \frac{2\pi}{V' c n_r \hbar \omega} \right)^{1/2} \mathbf{e}_\omega \cdot \nabla_{\mathbf{k}} \mathcal{E}_{\mathbf{k}} \quad (8.3)$$

where  $\psi_{ki(f)}$  is the total wavefunction for a state in  $i$ -th (or  $f$ -th) intersubband, the parameters  $i$  and  $f$  denote the initial and the final states,  $\mathbf{e}_\omega$  is the unit polarization vector of the incident photon,  $\omega$  is the light frequency,  $e$  is the electronic charge,  $V'$  is the volume of the crystal,  $n_r$  is the refractive index at the wavelength of incident IR radiation, and  $\mathcal{E}_{\mathbf{k}}$  is the conduction band energy of the X-valley material in the well.

It can be shown that the intersubband transition rate  $W$  may be expressed as [89, 91]

$$\begin{aligned} W &= \frac{2\pi}{\hbar} |M_{fi}|^2 \delta(E_f - E_i - \hbar\omega) \\ &= \frac{B_0 k_z^2}{\omega} \left[ \frac{\partial^2 \mathcal{E}_{\mathbf{k}}}{\partial k_z \partial k_x} (\mathbf{e}_\omega \cdot \mathbf{x}_0) + \frac{\partial^2 \mathcal{E}_{\mathbf{k}}}{\partial k_z \partial k_y} (\mathbf{e}_\omega \cdot \mathbf{y}_0) \right. \\ &\quad \left. + \frac{\partial^2 \mathcal{E}_{\mathbf{k}}}{\partial k_z \partial k_z} (\mathbf{e}_\omega \cdot \mathbf{z}_0) \right]^2 \delta(E_f - E_i - \hbar\omega) \end{aligned} \quad (8.4)$$

where  $B_0$  is a constant equal to  $\frac{e^2 \pi^2}{c V' n_r \hbar^2}$ ;  $\mathbf{x}_0$ ,  $\mathbf{y}_0$ , and  $\mathbf{z}_0$  are the directional unit vectors. The result indicates that the nonzero intersubband transition probability at normal incidence can be obtained only when either of the crossover terms in the second partial derivatives is nonzero.

For an indirect gap type-II AlAs quantum well layer grown along [110] direction of GaAs substrate, due to the tilted anisotropic energy band with minimum point away from BZ center (see Fig. 8.1(b)), the second partial derivatives  $\frac{\partial^2 \mathcal{E}_{\mathbf{k}}}{\partial k_z \partial k_i}$  ( $i = x, y$ ) can be different from zero. Therefore,

it is possible to excite long wavelength intersubband transitions in the quantum well under normal incidence IR radiation. However, for a direct type-I system (i.e. GaAs) due to the isotropic spherical energy surface and the axis symmetric parabolic band  $E = E_z + \hbar^2(k_y^2 + k_z^2)/2m^*$ , it always has  $\frac{\partial^2 \mathcal{E}_k}{\partial k_x \partial k_i} = 0$ , (where  $i \neq z$ ). The corresponding transition rate for direct type-I quantum well becomes

$$W = \frac{B_0 k_z^2}{\omega} \left[ \frac{\partial^2 \mathcal{E}_k}{\partial k_z \partial k_z} (\mathbf{e}_\omega \cdot \mathbf{z}_0) \right]^2 \delta(E_f - E_i - \hbar\omega) \quad (8.5)$$

The above equation reveals that, due to  $\mathbf{e}_\omega \perp \mathbf{z}_0$ , the optical transitions would become zero for type-I structures under normal incidence radiation.

### 8.3. Coupling between $\Gamma$ - and X-bands

To analyze the intersubband transition mechanism and energy level positions in a type-II AlAs/AlGaAs QWIP, theoretical calculations of the energy states  $E_n$ , ( $n = 0, 1, 2, \dots$ ) for the X-band and  $\Gamma$ -band and the transmission coefficient  $|T \cdot T|$  for the QWIP were performed by using a multi-layer transfer matrix method [13]. To determine the intersubband transition levels, we use the one-band effective mass envelope function approximation (see Appendix A) and take into account the effects of band nonparabolicity and electron-electron interaction. In comparison with the more sophisticated energy band models such as two-band and three-band models, the one-band effective mass envelope function approach will give the first order approximation, thus yielding a reasonable prediction for the QWIP performance. The simulated results are summarized in Table 8.1. Each energy level listed in the Table 8.1 is referred to the center of its bandwidth. It is noted that  $E_0$  (ground state) and  $E_1$  (first excited state) are bound states which are confined in the AlAs X-band well, while  $E_2$  to  $E_6$  are all continuum states in X-band. The continuum states in the X-band can find their resonant pair levels in the  $\Gamma$ -band except  $E_2$  which is located below the  $\Gamma$ -band minima (about 30 meV).

In a type-II indirect AlAs/AlGaAs QWIP, free carriers are confined in the AlAs quantum well formed in the X-conduction band minimum, which has a larger electron effective mass than that in the  $\Gamma$ -band valley. When normal incidence radiation impinges on this QWIP, electrons in the ground-state of the X-well are excited to either the excited state  $E_1$  or one of the continuum states  $E_2$  to  $E_6$ . If the continuum state in the X-band valley is resonantly aligned with a state in the  $\Gamma$ -band valley, the photon-generated electrons in the X-band will undergo resonant transport to the resonant state in the  $\Gamma$ -band provided that the  $\Gamma$ -band barrier layer (in the present case, AlAs layer) is so thin that it is transparent to the conduction electrons [93, 94]. This resonant transport from X-band to  $\Gamma$ -band is expected to be a coherent resonance which can greatly enhance the

transmission if the electron lifetime  $\tau_L^\Gamma$  in these continuum states is much shorter than the X-band to  $\Gamma$ -band scattering time constant  $\tau_S$ . The  $\tau_L^\Gamma$  can be estimated from the uncertainty principle,  $\tau_L^\Gamma = \frac{\hbar}{\Delta E_{FWHM}}$   $\sim 10$  fs (where  $\Delta E_{FWHM}$  is the spectral full width at half maximum), while  $\tau_S \sim 1$  ps [18], hence  $\tau_L^\Gamma \ll \tau_S$ . The peak transmission at resonance is expected to be increased by the ratio of  $\tau_S/\tau_L^\Gamma \sim 100$ . In addition, due to the effective mass difference between the X-band and the  $\Gamma$ -band, electron velocity and mobility in the  $\Gamma$ -valley will be much higher than the value in the X-band valley. Since the photocurrent is proportional to the electron velocity and mobility (i.e.,  $I_{ph} = A_d v_d G \tau_R$ , where  $A_d$  is the effective area of the detector,  $v_d$  is the drift velocity,  $G$  is the photogeneration rate,  $1/\tau_R$  is the recombination rate of electrons in the  $\Gamma$ -band), a large increase in the photocurrent is expected when photon-generated electron resonant transport from the X-band to  $\Gamma$ -band takes place under certain bias conditions as illustrated in Fig. 8.2. It is known that photoconductive gain  $g = \tau_L/\tau_T$ , where  $\tau_T$  is transit time ( $= \frac{l}{\mu F}$ ,  $l$  superlattice thickness,  $\mu$  electron mobility, and  $F$  electric field). In the coherent resonance and certain bias condition, the gain  $g$  will be significantly enlarged as well.

#### 8.4. Experiments

A BOMEM interferometer was used to measure the infrared absorbance of the AlAs/AlGaAs QWIP sample. In order to eliminate substrate absorption, we performed absorbance measurements with and without the quantum well layers. The absorbance data were taken using normal incidence at 77 K and room temperature. The absorption coefficients deduced from the absorbance data are shown in Fig. 8.3. Two broad absorption peaks at wavelengths  $\lambda_p = 6.8 \mu\text{m}$  and  $14 \mu\text{m}$  were detected, while four additional narrow absorption peaks at  $\lambda_p = 2.3 \mu\text{m}$ ,  $2.7 \mu\text{m}$ ,  $3.5 \mu\text{m}$ , and  $4.8 \mu\text{m}$  at NIR were also observed. The measured absorption peak wavelengths are in excellent agreement with the theoretical prediction. All the absorption coefficients measured at 77 K were found to be about a factor of 1.2 higher than the room temperature values. From our theoretical analysis, the  $14 \mu\text{m}$  peak with an absorption coefficient of about  $2000 \text{ cm}^{-1}$  is attributed to the transition between the ground state  $E_0$  and the first excited state  $E_1$  in quantum well, while the  $6.8 \mu\text{m}$  peak with absorption coefficient of about  $1600 \text{ cm}^{-1}$  is due to transition between the ground state  $E_0$  and the continuum state  $E_2$ . The absorption peaks at  $2.3 \mu\text{m}$ ,  $2.7 \mu\text{m}$ ,  $3.5 \mu\text{m}$ , and  $4.8 \mu\text{m}$  are attributed to the transitions between the ground state  $E_0$  and other high order continuum states listed in Table 8.1. It is interesting to note that the high order intersubband transitions have relatively larger absorption coefficient of about  $4000 \text{ cm}^{-1}$ , which is quite different from the intersubband transition in type-I QWIPs. However, the absorption at  $6.8 \mu\text{m}$ , which is also due to the transition between bound state and continuum state, has a small absorption coefficient

compared to the other high order continuum transitions. This indicates that the  $6.8 \mu\text{m}$  absorption peak has a different absorption and conduction mechanism, which we shall discuss it later.

To facilitate the normal incidence IR illumination, an array of  $210 \times 210 \mu\text{m}^2$  mesas were chemically etched down to  $n^+$ -GaAs buffer contact layer on the GaAs substrate. Finally, AuGe/Ni/Au ohmic contacts were formed on the QWIP structures, leaving a central sensing area of  $190 \times 190 \mu\text{m}^2$  for normal incidence illumination on top contact of the QWIP. Device characterization was performed in a liquid-helium cryogenic dewar. A HP4145 semiconductor parameter analyzer was used to measure the dark current versus bias voltage. Figure 8.4 shows the measured dark current as a function of the bias voltage for temperatures between 68 and 98 K. Substantial reduction of device dark current was achieved in the present type-II structure. The photocurrent was measured using a CVI Laser Digikrom 240 monochromator and an ORIEL ceramic element infrared source. A pyroelectric detector was used to calibrate the radiation intensity from the source. The measured data for the QWIP are tabulated in Table 8.2, which showed six absorption peaks. The peaks for  $\lambda_{p1,2}$  only exhibited the photoconductive (PC) detection mode, while the peaks for  $\lambda_{p3-6}$  operated in both the PC mode and photovoltaic (PV) mode.

Figure 8.5 shows the QWIP's photoresponse and absorption coefficient for wavelengths from 9 to  $18 \mu\text{m}$ . The peak photoresponse was observed at  $\lambda_{p1} = 12.5 \mu\text{m}$  with a cutoff wavelength at  $14.5 \mu\text{m}$  and a peak responsivity of  $R_A = 24 \text{ mA/W}$  at  $T = 77 \text{ K}$  and  $V_b = -2 \text{ V}$ . A broader spectral bandwidth of  $\Delta\lambda/\lambda_{p1} = 30\%$  was obtained for this QWIP, which is larger than the type-I QWIP [71]. The property of a broader spectral bandwidth within X-band intersubband transition was also found in [113] GaAs substrate growth direction [81, 92]. Detectivity for this peak wavelength  $\lambda_{p1} = 12.5 \mu\text{m}$  was found to be about  $1.1 \times 10^9 \text{ cm}\sqrt{\text{Hz}}/\text{W}$  under the above specified condition. A relative small absorption peak at  $\lambda_{p2} = 6.5 \mu\text{m}$  was detected, which is attributed to the transition between the ground state  $E_0$  and the first continuum state  $E_2$ . The peak responsivity for  $\lambda_{p2}$  was found to be about  $R_A = 5 \text{ mA/W}$  at  $T = 77 \text{ K}$  and  $V_b = -2 \text{ V}$ , which was not shown in the figure. About  $8 \sim 11 \text{ meV}$  blueshifts were found at these two peak wavelengths.

Figure 8.6 shows the normalized photovoltaic (PV) spectral response bands at the peak wavelengths of  $\lambda_{p4} = 3.5 \mu\text{m}$  and  $\lambda_{p6} = 2.2 \mu\text{m}$ . The two spectral response bands cover wavelengths from  $2.2 \mu\text{m}$  to  $6.5 \mu\text{m}$  for peak wavelength at  $\lambda_{p4} = 3.5 \mu\text{m}$  and from  $2.0 \mu\text{m}$  to  $3.25 \mu\text{m}$  for peak wavelength at  $\lambda_{p6} = 2.2 \mu\text{m}$ . The spectral band for  $\lambda_{p6}$  has an additional peak at  $\lambda_{p5} \sim 2.7 \mu\text{m}$ , while the spectral band for  $\lambda_{p4}$  also has a large tail which results from another peak contribution at about  $\lambda_{p3} \sim 4.8 \mu\text{m}$ . The positions for all four peak wavelengths  $\lambda_{p3-6}$  are in excellent agreement

with the values deduced from the FTIR measurements and theoretical calculations. The main peak responses occurred at  $\lambda_{p4} = 3.5 \mu\text{m}$  and  $\lambda_{p6} = 2.2 \mu\text{m}$  with responsivities of  $R_A = 29 \text{ mA/W}$  and  $32 \text{ mA/W}$ , respectively, at  $V_b = 0 \text{ V}$  and  $T = 77 \text{ K}$ . The responsivities of two main peaks have a different voltage dependence. The peak for  $\lambda_{p4}$  increases rapidly for  $V_b > -0.5 \text{ V}$ , and it reaches a saturation responsivity value of  $18.3 \text{ A/W}$  at  $V_b \geq -3 \text{ V}$  as shown in Fig. 8.7. On the other hand, the responsivity for  $\lambda_{p6}$  remains nearly constant for  $V_b \leq -2 \text{ V}$ , and then exponentially increases to  $R = 110 \text{ A/W}$  at  $V_b \sim -6 \text{ V}$ , as shown in Fig. 8.8. Extremely large photoconductivity gains of 630 and 3,200 for  $\lambda_{p4}$  and  $\lambda_{p6}$  (as compared to the value at  $V_b = 0 \text{ V}$ ) were obtained at  $V_b = -3 \text{ V}$  and  $-6 \text{ V}$ , respectively. The larger responses at  $\lambda_{p4}$  and  $\lambda_{p6}$  wavelengths are due to a better alignment of these resonant levels, while the relatively lower responses for the  $\lambda_{p3}$  and  $\lambda_{p5}$  wavelengths are ascribed to a slightly misalignment in the resonant levels, which results from the  $\Gamma$ -X coupling strength difference [95]. However, no photoconductivity gain is expected to be observed at  $\lambda_{p1}$  and  $\lambda_{p2}$  peak wavelengths due to the absence of the resonant transition from the X-band to the  $\Gamma$ -band in the electronic conduction.

The PV mode operation at peak wavelengths of  $\lambda_{p3\sim 6}$  in the type-II AlAs/AlGaAs QWIP is resulted from the macroscopic polarization field (i.e. Hartree potential) caused by the energy band bending effect and spatial separation of electrons and holes [44, 71, 96, 97]. However, the PV operation was not observed in the wavelengths of  $\lambda_{p1\sim 2}$ . This is probably due to the novel resonant transport feature which enhances the photogenerated electron conduction.

### **8.5. Conclusions**

In conclusion, we have demonstrated a normal incidence type-II QWIP using an indirect X-band AlAs/Al<sub>0.5</sub>Ga<sub>0.5</sub>As system grown on (110) GaAs substrate with multicolor responses for  $2 \sim 18 \mu\text{m}$  wavelength detection. The desirable normal incidence radiation is allowed due to the tilted and anisotropic energy band structure of AlAs/ AlGaAs grown on (110) GaAs substrate. The detector was found to have six peak wavelength responses at  $\lambda_{p1\sim 6} = 12.5, 6.5, 4.8, 3.5, 2.7$  and  $2.2 \mu\text{m}$ . The spectral responses for wavelengths at  $\lambda_{p3\sim 6} = 4.8, 3.5, 2.7$ , and  $2.2 \mu\text{m}$  are ascribed to the novel resonant interaction between the X-band and  $\Gamma$ -band that yields a large photoconductive gain in electron conduction. The spectral response at wavelength of  $12.5 \mu\text{m}$  has a broader bandwidth ( $\Delta\lambda/\lambda_{p1} = 30 \%$ ), covering wavelength ranging from 9 to  $18 \mu\text{m}$ . The capabilities of normal incidence, large spectral sensing range, ultra high photoconductive gain, multicolor detection, and ultra low noise characteristics make the type-II AlAs/AlGaAs QWIPs highly desirable for many infrared applications. Further studies of the interaction effects between the X- and  $\Gamma$ -bands, transi-

tion coupling, bandgap engineering, and hot electron transport mechanisms in the type II indirect III-V multiple quantum well structures may lead to the development of novel quantum well infrared detectors, lasers, and modulators.

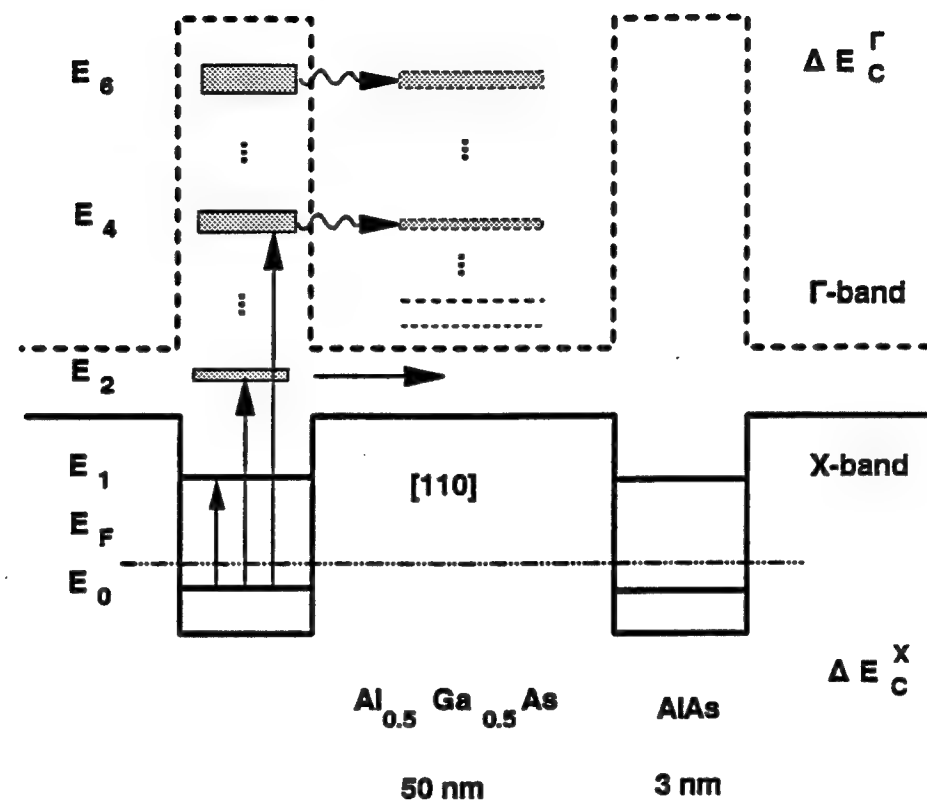
Table 8.1. The simulated intersubband transition energy levels in the X-band and  $\Gamma$ -band for the type-II AlAs/AlGaAs QWIP.

	$E_0$	$E_1$	$E_2$	$E_3$	$E_4$	$E_5$	$E_6$
X-band	20	110	189	270	365	475	600
$\Gamma$ -band				265	370	460	595

Notes: The energy levels,  $E_3$ ,  $E_4$ ,  $E_5$ , and  $E_6$  in the  $\Gamma$ -band and X-band formed the resonant levels for the photoexcited electrons in this QWIP. The parameters used in calculation of X-band and  $\Gamma$ -band, respectively, are  $m^* = 0.78 m_0$ ,  $0.15 m_0$  for AlAs and  $0.82 m_0$ ,  $0.11 m_0$  for  $Al_{0.5}Ga_{0.5}As$ . (All the energy levels shown are measured from the AlAs quantum well X-conduction band edge in unit of meV.)

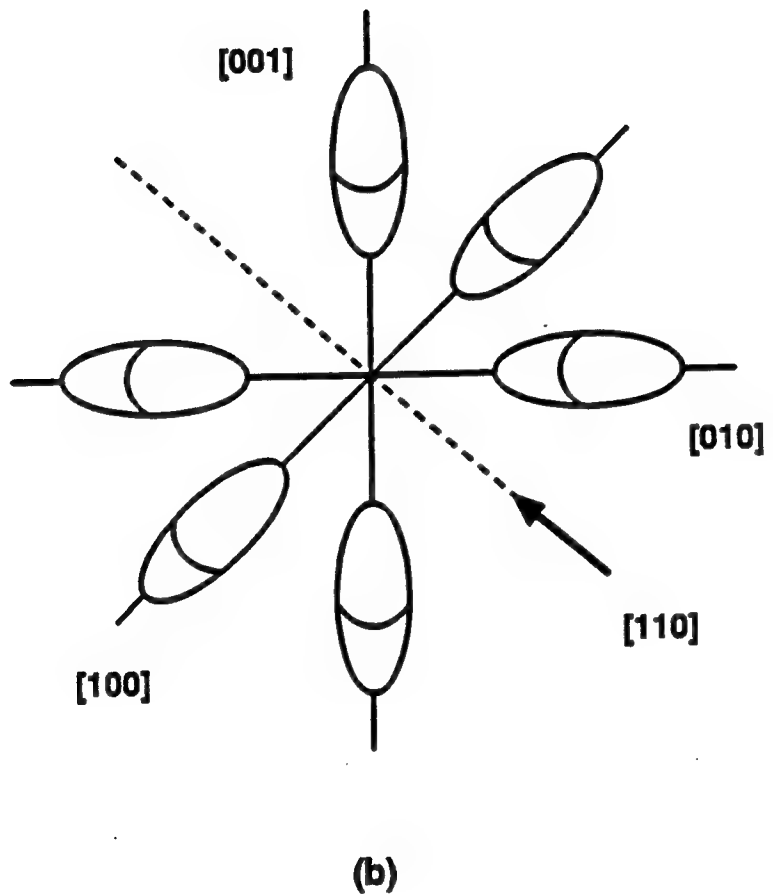
Table 8.2. The measured peak wavelengths, responsivities, and detectivities for the type-II AlAs/AlGaAs QWIP at T = 77 K.

	$\lambda_{p1}$	$\lambda_{p2}$	$\lambda_{p3}$	$\lambda_{p4}$	$\lambda_{p5}$	$\lambda_{p6}$
Peak ( $\mu\text{m}$ )	12.5	6.5	4.8	3.5	2.7	2.2
$R_A$ (A/W) (PV)				0.029		0.032
$R_A$ (A/W) (PC)	0.024	0.005		18.3		110
	2 V	2 V		3 V		6 V
$D_A^*$ (cm $\sqrt{\text{Hz}}/\text{W}$ )	$1.1 \times 10^9$			$3.0 \times 10^{11}$		$1.1 \times 10^{12}$



(a)

Figure 8.1. (a) The conduction band diagram for the type-II AlAs/Al<sub>0.5</sub>Ga<sub>0.5</sub>As QWIP. The solid line is for the X-band and the dashed line denotes the  $\Gamma$ -band. (b) The six ellipsoids of X-band minima along the  $\langle 100 \rangle$  axes with center of the ellipsoids located at about three-fourth of the distance from BZ center for AlAs. The preferred [110] growth direction is indicated by the arrow.



(b)

Figure 8.1. Continued.

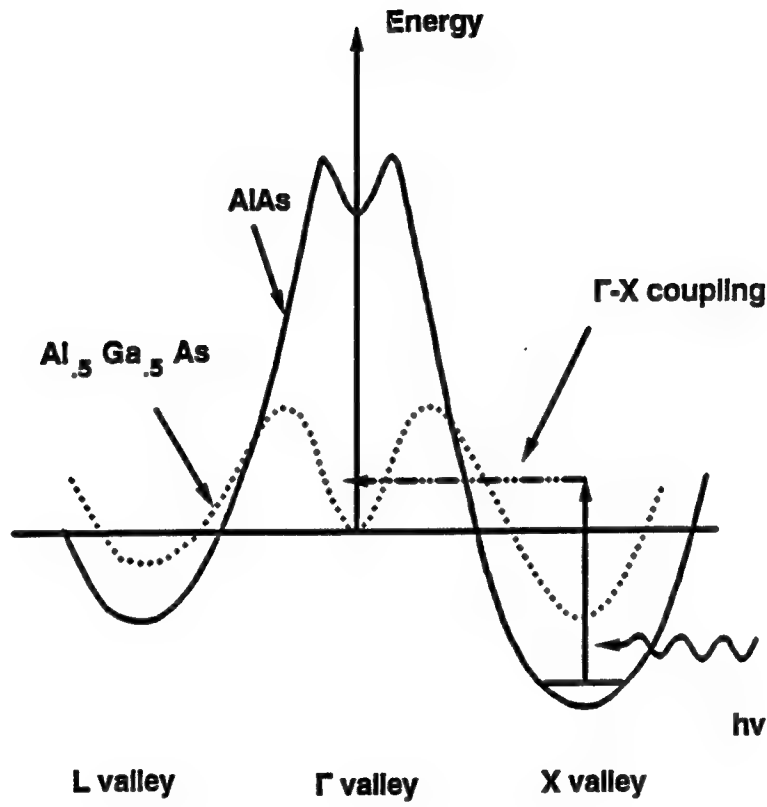


Figure 8.2. Schematic diagram of the conduction band minima for L-,  $\Gamma$ -, and X-valleys.  $\Gamma$ -X coupling transport is illustrated by the dot-dashed arrow.

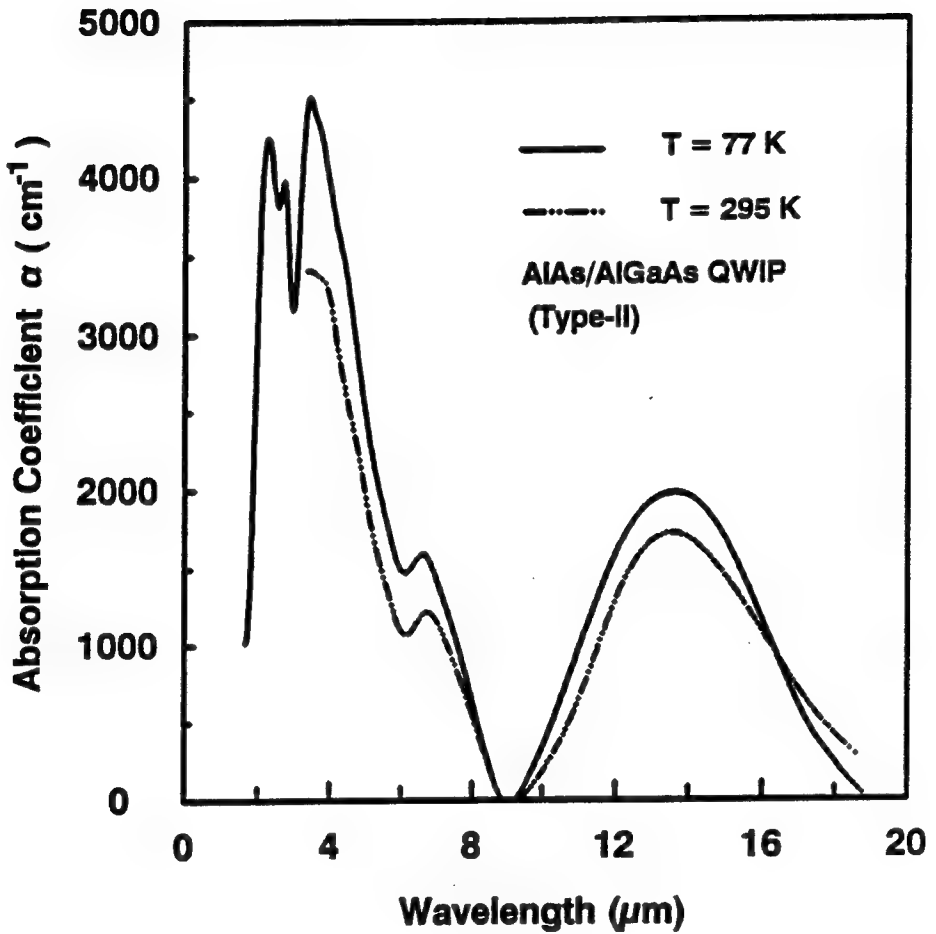


Figure 8.3. Absorption coefficients versus wavelength measured by BOMEN interferometer at normal incidence for the AlAs/AlGaAs QWIP at  $T = 77 \text{ K}$  and room temperature.

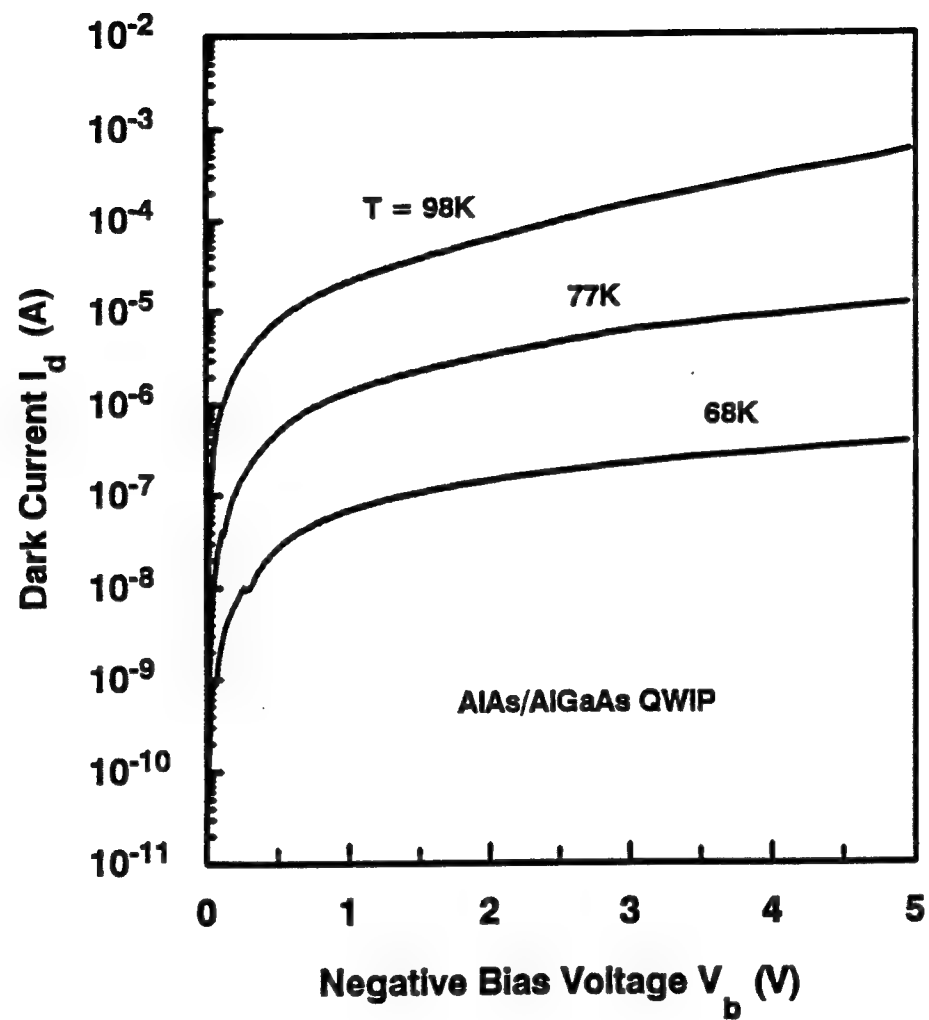


Figure 8.4. Dark currents versus negative bias voltage for the AlAs/AlGaAs QWIP measured at  $T = 68, 77, 98\text{ K}$ , respectively.

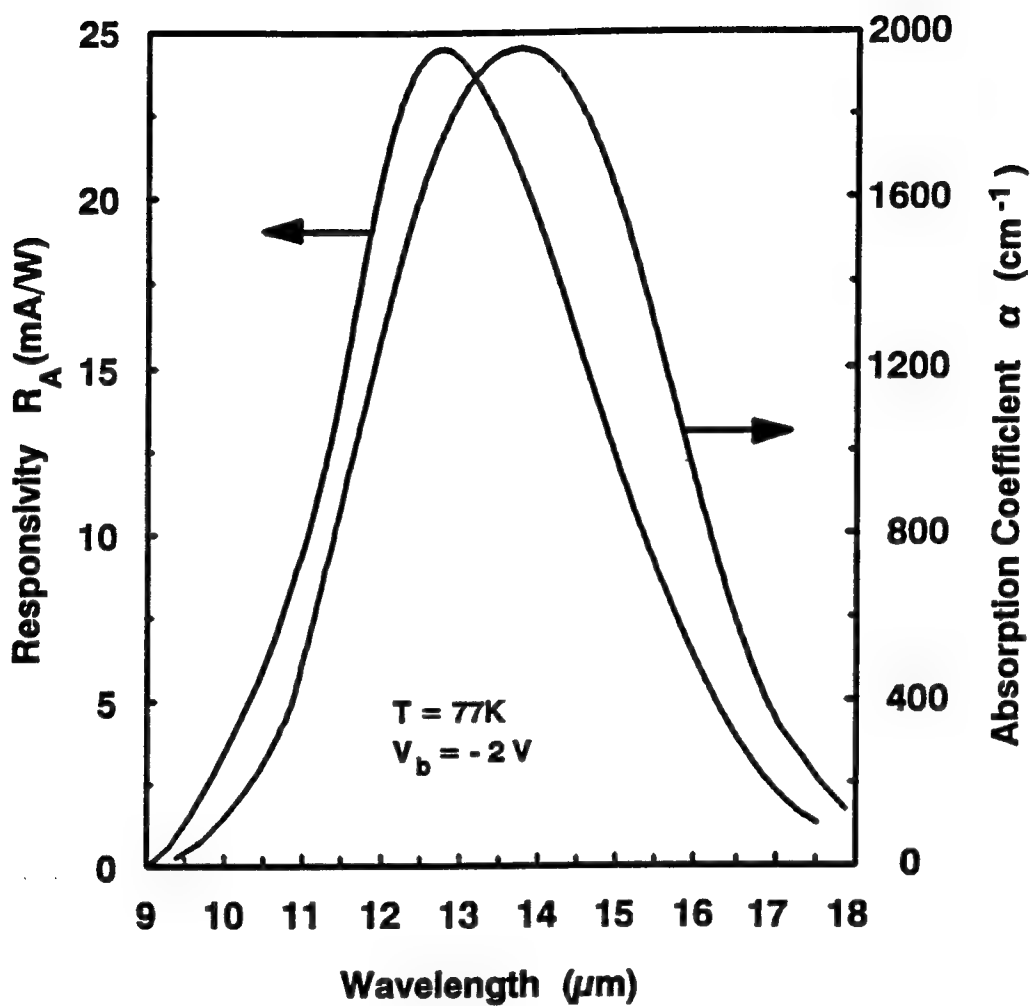


Figure 8.5. Spectral responsivity and absorption coefficient versus wavelength for  $\lambda_{p1} = 12.5\ \mu\text{m}$  transition at normal incidence,  $V_b = -2\text{ V}$  and  $T = 77\text{ K}$  for the AlAs/AlGaAs QWIP.

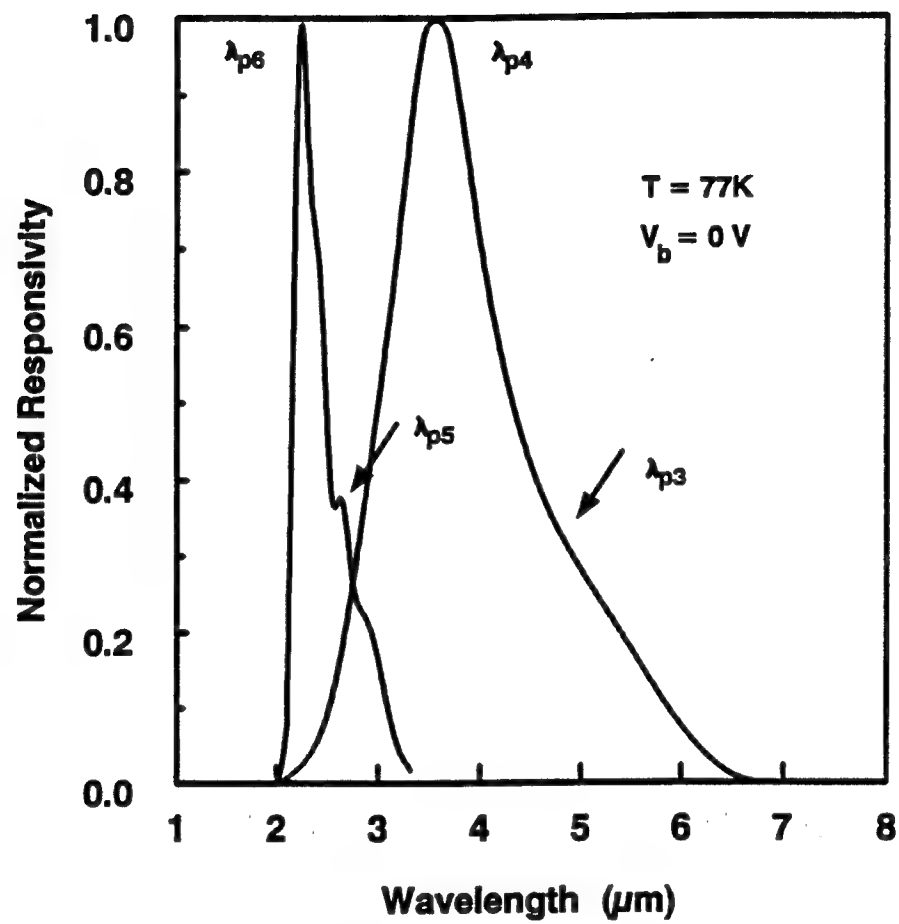


Figure 8.6. Normalized spectral responsivities versus wavelength for  $\lambda_{p4} = 3.5 \mu\text{m}$  and  $\lambda_{p6} = 2.2 \mu\text{m}$  transitions for the AlAs/AlGaAs QWIP measured at  $V_b = 0 \text{ V}$  and  $T = 77 \text{ K}$ .

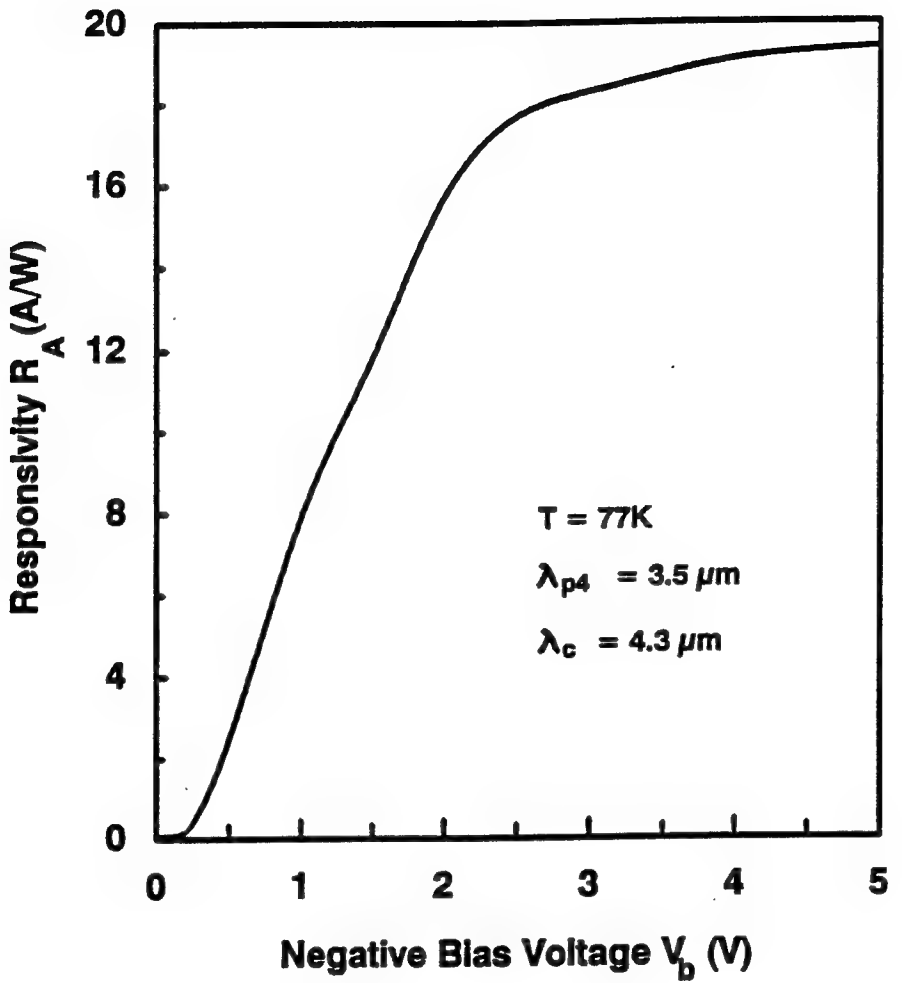


Figure 8.7. Responsivity versus negative bias voltage at the peak wavelength  $\lambda_{p4} = 3.5\mu\text{m}$  and  $T = 77\text{ K}$  for the AlAs/AlGaAs QWIP.

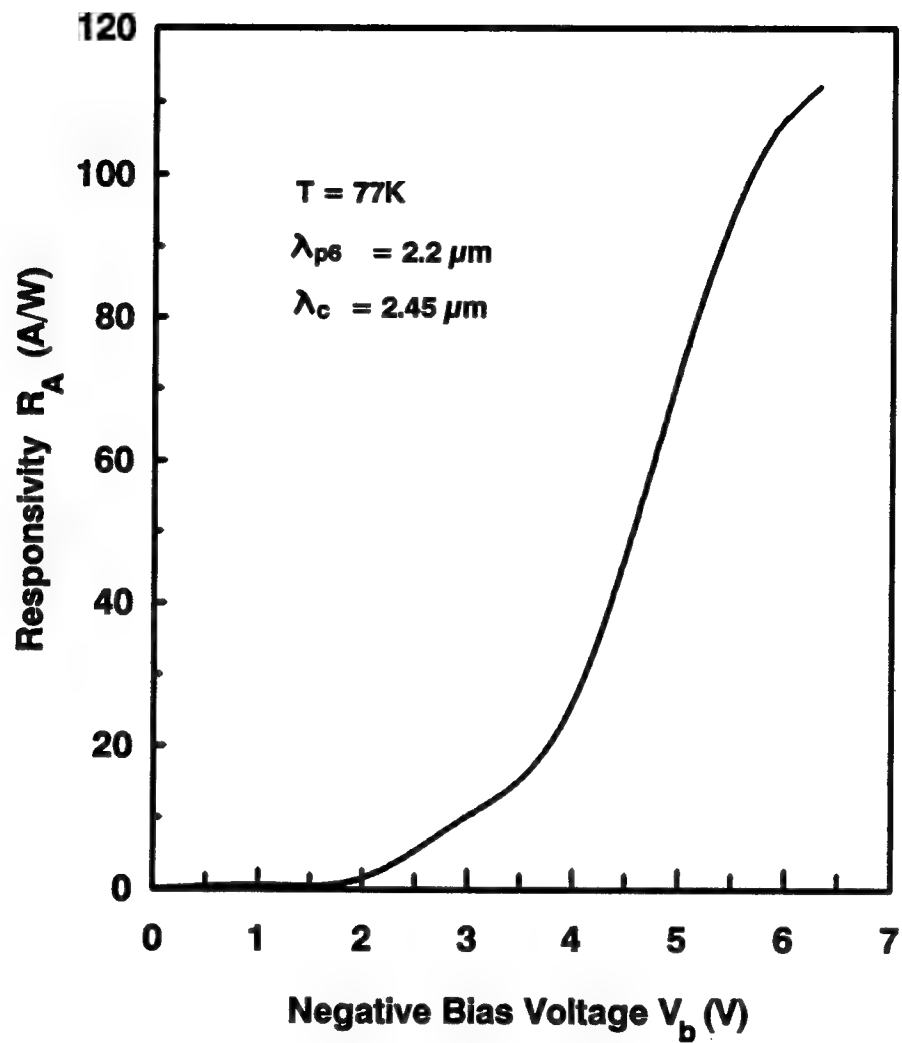


Figure 8.8. Responsivity versus negative bias voltage at the peak wavelength  $\lambda_{p6} = 2.2\text{ }\mu\text{m}$  and  $T = 77\text{ K}$  for the AlAs/AlGaAs QWIP.

## 9. A TWO-COLOR GaAs/AlAs/AlGaAs AND GaAs/AlGaAs STACKED QWIP FOR 3-5 AND 8-14 $\mu\text{m}$ DETECTION

### 9.1 Introduction

A new two-color GaAs/AlAs/AlGaAs and GaAs/AlGaAs quantum well infrared photodetector (QWIP) with photovoltaic (PV) and photoconductive (PC) dual-mode operation at 3-5 and 8-14  $\mu\text{m}$  has been demonstrated. It consists of a stack of the mid-wavelength infrared (MWIR) QWIP and the long-wavelength infrared (LWIR) QWIP. The PV detection scheme uses transition from the ground-state to the first excited state for the MWIR-QWI. The PC detection scheme has two different transitions, one is identical to the PV mode detection scheme and the other uses transition from the ground state to the miniband state of the LWIR QWIP. The peak responsivity at zero bias (PV mode) was found to be 17 mA/W at  $\lambda_p = 4.1 \mu\text{m}$  and  $T = 50 \text{ K}$  with a bandwidth  $\Delta\lambda/\lambda_p = 1.5 \%$ . The peak responsivities for the PC mode were found to be 25 mA/W at  $\lambda_p = 4.1 \mu\text{m}$ ,  $V_b = 1.0 \text{ V}$ , and 0.12 A/W at  $\lambda_p = 11.6 \mu\text{m}$ ,  $V_b = 3.2 \text{ V}$ , and at  $T = 50 \text{ K}$ , with a bandwidth  $\Delta\lambda/\lambda_p = 18 \%$ . The PV responsivity was found to be 68 % of the PC responsivity at  $\lambda_p = 4.1 \mu\text{m}$  and  $T = 50 \text{ K}$ , demonstrating the ability for efficient PV mode operation at 3-5  $\mu\text{m}$  by using the double barrier quantum well (DBQW) structure. This is the highest ratio reported for the spectral region of 3-5  $\mu\text{m}$  wavelength with a DBQW structure.

### 9.2 Stacked Structure

The QWIP layer structure was grown on a semi-insulating (SI) GaAs substrate by using the molecular beam epitaxy (MBE) technique. The quantum wells consist of two stacks designed as a mid-wavelength QWIP (MW-QWIP) and a long-wavelength QWIP (LW-QWIP). Figure 9.1 shows the entire layer structure of this two-stack QWIP. A 0.7- $\mu\text{m}$  GaAs buffer layer (doped to  $n = 2.0 \times 10^{18} \text{ cm}^{-3}$ ) was first grown on the SI GaAs substrate as an ohmic contact layer, followed by the growth of the first stack, designed as a MW-QWIP with a 20-period of GaAs/AlAs/AlGaAs double barrier quantum wells with a well width of 50 Å (doped to  $n = 1.5 \times 10^{18} \text{ cm}^{-3}$ ) and two undoped barriers which were of 14 Å AlAs inner barrier and 300 Å  $\text{Al}_{0.3}\text{Ga}_{0.7}\text{As}$  outer barrier. A second GaAs buffer layer of 0.5- $\mu\text{m}$  thick (doped to  $n = 2.0 \times 10^{18} \text{ cm}^{-3}$ ) was then grown on top of the first QWIP as an ohmic contact layer, followed by the growth of the second stack, designed

as a LW-QWIP, with a 21-period of GaAs/AlGaAs quantum wells with a well width of 88 Å and a dopant density of  $1.5 \times 10^{18} \text{ cm}^{-3}$ . The barrier layer on each side of the GaAs quantum wells consists of a 8-period undoped Al<sub>0.3</sub>Ga<sub>0.7</sub>As (50 Å)/GaAs (28 Å) superlattice layer which were grown alternatively with the GaAs quantum wells. Finally, an n<sup>+</sup>- GaAs cap layer of 0.3 μm thick with a dopant density of  $2 \times 10^{18} \text{ cm}^{-3}$  was grown on top of the QWIP layer structure to facilitate the top ohmic contact. The DBQW structure of the MW-QWIP offers a PV mode detection with excellent detection characteristics which are comparable to the PC mode QWIPs. The physical parameters of the LW-QWIP are chosen so that the first excited level  $E_2$  is lined up within the miniband  $E_{SL}$  on both sides of the quantum well to obtain a maximum intersubband absorption strength. In order to minimize the undesirable tunneling current through the barrier layers, a 8-period undoped Al<sub>0.3</sub>Ga<sub>0.7</sub>As (50 Å)/GaAs (28 Å) superlattice layer was used in this LW-QWIP structure to suppress the tunneling current from the heavily populated ground state  $E_1$  in the quantum wells.

### 9.3 Results and Discussion

The 2-color QWIP mesa structure with an active area of  $200 \times 200 \mu\text{m}^2$  was created by chemical etching through the two-stack quantum well active layers and stopped at the 0.7-μm thick heavily doped GaAs buffer layer for ohmic contact. A square contact ring composed of AuGe/Ni/Au materials was first deposited around the periphery of the mesa and alloyed for ohmic contact formation. To enhance the light coupling efficiency in the quantum well, we used a 2-D double periodic square mesh metal grating coupler on the QWIP for normal incident illumination. As discussed in the previous quarterly report, we found that  $g = 4 \mu\text{m}$  (where  $g$  is the grating period) and  $a/g = 0.5$  (where  $a$  is the width of square aperture in the metal mesh) are the optimum grating dimension and period for this 2-color QWIP. The metal grating was then deposited within the interior of the contact ring by using electron beam evaporation of Au followed by lift-off process.

Figure 9.2 shows the energy band diagram of this 2-color QWIP structure, which also illustrates the bound-to-miniband (BTM) and bound-to-quasi-bound (BQB) transition schemes for the two-color detection. The first transition scheme is from the localized ground-state  $E_1$  to the first quasi-bound state  $E_2$  in the GaAs quantum well of the MW-QWIP stack. The second transition scheme is from the localized ground-state  $E_1$  to the miniband  $E_{SL}$  in the GaAs quantum well of the LW-QWIP stack. To analyze these transition schemes, we performed theoretical calculations of the energy levels of the bound states and continuum states and the transmission probability  $|T * T|$  for this detector using a multi-layer transfer matrix method, and the results are shown in Fig. 9.3.

For comparison, we have also included in Fig. 9.3 the transmission probability for a single quantum well with the same barrier width of the bulk barrier. Considering the effects due to depolarization and the electron-electron interaction, we obtain two response peaks, one at  $\lambda = 3.9 \mu\text{m}$  and the other at  $\lambda = 11.7 \mu\text{m}$ .

To understand the behavior of this 2-color QWIP, we first prepared two samples with BTB and BTM quantum structures mentioned above separately. The MW-QWIP (BTB) and LW-QWIP (BTM) represent the first stack and the second stack of this 2-color QWIP structure, respectively. Fig. 9.4 shows the dark current versus bias voltage ( $I$ - $V$ ) curves of the MW-QWIP and the LW-QWIP measured at  $T = 30, 50$ , and  $77 \text{ K}$ . The results show that the dark current of the LW-QWIP is higher than that of the MW-QWIP at the same bias. This is due to the fact that the LW-QWIP has a shallower quantum well and the thermal-generated electrons can escape more easily from the quantum wells. Therefore, based on the  $I$ - $V$  curves shown in Fig. 9.4, we can see that when the two stacks are combined to form a 2-color detector, most of the voltage drop is across the MW-QWIP stack at low bias ( $< 1.5 \text{ V}$ ). Therefore, a high field domain always forms first in the MW-QWIP stack. The voltage drop across the LW-QWIP stack becomes significant only when the bias is greater than  $1.5 \text{ V}$ .

Figure 9.5 shows the dark current-voltage ( $I$ - $V$ ) for the 2-color stacked QWIP measured at  $T = 30, 50$ , and  $77 \text{ K}$ . It is noted that the  $300 \text{ K}$  background photocurrent curve (dashed) crosses the dark  $I$ - $V$  curve at  $V_b = -0.65 \text{ V}$  and  $T = 50 \text{ K}$ . Thus, the background limited performance (BLIP) condition occurs at  $T \leq 50 \text{ K}$  and  $V_b \leq 0.6 \text{ V}$ . The  $300 \text{ K}$  background photocurrent can be obtained from

$$I_B = A \int_{\lambda_1}^{\lambda_2} R(\lambda) S(\lambda) d\lambda \quad (9.1)$$

where  $A$  is the device area,  $R(\lambda)$  is the responsivity curve,  $\lambda_1$  and  $\lambda_2$  are the limits of the integration, and the blackbody power spectral density is given by

$$S(\lambda) = (2\pi hc/\lambda^5)(e^{hc/\lambda kT} - 1)^{-1} \quad (9.2)$$

Using  $A = 4 \times 10^{-4} \text{ cm}^2$ ,  $R_p = 0.018 \text{ A/W}$  (at  $\lambda = 4.1 \mu\text{m}$ ,  $V_b = 0 \text{ V}$ , and  $T = 30 \text{ K}$ ), and  $T = 300 \text{ K}$  gives a total calculated  $300 \text{ K}$  background photocurrent of  $I_B = 0.12 \text{ nA}$ . This is in good agreement with the measured photocurrent of  $I_B = 0.3 \text{ nA}$  (as shown in Fig. 9.5). Therefore, at  $T = 50 \text{ K}$  this 2-color detector is under BLIP condition only in the PV mode operation, but not the PC mode operation.

Figure 9.6 shows the bias dependent responsivity and detectivity for the single LW-QWIP

measured at  $\lambda_p = 11.6 \mu\text{m}$  and  $T = 50 \text{ K}$ . The peak responsivity  $R_A = 0.14 \text{ A/W}$  was obtained at  $V_b = 1.5 \text{ V}$ . From the measured responsivity and dark current, we calculate the detectivity  $D^*$  using the formula:  $D_\lambda^* = R_A(A\Delta f)^{1/2}/i_n$ , where  $A$  is the effective area of the detector,  $\Delta f$  is the noise bandwidth. The dark current shot noise  $i_n$  is given by  $i_n = \sqrt{4qI_{dg}\Delta f}$ , where  $g$  is the optical gain, and may be evaluated from the measured responsivity  $R_A = \eta\lambda g/1.24$  and the unpolarized quantum efficiency which was found to be equal to 18 %. Optical gain can also be derived from the noise measurement. The results yielded a peak detectivity  $D_\lambda^* = 1.23 \times 10^9 \text{ cm} \sqrt{\text{Hz}}/\text{W}$  at  $\lambda_p = 11.6 \mu\text{m}$ ,  $V_b = 3.0 \text{ V}$ , and  $T = 50 \text{ K}$  for the PC mode operation.

The spectral response of the 2-color QWIP was measured under back illumination as a function of temperature and bias voltage ( $V_b$ ) using a 0.25 m grating monochromator with a 1273 K blackbody source. The normalized spectral responsivity measured at  $V_b = 0, 3.2 \text{ V}$  and  $T = 50 \text{ K}$  is shown in Fig. 9.7. Two response peaks were observed: one at  $\lambda = 4.1 \mu\text{m}$  with  $V_b = 0 \text{ V}$  and the other at  $\lambda = 11.6 \mu\text{m}$  with  $V_b = 3.2 \text{ V}$ . The peak wavelengths are in good agreement with our theoretical calculations. The bias dependence of the responsivity at  $T = 50 \text{ K}$  is shown in Fig. 9.8. It is noted that the photoresponse of the MW-QWIP stack is dominated at low bias and saturated above  $V_b = 1 \text{ V}$ . When  $V_b > 1.5 \text{ V}$ , the LW-QWIP stack starts to work and reaches a maximum value at  $V_b = 3.2 \text{ V}$ . The results show the potential of this 2-stack QWIP structure as a 2-color QWIP with a PV and PC dual-mode operation at 3-5  $\mu\text{m}$  and 8-14  $\mu\text{m}$ . The peak responsivity at zero bias (PV mode) was found to be 17 mA/W at  $\lambda = 4.1 \mu\text{m}$  and  $T = 50 \text{ K}$ , with a bandwidth  $\Delta\lambda/\lambda_p = 1.5 \%$ . Two peak responsivities were found on the PC mode, one was 25 mA/W at  $\lambda_p = 4.1 \mu\text{m}$ ,  $V_b = 1.0 \text{ V}$ , and  $T = 50 \text{ K}$ , the other was 0.12 A/W at  $\lambda_p = 11.6 \mu\text{m}$ ,  $V_b = 3.2 \text{ V}$ ,  $T = 50 \text{ K}$ , and the bandwidth  $\Delta\lambda/\lambda_p = 18 \%$ . The PV responsivity was found to be 68 % of the PC responsivity at  $\lambda_p = 4.1 \mu\text{m}$  and  $T = 50 \text{ K}$ . This is one of the highest ratios reported in the spectral region of 3-5  $\mu\text{m}$  for the QWIPs. The PV response has been interpreted due to the doping migration effect with further enhancement by the DBQW structure. Since the dark current of the PV mode operation QWIP is much smaller than that of the PC mode, one can achieve a better performance in QWIP by using PV mode detection at 3-5  $\mu\text{m}$ .

#### 9.4 Conclusions

In conclusion, we have demonstrated a new two-color stacked GaAs/AlAs/AlGaAs BTB and GaAs/AlGaAs BTM QWIP with PV and PC dual-mode operation at 3-5 and 8-14  $\mu\text{m}$ . The PV detection scheme uses transition from the ground-state to the first excited state of the MW-QWIP. The PC detection scheme has two different transitions, one is similar to the PV detection scheme

and the other uses transition from the ground state to the miniband of the LW-QWIP. The peak responsivity at zero bias (PV mode) was found to be 17 mA/W at  $\lambda_p = 4.1 \mu\text{m}$ ,  $T = 50 \text{ K}$ , with a bandwidth  $\Delta\lambda/\lambda_p = 1.5 \%$ . Two peak responsivities for the PC mode detection, were found to be 25 mA/W at  $\lambda_p = 4.1 \mu\text{m}$ ,  $V_b = 1 \text{ V}$ , and  $T = 50 \text{ K}$ , and 0.12 A/W at  $\lambda_p = 11.6 \mu\text{m}$ ,  $V_b = 3.2 \text{ V}$ ,  $T = 50 \text{ K}$ , and the bandwidth  $\Delta\lambda/\lambda_p = 18 \%$ . The PV responsivity was found to be 68 % of the PC responsivity at  $\lambda_p = 4.1 \mu\text{m}$  and  $T = 50 \text{ K}$ , demonstrating the ability for an efficient PV mode operation at 3-5  $\mu\text{m}$ . The results reported here represent only a preliminary design of the 2-color detector. Further improvement on the performance of the 2-color stack QWIP is expected to raise the operating temperature to  $T = 77 \text{ K}$  for practical focal plane arrays image sensor applications.

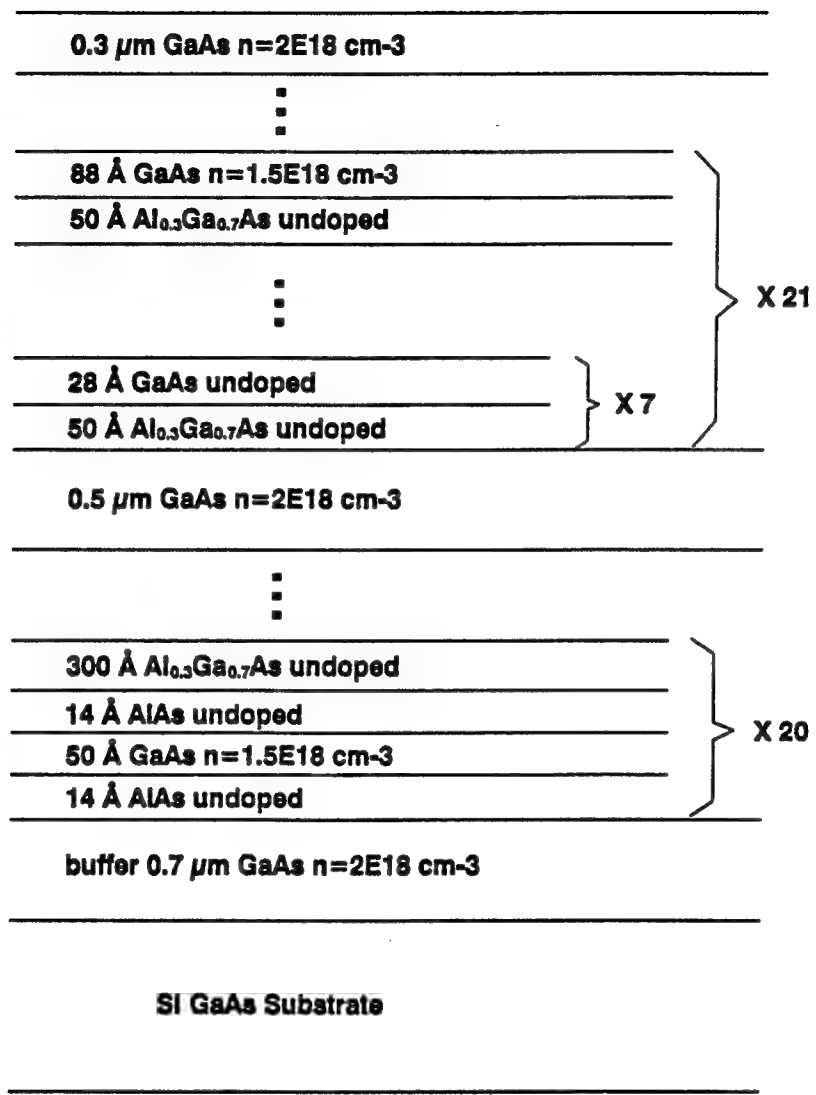
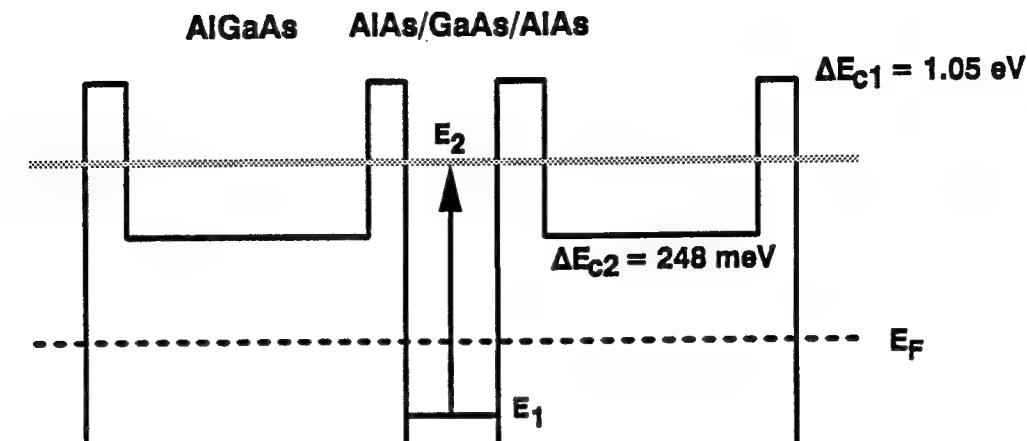
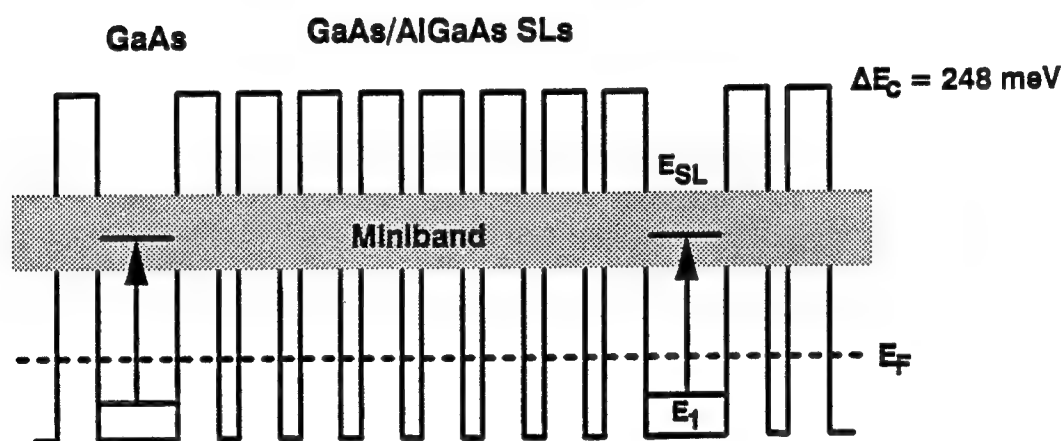


Figure 9.1. The quantum well layer structure for the 2-color MWIR QWIP and LWIR QWIP.

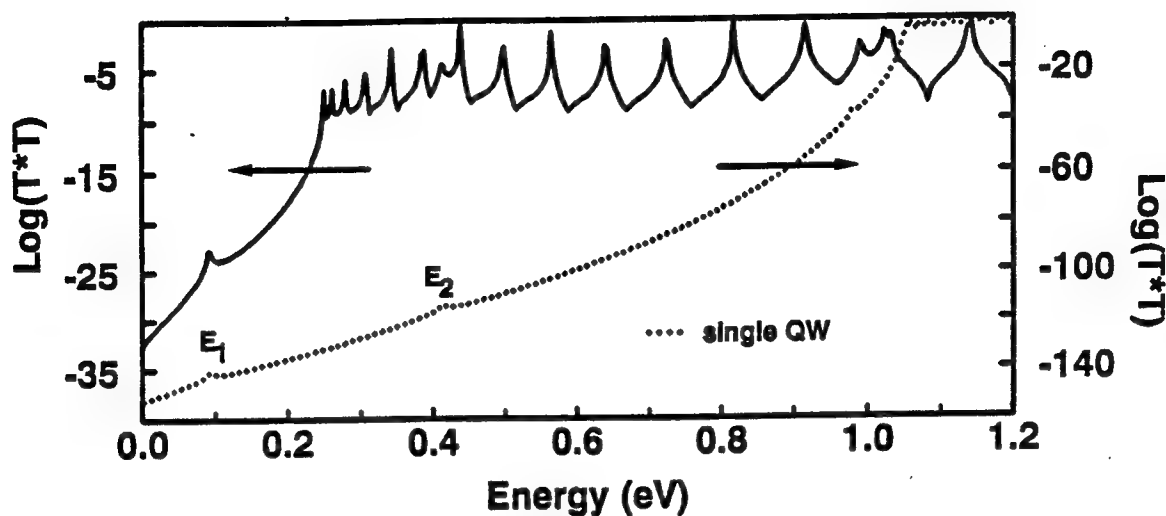


(a) MW-QWIP stack

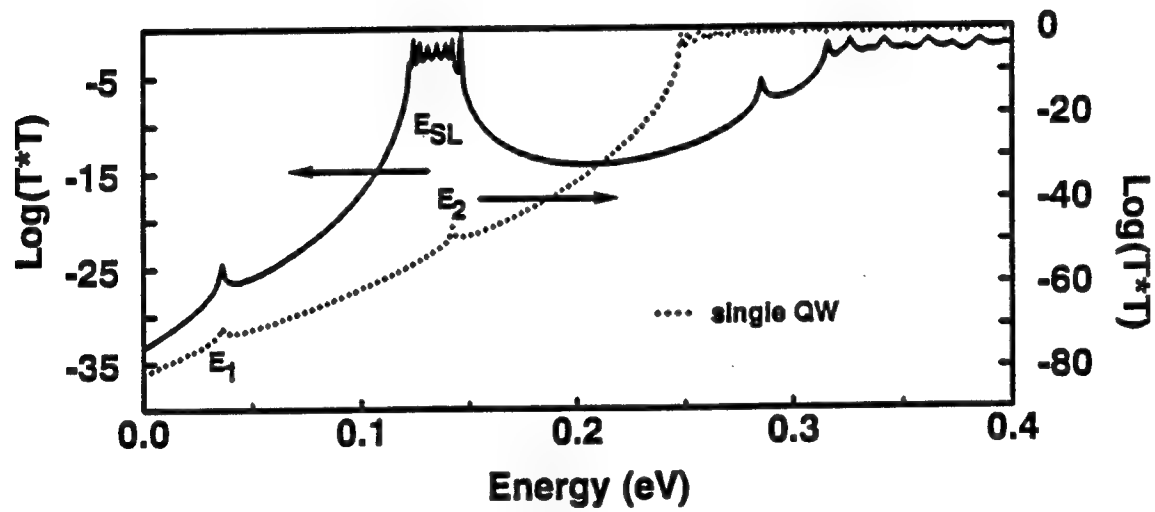


(b) LW-QWIP stack

Figure 9.2. The schematic energy band diagram for the 2-color QWIP structure, (a) MWIR QWIP stack and (b) LWIR QWIP stack.



(a) MW-QWIP stack



(b) LW-QWIP stack

Figure 9.3. The calculated energy states and transmission coefficient  $T^*T$  for the 2-color QWIP: (a) MWIR QWIP stack and (b) LWIR QWIP stack.

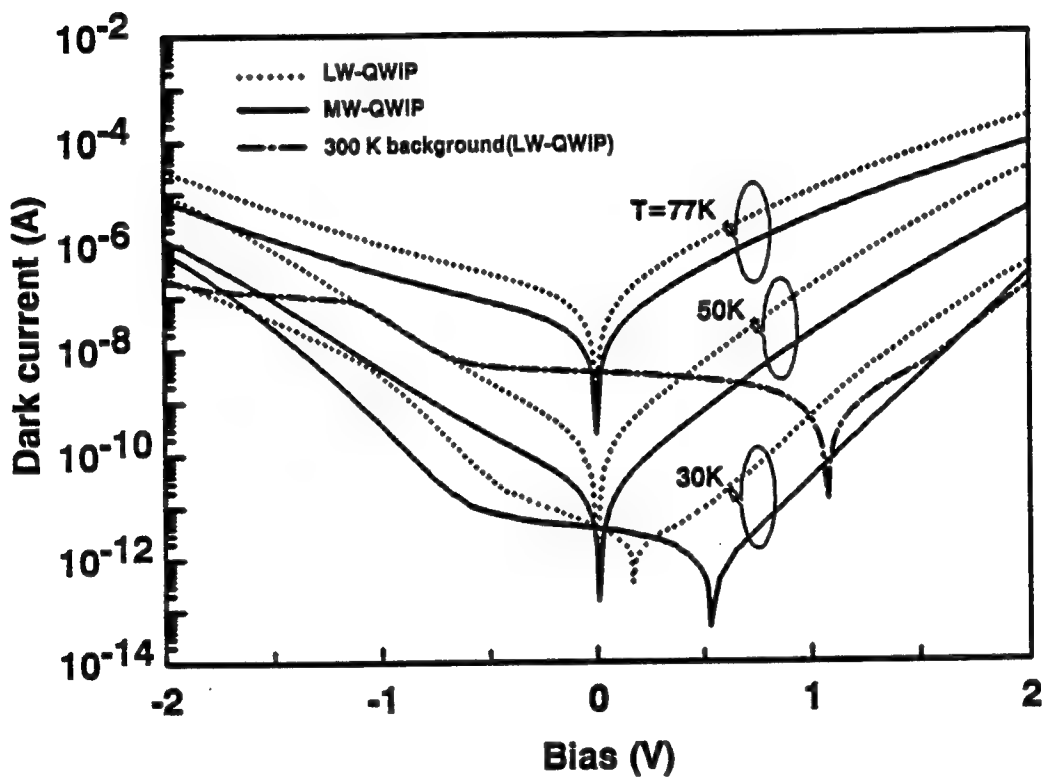


Figure 9.4. The dark current versus bias voltage and temperature for the single MWIR-QWIP and single LWIR-QWIP.

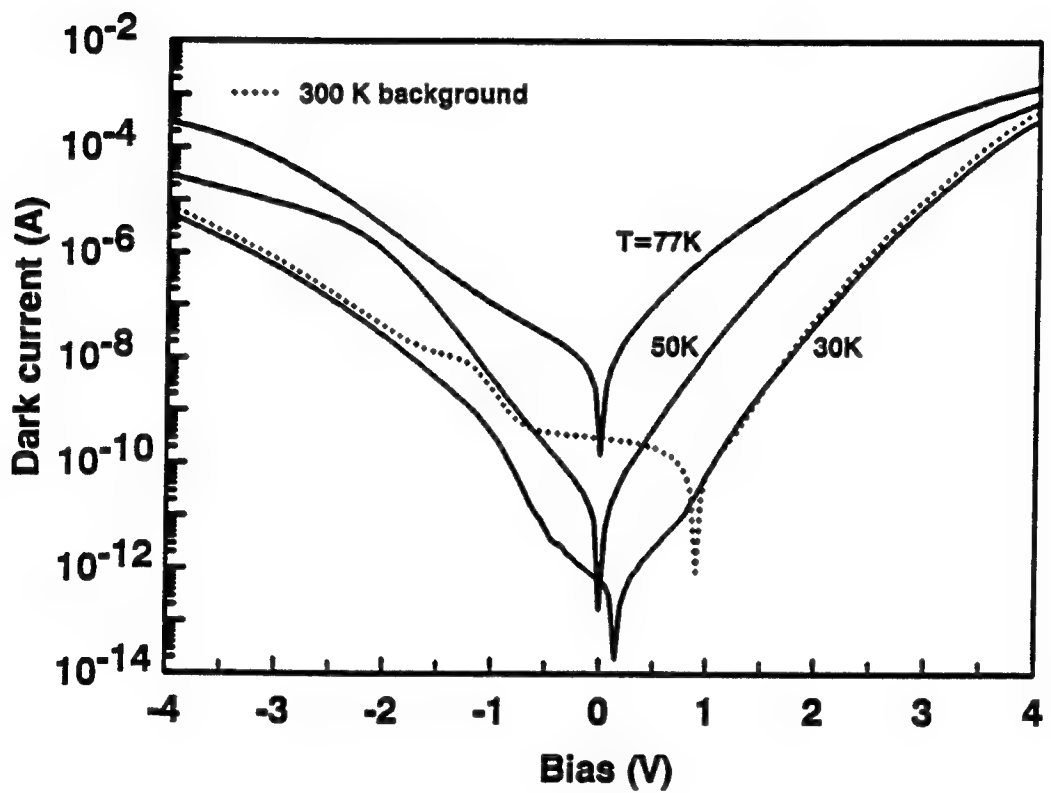


Figure 9.5. The dark current versus bias voltage for the 2-color stacked QWIP.

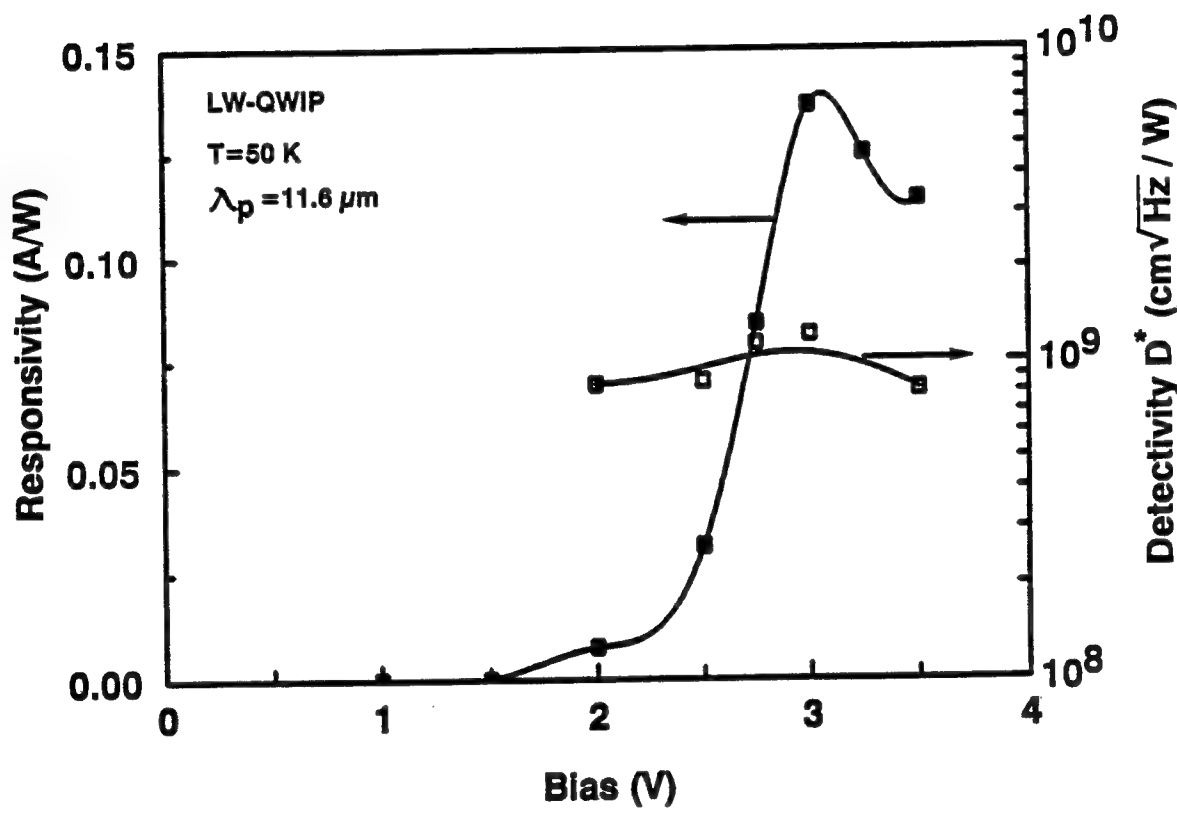


Figure 9.6. Bias dependence of the peak responsivity and detectivity for the single LWIR-QWIP at  $T = 50 \text{ K}$ .

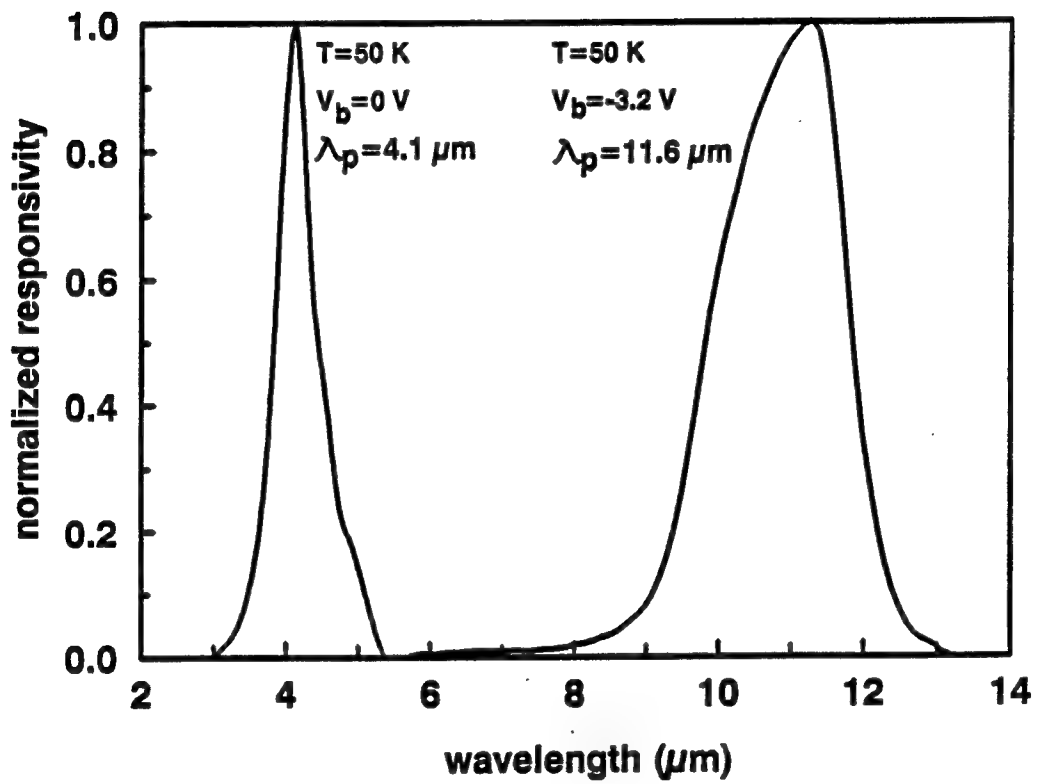


Figure 9.7. Normalized responsivity versus wavelength for the 2-color QWIP measured at  $T = 50 \text{ K}$ .

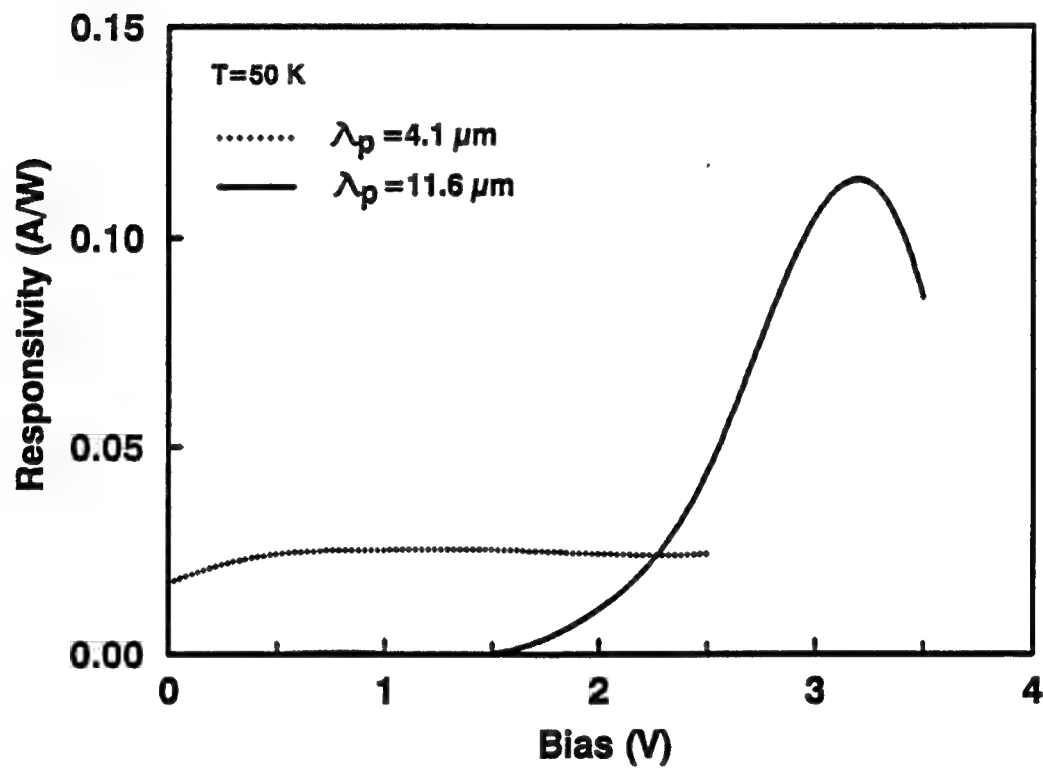


Figure 9.8. The peak responsivity versus bias voltage for the 2-color stacked QWIP measure at  $T = 50 \text{ K}$ .

## **Part II**

### **Metal Grating Couplers**

## 10. DESIGN OF 2-D REFLECTION SQUARE METAL GRATING COUPLER

### 10.1. Introduction

Metal grating operation in the diffraction region (i.e.,  $g > \lambda$ ) has drawn considerable interest in recent years since it can greatly improve the intersubband absorption in a quantum well infrared photodetectors (QWIPs) [47, 98, 99, 100]. A wide variety of QWIPs using intersubband transitions in the doped quantum wells have been demonstrated for operation in the atmospheric window of 8 to 12  $\mu\text{m}$  at 77 K [11, 63, 101].

One of the major problems encountered in the QWIPs is that the electric field of the incident light must have a component perpendicular to the quantum well (QW) layer planes to satisfy the selection rules of quantum mechanics infrared absorption [9, 102, 36]. Therefore, the angle of incidence with respect to QW layers must be non-zero and the incident radiation normal to the top or bottom faces of the QWIP will produce no photo-response. One way to couple light into the QWIPs is by back illumination through a 45° polished facet [10]. However, this scheme only allows incident light access to one edge of the detector, providing only a one-dimensional (1-D) array. For imaging applications in focal plane arrays (FPAs), it is necessary to be able to couple infrared light uniformly into the 2-D arrays of such detectors. An alternative way of light coupling is to construct a 1-D lamellar grating to scatter light into a non-zero angle either by etching the QWIPs to deflect light [47] or by coating the device with metal on one side [100] to reflect light. However, these approaches are polarization sensitive and only couple the transverse magnetic (TM) polarization components of the incident waves. A double periodic metal grating coupler formed on one face of the QWIP can be employed to efficiently couple the normal incident radiation into the quantum well. Such gratings are independent of the polarization direction of the incident waves, and hence are suitable for FPA applications.

Incident radiation scattered by the grating consists of transverse electric (TE) polarization with the electric field parallel to the QW planes and TM polarization with the electric field perpendicular to the planes. Only TM polarization leads to quantum well absorption. Within the absorption region of a QWIP, the absorption coefficient depends slightly on the wavelength of the incident

light but is determined mainly by the angle between the electric field vector of light and the motion vector of free carriers (i.e., in the direction orthogonal to the QW layer planes). The relationship is the cosine of the angle enclosed by the two vectors [101]. For this reason, once the magnitude and direction of the reflected light are obtained one can easily determine the power absorption ratio of the detector. Therefore, a high quantum efficiency value ( $\eta$ ) can be obtained by a proper selection of the grating constant.

The following analysis is based on a double periodic reflection grating with a square shape metal contact formed on the top surface of a QWIP device. The method of moment is employed in the analysis. The square metal grating is used to scatter the infrared radiation into the quantum well. The main advantage of this grating structure is that the coupling of radiation is independent of the polarization direction of the incident waves. Using two universal plots from the normalized parameters, the refracted power and angle versus wavelength can be determined readily. Let us consider a normal incident electromagnetic (EM) wave impinging on the substrate side of the detector. For simplicity, we assume that the amplitude of the power for the incident wave equals unity. The power of the higher order diffracted waves depend only on the 'normalized wavelength'  $s$  (where  $s = \lambda/g$ ,  $g$  is the grating period and  $\lambda$  is the wavelength). The angle between the diffracted waves and the grating normal also depends on  $s$ . Therefore, in the design of such a grating structure the number of parameters can be reduced. The purpose of this task is to develop universal plots relating the coupling efficiency to the normalized wavelength for a 2-D square metal grating. From these plots, the higher order refracted magnitudes and refracted angles can be determined for any square grating sizes. These universal plots (refracted power versus normalized wavelength) provide a design tool for the 2-D refraction grating coupler on a QWIP device.

## 10.2. Theoretical Consideration

The reflected EM waves in the reflection grating are modeled by using a *modal expansion* technique [100, 105]. The grating consists of arrays of perfectly conducting plates with infinitesimal thickness compared to wavelength. The square conducting plate arrays are arranged periodically along two orthogonal coordinates  $\vec{x}$  and  $\vec{y}$  as shown in Fig. 10.1. In the figure we employed spherical coordinates, where  $\theta$  is the angle between the propagation vector  $\vec{k}$  and the normal to the plane of the grating, and  $\phi$  is the angle between the  $x$  axis and the projection of  $\vec{k}$  on the  $x-y$  plane. The distribution of electromagnetic field near the array is in the form of Floquet mode functions according to wave theory in periodic structure. Furthermore, for normal incidence the solution to

the scalar time independent wave equation is given by

$$\psi_{pq} = e^{-ju_p x} \cdot e^{-jv_q y} \cdot e^{-jw_{pq} z} \quad (10.1)$$

where the wave vectors  $u_p$ ,  $v_q$ , and  $w_{pq}$  are given respectively by

$$u_p = \frac{2\pi p}{g} = k \cdot \sin \theta \cdot \cos \phi \quad (10.2)$$

$$v_q = \frac{2\pi q}{g} = k \cdot \sin \theta \sin \phi \quad (10.3)$$

$$w_{pq} = \begin{cases} \sqrt{k^2 - t_{pq}^2} & \text{for } k^2 \geq t_{pq}^2 \\ -j\sqrt{t_{pq}^2 - k^2} & \text{for } k^2 \leq t_{pq}^2 \end{cases}$$

where  $p,q=0,\pm 1,\pm 2,\dots,\pm \infty$

and

$$t_{pq}^2 = u_p^2 + v_q^2$$

The orthonormal mode functions for the TE and TM modes with respect to  $\hat{z}$  can be expressed as

$$\begin{aligned} \vec{\Phi}_{pq}^{TE} &= \frac{1}{g} \left( \frac{v_q}{t_{pq}} \hat{x} - \frac{u_p}{t_{pq}} \hat{y} \right) \psi_{pq} && \text{for TE modes} \\ \vec{\Phi}_{pq}^{TM} &= \frac{1}{g} \left( \frac{u_p}{t_{pq}} \hat{x} + \frac{v_q}{t_{pq}} \hat{y} \right) \psi_{pq} && \text{for TM modes} \end{aligned} \quad (10.4)$$

The wave impedances in the  $\hat{z}$  direction are

$$\begin{aligned} \eta_{pq}^{TE} &= \frac{k}{w_{pq}} Z_0 \\ \eta_{pq}^{TM} &= \frac{w_{pq}}{k} Z_0 \end{aligned} \quad (10.5)$$

where  $Z_0 = \sqrt{\frac{\mu_0}{\epsilon_0 \epsilon_s}}$  is the characteristic impedance. A plane wave with unit electric field intensity normal incidence in the  $\phi$  plane can be expressed as the sum of TE and TM plane waves, that is

$$\vec{E}^i = \sum_{r=1}^2 A_{00r} \vec{\Phi}_{00r} \quad (10.6)$$

where  $A_{00r}$  is the magnitude of the incident field component which depends on the polarization direction. The third subscript  $r=1$  or  $r=2$  is used to designate respectively the TE and TM Floquet modes. Similarly, the scattered field can also be expressed in terms of the Floquet modes and reflection coefficients  $R_{pqr}$  as follows:

$$\vec{E}^s = \sum_p \sum_q \sum_{r=1}^2 R_{pqr} \vec{\Phi}_{pqr} \quad (10.7)$$

The boundary condition is that the electric field in the conducting plate equals zero:

$$\vec{E}^i + \vec{E}^s = 0 \quad \text{over the plate (at } z=0) \quad (10.8)$$

It has been shown that the current modes  $\tilde{\Psi}_{mnl}$  other than the Floquet modes  $\tilde{\Phi}_{pqr}$  were used to expand the induced current  $-\hat{z} \times \vec{H}^s$  in the conducting plate in order to provide a faster convergence, which are the dual field functions of the transverse electric field function of the conducting plate aperture. Finally, an equation in the following matrix expression can be obtained

$$[Z_{MNL}^{mnl}] [B_{mnl}] = [D_{mnl}] \quad (10.9)$$

where the unknown  $B_{mnl}$  are the coefficients given in the current expression with

$$Z_{MNL}^{mnl} = \sum_p \sum_q \sum_{r=1}^2 \eta_{pqr} C_{pqr}^{MNL*} C_{pqr}^{mnl}$$

$$C_{pqr}^{mnl} = \int_{\text{plate}} \tilde{\Phi}_{pqr}^* \cdot \tilde{\Psi}_{mnl} da \quad (10.10)$$

and the reflection coefficients can be expressed by

$$R_{pqr} = -\eta_{pqr} \sum_m \sum_n \sum_{l=1}^2 B_{mnl} C_{mnl}^{pqr} \quad (10.11)$$

Due to the dependence of  $B_{mnl} \propto 1/\lambda$  and  $C_{pqr}^{mnl} \propto \lambda$  for a given  $g$ , the reflection coefficients  $R_{pqr}$  are a function of  $\lambda/g$ . The angle between the electric field of the refracted mode  $R_{pqr} \tilde{\Phi}_{pqr}$  and the  $\hat{z}$  direction is  $\gamma_{pqr}$ , which depends on the higher order refracted waves and the normalized wavelength  $s = \lambda/g$  given by the following equation

$$\cos \gamma_{pqr} = \frac{\lambda}{g} \cdot \sqrt{p^2 + q^2} \quad (10.12)$$

### 10.3. Results and Discussion

As mentioned above, neither the evanescent modes nor the TE modes would have any effect on the intersubband absorption [47] in the quantum wells. Therefore, the following discussion focuses only on the propagating TM modes. It is convenient to introduce two parameters to illustrate the plots, these are the normalized wavelength  $s = \lambda/g$ , and the strip factor  $h = a/g$ . The numerical results obtained from the computer simulation consist of the lowest twenty current modes. The number of modes selected here is sufficient to be accurate to  $\pm 0.1$ . For larger strip factor ( $a/g > 0.85$ ), a much larger number of current modes is required to expand the induced current. Large strip

factor is also disadvantageous for the real QWIP device since it is more difficult to process. The incident wave is a plane wave that has an angle of zero degree with respect to the array normal. In order to interact with the doped quantum well, the effective coupling of the reflected waves is due to the TM Floquet modes. For grating period  $g$  less than wavelength  $\lambda$ , the grating is operated in a non-refraction region, with only one far field propagating mode  $R_{001}\vec{\Phi}_{001}$ . It is impossible to excite the TM component of the zeroth order mode. This is due to the structure symmetry of  $x$  and  $y$  coordinates in normal incidence. The approach here to create an effective coupling 2-D metal grating plates is to induce the higher order TM refracted waves into the quantum wells. Figure 10.2 shows a universal plot, which illustrates the total power of the first order refracted waves  $R_{012}\vec{\Phi}_{012}$ ,  $R_{0-12}\vec{\Phi}_{0-12}$ ,  $R_{-102}\vec{\Phi}_{-102}$  and  $R_{102}\vec{\Phi}_{102}$  as a function of the normalized wavelength  $s$ , for  $s = \lambda/g < 1$ . For a square shape metal grating, the total power of the first order TM refracted waves depends strongly on  $s$  but is independent of the polarization direction of the incident waves. The absorption coefficient depends roughly on the angle between the electric field vector and the normal of quantum well layers [101]. For a given quantum well structure, the total power absorbed by the detector can be readily determined. Figure 10.2(a) shows that the total power of the first order refracted waves will increase with increasing values of  $h$ . Figure 10.3 shows the total power of the second order TM refracted wave components

$R_{\pm 112}\vec{\Phi}_{\pm 112}$  and  $R_{1\pm 12}\vec{\Phi}_{1\pm 12}$  as a function of the normalized wavelength  $s$  for different values of  $h$ . A comparison of Figs. 10.2(a) and 10.3 reveals that the first order refracted power is much larger than the second order refracted power, particularly for larger values of  $h$ . The second order refracted modes emerge for  $s < \frac{1}{\sqrt{2}}$  with total power about one fifth that of the first order refracted modes.

Figure 10.4 shows a plot that relates  $\cos \gamma_{pqr}$  to the normalized wavelength of the higher order refracted waves, where  $\gamma$  is the angle between the electric field vector and the grating normal. The relationship between  $\gamma$  and  $\lambda$  for the first order refracted waves ( i.e.  $| p | + | q | = 1$  in the notation of Floquet modes  $\vec{\Phi}_{pqr}$  ) is given by

$$\cos \gamma_{pq2} = \frac{\lambda}{g} \quad (10.13)$$

The relationship for the second order refracted waves with  $| p | = | q | = 1$  is given by

$$\cos \gamma_{pq2} = \frac{\lambda}{g} \cdot \sqrt{2} \quad (10.14)$$

Due to the dependence of the absorption coefficient on  $\cos^2 \gamma_{pqr}$  we propose that the metal grating period be selected in the region where  $s$  falls between 0.7 and 1 when utilizes the first order

refracted waves. Referring to Fig. 10.2., it is noted that for  $h = 0.8$ , the absorption is relatively flat over a broad wavelength regime. Thus,  $h = 0.8$  may be considered as a good selection for coupling IR light (8 - 12  $\mu\text{m}$ ) into the quantum well. For example, for a GaAs QWIP with peak response at 10  $\mu\text{m}$ , by choosing  $s = \lambda/g = 0.8$  and  $h = 0.8$ , we obtain a relatively flat effective coupling covering the wavelength from 7 to 13  $\mu\text{m}$ . Since the refraction index  $n$  for the GaAs contact layer is 3.25 at 77 K, the grating period was found to be  $g = 4.0 \mu\text{m}$  and the width of the metal plate was found to be  $a = 3.2 \mu\text{m}$ .

In conclusion, we have performed the numerical analysis of a normal incident 2-D square metal grating coupler for the QWIP device. It is shown that the total power and the angle of the higher order refracted waves depend on two normalized parameters:  $s = \lambda/g$  and  $h = a/g$ . Using the universal plots shown in this section ,the optimized grating period and square metal grating width can be obtained for a specified bandwidth IR detection applications.

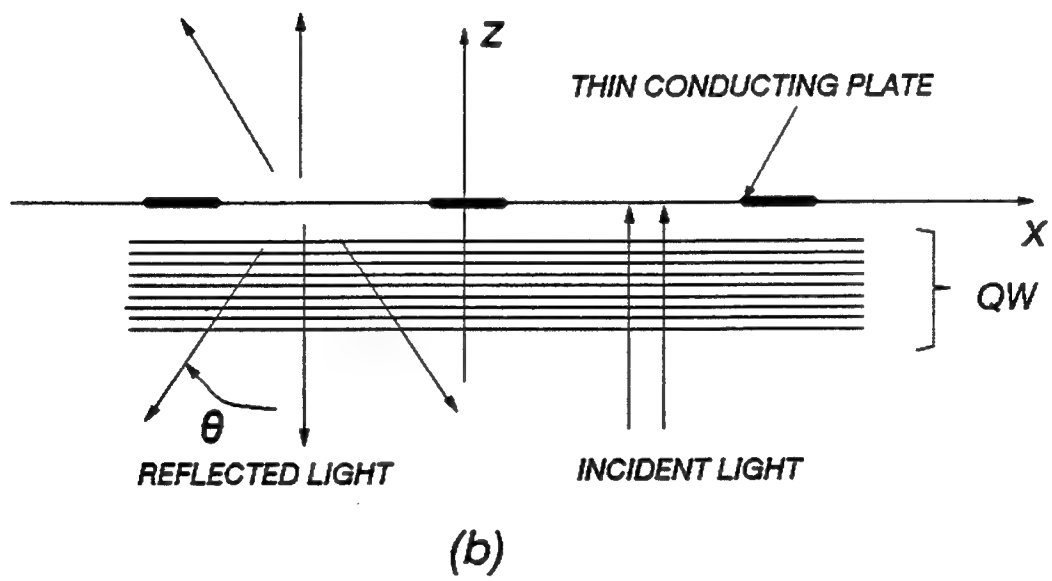
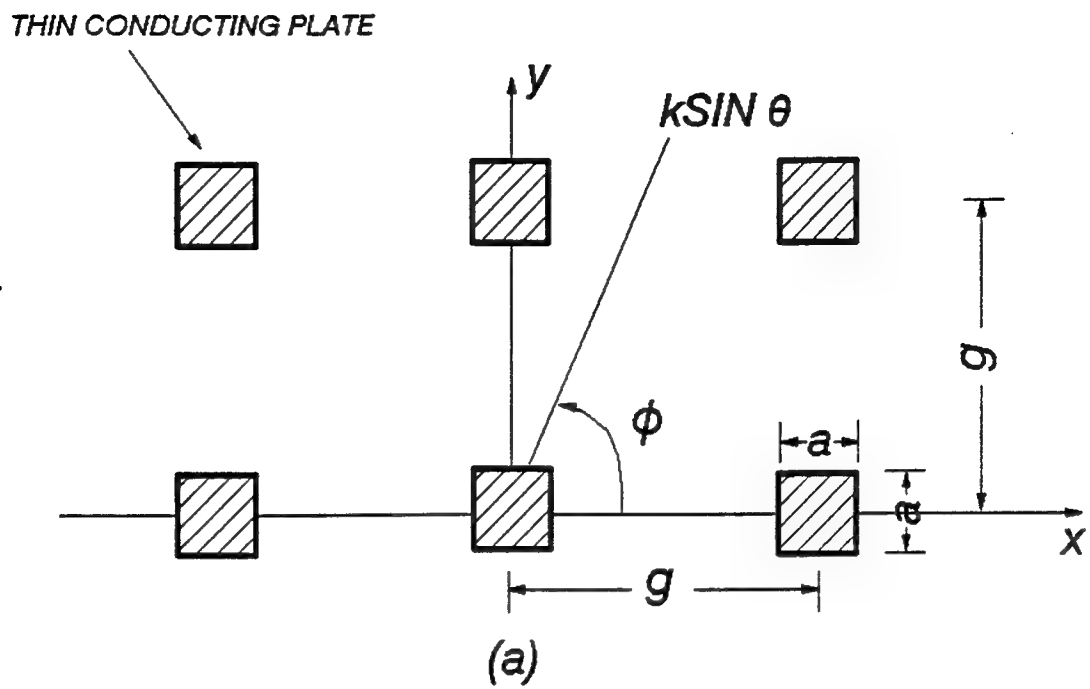


Figure 10.1. Schematic diagram showing the square reflection metal grating and the directions of incident and refracted waves. (a) Top view and (b) side view.

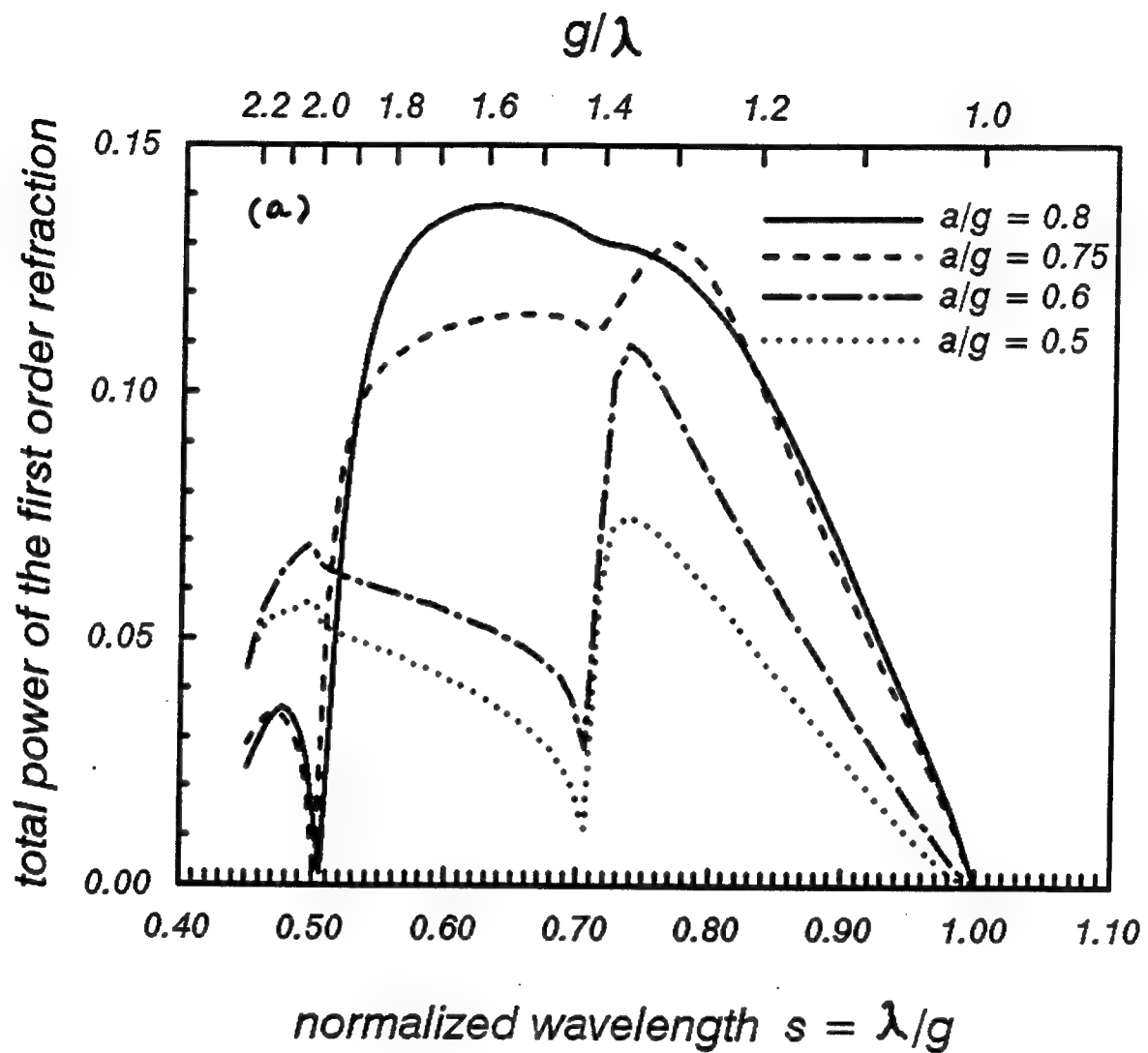


Figure 10.2. (a) Total power of the first order refracted waves versus  $s = \lambda/g$  for different values of  $h = a/g$ .

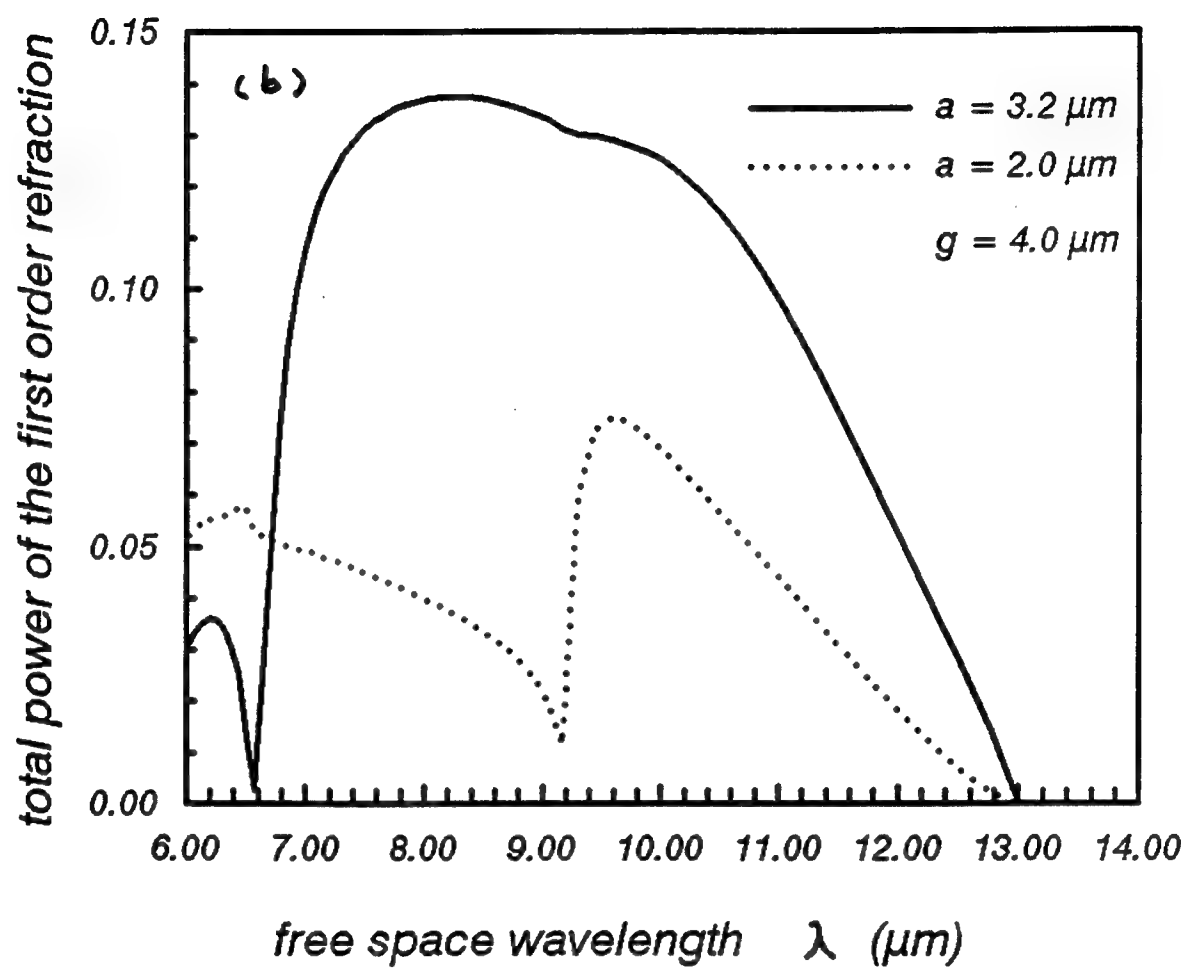


Figure 10.2. (b) Replot Fig. 10.2 (a) versus wavelength for  $g = 4.0 \mu\text{m}$  and  $a = 2.0, 3.2 \mu\text{m}$ .

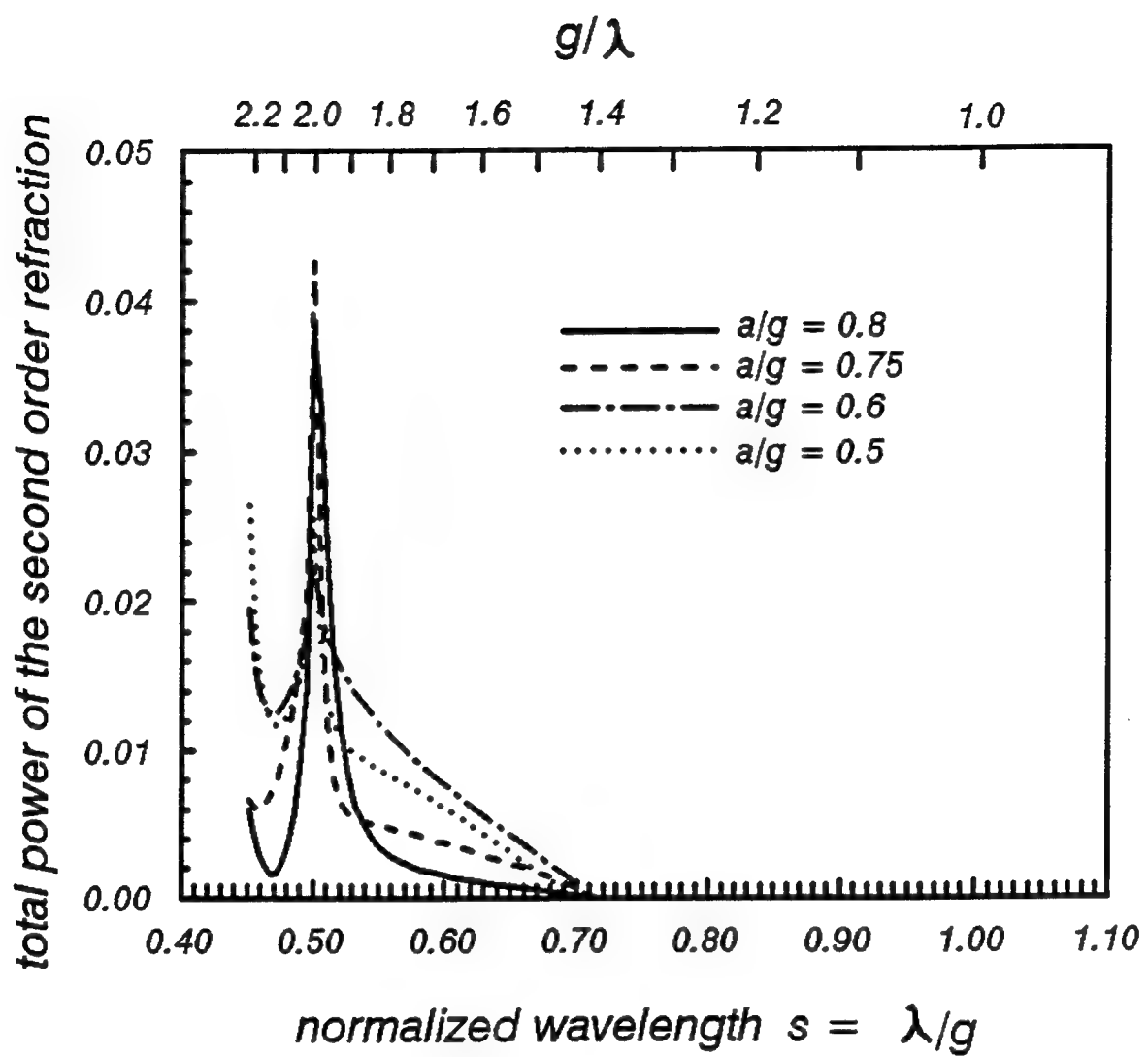


Figure 10.3. Total power of the second order refracted waves as a function of  $s = \lambda/g$  for different values of  $h = a/g$ .

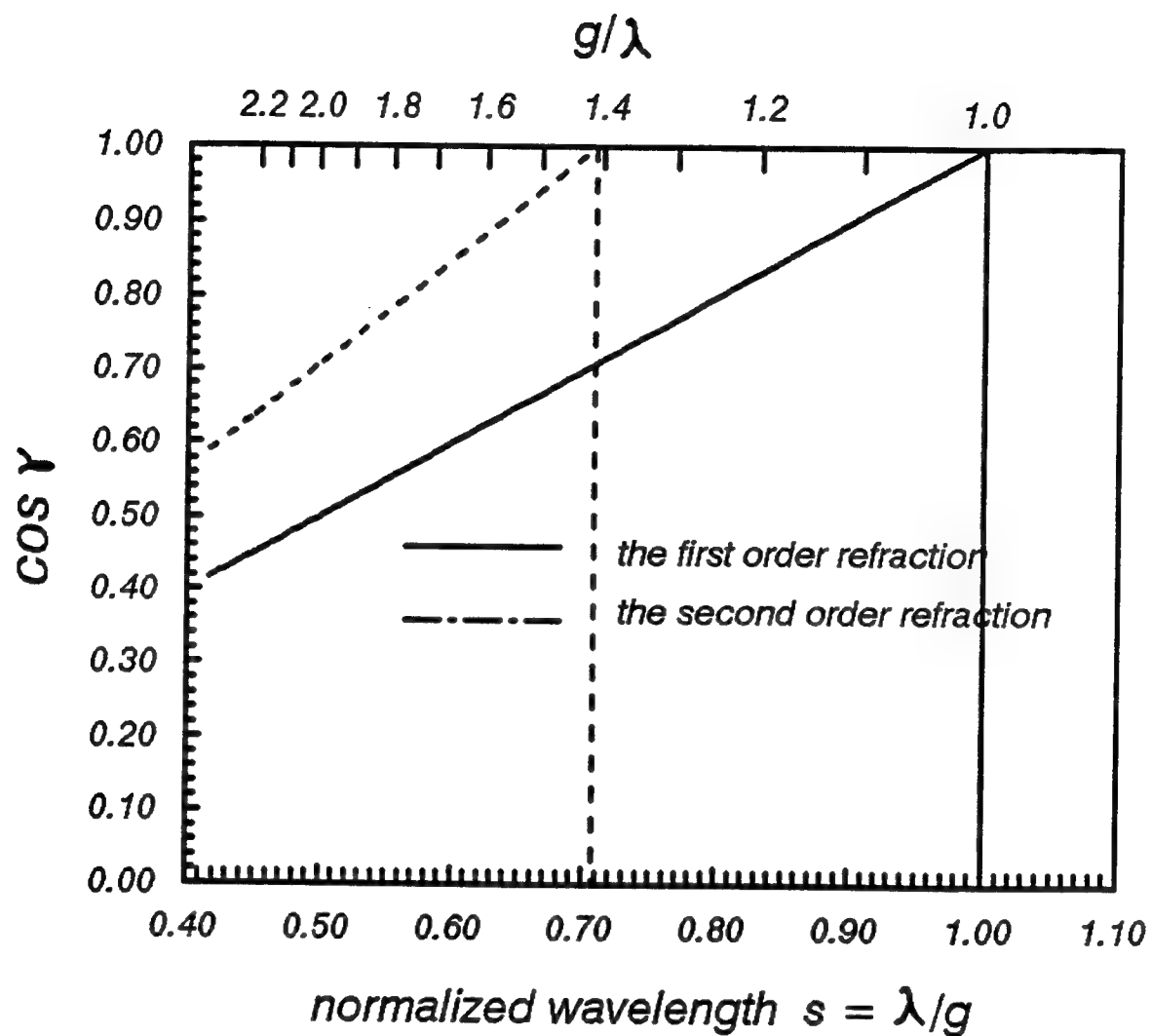


Figure 10.4. Cosine of the angle between the electric field vector and the z direction versus normalized wavelength.

## 11. DESIGN OF 2-D SQUARE MESH METAL GRATING COUPLER

### 11.1. Introduction

Recently, there has been a considerable interest in the long wavelength intersubband quantum well infrared photodetectors (QWIPs) for operating in the  $8\mu\text{m}$  to  $12\mu\text{m}$  atmospheric window region at 77K. Most of the QWIPs reported in the literature are fabricated using a larger bandgap III-V semiconductor material system such as GaAs/AlGaAs instead of the more difficult narrow bandgap material such as HgCdTe. The GaAs QWIP offers a very promising approach for the low background, long wavelength infrared detection due to the matured GaAs growth and processing technology. Thus, low cost and extremely uniform large area focal plane arrays (FPAs) can be fabricated using GaAs QWIPs for staring IR image sensor applications. However, the intersubband transition QWIPs using GaAs/AlGaAs material system do not absorb normal incident IR radiation on the surface of QWIP, since the electric field vector of incident light must be polarized perpendicular to the quantum well in order to induce intersubband transitions [36, 102]. As a result, the angle of incidence with respect to the QW layers must be different from zero in order to induce intersubband absorption in the quantum well. However, for FPAs applications, a response in normal incident light is required. This may be solved by incorporating a lamellar grating [47, 98, 104], which has a low coupling efficiency due to its polarization sensitivity. A double periodic metal grating formed on the top of a QWIP can be employed to deflect the normal incident light into an absorbable angle independent of light polarization. There are two approaches to form a double periodic grating on the QWIP: one approach is to deposit a metal grating directly onto the detectors, and the other approach is to etch the top surface layer of the QWIP followed by metal deposition. The former has the advantages over the latter in that it uses a simple and planar metal grating structure which can avoid the unwanted nonuniform etching on the detector surface and hence reduces the processing difficulties. In this section we report a numerical analysis of a 2-D transmission square mesh and reflection square cross metal grating formed directly on the top cap layer of the GaAs BTM QWIP.

Let us consider the electromagnetic (EM) waves impinging on a QWIP under normal incidence illumination. The radiation scattered by the metal grating consists of the transverse electric (TE)

polarization with the electric field parallel to the QW planes and the TM polarization with one component of the electric field perpendicular to the planes. Only TM components of the incident IR radiation leads to intersubband absorption in the quantum well. In the transmission square mesh metal grating structure shown in Fig. 11.1, for a unit amplitude normal incident light, the total power of each order refracted mode depends on the ‘normalized wavelength’  $s = \lambda/g$  (where  $g$  is the grating period and  $\lambda$  is the wavelength) and the ‘strip factor’  $h = a/g$  (where  $a$  is the width of the square aperture in the metal mesh). Furthermore, the angle between higher order transmitted wave and grating normal is determined solely by the parameter  $s$ . Thus, the intersubband absorption in the quantum well of a BTM QWIP is determined by the total power of the higher order transmitted TM waves and the refracted angle. The purpose of this work is to produce universal plots from which the power of higher order transmitted TM waves and the refracted angle can be determined for different sizes and grating period of 2-D square aperture mesh grating couplers formed on a GaAs BTM QWIP. Together with the absorption constant of intersubband transition, these plots provide a convenient overview of the mesh metal grating characteristics and of the various design possibilities for the BTM QWIPs.

## 11.2. Basic Theory

The basic theory used in deriving the unknown scattered waves for the transmission square mesh metal grating coupler in a BTM QWIP is based on the modal expansion technique [105]. The mesh metal grating consists of an infinitesimal perfect conducting screen perforated with square apertures distributed periodically along two orthogonal coordinates  $\tilde{x}$  and  $\tilde{y}$  as shown in Fig. 11.1. In this figure we employed spherical coordinates,  $\theta$  is the angle between the wave propagation vector  $\vec{k}$  and the normal to the plane of the grating, and  $\phi$  is the angle between the  $x$ -axis and the projection of  $\vec{k}$  on the  $x$ - $y$  plane. The mesh metal grating is formed on top of the QWIP. The distribution of the electromagnetic waves near the grating array is in the form of Floquet mode functions according to wave theory in a periodic structure. For this reason, under normal incidence radiation condition the solution of scalar time independent wave equation is given by

$$\psi_{pq} = e^{-j u_p x} \cdot e^{-j v_q y} \cdot e^{-j w_{pq} z} \quad (11.1)$$

where the wave vectors  $u_p$ ,  $v_q$ , and  $w_{pq}$  are given respectively by

$$u_p = \frac{2\pi p}{g} = k \cdot \sin \theta \cdot \cos \phi \quad (11.2)$$

$$v_q = \frac{2\pi q}{g} = k \cdot \sin \theta \cdot \sin \phi \quad (11.3)$$

$$w_{pq} = \begin{cases} \sqrt{k^2 - t_{pq}^2} & \text{for } k^2 \geq t_{pq}^2 \\ -j\sqrt{t_{pq}^2 - k^2} & \text{for } k^2 \leq t_{pq}^2 \end{cases}$$

where  $p, q = 0, \pm 1, \pm 2, \dots, \pm \infty$

and

$$t_{pq}^2 = u_p^2 + v_q^2$$

The vector orthonormal mode functions for the TE and TM modes transverse with respect to  $\hat{z}$  can be expressed as

$$\begin{aligned} \vec{\Phi}_{pq}^{TE} &= \frac{1}{g} \left( \frac{v_q}{t_{pq}} \hat{x} - \frac{u_p}{t_{pq}} \hat{y} \right) \psi_{pq} && \text{for TE modes} \\ \vec{\Phi}_{pq}^{TM} &= \frac{1}{g} \left( \frac{u_p}{t_{pq}} \hat{x} + \frac{v_q}{t_{pq}} \hat{y} \right) \psi_{pq} && \text{for TM modes} \end{aligned} \quad (11.4)$$

The wave admittances looking into the air in  $+\hat{z}$  direction are

$$\begin{aligned} \xi_{pq}^{TE} &= \frac{w_{pq}}{k} \frac{1}{Z_0} \\ \xi_{pq}^{TM} &= \frac{k}{w_{pq}} \frac{1}{Z_0} \end{aligned} \quad (11.5)$$

where  $Z_0 = \sqrt{\frac{\mu_0}{\epsilon_0}}$  is the free space characteristic impedance. Assuming that the impedance between all the quantum well layers are perfectly matched and the intersubband absorption is complete, no waves will be reflected from the other end of the QWIP. Under this condition, the modal admittances for TE and TM waves looking into the QW region from  $z = 0^+$  plane are to replace  $Z_0$  in Eq. (11.5) by  $Z_d = \sqrt{\frac{\mu_0}{\epsilon_0 \epsilon_s}}$  of GaAs as following

$$\begin{aligned} \xi_{pq}^{dTE} &= \frac{w_{pq}}{k} \frac{1}{Z_d} \\ \xi_{pq}^{dT M} &= \frac{k}{w_{pq}} \frac{1}{Z_d} \end{aligned} \quad (11.6)$$

A plane wave with unit electric field intensity normal incidence in the  $\phi$  plane can be expressed as the sum of TE and TM plane waves, i.e.,

$$\vec{E}^i = \sum_{r=1}^2 A_{00r} \vec{\Phi}_{00r} \quad (11.7)$$

where  $A_{00r}$  is the magnitude of the incident field component which depends on the polarization direction. The third subscript  $r = 1$  or  $2$  is used to designate the TE and TM Floquet modes respectively. Similarly, the reflected waves and transmitted waves can also be expressed in terms

of the Floquet modes with reflection coefficients  $R_{pqr}$  and transmission coefficients  $B_{pqr}$  as follows:

$$\begin{aligned}\vec{E}^t &= \sum_{r=1}^2 A_{00r} \vec{\Phi}_{00r} + \sum_p \sum_q \sum_{r=1}^2 R_{pqr} \vec{\Phi}_{pqr} \\ &= \sum_p \sum_q \sum_{r=1}^2 B_{pqr} \vec{\Phi}_{pqr}\end{aligned}\quad (11.8)$$

where Eq. (11.8) includes the boundary condition that the tangential electric field in the aperture is continuous. The orthonormal waveguide modes  $\vec{\Psi}_{mnl}$  span the space of the aperture itself other than the Floquet modes  $\vec{\Phi}_{pqr}$  were used to expand the unknown electric field distribution in the aperture in order to satisfy the boundary condition, which has been shown to provide a faster convergence.

$$\vec{E}^t = \sum_m \sum_n \sum_{l=1}^2 F_{mnl} \vec{\Psi}_{mnl} \quad (11.9)$$

where the unknowns  $F_{mnl}$  are the coefficients given in the waveguide modes expression. Finally, a matrix equation can be obtained as

$$\begin{bmatrix} Y_{MNL}^{mnl} \end{bmatrix} [F_{mnl}] = [I_{mnl}] \quad (11.10)$$

where

$$\begin{aligned}Y_{MNL}^{mnl} &= \sum_p \sum_q \sum_{r=1}^2 (\xi_{pqr} + \xi_{pqr}^d) C_{pqr}^{MNL*} C_{pqr}^{mnl} \\ C_{pqr}^{mnl} &= \int \int_{\text{aperture}} \vec{\Phi}_{pqr}^* \cdot \vec{\Psi}_{mnl} da\end{aligned}\quad (11.11)$$

and

$$I_{mnl} = \sum_{r=1}^2 A_{00r} \xi_{00r} C_{00r}^{mnl*} \quad (11.12)$$

is the input matrix. The higher order transmission coefficients are given by

$$B_{pqr} = \sum_m \sum_n \sum_{l=1}^2 F_{mnl} C_{pqr}^{mnl} \quad p, q \neq 0, 0 \quad (11.13)$$

Since  $F_{mnl} \propto \lambda$  and  $C_{pqr}^{mnl} \propto 1/\lambda$  for a given  $g$ , the transmission coefficient  $B_{pqr}$  is a function of  $\lambda/g$ . The angle between the electric field of the higher order transmitted TM Floquet mode  $B_{pq2} \vec{\Phi}_{pq2}$  and the  $\hat{z}$  direction is designated as  $\gamma_{pq2}$ , and cosine of this angle depends on the order of transmitted waves and normalized wavelength  $s = \lambda/g$  as given by

$$\cos \gamma_{pq2} = \frac{\lambda}{g} \cdot \sqrt{p^2 + q^2} \quad (11.14)$$

The 2-D grating coupled GaAs/AlGaAs BTM QWIP structure used in the present analysis is based on the bound ground state in the enlarged well to the global miniband in the superlattice which has been reported by Yu and Li [13], as shown in Fig. 11.2. Only in the miniband the electrons are freely to move in the perpendicular direction to the QW layers and may give rise to an electric signal. The intersubband absorption constant can be expressed by

$$\alpha = \left( \frac{e^2 \hbar^3}{m^* n_r \epsilon_0 c} \right) \cdot \frac{n_e \cos^2 \gamma}{\hbar \omega} \cdot \frac{T^2 \sqrt{(E - E_{min})(E_{max} - E)}}{(U + S_1)^2 - S_1(E_{max} - E)} \quad (11.15)$$

where  $e$  is the electronic charge,  $m^*$  is the effective mass,  $n_r$  is the refractive index of the medium,  $c$  is the speed of light,  $n_e$  is the electron density in the wells,  $\omega$  is the angular frequency of the EM waves,  $\gamma$  is the angle between the electric vector of the incident IR radiation and the motion vector of electrons,  $E_{max}$  and  $E_{min}$  are the two extreme edge of the miniband as shown in Fig. 11.2. All other parameters,  $T$ ,  $U$ , and  $S_1$  in Eq. (11.14) depend on the specific quantum well structure. Substituting Eq. (11.14) into (11.15), we can readily calculate the absorption constant in the spectral range of interest.

### 11.3. Results and Discussion

The evanescent modes excited by the square mesh metal grating produce no photoresponse in the quantum well intersubband transition, neither do the TE modes. Therefore, the following discussion will focus on the propagating TM modes in the transmitted region (i.e., the side where the QW is located). It is convenient to use the two normalized parameters ' $s = g/\lambda$ ' and the strip factor  $h = a/g$  to illustrate the universal plots for the transmission square mesh metal grating coupled BTM QWIP.

Rigorous calculations were made by using forty waveguide modes, the addition of more modes made no significant change in the transmission coefficients. When analyzing meshes with larger strip factor ( $a/g > 0.85$ ), a much larger number of waveguide modes were required to simulate the wave distribution at the metal edge. Large strip factor is undesirable for the practical QWIP, since it is more difficult to fabricate grating coupler with periodicity and aperture size less than  $2 \mu\text{m}$ . Let us now consider the case of a normal incident unit amplitude electromagnetic wave impinging on the square mesh metal grating at zero degree angle with respect to the grating normal. The effective coupling is due to nonzero order transmitted TM Floquet modes, since the TE Floquet modes have an angle  $\gamma = 90^\circ$  in Eq. (11.15). Figure 11.3 shows the first universal plot, which illustrates the normalized total power of the first order TM transmitted wave  $B_{012}\tilde{\Phi}_{012}$ ,  $B_{0-12}\tilde{\Phi}_{0-12}$ ,  $B_{-102}\tilde{\Phi}_{-102}$  and  $B_{102}\tilde{\Phi}_{102}$  varies with the normalized wavelength  $s = \lambda/g$  for different  $h = a/g$ . In this figure, we modified the transmitted power by a factor  $\frac{2+3.25^2}{1+3.25^2}$  to eliminate the reflection effect owing to the

impedance mismatch between air ( $n_r = 1$ ) and GaAs ( $n_r = 3.25$  at 77 K). The first order transmitted waves emerge when the wavelength of IR radiation in GaAs is smaller than the grating period, that is,  $s = \lambda/g < 3.25$ . For the same reason, within the spectral range in Fig. 11.3, only one far field reflected waves  $R_{001}\Phi_{001}$  in the free space was found, and all other higher order refracted waves were eliminated. This is due to the fact that free space wavelength  $\lambda$  is greater than the grating period  $g$  and thus makes the grating coupler operating in the non-refraction region. Next, the square mesh metal grating is indistinguishable in both  $x$  and  $y$  directions. The total normalized power of the first order transmitted wave generated by  $x$  and  $y$  components of the incident wave remains the same for different input polarizations. In other words, the grating is independent of polarization. A relatively flat curve for  $h = a/g = 0.5$  as shown in Fig. 11.3 may be treated as a better choice for coupling the IR radiation more effectively into the QWIP. Figure 11.4 illustrates the normalized total power of the second order TM transmitted components  $B_{\pm 112}\tilde{\Phi}_{\pm 112}$  and  $B_{1\pm 12}\tilde{\Phi}_{1\pm 12}$  as a function of the normalized wavelength  $s$  for various values of  $h$ . A comparison of Figs. 11.3 and 11.4 reveals that the larger the first order transmission modes the larger the power of the second order transmitted modes is. The second order transmitted wave emerges for  $s < \frac{3.25}{\sqrt{2}}$  with total power about 50 % smaller than that of the first order transmitted modes.

Figure 11.5 shows a universal plot that relates  $\cos \gamma_{pq2}$  to the normalized wavelength of the higher order transmitted waves, where  $\gamma$  is the angle between the electric field vector and the grating normal. The relationship for the first order transmitted waves ( i.e.  $| p | + | q | = 1$  in the notation of Floquet modes  $\tilde{\Phi}_{pqr}$  ) is given by

$$\cos \gamma_{pq2} = \frac{\lambda}{g} \quad (11.16)$$

The relationship for the second order transmitted waves with  $| p | = | q | = 1$  is :

$$\cos \gamma_{pq2} = \frac{\lambda}{g} \cdot \sqrt{2} \quad (11.17)$$

We next calculate absorption constant on  $\cos^2 \gamma_{pq2}$  versus wavelength in a 2-D square mesh grating coupled GaAs BTM QWIP. The mesh grating period is selected in the region where  $s$  falls between 0.7 and 1 for the first order refracted waves. In this case  $\cos^2 \gamma$  is greater than 1/2, which corresponds to the 45° launching. If we select the curve with  $h = 0.5$  in Fig. 11.3 by multiplying the grating period  $g = 4\mu\text{m}$  to the coordinate, a rather flat coupling curve over a broad wavelength range from 9 to 12  $\mu\text{m}$  appears, as shown in Fig. 11.6. By substituting the corresponding  $\cos \gamma$  in Fig. 11.5 and using the QWIP parameters given in Fig. 11.2 in Eq. (11.15), we obtained the absorption constant versus wavelength for the GaAs BTM QWIP as shown in Fig. 11.7(a). The

aperture width of the mesh grating in the above design example was found to be  $a = (4\mu\text{m}) \cdot 0.5 = 2\mu\text{m}$ . From Fig. 11.7(a), the quantum efficiency<sup>12</sup>  $\eta$  can be determined by using the expression

$$\eta = (\mathcal{P}_{eff}) \cdot (1 - e^{-\alpha l}) \quad (11.18)$$

where  $\mathcal{P}_{eff}$  is the effective coupling power of the light and  $l$  is the total length of the doped quantum wells. In the present case,  $l = (88\text{\AA}) \cdot (40\text{periods}) = 3520\text{\AA}$  and  $\eta$  is shown in Fig. 11.7(b).

Similarly, the characteristic curves of the first order TM refraction waves for a reflection square cross metal grating coupler shown in Fig. 11.8 may be plotted in Fig. 11.9. The basic equations for design such a metal grating coupler are described in Chapter 10. A strong coupling region located in the 8.5 to 11.5  $\mu\text{m}$  wavelength range as shown in Fig. 11.9 is available for coupling the reflection mode normal incident IR radiation into the QWIP. The absorption constant spectrum of the square cross metal reflection grating is the same as that of square mesh metal grating, as illustrated in Fig. 11.7(a). Figure 11.10 shows a comparison of the quantum efficiency for the GaAs BTM QWIP shown in Fig. 11.2 coupled by the 2-D square mesh and cross metal grating couplers. Basically, they have the same coupling characteristics in the 9 to 12  $\mu\text{m}$  wavelength range and are both polarization independent. A minor drawback exists for the square mesh metal grating coupler in that a sharp dip of the first order refracted wave coupling power occurs at about  $9.2\mu\text{m}$  as shown in Fig. 11.6, which corresponds to the normalized wavelength  $s = \frac{1}{\sqrt{2}}$  of medium refractive index  $n_r = 3.25$  for GaAs at 77K.

#### 11.4. Grating Pattern Variation Effect

In the fabrication of small grating coupler structure on QWIPs, some distortion in the aperture's shape and size may occur during processing. This may lead to nonuniformed photoresponse of cell-to-cell in the QWIP arrays, introduce spatial noise, and limit the sensitivity of IR image arrays. Therefore, the effect of changing the aperture width and shape on the coupling quantum efficiency must be considered in the grating design.

Figure 11.11(a) shows the distorted shape of the aperture. In the extreme case, the aperture becomes a circular shape with a radius  $r$  equal to half of the square aperture width  $a$ , and the grating coupler consists of a conducting screen perforated periodically with circular apertures. The characteristic curve of such a grating is plotted in Fig. 11.11(b). Almost invariant coupling curve is obtained for  $r/g = 0.3$  to  $a/g = 0.6$ , which implies that the square mesh metal grating with a normalized aperture width  $a/g = 0.6$  is insensitive to the aperture shape even if the pattern is not processed properly. Another approach to reduce the effect of deformation in the grating

aperture is to use a larger grating geometry with a lower coupling quantum efficiency. For example, a square mesh grating coupler with  $g = 6\mu\text{m}$  and  $a = 3\mu\text{m}$  instead of  $g = 4\mu\text{m}$ ,  $a = 2\mu\text{m}$  can be used to couple a GaAs/AlGaAs QWIP for 9-11 $\mu\text{m}$  detection. Figure 11.12 illustrates the coupling characteristic curves for the 6/3 ratio grating coupler. This larger scale grating has larger aperture size, and hence is easier to fabricate within the same error tolerance limits. Figure 11.13(a) and (b) show the calculated optical absorption constants of the first, second and third order diffracted waves, and the calculated coupling quantum efficiency of a GaAs/AlGaAs QWIP using two different sets of grating parameters. The grating pattern variation effect can be minimized by either selecting a larger aperture size or using a larger grating period. The spatial noise generated by grating pattern variation can be reduced either by using noncritical grating geometry or using a larger grating dimension.

In conclusion, we have performed a detailed numerical analysis of a GaAs BTM QWIP covered with two different types of 2-D square metal gratings. It is shown that for a given QWIP the total power and the refracted angle of the higher order TM transmitted waves depend on two normalized parameters,  $s = \lambda/g$  and  $h = a/g$ , which are functions of wavelength and grating dimensions. By using the universal plots shown in Figs. 11.3 and 11.5, the optimum grating period and grating width can be determined for any specified IR spectrum. In addition, the absorption constant and quantum efficiency for a 2-D metal grating coupled QWIP can be calculated from these universal plots.

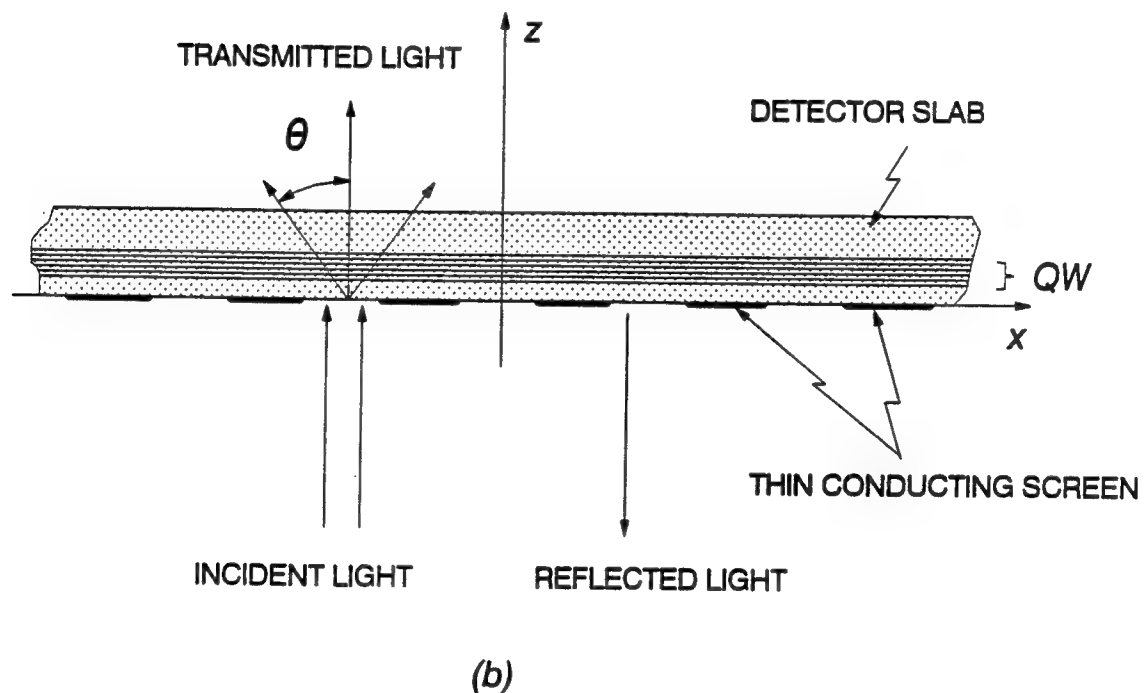
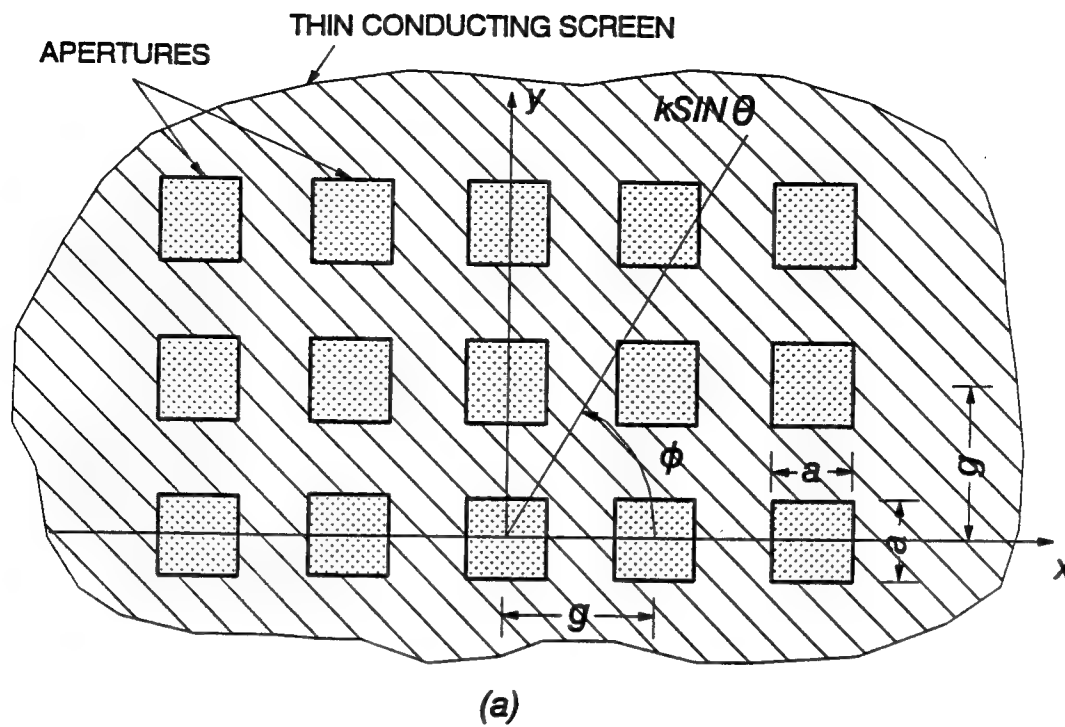


Figure 11.1. Schematic diagram showing the square mesh metal grating and the directions of incident and scattered waves. (a) Top view and (b) side view.

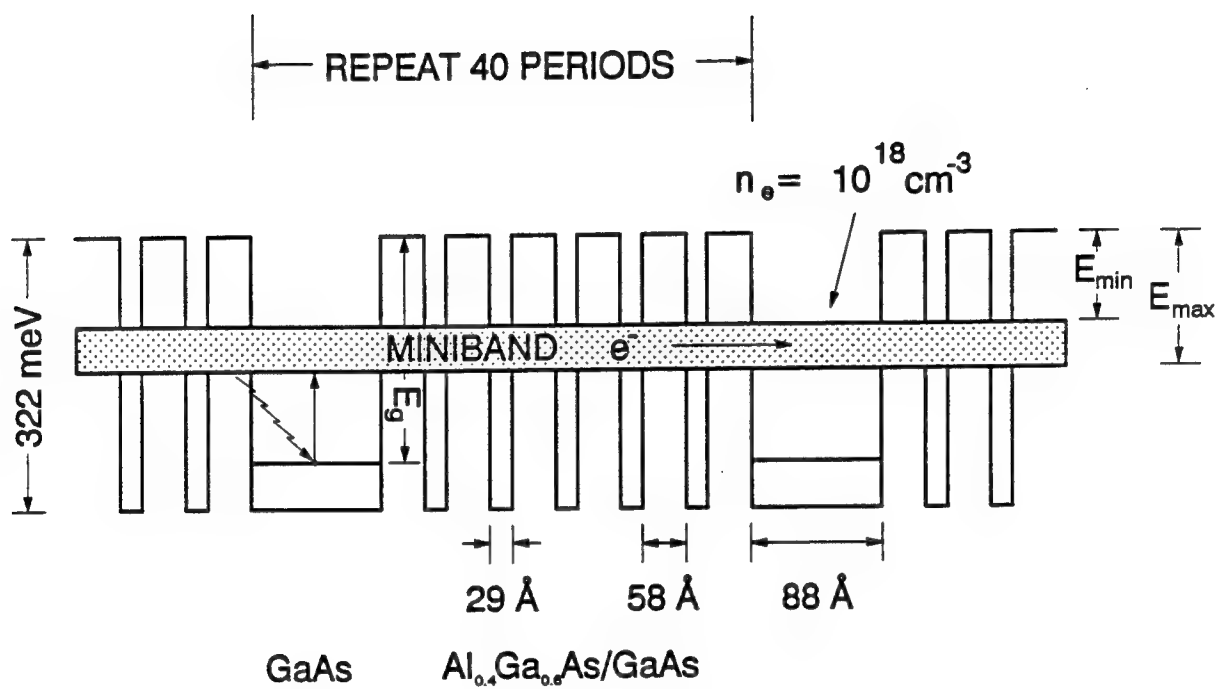


Figure 11.2. The energy band diagram for a bound-to-miniband (BTM) transition GaAs/AlGaAs quantum well infrared photodetector (QWIP).

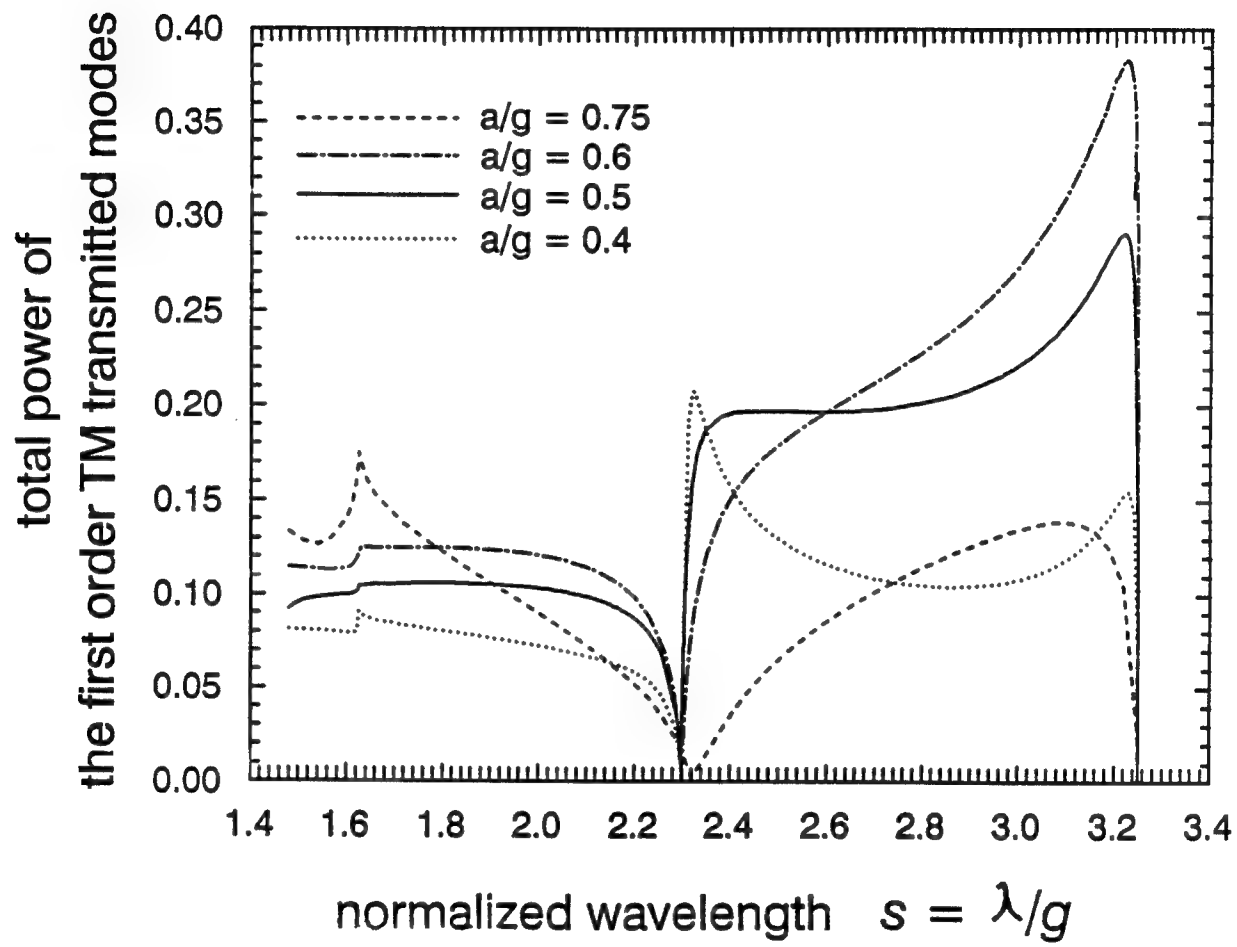


Figure 11.3. Normalized power of the first order transmitted waves versus normalized wavelength  $s = \lambda/g$  for different values of  $h = a/g$ , where  $a$  is the size of square mesh metal grating and  $g$  is the grating period.

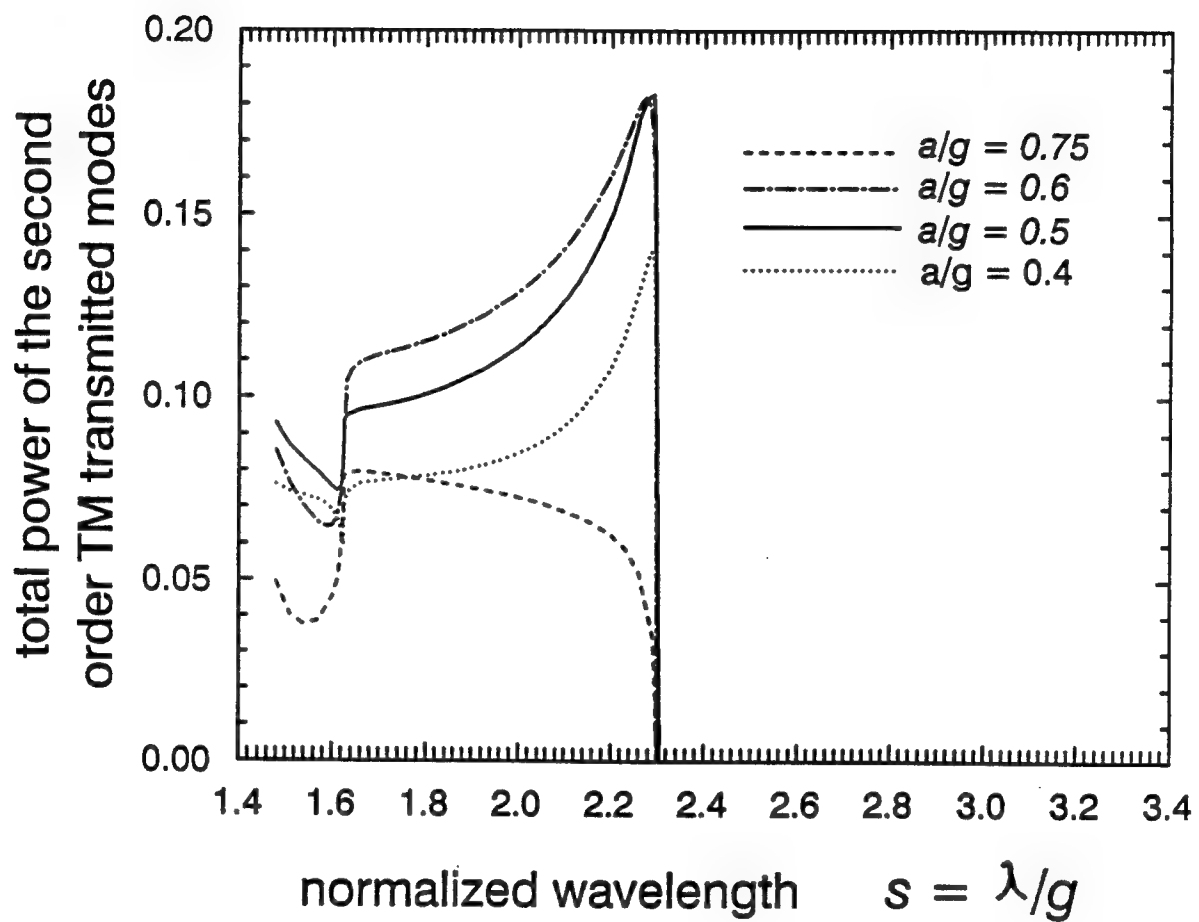


Figure 11.4. Normalized power of the second order transmitted waves as a function of  $s = \lambda/g$  for different values of  $h = a/g$ .

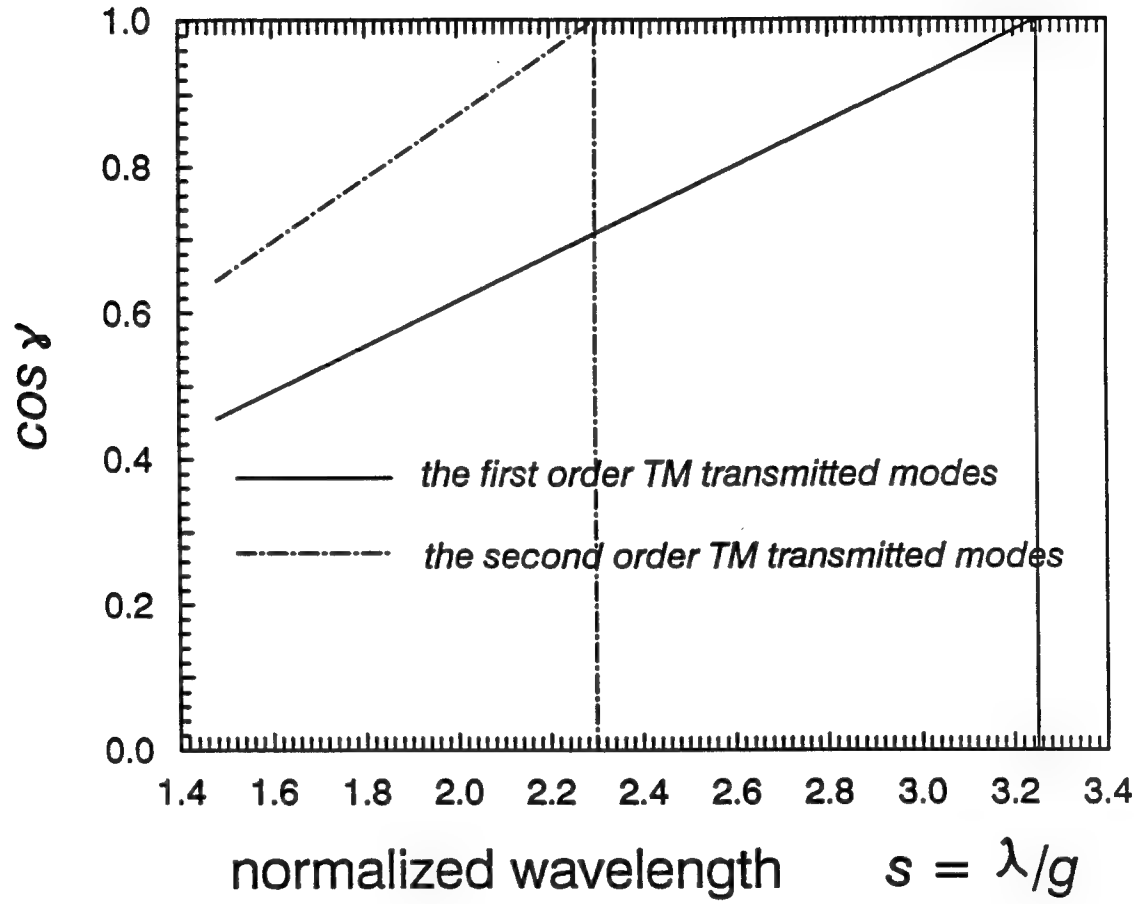


Figure 11.5. Cosine of the angle between the electric field vector and the normal of quantum well layers versus normalized wavelength.

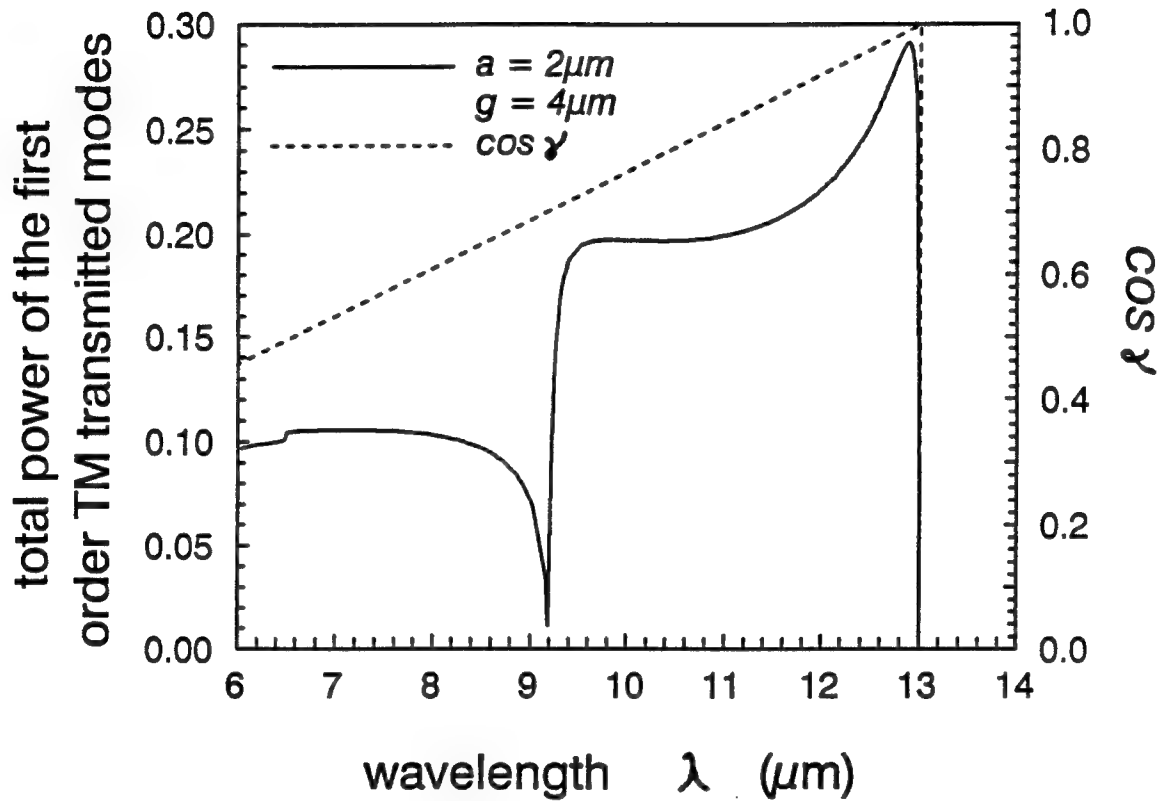


Figure 11.6. Replot of Figs. 11.3 and 10.5 versus wavelengths for  $g = 4.0 \mu m$  and  $a = 2.0 \mu m$ .

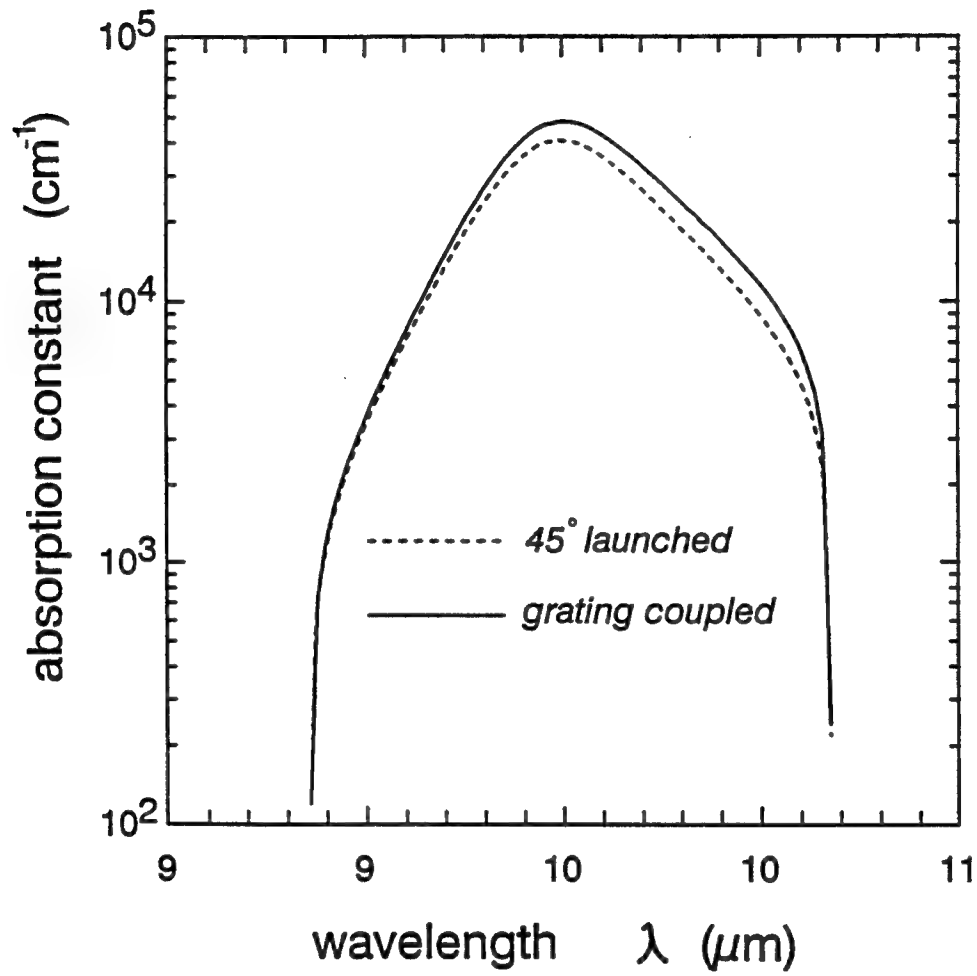


Figure 11.7. (a). Absorption constant of the QWIP shown in Fig. 11.2 covered with a square mesh metal grating coupler, compared to that of a 45° polished facet. (b). Quantum efficiency of a square mesh metal grating coupled GaAs BTM QWIP.

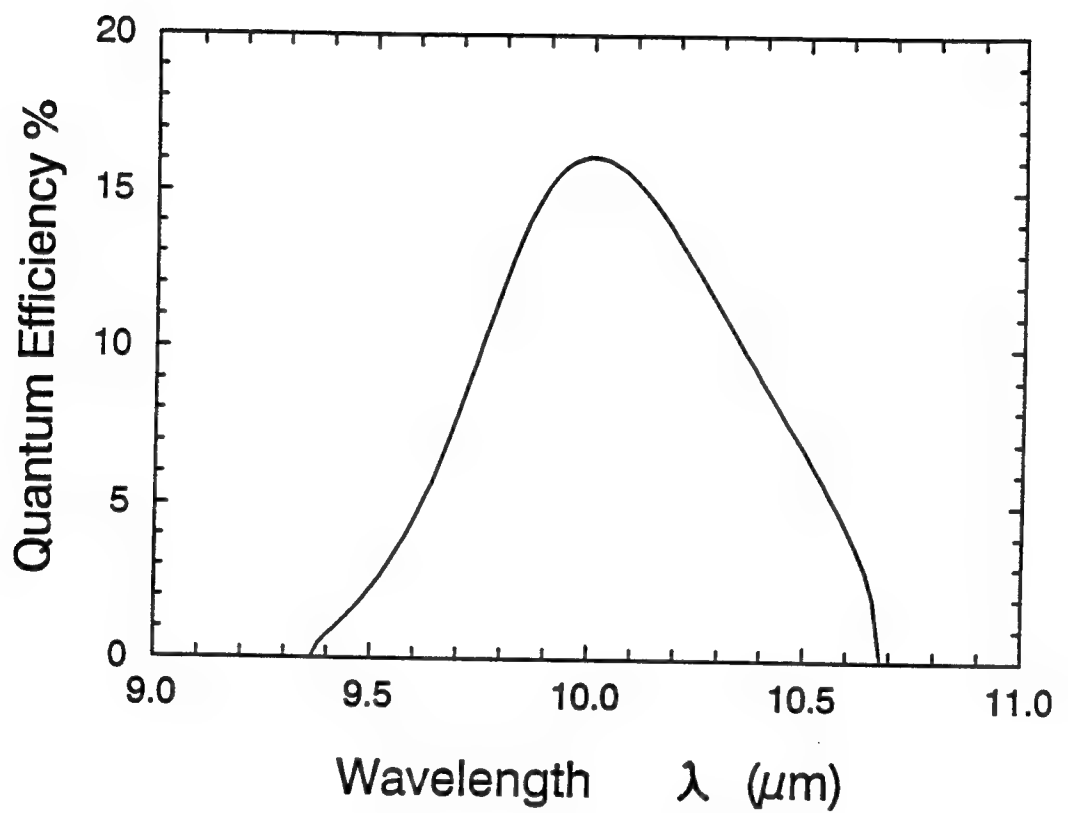
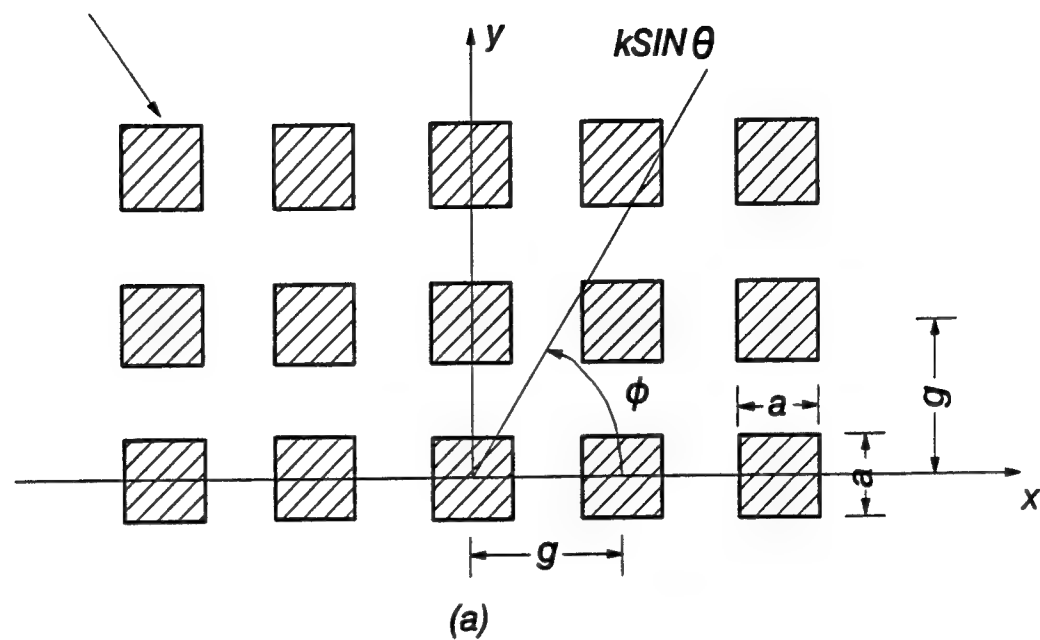


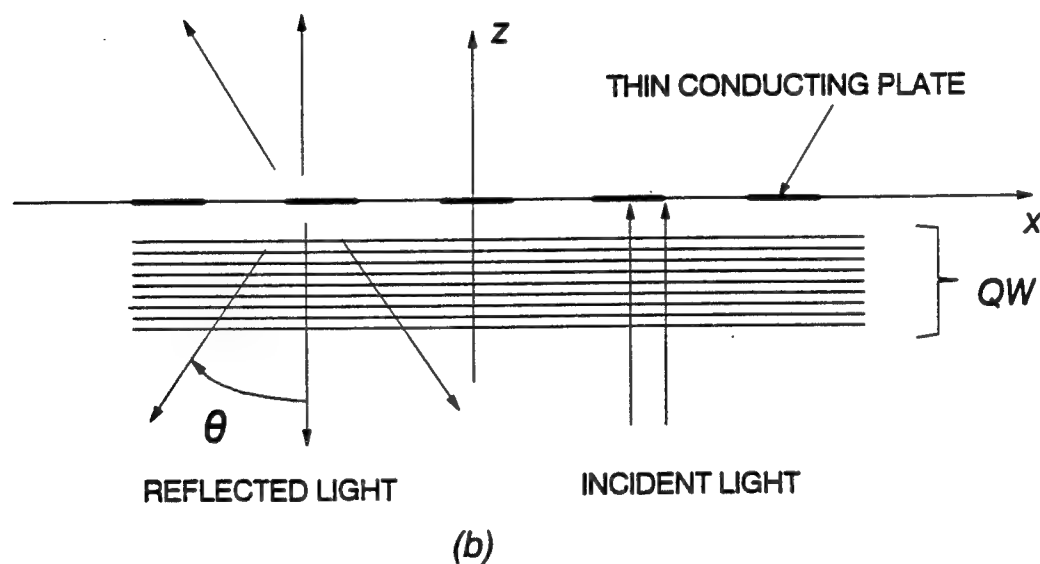
Figure 11.7. Continued.

THIN CONDUCTING PLATE



(a)

THIN CONDUCTING PLATE



(b)

Figure 11.8. Schematic diagram showing a reflection square cross metal grating and the directions of incident and reflected waves.  
(a) Top view and (b) side view.

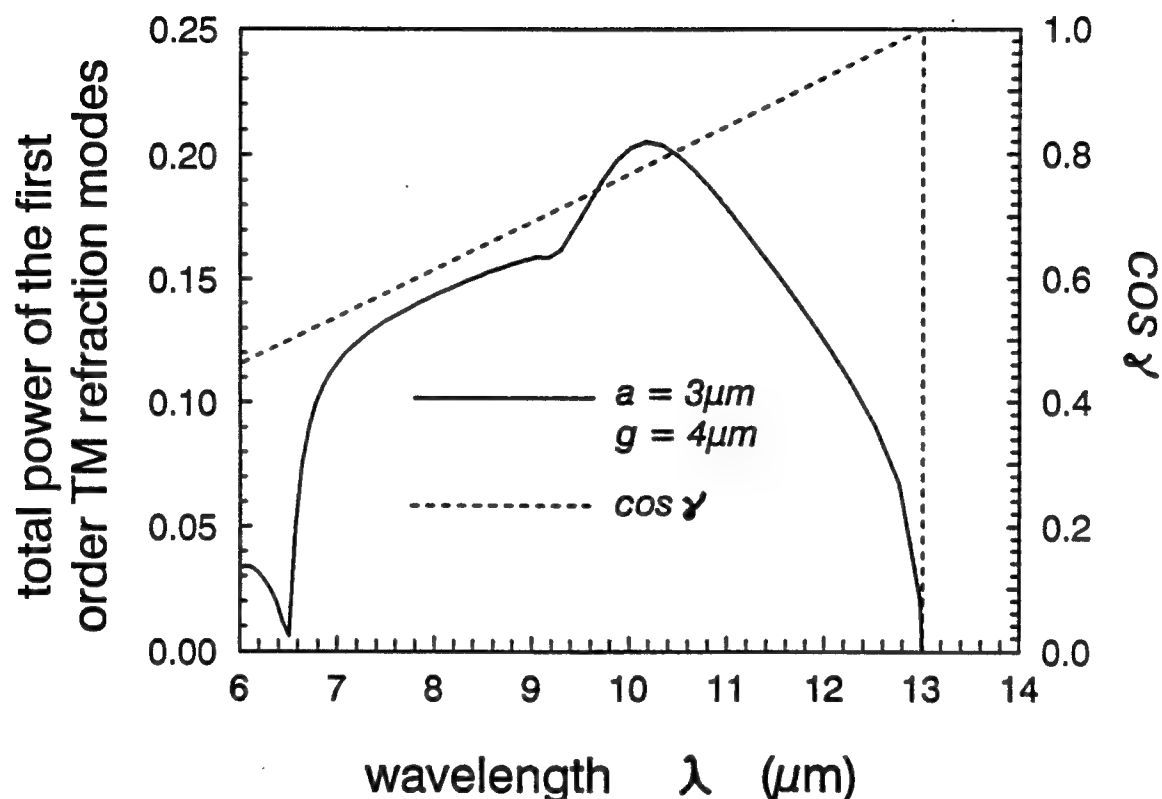


Figure 11.9. Normalized power of the first order TM refraction waves versus wavelength for  $g = 4.0 \mu m$  and  $a = 3.0 \mu m$ .

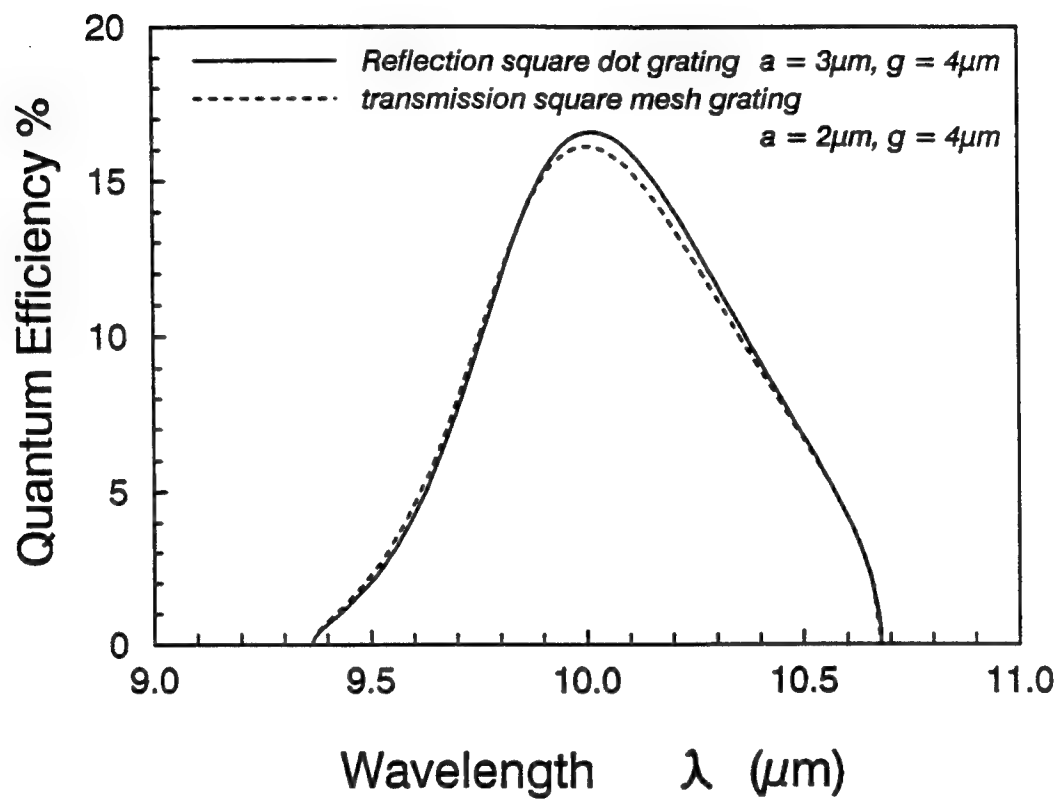


Figure 11.10. A comparison of the quantum efficiency for a square mesh metal grating and a square cross metal grating coupled GaAs BTM QWIP with the same grating period.

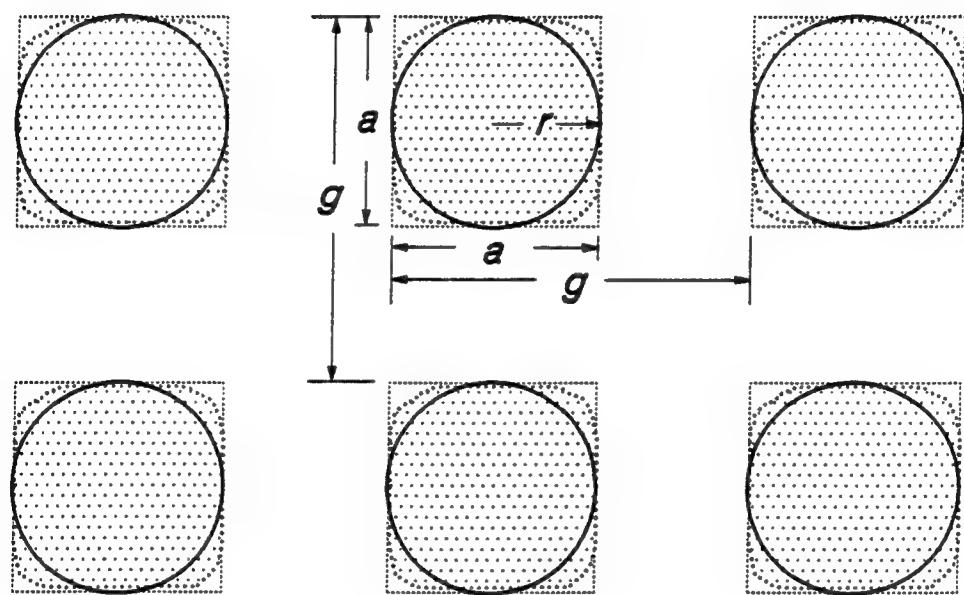


Figure 11.11. (a) Top view of the square and circular shape apertures for a 2-D square mesh metal grating coupler, (b) relative coupling power of the first order diffracted waves versus normalized wavelength for a square and circular shape aperture.

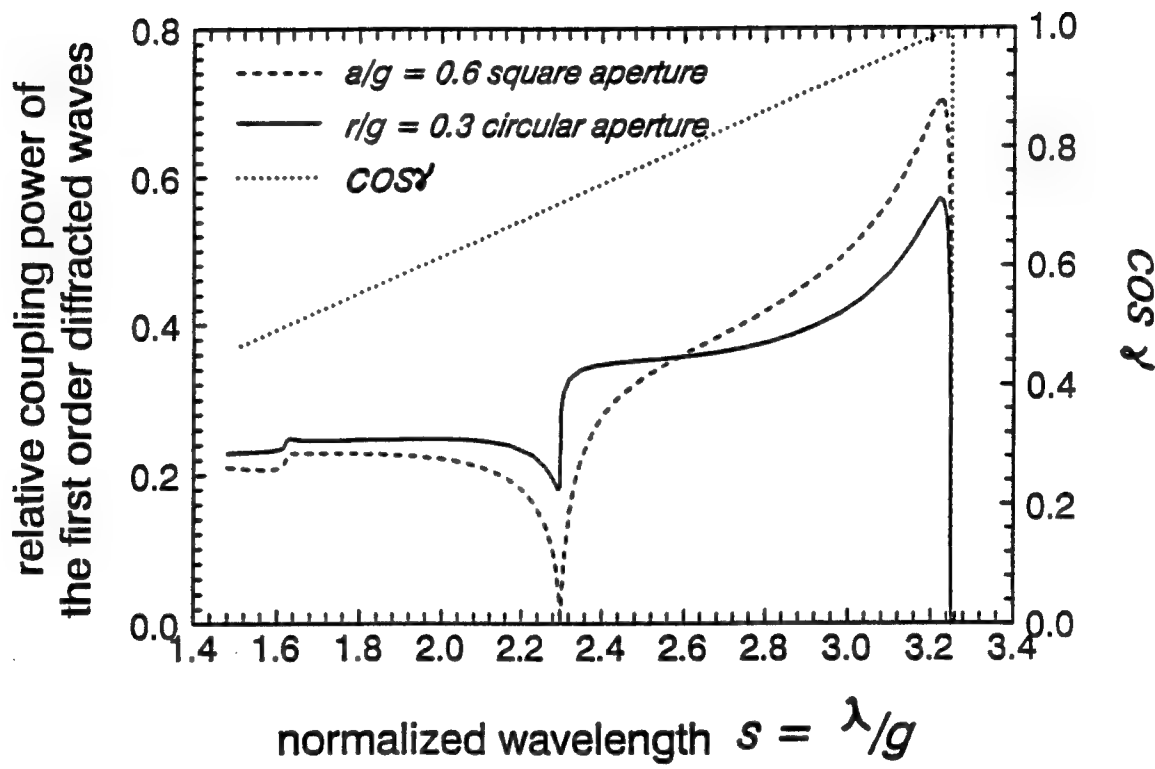


Figure 11.11. Continued.

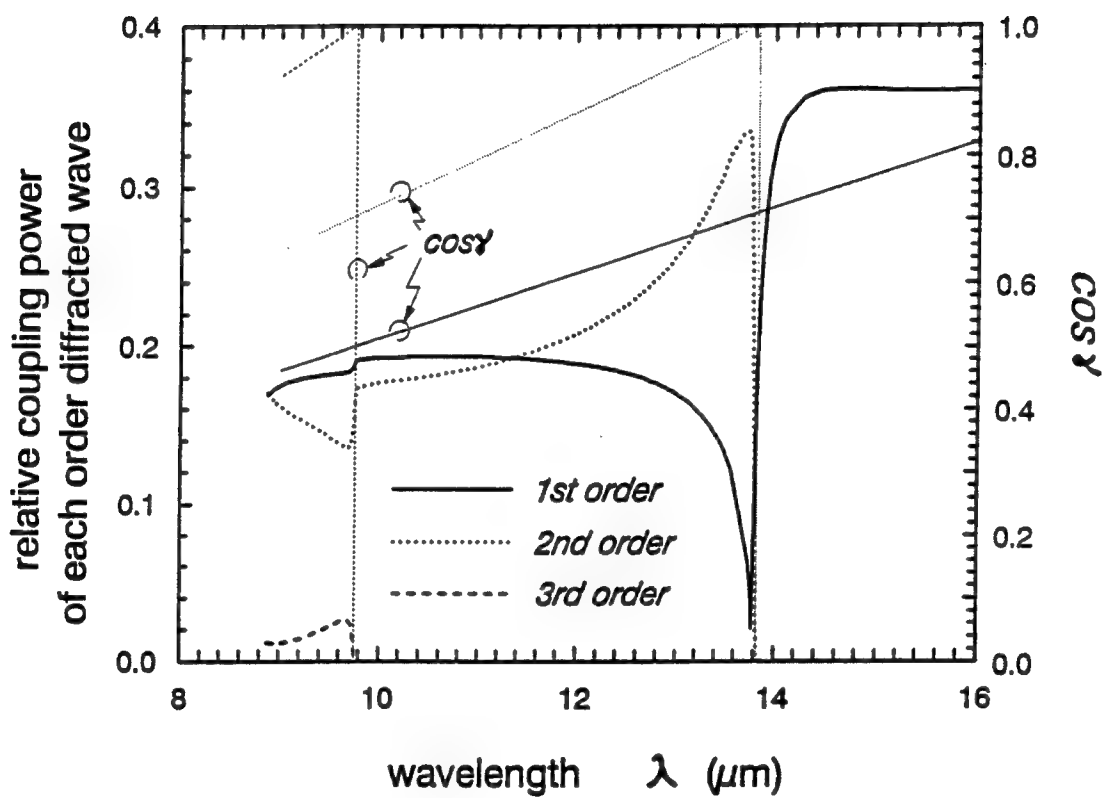


Figure 11.12. The relative coupling power of the first, second, and third order diffracted waves versus wavelength for a 2-D square mesh grating coupler with  $g = 6 \mu\text{m}$  and  $a = 3 \mu\text{m}$ .

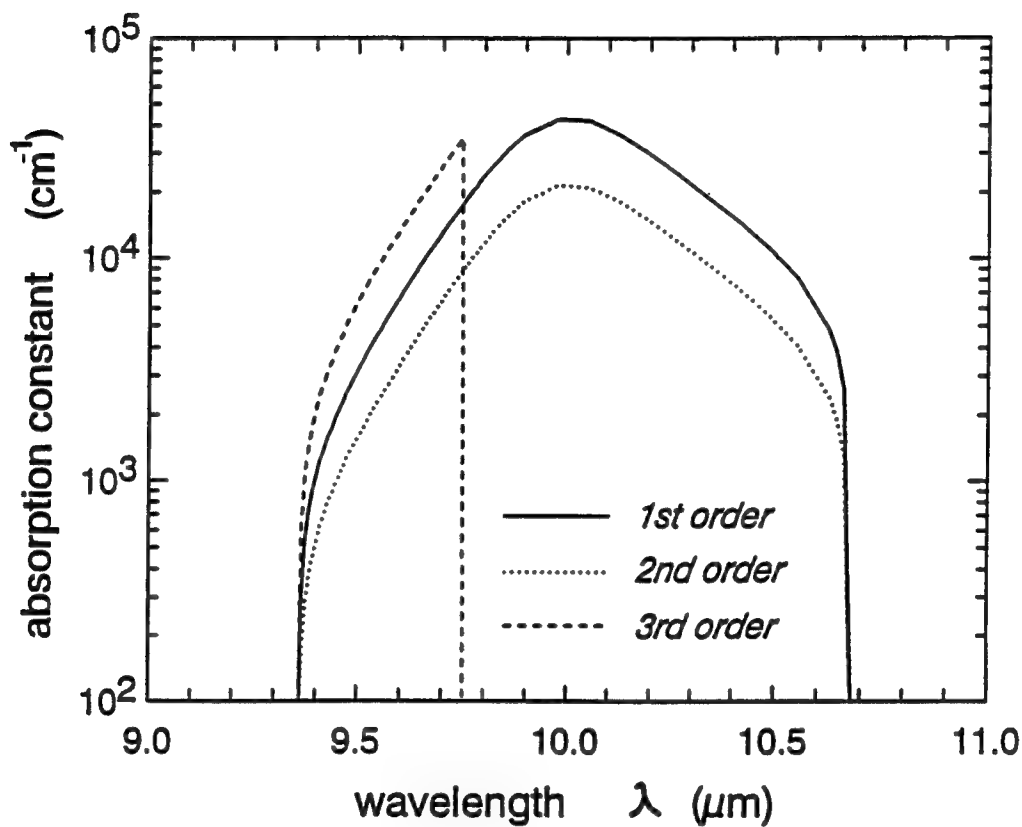


Figure 11.13. (a) Optical absorption constant of the first, second, and third order diffracted waves, (b) coupling quantum efficiency versus wavelengths for a 2-D square mesh metal grating coupled GaAs/AlGaAs QWIP.

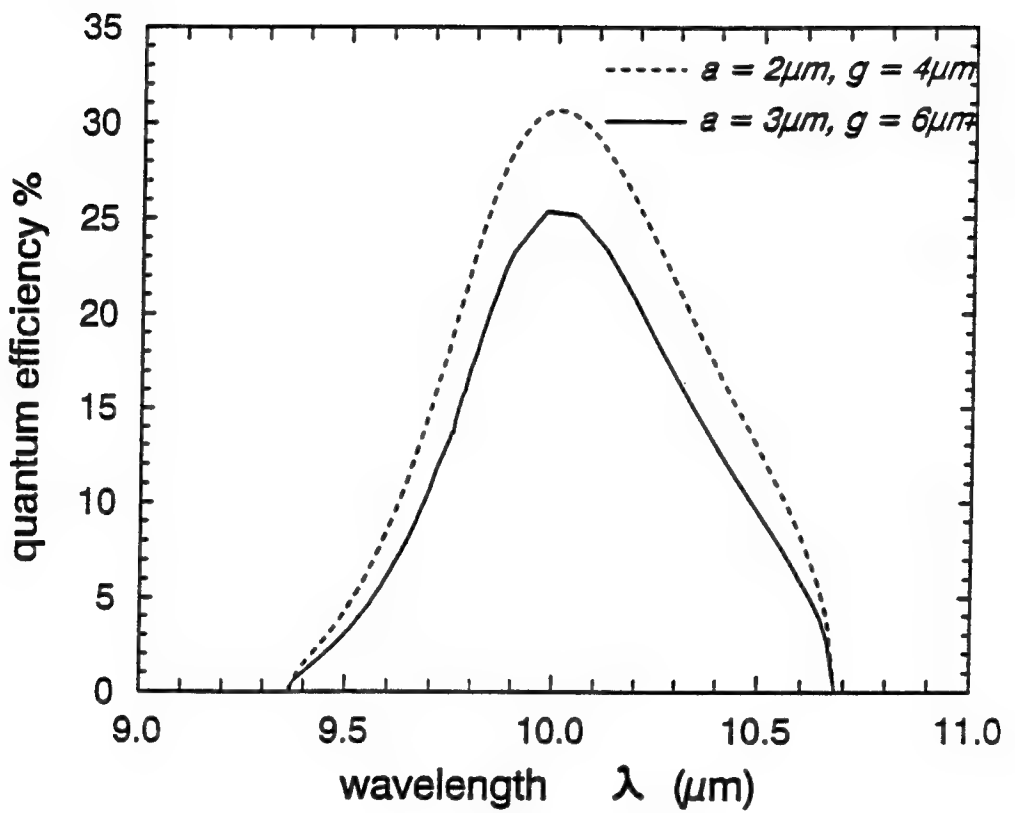


Figure 11.13. Continued.

## 12. DESIGN OF 2-D CIRCULAR MESH METAL GRATING COUPLER

### 12.1. Introduction

In our previous work we have reported the design of 2-D square dot reflection metal grating and 2-D square mesh metal grating couplers for n-type QWIPs [83, 106]. In this section, we present the theoretical and experimental study of a planar 2-D circular mesh metal grating coupler formed on a GaAs QWIP. The results showed that back illumination performs better than that of front illumination for the circular mesh metal grating coupled QWIP. In the following, we consider the electromagnetic (EM) waves impinging on a 2-D circular mesh metal grating coupled QWIP under normal incident back illumination.

Light coupling is polarization independent provided that the individual unit cell and cell arrangement of the grating are of highly symmetry. For the circular aperture mesh metal grating both square symmetry (Fig. 12.1(a)) and hexagonal symmetry (Fig. 12.1(b)) structures possess the highest possible symmetry, and are polarization independent. It has been shown that only the TM components of the grating diffracted waves lead to intersubband transition in the quantum wells. Besides, the quantum efficiency of a QWIP is a function of the total power and absorption angle of the higher-order TM diffracted waves. In the 2-D circular aperture metal grating shown in Fig. 12.1, under normal incident illumination, the normalized total power of each order diffracted waves depends on the ‘normalized wavelength’  $s = \lambda/g$  and the ‘normalized aperture radius’  $h = a/g$  (where  $g$  is the grating period and  $\lambda$  is the free space wavelength, and  $a$  is the radius of the circular aperture in the metal grating). The universal plots displaying the normalized total power and absorption angle of the higher-order diffracted waves versus normalized wavelength provide a convenient way for designing the optimum grating coupler for the GaAs QWIPs. Furthermore, the absorption angle used in determining the absorption constant depends on the parameter  $s$  and the order of diffraction. Based on this analysis, several universal charts of total power and absorption angle of higher-order TM diffracted waves are presented below to provide a convenient designing tools for the 2-D circular aperture mesh metal grating coupled GaAs QWIPs. The results showed a 2.7 times enhancement of photo-responsivity for such a grating coupler over the 45° edge illuminated QWIP.

## 12.2. Basic Formulation

According to the diffraction properties of grating, the unknown scattered waves on both side of the grating can be expanded into a complete set of Floquet modes  $\vec{\Phi}_{pqr}$ , with two spatial harmonic number  $p$  and  $q$ , and a third subscript  $r$  used to denote TE or TM modes. The unit power density EM wave is normally incident on the perfect conducting grating of infinitesimal thickness as shown in Fig. 12.1(c). The vector orthonormal mode functions for the TE and TM Floquet modes transverse with respect to  $\hat{z}$  can be expressed by

$$\begin{aligned}\vec{\Phi}_{pq1} &= G(\sin \phi_{pq} \hat{x} - \cos \phi_{pq} \hat{y}) e^{-j(k_x^p x + k_y^q y)} && \text{for TE modes} \\ \vec{\Phi}_{pq2} &= G(\cos \phi_{pq} \hat{x} + \sin \phi_{pq} \hat{y}) e^{-j(k_x^p x + k_y^q y)} && \text{for TM modes}\end{aligned}\quad (12.1)$$

where the normalized factor  $G$  is written in terms of grating period  $g$

$$\begin{aligned}G &= \frac{1}{g} && \text{for square symmetry} \\ &= \sqrt{\frac{2}{\sqrt{3}}} \frac{1}{g} && \text{for hexagonal symmetry}\end{aligned}\quad (12.2)$$

the time dependence  $e^{j\omega t}$  is omitted, and the wave vectors  $k_x^p$  and  $k_y^q$  in the  $x$  and  $y$  axes are given respectively by

$$\begin{aligned}k_x^p &= \frac{2\pi}{g} p = k \sin \theta_{pq} \cos \phi_{pq} \\ k_y^q &= \frac{2\pi}{g} q = k \sin \theta_{pq} \sin \phi_{pq} && \text{for square symmetry} \\ &= \frac{2\pi}{\sqrt{3}g} (2q - p) = k \sin \theta_{pq} \sin \phi_{pq} && \text{for hexagonal symmetry}\end{aligned}\quad (12.3)$$

where  $\theta_{pq}$  and  $\phi_{pq}$  are the corresponding spherical coordinates for the wave propagating vector  $\vec{k}$  of  $(p, q)$  order Floquet mode, and  $p, q = 0, \pm 1, \pm 2, \dots, \pm \infty$ . The  $z$  direction wave vector  $k_z^{pq}$  depends on  $p$  and  $q$ , which is real for propagating modes, pure imaginary for evanescent modes. Assuming that the impedances looking into the quantum well region from  $z = 0^-$  plane are equal to that of bulk GaAs, the modal impedances  $\eta_{pqr}^d$  and  $\eta_{pqr}$  on both sides of the metal grating for the TE and TM waves can be easily derived. The boundary condition needs the tangential electric field vectors to be continuous within the circular aperture located at  $z = 0$ , that is

$$\sum_{r=1}^2 A_{00r} \vec{\Phi}_{00r} + \sum_{p,q} \sum_{r=1}^2 R_{pqr} \vec{\Phi}_{pqr} = \sum_{p,q} \sum_{r=1}^2 T_{pqr} \vec{\Phi}_{pqr} \quad \text{within the aperture}\quad (12.4)$$

where the first summation on the left-hand side is the expansion of the incident wave with a unit power density, the second summation on the left-hand side is the expansion of the reflected

waves, the summation on the right-hand side is the expansion of the transmitted waves,  $A_{00r}$  is the magnitude of incident field component which depends on the polarization direction,  $R_{pqr}$  and  $T_{pqr}$  is the reflection coefficient and transmission coefficient of the Floquet mode, respectively.

The orthonormal waveguide modes  $\vec{\Pi}_{mnl}$  that satisfy the aperture boundary condition of the circular aperture itself other than the Floquet modes  $\vec{\Phi}_{pqr}$  are selected as the second set of linear independent basis to represent the unknown electric field distribution in the aperture. As a result, the transverse electric field vector is written as  $\sum_{p,q} \sum_r T_{pqr} \vec{\Phi}_{pqr} = \sum_{mn} \sum_l W_{mnl} \vec{\Pi}_{mnl}$ , where

$$\begin{aligned}\vec{\Pi}_{mn1}(\rho, \psi) &= \sqrt{\frac{2 - \delta_{0n}}{\pi}} \frac{1}{J_m(x'_{mn})\sqrt{(x'_{mn})^2 - m^2}} \frac{x'_{mn}}{a} \\ &\left[ \hat{\rho} \frac{m}{\frac{x'_{mn}}{a} \rho} J_m \left( \frac{x'_{mn}}{a} \rho \right) \begin{Bmatrix} \sin m\psi \\ -\cos m\psi \end{Bmatrix} + \hat{\psi} J'_m \left( \frac{x'_{mn}}{a} \rho \right) \begin{Bmatrix} \cos m\psi \\ \sin m\psi \end{Bmatrix} \right] \quad (12.5)\end{aligned}$$

and

$$\begin{aligned}\vec{\Pi}_{mn2}(\rho, \psi) &= \sqrt{\frac{2 - \delta_{0n}}{\pi}} \frac{1}{a J_{m-1}(x_{mn})} \\ &\left[ \hat{\rho} J'_m \left( \frac{x_{mn}}{a} \rho \right) \begin{Bmatrix} \cos m\psi \\ \sin m\psi \end{Bmatrix} - \hat{\psi} \frac{m}{\frac{x_{mn}}{a} \rho} J_m \left( \frac{x_{mn}}{a} \rho \right) \begin{Bmatrix} \sin m\psi \\ -\cos m\psi \end{Bmatrix} \right] \quad (12.6)\end{aligned}$$

where  $a$  is the radius of the circular aperture,  $(\rho, \psi, z)$  are the cylindrical coordinates system used,  $J_m$  is the Bessel function of the first kind with order  $m$ ,  $x_{mn}$  is the  $n$ th zero of  $J_m(x)$  and  $x'_{mn}$  is the  $n$ th zero of  $J'_m(x)$ ,  $\delta_{0n}$  equals 1 for  $n = 0$  and  $\delta_{0n}$  equals 0 for  $n \geq 1$ . Employing method of moments, a final matrix equation can be obtained as

$$[Y_{mnl}^{MNL}] [W_{mnl}] = [I_{mnl}] \quad (12.7)$$

where

$$\begin{aligned}Y_{mnl}^{MNL} &= \sum_{p,q} \sum_{r=1}^2 \left( \frac{1}{\eta_{pqr}^d} + \frac{1}{\eta_{pqr}} \right) C_{pqr}^{MNL*} C_{pqr}^{mnl} \\ C_{pqr}^{mnl} &= \int_0^{2\pi} \int_0^a \vec{\Phi}_{pqr}^*(x, y) \cdot \vec{\Pi}_{mnl}(\rho, \phi) d\rho d\phi \quad (12.8)\end{aligned}$$

both terms depend on grating geometry,  $W_{mnl}$  is the unknown coefficient, and  $I_{mnl}$  is the matrix depending on incident waves. However, it is impractical to calculate  $C_{pqr}^{mnl}$  by using numerical integral. To solve this, a hand calculated complete form of the inner product  $C_{pqr}^{mnl}$  of vector functions is found in Appendix A. The higher-order reflection coefficients are given by

$$R_{pqr} = \sum_{mn} \sum_{l=1}^2 W_{mnl} C_{pqr}^{mnl} \quad p, q \neq 0, 0 \quad (12.9)$$

The normalized power associated with  $(p, q)$ -order TM reflected wave is given by

$$\mathcal{P}_{pq2}^{refl} = \frac{|R_{pq2}|^2}{\cos \theta_{pq2}^{refl}} \quad (12.10)$$

Since  $W_{mn}$  is proportional to  $\lambda^2$  and  $C_{pqr}^{mn}$  varies as  $1/\lambda^2$  for a given  $g$ , the reflection coefficient  $R_{pqr}$  is a function of  $\lambda/g$ . Accordingly, the normalized power  $\mathcal{P}_{pq2}$  is also a function of  $\lambda/g$ . The angle between the electric field vector of the higher-order TM reflected modes  $R_{pq2}\tilde{\Phi}_{pq2}$  and the  $\hat{z}$  direction is defined as absorption angle  $\gamma_{pq2}$ , and the cosine of this angle depends on the order of diffraction and the normalized wavelength  $s (= \lambda/g)$ , which is given by

$$\begin{aligned} \cos \gamma_{pq2} &= \frac{s}{n_r} \sqrt{p^2 + q^2} && \text{for square symmetry} \\ &= \frac{s}{n_r} \frac{2}{\sqrt{3}} \sqrt{p^2 + q^2 - pq} && \text{for hexagonal symmetry} \end{aligned} \quad (12.11)$$

where  $n_r$  is the refractive index of the detector medium, and  $n_r = 3.25$  for GaAs at 77 K.

### 12.3. Results and Discussion

In the calculation, the lowest 52 waveguide modes and all the Floquet modes with  $2\pi/g\sqrt{p^2 + q^2} \leq 25(2\pi/\lambda)$  were included; the addition of more higher order modes made no noticeable change in the transmission and reflection coefficients. For simplicity we consider a unit power density EM wave impinging normally on the mesh metal grating, as shown in Fig. 12.1(c). The effective coupling is due to nonzeroth-order reflected TM Floquet modes, since the TE Floquet modes have an absorption angle  $\gamma = 90^\circ$  and the evanescent mode produce no photo-signal in intersubband absorption. In order to develop the universal relationship of the 2-D circular aperture metal grating coupler, the grating parameters are normalized to grating period  $g$ , that is, normalized wavelength ' $s = \lambda/g$ ' and normalized aperture radius ' $h = a/g$ ' to facilitate illustration.

#### A. Circular Mesh Grating with Square Symmetry

Figure 12.2 illustrates a universal plot, which shows the normalized total power of the first-order TM diffracted waves  $R_{012}\tilde{\Phi}_{012}$ ,  $R_{0-12}\tilde{\Phi}_{0-12}$ ,  $R_{-102}\tilde{\Phi}_{-102}$  and  $R_{102}\tilde{\Phi}_{102}$  as a function of  $s$  for different values of  $h$ . The first-order diffracted waves emerge when the wavelength of the IR radiation in GaAs is smaller than the grating period, that is,  $s = \lambda/g < 3.25$ . For the same reason, within the spectral range shown in Fig. 12.2, only zeroth-order far field transmitted waves  $T_{00i}\tilde{\Phi}_{00i}$  ( $i = 1, 2$ ) in the free space might be found, and all other higher-order transmitted waves were evanescent modes. This is due to the fact that free space wavelength  $\lambda$  is much greater than the grating period  $g$ . In addition, the square symmetry arrangement of the grating is indistinguishable between  $x$  and  $y$  directions.

The total normalized power of the first order diffracted waves generated by  $x$  and  $y$  components of the incident waves remain the same for different incident polarizations. In other words, the coupling of the grating is polarization independent. Figure 12.3 illustrates the normalized total power of the second-order TM diffracted components  $R_{\pm 112}\tilde{\Phi}_{\pm 112}$  and  $R_{\pm 1-12}\tilde{\Phi}_{\pm 1-12}$  as a function of  $s$  for different values of  $h$ . A comparison of Figs. 12.2 and 12.3 reveals that the grating which excites larger power of the first-order diffracted waves will prohibit the power of the second-order diffracted waves. The second-order diffracted waves emerge for  $s < 2.298$  with a total power about 50 % smaller than that of the first-order diffracted waves.

During grating fabrication process, it is noted that the grating period  $g$  remains constant, while the aperture radius may be varied. Under this process consideration, a figure relates the total power of the first-order diffracted waves to  $h = a/g$  within the most effective coupling regime  $2.8 \leq s \leq 3.2$  is plotted in Fig. 12.4. It is shown that  $a/g = 0.36$  is the ratio of aperture radius which not only is insensitive to the variation in aperture radius but also maximizes the normalized diffracted power  $P_{eff}$ . This implies that  $a/g = 0.36$  is the optimum aperture radius for the square symmetry circular aperture metal grating.

#### B. Circular Mesh Grating with Hexagonal Symmetry

Figure 12.5 shows the universal plot illustrating the normalized total power of the first-order TM diffracted waves  $R_{\pm 102}\tilde{\Phi}_{\pm 10}^{TM}$ ,  $R_{0\pm 12}\tilde{\Phi}_{0\pm 1}^{TM}$  and  $R_{\pm 1\pm 12}\tilde{\Phi}_{\pm 1\pm 1}^{TM}$  as a function of  $s$  for different values of  $h$ . The first-order diffracted waves emerge when the wavelength of the IR radiation in GaAs is smaller than  $\sqrt{3}/2g$ . The second-order TM diffracted waves consist of  $R_{\mp 1\pm 12}\tilde{\Phi}_{\mp 1\pm 1}^{TM}$ ,  $R_{\pm 1\pm 22}\tilde{\Phi}_{\pm 1\pm 2}^{TM}$ , and  $R_{\pm 212}\tilde{\Phi}_{\pm 21}^{TM}$ , which exist only for  $s < 2.298$  with a total power about one tenth of that of the first-order diffracted waves. Of course, the total normalized power of each order diffracted waves is independent of the incident polarization. Again, the figure relates the total power of the first-order diffracted waves to  $h$  within the most effective coupling regime  $2.4 \leq s \leq 2.8$  is plotted in Fig. 12.6. It is shown that  $a/g = 0.31$  is the optimum normalized radius for the hexagonal symmetry circular aperture metal grating.

By comparing Figs. 12.2 and 12.5, it is seen that a maximum coupling efficiency for the square symmetry circular aperture grating is about 1.08 times larger than that of hexagonal symmetry grating coupler. On the other hand, the latter has a 1.44 times wider available bandwidth (the band between the normalized wavelength at which the 1st and 2nd diffracted waves begin to propagate) than that of the former.

The circular aperture mesh metal grating coupler used in our experiment is the square symmetry one discussed above. For effective coupling, the period of mesh metal grating is selected in the region where  $s$  falls between 2.298 and 3.25 by using the first-order TM diffracted waves. Within this region, the  $\cos^2 \gamma$  is greater than 1/2, which is corresponding to that of a 45° angle light launching. The grating parameters are  $g = 3.3\mu\text{m}$ ,  $a = 1\mu\text{m}$ , or  $a/g = 0.6$  with the grating coupling characteristic curve shown in Fig. 11.7, which is obtained by multiplying the grating period  $g = 3.3\mu\text{m}$  to the coordinate of curve  $a/g = 0.6$  in Fig. 12.2. The cut-off wavelength of the grating is  $10.725\mu\text{m}$ . The grating coupled GaAs QWIP used in the present analysis is composed of 20-period GaAs multiquantum wells with a well width of  $40\text{\AA}$  and a dopant density  $1.2 \times 10^{18} \text{ cm}^{-3}$  and an  $\text{Al}_{0.25}\text{Ga}_{0.75}\text{As}$  barrier thickness of  $480\text{\AA}$ . In this QWIP, the 2-D electrons in the continuous band can move freely in the direction perpendicular to the quantum well layers, which in turn produce an electric current through the QWIP.

The responsivity  $R_I$  for the QWIP can be calculated by

$$R_I = \left[ \mathcal{P}_{eff}(1 - e^{-\alpha l}) \right] g_o \frac{\lambda}{1.24} \quad (12.12)$$

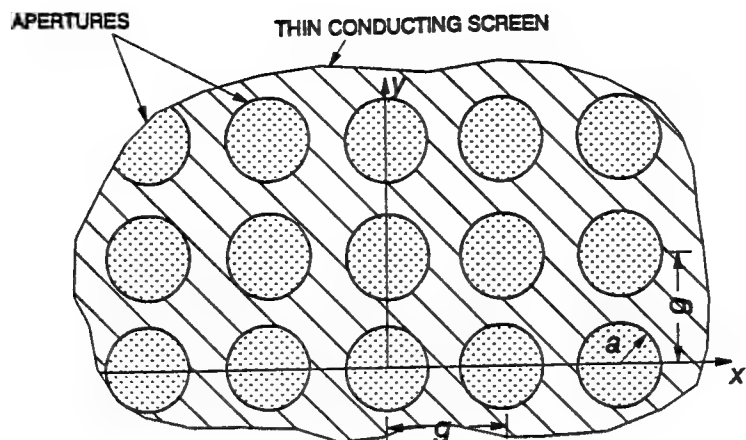
where  $\mathcal{P}_{eff}$  is the effective coupling power of the IR radiation, and  $l$  is the total length of the doped quantum wells, and the terms in the square brackets is the expression of quantum efficiency  $\eta$ . In the present case,  $\mathcal{P}_{eff}$  is the normalized total power of the first order diffracted waves, and  $l = (40\text{\AA}/\text{period}) \cdot (20 \text{ periods}) = 800\text{\AA}$ . The optical gain  $g_o$  is estimated by the measured results of a 45° angle edge detector at bias  $V_b = -1V$ . The intersubband absorption constant is given by

$$\alpha = |M|^2 F \cos^2 \gamma \quad (12.13)$$

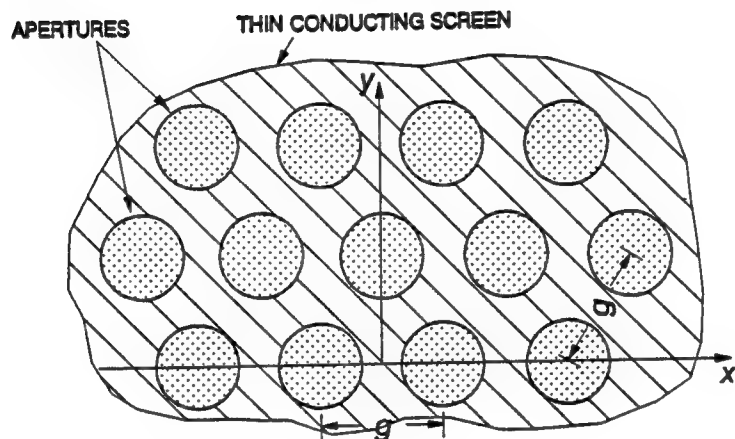
where  $\gamma$  is the absorption angle given in Eq. (12.11) or Fig. 12.7.  $F$  is a function of wavelength  $\lambda$  and the parameters of a specific quantum well structure;  $M$  is the envelop matrix element, and a 60% continuous band split is assumed. A comparison between the theoretical calculation and the experimental data of responsivity is illustrated in Fig. 12.8. As shown in this figure, the solid line represents the theoretical responsivity of the grating with parameters  $g = 3.3\mu\text{m}$  and  $a = 1\mu\text{m}$ , which results in a 2.7 times enhancement over that of 45° edge detector. The responsivity of the grating with parameters  $g = 4\mu\text{m}$  and  $a = 1.1\mu\text{m}$  is also illustrated in Fig. 12.8, which shows that the grating having normalized wavelength  $2.298 \leq s \leq 3.25$  is a more effective grating coupler. Furthermore, by choosing a grating of  $g = 3.3\mu\text{m}$ ,  $a = 1.2\mu\text{m}$ , i.e.  $a/g = 0.36$ , a greater responsivity enhancement can be obtained.

In conclusion, we have performed a detailed analysis and numerical calculations of a 2-D circular aperture mesh metal grating coupled GaAs QWIP. It is shown that for a given QWIP

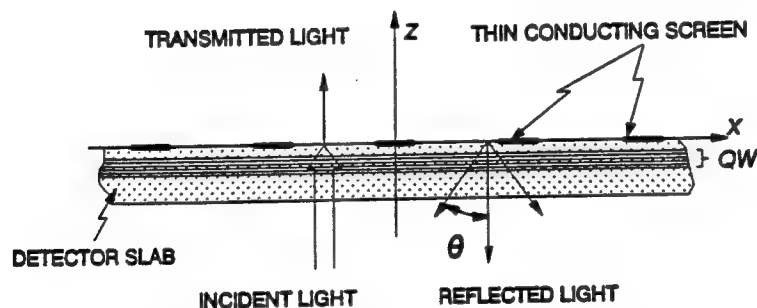
material, the total power and the diffracted angle of the higher-order TM diffracted waves depend on two normalized parameters  $s = \lambda/g$  and  $h = a/g$ , which are functions of wavelength and grating dimension. The optimum grating period and aperture radius can be obtained for any specific infrared spectrum by scaling the universal curves shown in Fig. 12.2 and Fig. 12.4. Moreover, the responsivity for a 2-D metal grating coupled QWIP can be calculated from these universal plots.



(a)



(b)



(c)

Figure 12.1. Top view of a circular mesh metal grating coupler (a) with square symmetry and (b) hexagonal symmetry. (c) Cross sectional view of a circular mesh metal grating with normal incident back illumination.  $g$  is the grating period and  $a$  is the radius of circular aperture.

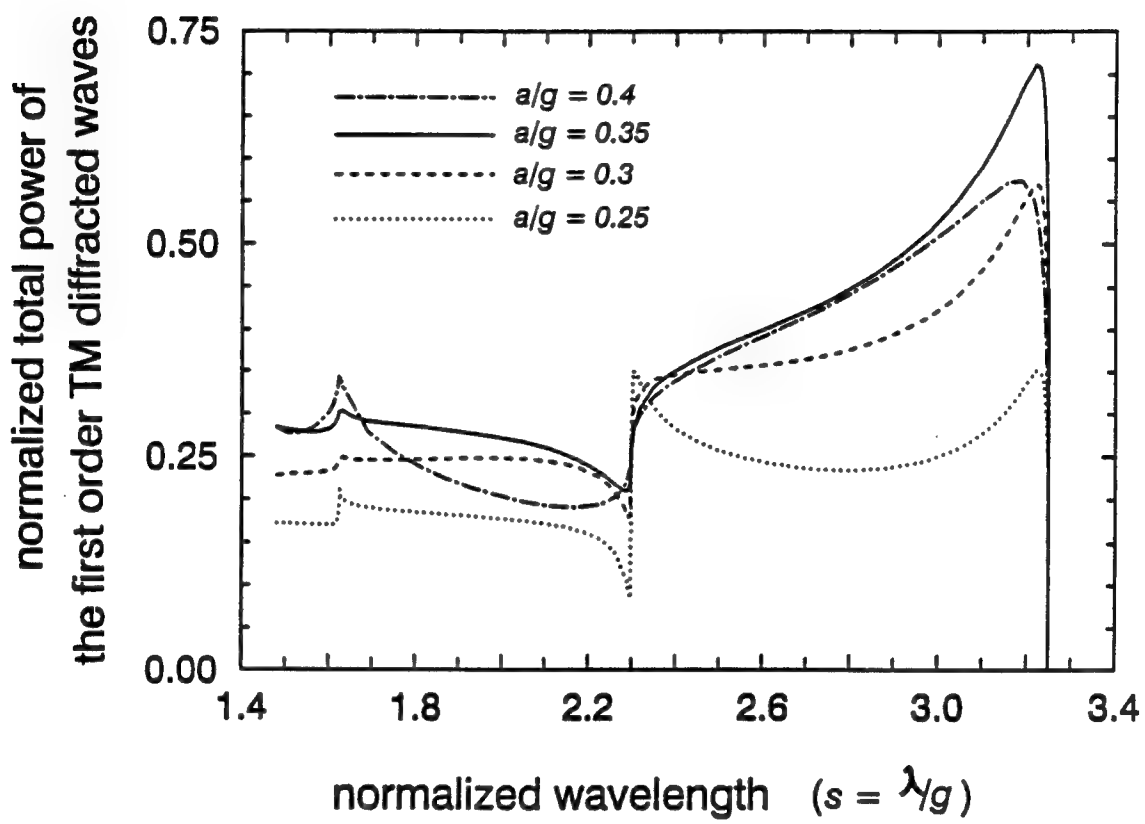


Figure 12.2. Normalized total power of the first-order diffracted waves versus normalized wavelength ( $s = \lambda/g$ ) for a circular mesh metal grating coupler with square symmetry and different values of  $h = a/g$ .

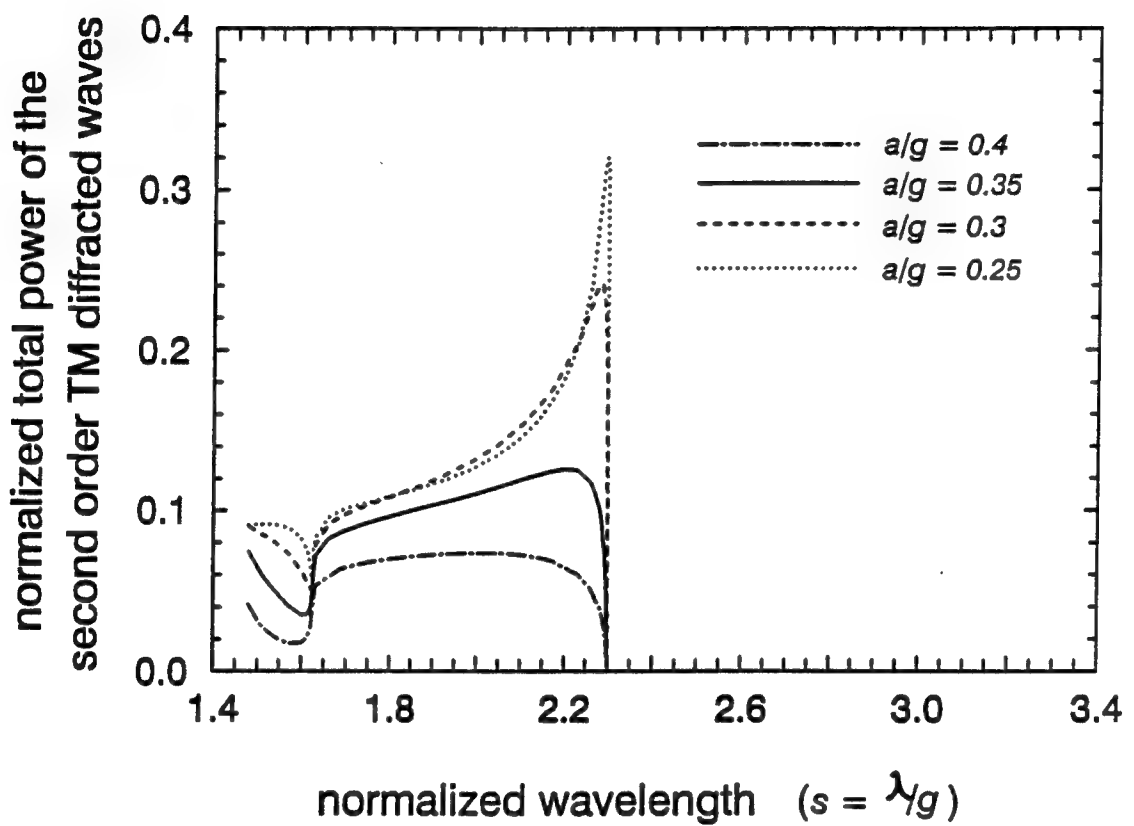


Figure 12.3. Normalized total power of the second-order diffracted waves versus normalized wavelength ( $s = \lambda/g$ ) for a circular mesh metal grating coupler with square symmetry and different values of  $h = a/g$ .

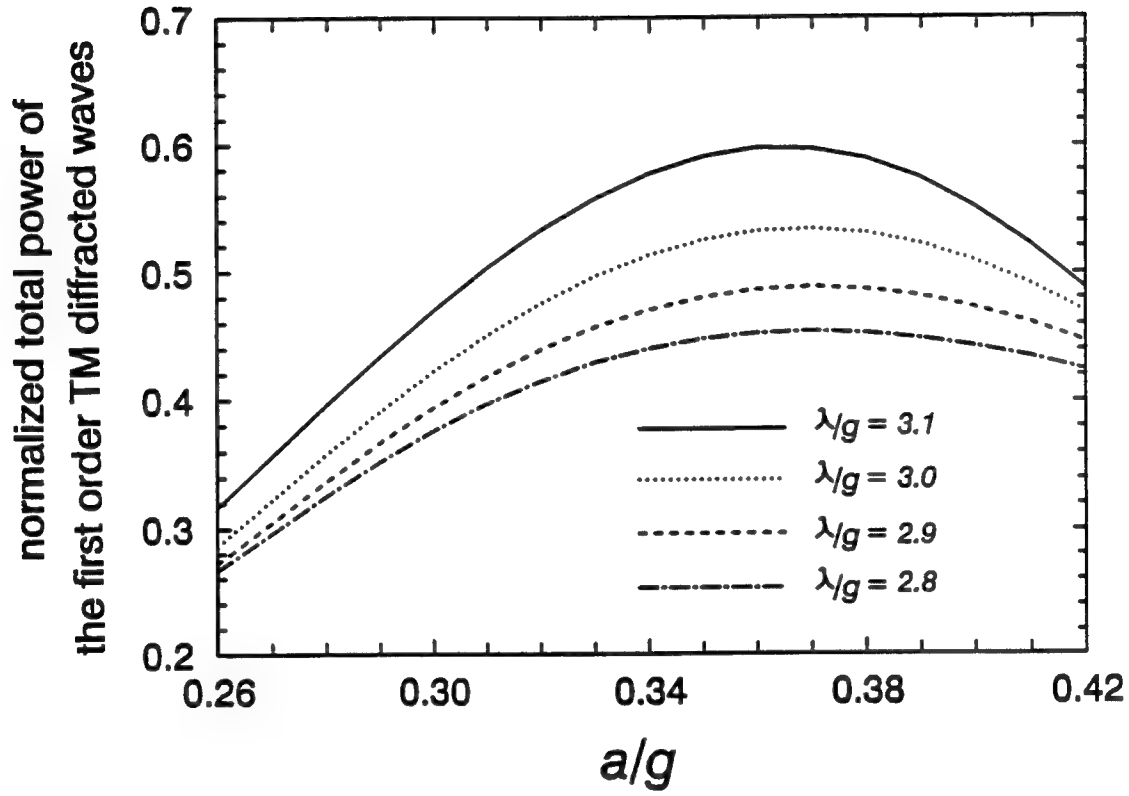


Figure 12.4. Normalized total power of the first-order diffracted waves versus normalized wavelength ( $s = \lambda/g$ ) for a circular mesh metal grating coupler with square symmetry structure and different values of normalized wavelength,  $s$ .

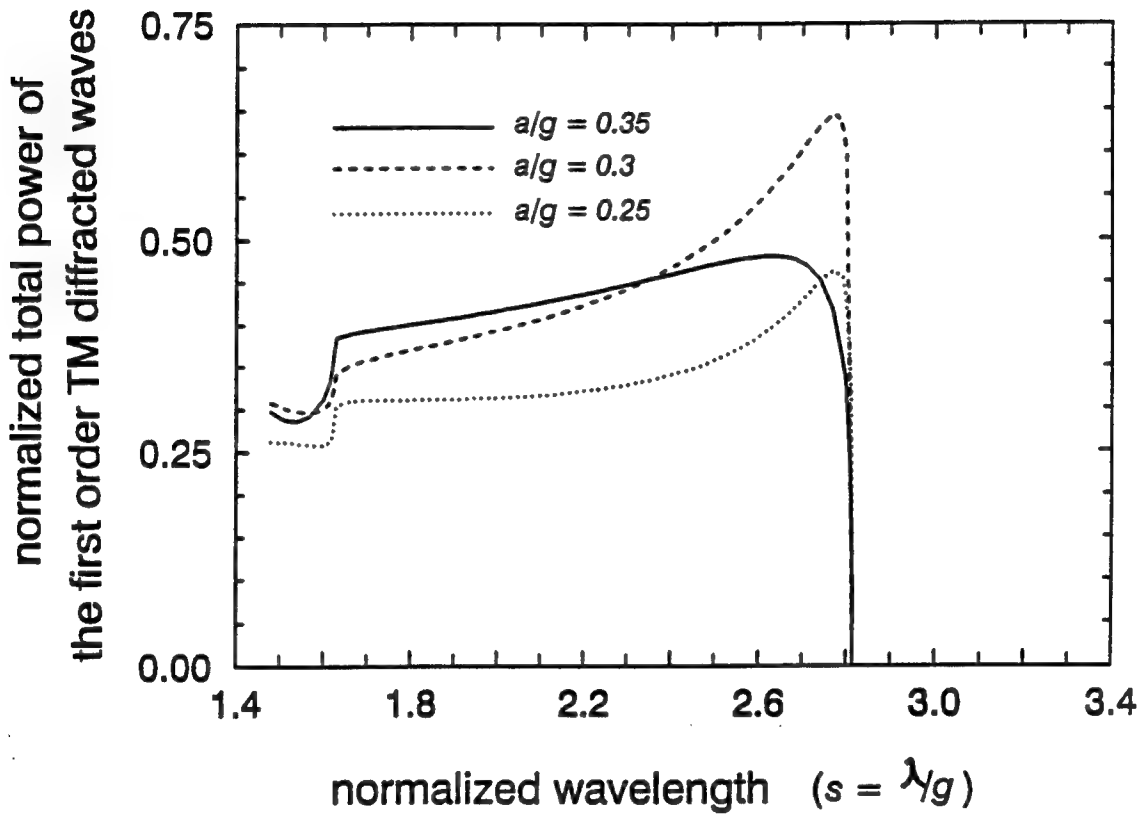


Figure 12.5. Normalized total power of the first-order diffracted waves versus normalized wavelength ( $s = \lambda/g$ ) for a circular mesh metal grating coupler with hexagonal symmetry structure and different values of  $h = a/g$ .

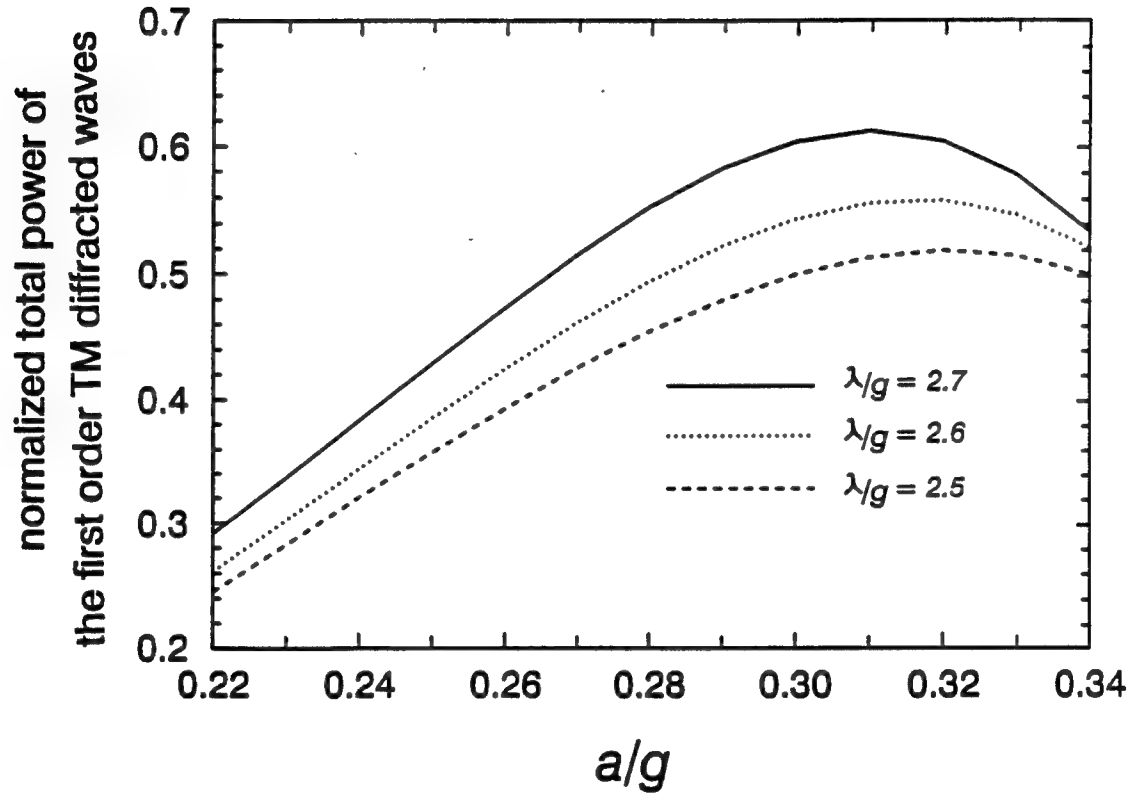


Figure 12.6. Normalized total power of the first-order diffracted waves versus normalized wavelength ( $s = \lambda/g$ ) for a circular mesh metal grating coupler with hexagonal symmetry structure and different values of normalized wavelength,  $s$ .

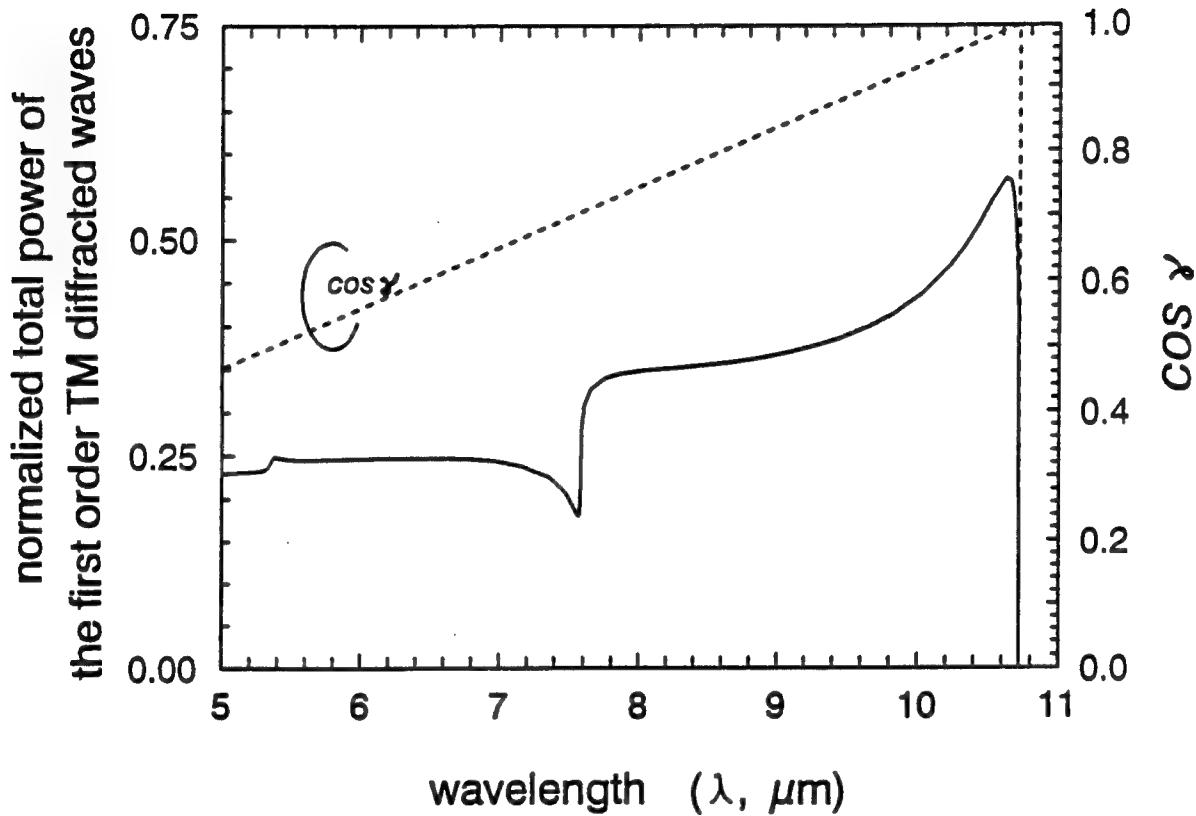


Figure 12.7. Normalized total power of the first-order diffracted waves and  $\cos \gamma$  versus wavelength for a 2-D square mesh metal grating with  $g = 3.3 \mu\text{m}$  and  $a = 2 \mu\text{m}$ .

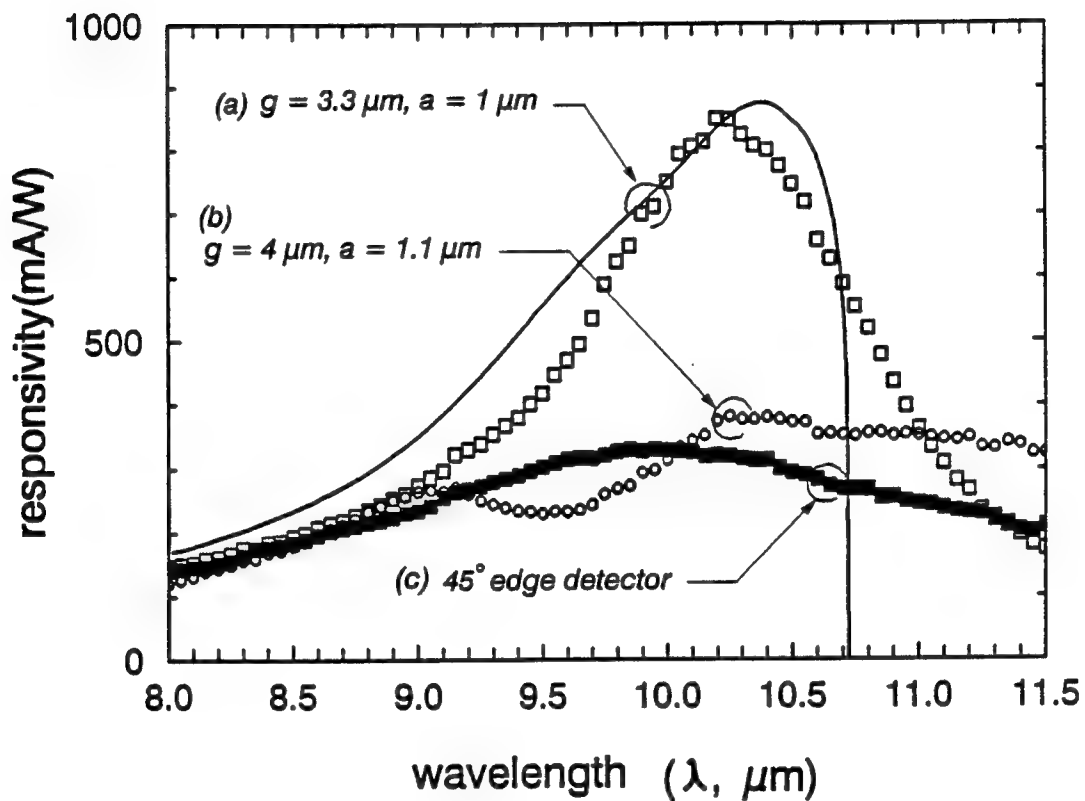


Figure 12.8. Spectral responsivity of a GaAs QWIP for a circular mesh metal grating coupler (a) and (b), and (c) 45° edge illuminated. Solid line is the calculated value for square symmetry structure at  $V_b = -1$  V.

## **Part III**

### **P-type Strained-layer QWIPs**

## 13. PHYSICS OF P-TYPE STRAINED-LAYER QUANTUM WELL INFRARED PHOTODETECTORS

### 13.1. Introduction

Quantum well infrared photodetectors (QWIPs) using n-type GaAs/AlGaAs and InGaAs/InAlAs material systems for the  $3 - 5 \mu\text{m}$  mid-wavelength infrared (MWIR) and  $8 - 14 \mu\text{m}$  long-wavelength infrared (LWIR) atmospheric transmission windows have been extensively studied in recent years [69]. With low electron effective mass and high electron mobility, the n-type GaAs and InGaAs QWIPs offer excellent IR detection properties. However, quantum mechanical selection rule for the intersubband transition requires that the radiation electric field has a component perpendicular to the quantum well plane in order to induce intersubband absorption in the quantum wells. As a result, for n-type QWIPs, it is necessary to use planar metal or dielectric grating structures for coupling the normal incident IR radiation into absorbable angles [47, 83, 84].

P-type QWIPs using valence intersubband transitions have been demonstrated in the lattice-matched GaAs/AlGaAs and InGaAs/InAlAs material systems [107, 108, 109, 110]. Due to band mixing between the light-hole and heavy-hole states, the normal incident illumination is allowed for the intersubband transition in p-type QWIPs. In general, the intersubband transitions under normal incident radiation in p-type quantum wells are induced by the linear combination of P-like valence-band Bloch states that provides a nonzero coupling between these components and the normal radiation field. The strong mixing between the light- and heavy-hole states for  $\mathbf{k} \neq 0$  greatly enhances the normal incidence intersubband absorption. However, in the unstrained lattice-matched quantum well systems, these intersubband transitions occur between the heavy-hole ground state and the upper heavy-hole excited states. Due to large heavy-hole effective mass, weak absorption and low responsivity are expected in the unstrained p-QWIPs.

Strain effects induced by lattice-mismatch can modify the energy bandgap of the quantum well and superlattice, split the degeneracy of the heavy- and light-hole bands at the center of Brillouin Zone (BZ) as shown schematically in Fig. 13.1, and modify carrier transport properties [111]. Matthews and Blakeslee [112] reported that a high quality of coherently strained-layers can be grown if the individual layer thickness of the system is within its critical thickness. Osbourn

[8, 113] demonstrated that coherently strained-layer superlattices (SLS) can be used for a wide variety of novel optoelectronic devices such as lasers, modulators, enhanced-mobility field effect transistors, light-emitting diodes, and photodetectors.

### 13.2. Coherent Strained-layers

When a biaxial strain is applied between two thin superlattice layers, the pseudomorphic or coherent heterointerfaces can be obtained if the individual layer thickness is within the critical thickness. As a result, the misfit due to the lattice constant mismatch is totally accommodated by the elastic strain. The biaxial strain can be either compressive or tensile depending on the lattice constants and layer growth direction. Based on the force balance model [112], the equilibrium critical layer thickness  $h_c$  for an epilayer with lattice constant  $a$  grown on a substrate with a lattice constant  $a_s$  is given by

$$h_c = \left( \frac{a}{\sqrt{2}\delta_o} \right) \frac{1 - \nu \cos^2 \Theta}{8\pi(1 + \nu) \cos \alpha} \left[ 1 + \ln(h\sqrt{2}/a) \right] \quad (13.1)$$

where  $h$  is the epilayer thickness,  $\Theta$  is the angle between dislocation line and Burges' vector,  $\alpha$  is the angle between slip direction and the layer plane direction,  $\delta_o$  is the lattice-mismatch or in-plane strain,  $\delta_o = (a_s - a)/a$ , ( $\delta_o > 0$  for tensile strain,  $\delta_o < 0$  for compressive strain), and  $\nu$  is the Poisson ratio,  $\nu = -C_{12}/C_{11}$ .  $C_{ij}$  are the elastic constants which can be found in reference [114].

For a coherent strained multiple layer QWIP structure, the multilayers can also be grown on a substrate having a lattice constant  $a_s$  with misfit-free quality if  $a_s = a_{||}$ , where  $a_{||}$  is the equilibrium in-plane lattice constant for the multi-layers. It can be calculated by [112]

$$a_{||} = \frac{a_1 \xi_1 L_1 + a_2 \xi_2 L_2}{L_1 \xi_1 + L_2 \xi_2}, \quad (13.2)$$

where  $a_{1,2}$  and  $L_{1,2}$  are the individual layer lattice constant and thickness, respectively.  $\xi$  is the shear modulus given by  $\xi = (C_{11} + C_{12} - 2C_{12}^2/C_{11})$ . In the case  $a_{||} \neq a_s$ , the coherently strained-layer superlattice structure is no longer in equilibrium with the substrate. For instance, if the lattice constant of the barrier layers is equal to that of substrate, then the strain will be entirely accommodated in the well layers with no strain in the barrier layers. However, Hull et al. [115] showed that, even though  $a_{||} \neq a_s$ , if the individual layer thickness in the superlattice is less than its critical thickness, the loss of coherence only occurs at the interface between whole superlattice and substrate, and whole superlattice still remains coherent itself. If the coherently strained-layer structure of a QWIP is grown along [100] direction, the components of the strain tensor [ $\epsilon$ ] for layers are reduced to

$$\epsilon_{xx} = \epsilon_{yy} = \epsilon_{||} = \frac{a_s - a_{||}}{a_{||}}; \quad (13.3)$$

$$e_{zz} = -e_{\parallel} \left( \frac{2C_{12}}{C_{11}} \right); \quad (13.4)$$

$$e_{xy} = e_{yz} = e_{zx} = 0. \quad (13.5)$$

### 13.3. k.p Model

In order to fully describe the optical and electronic properties (such as energy bandgap, sub-band energy level splitting, intersubband transition etc.,) for a coherently strained-layer structure, the multiband effective-mass **k.p** model based on the perturbation approximation should be used. In the **k.p** model, the interactions of S-P type coupling among conduction (C), heavy-hole (HH), light-hole (LH), and spin-orbit (SO) states combined with spinorlike coupling are taken into consideration to derive the band structures, thus, resulting in  $8 \times 8$  **k.p** Hamiltonian and momentum matrix elements. Under the perturbation approximation, a set of wave functions of  $S_{1/2}$ : ( $|1/2, \pm 1/2\rangle_c$ ),  $P_{3/2}$ : ( $|3/2, \pm 3/2\rangle$ ;  $|3/2, \pm 1/2\rangle$ ), and  $P_{1/2}$ : ( $|1/2, \pm 1/2\rangle$ ) are used as the unperturbed and unstrained basis in the  $|J, m_J\rangle$  representation [116].  $m_J = \pm 1/2$  represent light-particle states (either for electron or for LH), while  $m_J = \pm 3/2$  denote heavy-particle states (for HH). When a larger bandgap exists such as in InGaAs and GaAs layers compared with the elements of the **k.p** matrix between the conduction band and valence band states, a reduced  $6 \times 6$  **k.p** Hamiltonian can be roughly used to depict the P-like properties of the coherently strained-layers by considering the S-like conduction band states as a perturbation. The wave functions of the coherently strained-layer superlattice at the zone center (i.e.  $\mathbf{k} = 0$ ) are given by [117],

$$|3/2, \pm 3/2\rangle \quad \text{HH states} \quad (13.6)$$

$$\gamma|3/2, \pm 1/2\rangle + \beta|1/2, \pm 1/2\rangle \quad \text{LH states} \quad (13.7)$$

$$-\beta|3/2, \pm 1/2\rangle + \gamma|1/2, \pm 1/2\rangle \quad \text{SO states} \quad (13.8)$$

where  $\gamma$  and  $\beta$  are constants depending on the strain parameters. It is seen that the heavy-hole states  $|3/2, \pm 3/2\rangle$  are still decoupled with other valence states even under the biaxial strain at  $\mathbf{k} = 0$ , while light-hole states and spin-orbit split-off states are coupled at  $\mathbf{k} = 0$ . However, HH, LH, and SO states are variedly mixed [118, 119] in the coherently strained-layer superlattice if  $\mathbf{k} \neq 0$ . This kind of mixtures (between the states with different  $m_J$ 's) is due to boundary conditions across the interface of the quantum well layers. From the **k.p** matrix, the interaction between the different  $m_J$ 's states is proportional to the transverse components of the wave vector (i.e.  $k_{x,y}$ ), so that HH-states are decoupled when  $k_{x,y} = 0$ . Note that  $k_{x,y}$  are conserved across the interfaces since interface potential depends only on  $z$ , the quantum well growth direction. The band mixing can be significant if the  $\Gamma$ -bandgap is small (e.g., GaAs and InGaAs) and if LH- and SO-bands

involved in the transition have a large  $k_z$  [118].

### 13.4. Strain Effects

From the elasticity theory [111], the biaxial strain can be divided into two independent components, one is isotropic or hydrostatic component and the other is anisotropic or shear uniaxial component. The strain-induced energy shifts,  $\Delta E_H$  due to the hydrostatic component and  $\Delta E_U$  due to the shear uniaxial component, can be expressed, respectively, by [120]

$$\Delta E_H = 2V_{cd} \frac{C_{11} - C_{12}}{C_{11}} \delta_o \quad (13.9)$$

$$\Delta E_U = V_{sd} \frac{C_{11} + 2C_{12}}{C_{11}} \delta_o \quad (13.10)$$

where  $V_{cd}$  and  $V_{sd}$  are the conduction-band deformation potential and shear deformation potential, respectively.

The energy bandgaps due to the strain for the heavy-hole, light-hole, and spin-orbit states at  $\mathbf{k} = 0$  are given by [120]

$$E_{HH} = E_{go} + \Delta E_H - \Delta E_U \quad (13.11)$$

$$E_{LH} = E_{go} + \Delta E_H + \Delta E_U - \frac{(\Delta E_U)^2}{2\Delta_o} + \dots \quad (13.12)$$

$$E_{SO} = E_{go} + \Delta_o + \frac{(\Delta E_U)^2}{2\Delta_o} + \dots \quad (13.13)$$

where  $E_{go}$  is the unstrained bandgap and  $\Delta_o$  is the spin-orbit splitting energy. From the above equations, it can be shown that both the heavy-hole and light-hole states can be shifted as a result of the biaxial strain and spin-orbit splitting energy.

The calculation of both intersubband and interband transitions in a p-type strained-layer QWIP requires the use of  $6 \times 6$  Hamiltonian which includes the above  $\mathbf{k.p}$  Hamiltonian [117] and the strain Hamiltonian [111]. The strain and spin-orbit coupling terms do not lift the spin degeneracy, and hence the  $6 \times 6$  Hamiltonian matrix can be factorized into two  $3 \times 3$  irreducible matrices. In order to simplify the problem without lost correct prediction, we assume Fermi distribution function is equal to one for the confined ground state and zero for the excited states in equilibrium. The absorption coefficient for the intersubband (or interband) transition between the initial ground state  $i$  and the final continuum states  $f$  is given by [121]

$$\alpha_i(\omega) = \sum_f \frac{4\pi^2 e^2}{n_r c m_o^2 \omega} \int_{BZ} \frac{2d\mathbf{k}}{(2\pi)^3} \left[ (f_i - f_f) |\hat{\epsilon} \cdot \mathbf{P}_{i,f}|^2 \frac{\Gamma/2\pi}{[\Delta_{i,f}(\mathbf{k}) - \hbar\omega]^2 + \Gamma^2/4} \right] \quad (13.14)$$

where  $n_r$  is the refractive index in the quantum well,  $m_e$  is the free electron mass,  $\Delta_{i,f}$  is the energy difference between the initial state  $i$  (with energy  $E_i(\mathbf{k})$ ) and the final state  $f$  (with energy  $E_f(\mathbf{k})$ ),  $\hat{\epsilon}$  and  $\omega$  are the unit polarization vector and the frequency of the incident IR radiation,  $f_i$  (or  $f_f$ ) is the Fermi distribution function of initial (or final) state,  $\Gamma$  is the full width of level broadening ( $\sim \hbar/\tau_{i,f}$ ,  $\tau_{i,f}$  lifetime between states  $i$  and  $f$ ).  $|\hat{\epsilon} \cdot \mathbf{P}_{i,f}|$  is the optical transition elements between the quantum well valence ground subband states  $i$  and the continuum subband states  $f$  in HH-, LH-, and SO-bands, and can be derived from two  $3 \times 3$   $\mathbf{k.p}$  matrix elements (see Appendix B). The optical transition elements show the selection rule of the intersubband transition for the p-type coherently strained-layer quantum well. For the same type intersubband transitions such as  $\text{HH} \leftrightarrow \text{HH}$ ,  $\text{LH} \leftrightarrow \text{LH}$ , and  $\text{SO} \leftrightarrow \text{SO}$ , the oscillator strength is proportional to either  $\mathbf{k}_\perp$  (or  $k_z$ ) or  $\mathbf{k}_\parallel$  (or  $k_{x,y}$ ). For the mixing type interband transitions such as  $\text{HH} \leftrightarrow \text{LH}$ ,  $\text{HH} \leftrightarrow \text{SO}$ , and  $\text{LH} \leftrightarrow \text{SO}$ , each polarization of the normal incident light can contribute to the intersubband absorption.

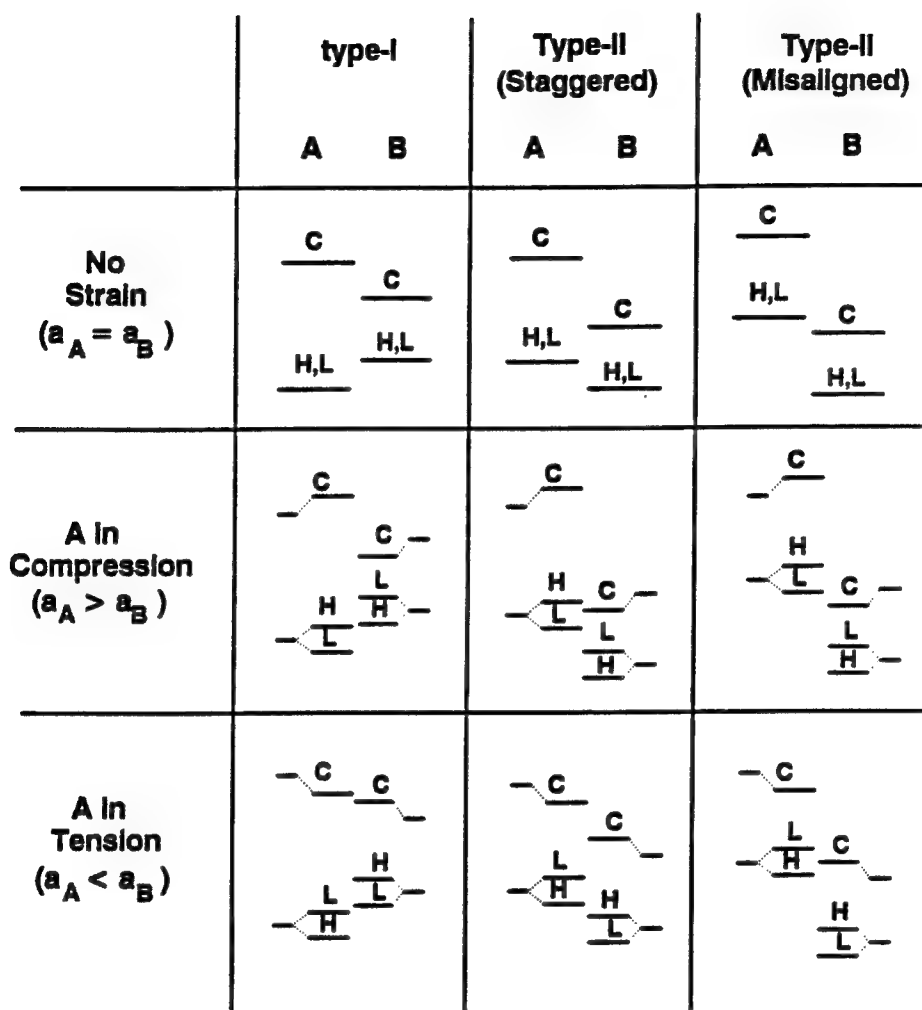


Figure 13.1. Schematic illustration of the band-edge lineup in type-I and type-II superlattice. A and B indicate two semiconductor thin layers in the superlattice basis. (C, H, and L indicate conduction, heavy-hole, and light-hole bands, respectively.)

## 14. A P-TYPE TENSILE STRAINED-LAYER InGaAs/InAlAs QUANTUM WELL INFRARED PHOTODETECTOR

A p-type tensile strained-layer (PTSL)  $\text{In}_{0.3}\text{Ga}_{0.7}\text{As}/\text{In}_{0.52}\text{Al}_{0.48}\text{As}$  quantum well infrared photodetector (QWIP) grown on semi-insulating (100) InP substrate with MBE technique for 8–14  $\mu\text{m}$  detection has been developed. This PTSL-QWIP shows background limited performance (BLIP) for  $T \leq 100$  K, which is the highest BLIP temperature ever reported for the QWIP family [122].

### 14.1. Inversion between Heavy- and Light-hole States

Due to the lattice mismatch between the InP substrate and the  $\text{In}_{0.3}\text{Ga}_{0.7}\text{As}$  quantum well, a biaxial tensile strain is created in the quantum well while no strain exists in the barrier layer [123, 124]. The tensile strain in the wells can push the light-hole levels upward and pull the heavy-hole levels downward. As a result, the ground heavy-hole and light-hole states are inverted for a certain strain and quantum well thickness, and the light-hole state becomes the ground state in the quantum well. Thus for the PTSL-QWIP, the intersubband transition is from the populated light-hole ground state to the heavy-hole continuum states. Since the light-hole has a small effective mass, the optical absorption and photoresponsivity in the PTSL-QWIP can be greatly enhanced by using this new approach. In fact, the calculated absorption coefficient by Xie et al. [123] for the  $\text{In}_{0.3}\text{Ga}_{0.7}\text{As}/\text{In}_{0.52}\text{Al}_{0.48}\text{As}$  system with a 60 Åwell width was found to be  $8,500 \text{ cm}^{-1}$  at  $\lambda_p = 12 \mu\text{m}$ .

### 14.2. Experiments

The normal incidence p-type tensile strained-layer  $\text{In}_{0.3}\text{Ga}_{0.7}\text{As}/\text{In}_{0.52}\text{Al}_{0.48}\text{As}$  QWIP uses the intersubband transition scheme between the confined ground light-hole state to the continuum heavy hole states. Figure 14.1 shows the energy band diagram for the PTSL-QWIP. The band bending may be attributed to the dopant migration effect occurred during the layer growth. The PTSL-QWIP structure was grown on a (100) semi-insulating (SI) InP substrate by using MBE technique. The PTSL-QWIP structure consists of 20 periods of 4-nm Be-doped  $\text{In}_{0.3}\text{Ga}_{0.7}\text{As}$  quantum well with a dopant density of  $1 \times 10^{18} \text{ cm}^{-3}$  separated by 45-nm  $\text{In}_{0.52}\text{Al}_{0.48}\text{As}$  undoped barrier layer. A 0.3- $\mu\text{m}$  cap layer and a 1- $\mu\text{m}$  buffer layer of Be-doped  $\text{In}_{0.53}\text{Ga}_{0.47}\text{As}$  with a dopant density of

$2 \times 10^{18} \text{ cm}^{-3}$  were grown for the top and bottom ohmic contacts. The contact and barrier layers are lattice-matched to the InP substrate, and the quantum well layer is in biaxial tension with a lattice mismatch of approximately 1.5 %. In order to measure the spectral responsivity and dark current of this PTSL-QWIP, a  $200 \times 200 \mu\text{m}^2$  mesa structure was created by using the chemical etching process. The Au/Zn alloy was thermally evaporated onto the QWIP mesas with a film thickness of 1500 Å, followed by annealing at  $480^\circ\text{C}$  for 3 minutes to obtain stable and low contact resistance.

Figure 14.2 shows the measured dark current density and 300-K background photocurrent density for the PTSL-QWIP. The device shows asymmetric dark current characteristic under positive and negative bias, which is attributed to the band bending due to dopant migration effect as shown in Fig. 14.1. The dark current density was found to be equal to  $7 \times 10^{-8} \text{ A/cm}^2$  at  $V_b = 2 \text{ V}$  and  $T = 77 \text{ K}$ . In fact, this PTSL-QWIP is under background limited performance (BLIP) with field of view (FOV)  $90^\circ\text{C}$  for  $V_b \leq 3 \text{ V}$  and  $T \leq 100 \text{ K}$ , which is believed to be the highest BLIP temperature ever observed in a QWIP. The ultra low dark current density observed in the PTSL-QWIP can be attributed to the following factors, (1) the dark current is dominated by the thermionic emission from the ground light-hole state and transports through the heavy-hole continuum states above the barrier. The thermionic emission current is drastically reduced due to the increase of the effective barrier height by the strain in the quantum well, (2) since the bandwidth of the heavy-hole continuum states is very narrow ( $\sim 10 \text{ meV}$  compared to the unstrained p-type QWIP of about 25 meV), a reduction of dark current by about ten times is expected, (3) due to large heavy-hole effective mass and short heavy-hole lifetime in the continuum states (i.e., lower photoconductive gain) the dark current can be further reduced, and (4) lower thermally generated hole density also contributes to a lower dark current.

The responsivity of the QWIP under normal incidence illumination was measured as a function of temperature, bias voltage, and wavelength using a globar and automatic PC-controlled single-grating monochromator system. The measured photocurrents versus wavelength for both positive and negative biases are shown in Fig. 14.3 (a) and (b), respectively. A peak response wavelength was found to be at  $\lambda_p = 8.1 \mu\text{m}$ , which is attributed to the intersubband transition between the confined ground light-hole state  $E_{\text{LH}1}$  to the continuum heavy-hole band states  $E_{\text{HH}3}$  as illustrated in Fig. 14.1. The cutoff wavelength for this QWIP was found to be  $8.8 \mu\text{m}$  with a spectral bandwidth of  $\Delta\lambda/\lambda_p = 12 \%$ . Since two other heavy-hole bound excited states are confined inside the quantum wells with very low tunneling probability off the thicker barrier layer, no photoresponse from these two heavy-hole states was detected. The responsivities for the PTSL-QWIP were calibrated by

using a standard pyroelectric detector and lock-in amplifier technique. Responsivities of 34 mA/W at  $V_b = 4$  V and 51 mA/W at  $V_b = -4$  V were obtained for this PTSL-QWIP. The maximum BLIP detectivity  $D_{BLIP}^*$  at  $\lambda_p = 8.1 \mu\text{m}$  was found to be  $5.9 \times 10^{10} \text{ cm} \cdot \sqrt{\text{Hz}}/\text{W}$  (with a responsivity  $R_A = 18 \text{ mA/W}$ ) at  $V_b = 2$  V, FOV = 90° and T = 77 K. The quantum efficiency for the PTSL-QWIP was estimated to be 18 % from the responsivity measurement with a photoconductive gain  $g = 0.015$ .

When Johnson noise and readout circuit noise are ignored, %BLIP for positive and negative bias are evaluated by using

$$\%BLIP \approx \frac{i_{nb}}{(i_{nb}^2 + i_{nd}^2)^{1/2}} \quad (14.1)$$

where  $i_{nb,nd}$  are the 300 K background photocurrent noise and dark current noise, respectively. The insets in Fig. 14.3 show the calculated %BLIP results for the positive and negative biases. A nearly full BLIP detection was achieved at bias voltage between -2 V and 5 V. As a result of the full BLIP detection in our PTSL-QWIP, the noise equivalent temperature difference ( $\text{NE}\Delta\text{T}$ ) in the focal plane array imaging applications is expected to be significantly improved.

#### 14.3. Conclusions

We have demonstrated a new normal incidence p-type tensile strained-layer InGaAs/InAlAs QWIP with BLIP for  $V_b \leq 3$  V and  $T \leq 100$  K. The BLIP detectivity for the PTSL-QWIP was greatly enhanced by the biaxial tensile strain introduced in the wells leading to the inversion of heavy- and light-hole subbands in the well. By further optimizing the quantum well dopant density, biaxial strain strength, and structure parameters, high performance PTSL-QWIPs can be fabricated for large-area infrared focal plane array image sensor system under BLIP for  $T \leq 100$  K.

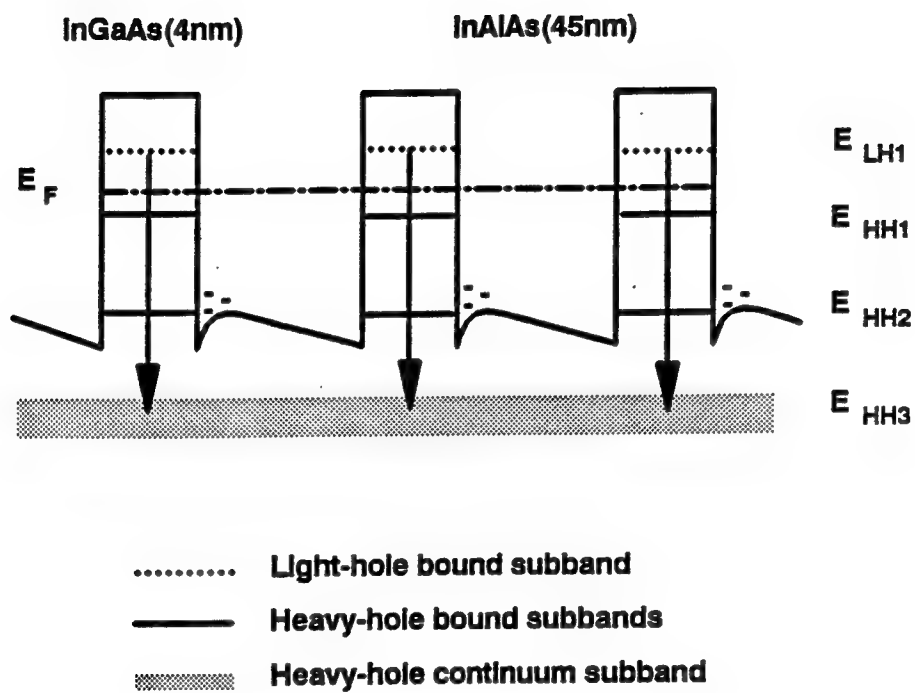


Figure 14.1. Schematic energy band diagram for the p-type tensile strained-layer InGaAs/InAlAs QWIP with consideration of band bending effect. The subband energy levels were calculated to be  $E_{LH1} \approx 42$  meV,  $E_{HH1} \approx 78$  meV,  $E_{HH2} \approx 135$  meV, and  $E_{HH3} \approx 198$  meV from the InGaAs quantum well band edge.

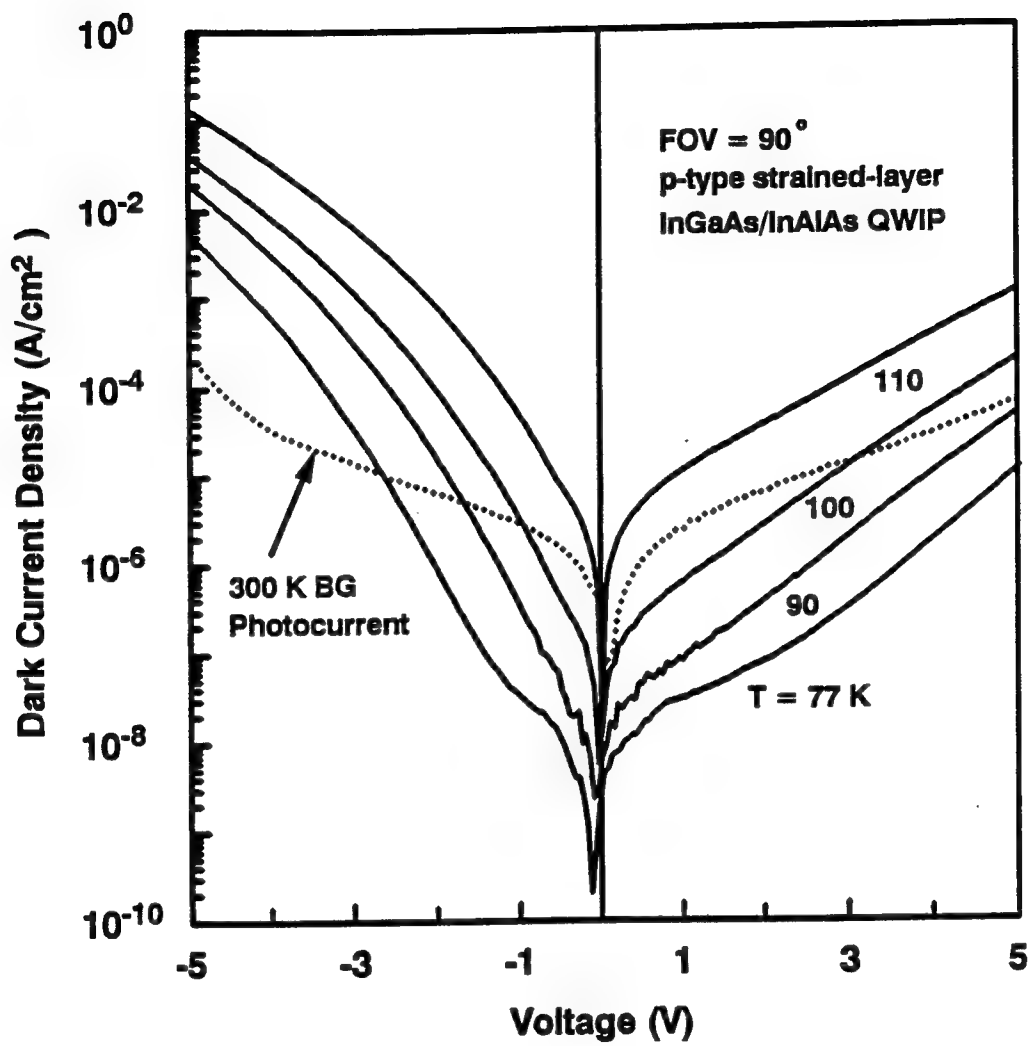


Figure 14.2. Measured dark current density and 300-K background photocurrent density for the PTSL-QWIP at  $\text{FOV} = 90^\circ$ .

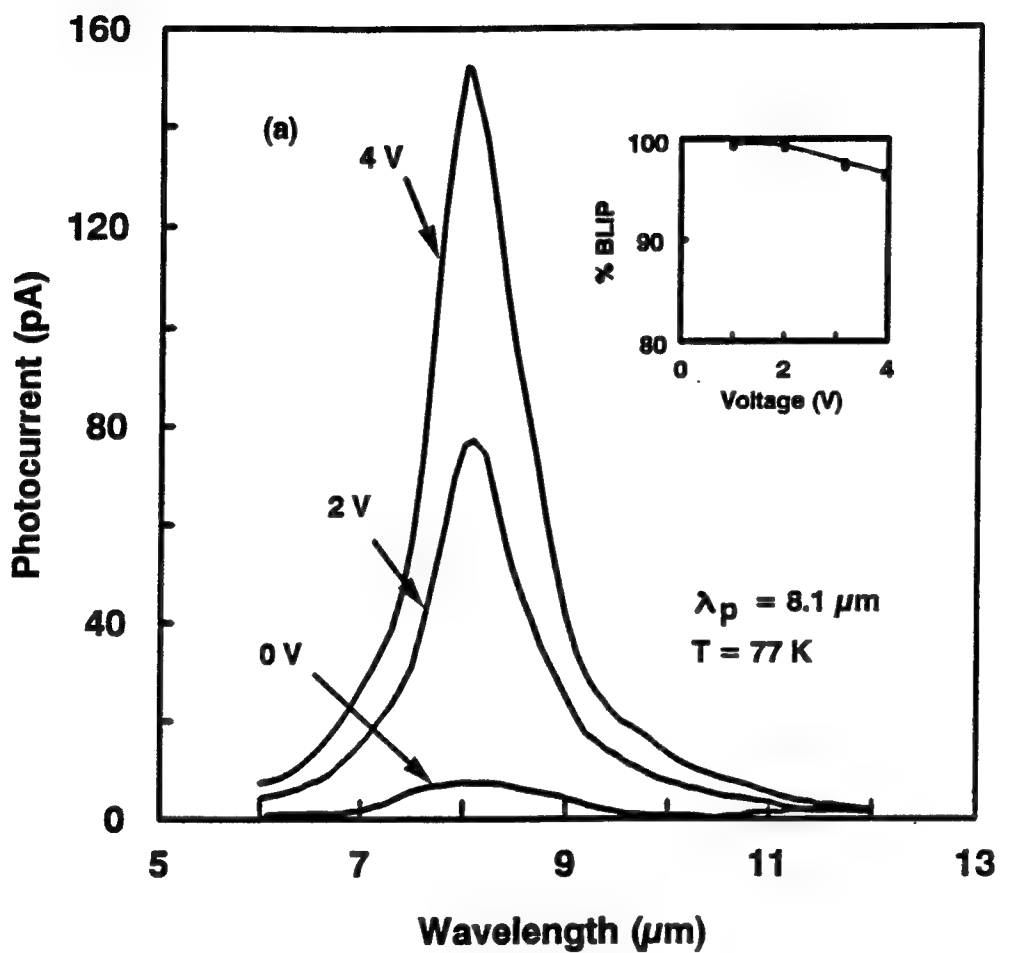


Figure 14.3. Normal incidence photocurrents versus wavelength with (a) positive biases and (b) negative biases for the PTSL-QWIP. The insets are the %BLIP at  $T = 77 \text{ K}$ .

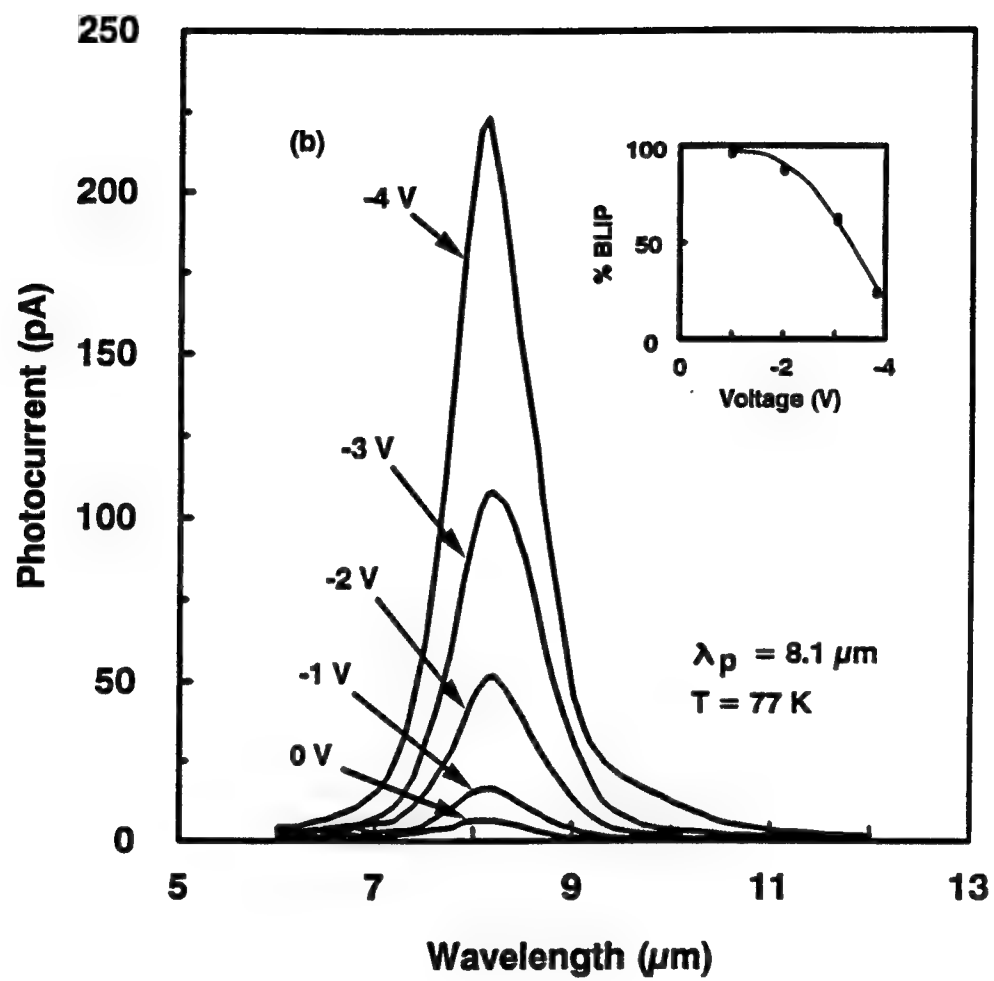


Figure 14.3. Continued.

## 15. A P-TYPE COMPRESSIVE STRAINED-LAYER InGaAs/GaAs QUANTUM WELL INFRARED PHOTODETECTOR

A normal incidence p-type compressive strained-layer (PCSL)  $\text{In}_{0.4}\text{Ga}_{0.6}\text{As}/\text{GaAs}$  quantum well infrared photodetector (QWIP) grown on (100) semi-insulating GaAs substrate by MBE technique for 3-5  $\mu\text{m}$  MWIR and 8-14  $\mu\text{m}$  LWIR two-color detection has been demonstrated for the first time. This PCSL-QWIP shows a broadband double-peak response at MWIR and LWIR detection bands by utilizing the resonant transport coupling mechanism between the heavy-hole type-I states and the light-hole type-II states. By using the compressive strain in the InGaAs quantum well [125], normal incidence absorption was greatly enhanced by reducing the heavy-hole effective mass (by a factor of 3) and increasing the density of states off zone center. Maximum responsivities of 93 mA/W and 30 mA/W were obtained at peak wavelengths of  $\lambda_{p1} = 8.9 \mu\text{m}$  and  $\lambda_{p3} = 5.5 \mu\text{m}$ , respectively, with  $V_b = 1.6 \text{ V}$  and  $T = 70 \text{ K}$ . Detectivity at  $\lambda_{p1} = 8.9 \mu\text{m}$  was found to be  $4.0 \times 10^9 \text{ cm} \cdot \sqrt{\text{Hz}}/\text{W}$  at  $V_b \leq 0.3 \text{ V}$  and  $T = 70 \text{ K}$ .

### 15.1. Interaction between Type-I and Type-II QW States

In general, strain can strongly affect the energy band structure and induce splitting between the heavy-hole and light-hole states in the valence band zone-center, which is degenerated in the unstrained case. In the  $\text{In}_{0.4}\text{Ga}_{0.6}\text{As}/\text{GaAs}$  QWIPs, a biaxial compressive strain is introduced in the InGaAs quantum well layers while no strain is present in the GaAs barrier layers. The strain pushes the heavy-hole states upward and pulls the light-hole states downward in the InGaAs well region. The light- and heavy-hole bands are split in the InGaAs well region and degenerated in the GaAs barrier region at the Brillouin zone (BZ) center (i.e.  $\mathbf{k} = 0$ ).

The p-type compressive strained-layer  $\text{In}_{0.4}\text{Ga}_{0.6}\text{As}/\text{GaAs}$  PCSL-QWIP was grown on a SI GaAs substrate by using MBE technique. This PCSL-QWIP structure consists of 20 periods of 4-nm Be-doped  $\text{In}_{0.4}\text{Ga}_{0.6}\text{As}$  quantum well with a dopant density of  $4 \times 10^{18} \text{ cm}^{-3}$  separated by a 35-nm GaAs undoped barrier layer. A 0.3- $\mu\text{m}$  cap layer and a 0.7- $\mu\text{m}$  buffer layer of Be-doped GaAs with a dopant density of  $5 \times 10^{18} \text{ cm}^{-3}$  were grown for the top and bottom ohmic contacts. The contact and barrier layers are lattice-matched to the SI GaAs substrate, and the  $\text{In}_{0.4}\text{Ga}_{0.6}\text{As}$  quantum well layers are under biaxial compression with a lattice mismatch of approximately 2.8

%. The ground subband energy levels confined in the quantum wells are the highly populated heavy-hole states  $E_{HH1}$ . The mobility of the heavy-hole is enhanced by the compressive strain created in the InGaAs quantum well layers due to the reduction of the heavy-hole effective mass [126] (i.e., by a factor 3). In addition, due to the compressive strain in the quantum well, the density of states in the well will decrease, and hence many more free holes have to reside at higher energy states, which implies that the effective Fermi level is elevated by the compressive strain effect compared to the unstrained case. The elevation of the effective Fermi level will result in the increase of the number of the off-BZ-center free holes (i.e.,  $k \neq 0$ ) with lighter effective mass, and hence a larger intersubband absorption under normal IR incidence is expected. In this InGaAs/GaAs strained-layer QWIP, heavy-holes are in type-I band alignment configuration, while light-holes are in type-II band alignment configuration. In addition, a binary GaAs barrier layer is employed so that a superior current transport is expected to that of a ternary barrier layer. It should be noted that unlike other types of QWIPs, the heavily doped contact layers of this PCSL-QWIP are made on large-bandgap GaAs. A large tunneling current from the triangle barrier potential near the ohmic contact region may be the dominant factor. In order to reduce this dark current component, a thick (550 Å) undoped GaAs barrier layer is grown next to the top and bottom contact layers.

Figure 15.1 (a) and (b) show the energy band diagram and subband energy states for this PCSL-QWIP. The intersubband transitions occurs from the highly populated ground heavy-hole state ( $E_{HH1}$ ) to the upper heavy-hole continuum states ( $E_{HH3}$  and  $E_{HH4}$ ) for the 8.8  $\mu\text{m}$  LWIR detection and 5  $\mu\text{m}$  MWIR detection, respectively. As shown in Fig. 15.1, the combination of type-I (for heavy-hole) and type-II (for light-hole) energy band configurations has three main ingredients to improve the performance of the PCSL-QWIP. First, the mobility of the heavy-holes confined in the ground states (i.e. HH1) of type-I configuration is enhanced by the internal biaxial compressive strain effect, from which a larger normal absorption can be achieved. Second, the heavy-hole excited continuum states (i.e. HH3) are resonant with the GaAs barrier which can maximize the absorption oscillator strength. Finally, the heavy-hole excited continuum states are resonantly lined up with the light-hole states, which may give rise to a strong quantum state coupling effect. It is the resonant-line-up effect that makes the conducting holes behaving like light-holes with high mobility, small effective mass, and long mean free path. Thus, a larger photoconductive gain and a higher photoconductivity are expected in the PCSL-QWIP.

## 15.2. Experiments

In order to measure the device dark current and spectral responsivity of this PCSL-QWIP,

a  $200 \times 200 \mu\text{m}^2$  mesa structure was created by using the chemical etching process. Cr/Au metal films were deposited onto the QWIP mesas with a thickness of about  $1500 \text{ \AA}$ . The substrate of the QWIP device was thinned down to about  $50 \mu\text{m}$  to partially eliminate the substrate absorption screening effect, and polished to mirror-like surface to reduce the reflection of the normal incident IR radiation.

Figure 15.2 shows the measured dark current at  $T = 30, 60$ , and  $77 \text{ K}$ . The device shows the asymmetrical dark current characteristic under the positive and negative bias, which is attributed to the band bending due to dopant migration effect occurred during the layer growth [127]. This PCSL-QWIP is under background limited performance (BLIP) at  $V_b = 0.3 \text{ V}, 0.7 \text{ V}$ , and  $T = 70, 55 \text{ K}$  respectively, for a field of view (FOV)  $90^\circ$ .

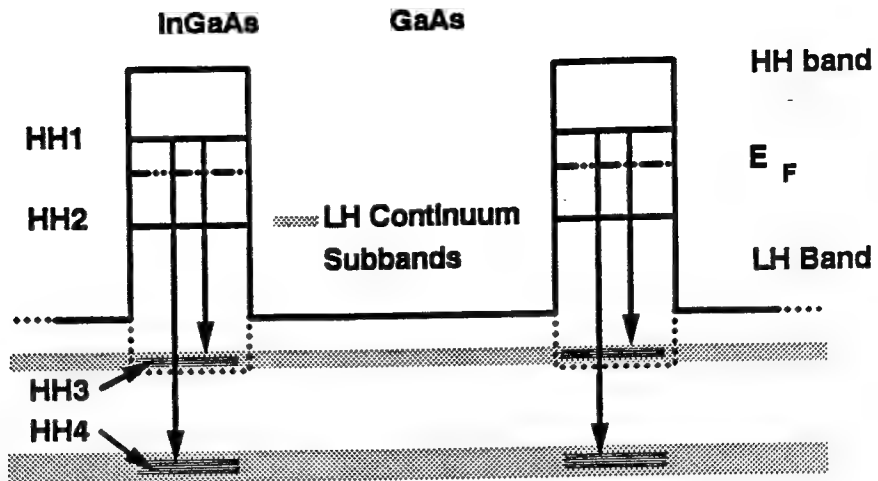
The responsivity of this QWIP under normal incidence illumination was measured as a function of temperature, bias voltage, and wavelength using a blackbody radiation source and automatic PC-controlled single-grating monochromater system. Two dominant peaks were detected: a twin peak in the LWIR of  $\lambda_{p1,2} = 8.9, 8.4 \mu\text{m}$  was observed, as shown in Fig. 15.3 (a), and the other is in the MWIR of  $\lambda_{p3} = 5.5 \mu\text{m}$ , as shown in Fig. 15.3 (b). The LWIR twin peaks at  $\lambda_{p1,2} = 8.9, 8.4 \mu\text{m}$  cover a broad wavelength band from  $6.5$  to  $12 \mu\text{m}$ . Responsivities of  $24 \text{ mA/W}$  at  $V_b = 0.3 \text{ V}$  and  $45 \text{ mA/W}$  at  $V_b = 0.7 \text{ V}$  were obtained at  $T \leq 75 \text{ K}$  for the two peak wavelengths. The cutoff wavelength for the LWIR detection band was found to be  $\lambda_c \approx 10 \mu\text{m}$  with a spectral bandwidth of  $\Delta\lambda/\lambda_p = 35 \%$ . Detectivity at  $\lambda_{p1} = 8.9 \mu\text{m}$  was found to be about  $4.0 \times 10^9, 3.2 \times 10^9 \text{ cm}\cdot\sqrt{\text{Hz}}/\text{W}$  at  $V_b = 0.3, 0.7 \text{ V}$  and  $T = 75 \text{ K}$ , respectively. These twin peak wavelengths are attributed to the intersubband transition between the confined ground heavy-hole state ( $E_{HH1}$ ) to the continuum heavy-hole states ( $E_{HH3}$ ), which is resonantly lined up with the type-II light-hole continuum states, as illustrated in Fig. 15.1. The transition energy for these peak wavelengths is in reasonable agreement with our theoretical calculation. These twin peaks broaden the LWIR detection bandwidth by about a factor of 2. The physical origin for the twin peaks feature is not clear, but a possible explanation may be given as follows. When the continuum HH- and LH-bands are strongly mixed, an individual subband (either HH-band or LH-band) further splits into two subsubband due to the coupling and interaction: one upward and the other downward. This gives rise to the observed twin-peak detection in the LWIR band. The MWIR peak observed at  $\lambda_{p3} = 5.5 \mu\text{m}$  covering the wavelengths of  $4$  to  $6.5 \mu\text{m}$ . Responsivities for the MWIR band were found to be  $7 \text{ mA/W}, 13 \text{ mA/W}$  at  $V_b = 0.3, 0.7 \text{ V}$  and  $T = 75 \text{ K}$ , respectively. The spectral bandwidth of  $\Delta\lambda/\lambda_{p3} = 27 \%$  was obtained with a cutoff wavelength at  $\lambda_c = 6 \mu\text{m}$ . The intersubband transition occurred between  $E_{HH1}$  and  $E_{HH4}$  subbands was responsible for the MWIR detection. However,

no mixing and interaction between HH-band and LH band was observed in this transition. This may be due to the weak overlap interaction at higher subbands. Since  $E_{HH2}$  subband is confined inside the quantum wells with very low tunneling probability off the thicker barrier layer, the photoresponse from this heavy-hole state was not detected.

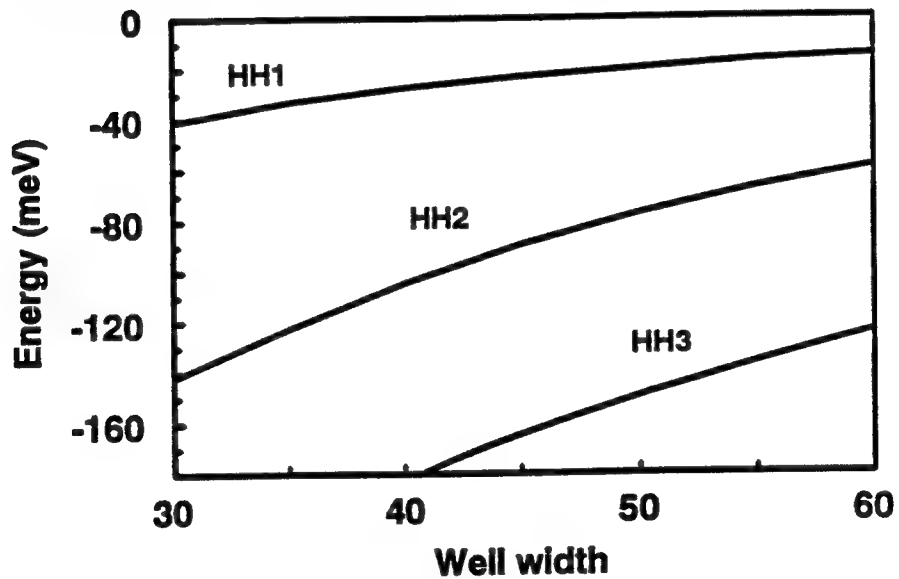
Responsivities versus bias voltage for the LWIR and MWIR peak wavelengths were measured at  $T = 75$  K, and the results are shown in Fig. 15.4. The responsivity of  $\lambda_{p1} = 8.9 \mu\text{m}$  (or  $\lambda_{p2} = 8.4 \mu\text{m}$ ) was found to increases linearly with bias voltage for  $V_b \leq -1.6\text{V}$  and  $V_b \leq +1.2\text{V}$ , and then rapidly falls to zero from the peak value with bias interval of 0.15 V. Similar photoresponse was observed for  $\lambda_{p3} = 5.5 \mu\text{m}$ . It is noted that the responsivity is higher at positive bias than that at negative bias for both MWIR and LWIR bands when  $|V_b| \leq 0.5 \text{ V}$  and then becomes nearly equal for  $|V_b| > 0.6 \text{ V}$ . Figure 15.5 shows the photoconductive gain versus bias voltage. A maximum gain of 0.13 was obtained at  $V_b = 1.6 \text{ V}$ , and then decreases rapidly for higher bias voltage. The linear photoresponse versus bias voltage is due to the linear photoconductive gain with bias voltage as shown in Fig. 15.5. When the bias voltage increases, the coupling transport breaks down, and then photoconductive gain becomes very small. As a result, no photocurrent was detected for  $V_b > 1.6 \text{ V}$ . Furthermore, a photovoltaic (PV) response for both MWIR and LWIR bands was also observed for the first time for the p-type QWIP.

### 15.3. Conclusions

In conclusion, we have demonstrated for the first time a new normal incidence p-type compressive strained-layer InGaAs/GaAs QWIP grown on GaAs substrate for the MWIR and LWIR two-band detection. The intersubband absorption and photoresponse in this PCSL-QWIP were enhanced by the biaxial compressive strain in the InGaAs quantum well layers. The improvement in the performance of the bandwidth and responsivity in this PCSL-QWIP was achieved by using type-I and type-II configuration coupling transport mechanism. Since the total layer thickness of this PCSL-QWIP is greater than the coherent strained-layer limitation, certain strain relaxation might occur, which will result in a larger dark current and lower photoconductive gain than theoretical prediction. By further optimizing the quantum well dopant density, barrier layer thickness, biaxial strain strength, and layer structure parameters, a high performance PCSL-QWIP can be developed for the MWIR and LWIR two-color infrared focal plane arrays image sensor systems with background limited performance (BLIP) at  $T = 85 \text{ K}$ .



(a)



(b)

Figure 15.1. Schematic energy band diagram (a) and the subband energy levels at zone center as a function of the well width (b) for the  $\text{In}_{0.4}\text{Ga}_{0.6}\text{As}/\text{GaAs}$  QWIP.

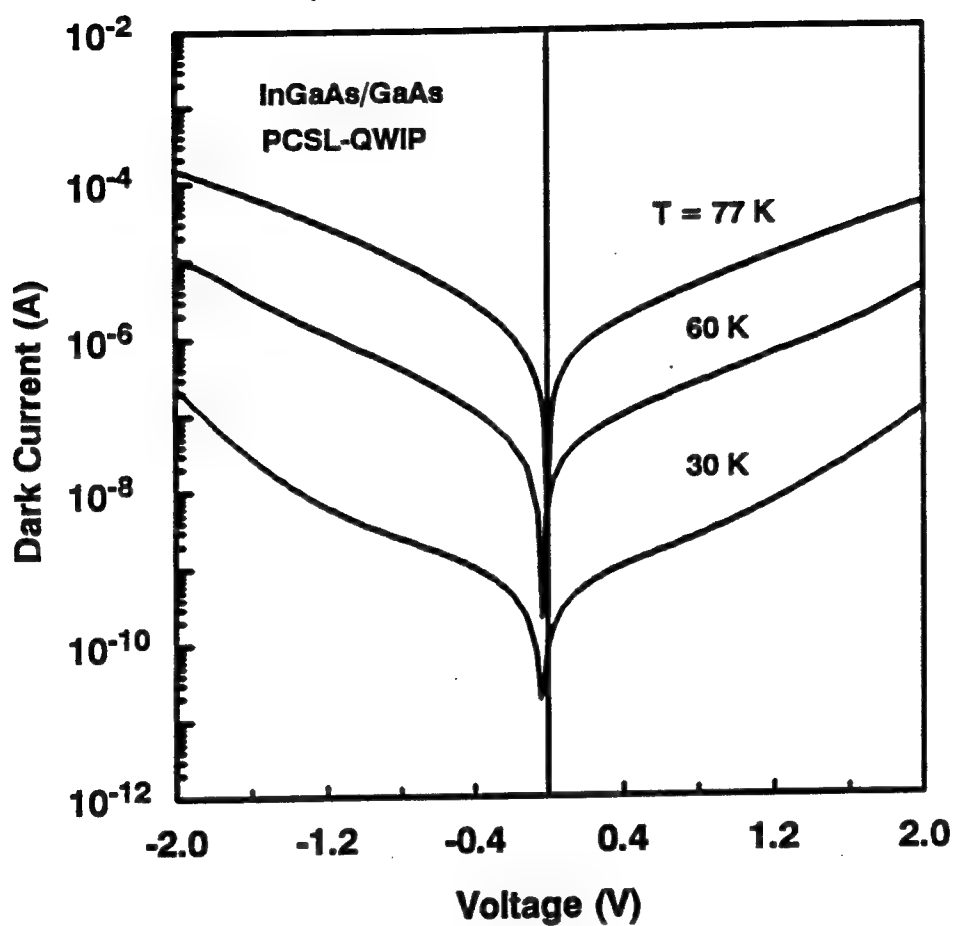


Figure 15.2. Dark current versus bias voltage measured at  $T = 30$ ,  $60$  and  $77\text{ K}$  for the  $\text{In}_{0.4}\text{Ga}_{0.6}\text{As}/\text{GaAs}$  PCSL-QWIP.

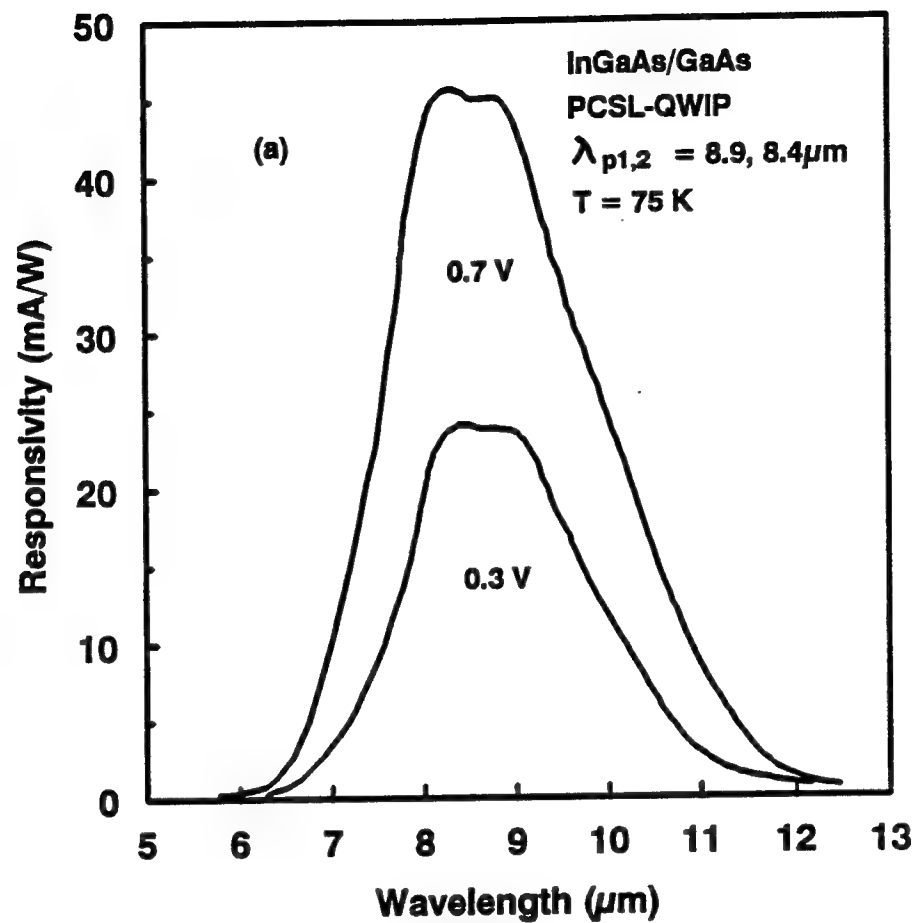


Figure 15.3. Responsivities of (a)  $\lambda_{p1,2}$  and (b)  $\lambda_{p3}$  versus wavelength with  $V_b = 0.3, 0.7 \text{ V}$  at  $T = 75 \text{ K}$ .

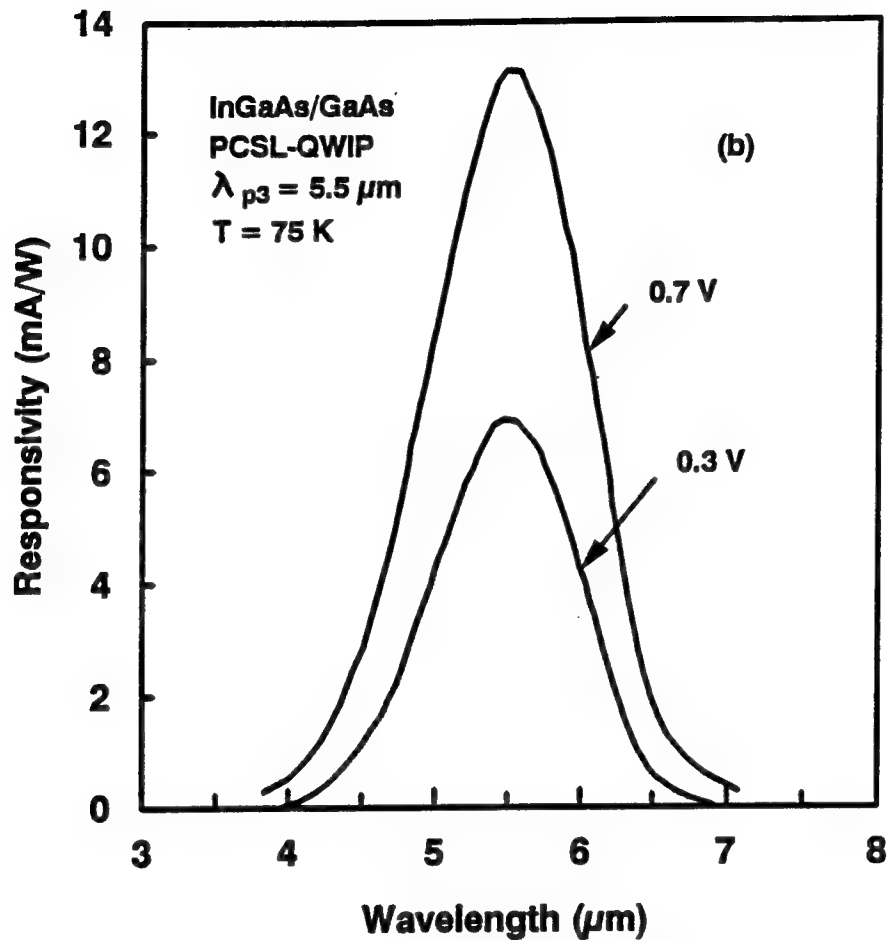
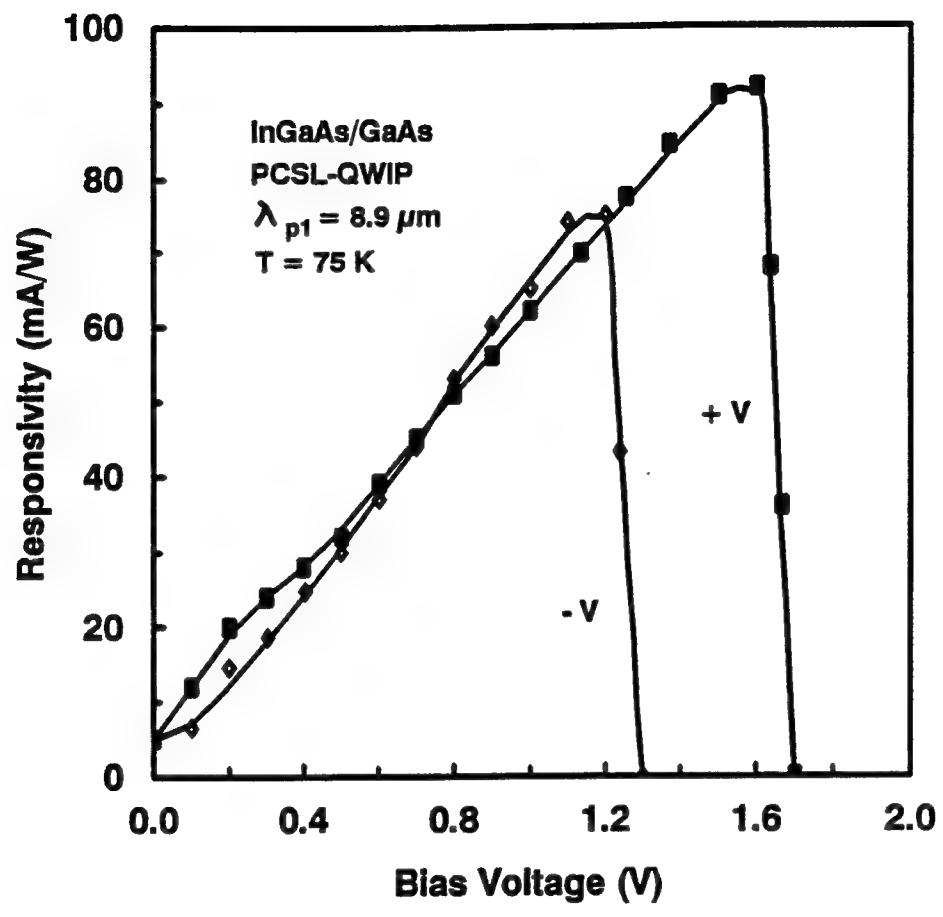
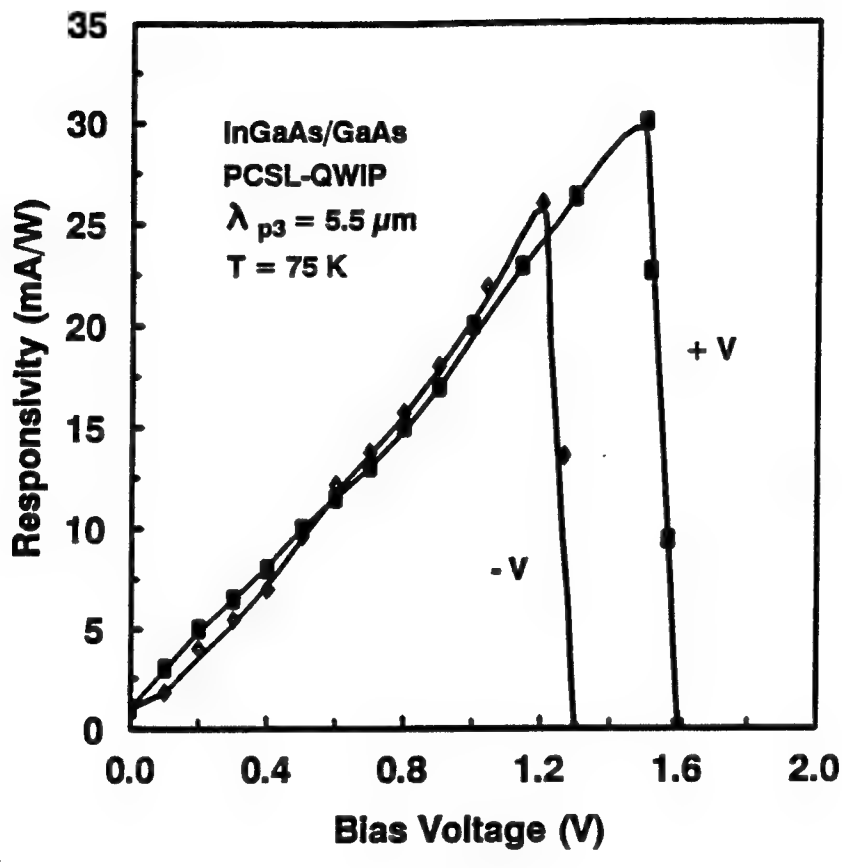


Figure 15.3. Continued.



(a)

Figure 15.4. Responsivities of (a)  $\lambda_{p1}$  and (b)  $\lambda_{p3}$  versus positive and negative bias at  $T = 75 \text{ K}$ .



(b)

Figure 15.4. Continued.

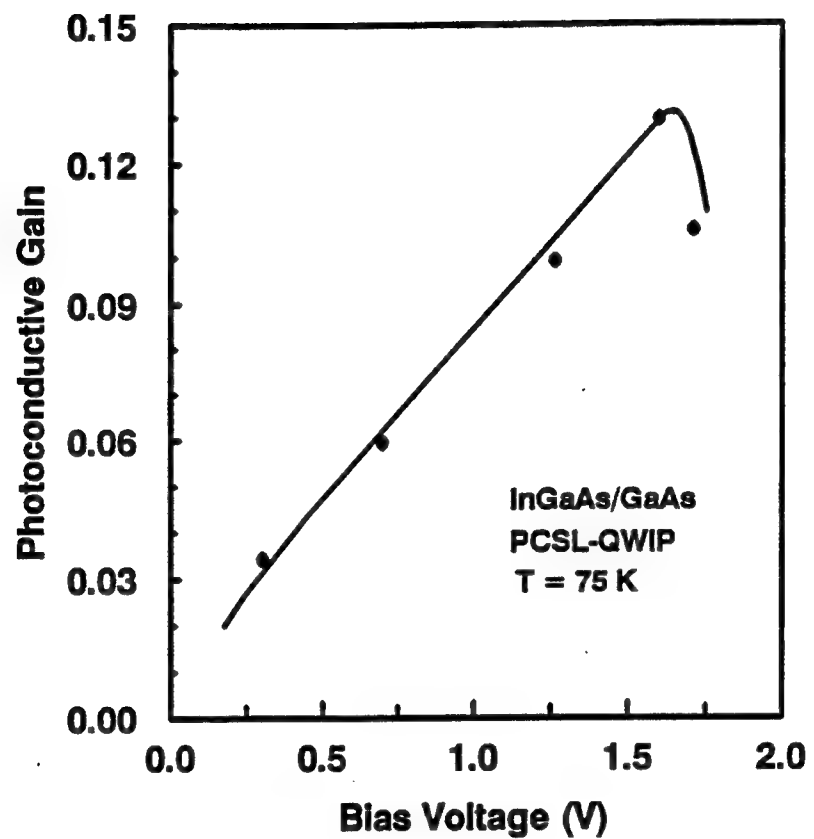


Figure 15.5. Photoconductive gain versus bias voltage at  $T = 75\text{ K}$ .

## 16. CONCLUSIONS

In this report, we have presented several novel III-V semiconductor quantum well infrared photodetectors (QWIPs) developed by us using bound-to-miniband (BTM) and bound-to-continuum (BTC) intersubband transition schemes for 3-5  $\mu\text{m}$  MWIR and 8-14  $\mu\text{m}$  LWIR detection. In addition, design and fabrication of several 2-D metal grating couplers for n-type QWIPs have also been carried out. Detectivities in the high  $10^9$  to low  $10^{12} \text{ cm}\cdot\sqrt{\text{Hz}}/\text{W}$  have been obtained for the QWIPs developed in this work at 77 K operation. The results are summarized as follows:

- The GaAs/AlGaAs and InGaAs/InAlAs BTM QWIPs and GaAs/AlGaAs BTC QWIP have both PC and PV dual-mode detection characteristics. The PV mode detection for these QWIPs may result from dopant migration effect during the QWIP growth. The BTM intersubband transition is from the highly populated bound ground state in the enlarged quantum wells to the global miniband states formed by the superlattice barrier layers inside the quantum wells. By utilizing resonant tunneling and coherent transport along the superlattice miniband for the BTM QWIPs, voltage-tunable spectral bandwidth with  $\Delta\lambda/\lambda_p = 7\%$  to 24 % has been obtained at peak wavelength 10  $\mu\text{m}$ . A GaAs/AlGaAs QWIP using an enlarged GaAs (110 Å) quantum well with dopant density of  $5\times 10^{18} \text{ cm}^{-3}$  and an enlarged AlGaAs (875 Å) barrier for two-color detection at peak wavelengths of 7.7 and 12  $\mu\text{m}$  has been realized at T = 77 K. The detection scheme uses transition from the confined ground-state and the first excited-state inside the enlarged GaAs quantum well to the continuum states slightly above the AlGaAs barrier layers. By using intersubband transition from the first excited states to the continuum states for the PC mode operation, detectivity of  $2\times 10^{10} \text{ cm}\cdot\sqrt{\text{Hz}}/\text{W}$  is obtained at  $\lambda_p = 12 \mu\text{m}$ ,  $V_b = 1 \text{ V}$ , and T = 77 K.
- A type-II indirect bandgap AlAs/Al<sub>0.5</sub>Ga<sub>0.5</sub>As QWIP grown on the (110) GaAs substrate has been developed which shows the normal incidence multi-color infrared detection schemes in the 2-18  $\mu\text{m}$  wavelength range with six response peaks. The intersubband absorption for the normal incidence is created by indirect anisotropic band structure in X-valley and tilted [110] growth direction with respect to the principle axes of the ellipsoidal valleys. By using X- $\Gamma$  valley resonant transport mechanism in this type-II QWIP, the enhancement of the photoconductive gain and photoresponsivity has been achieved in both the MWIR and

LWIR detection bands.

- A p-type tensile strained-layer InGaAs/InAlAs QWIP has been developed which shows an ultra low dark current density of  $7 \times 10^{-7} \text{ A/cm}^2$ , six orders of magnitude smaller than the BTC transition GaAs/AlGaAs QWIP. This QWIP is under background limited performance (BLIP) at  $\lambda_p = 8.1 \mu\text{m}$  for  $T \leq 100 \text{ K}$ , which is the highest BLIP temperature ever reported for a QWIP. By applying the tensile strain between the quantum well and the barrier layer, the light-hole levels are pushed upward and the heavy-hole levels are pulled downward. As a result, the ground heavy- and light-hole states are inverted, and the light-hole state becomes the ground bound state in the quantum well. Since the light-hole has a small effective mass, the optical absorption is greatly enhanced. In addition, the p-type compressive strained-layer InGaAs/GaAs QWIP developed in this work has two-color detection at peak wavelengths of 5.5 and  $8.9 \mu\text{m}$ . By applying coupling transport from the heavy-hole type-I states to the light-hole type-II states, large photoresponse is achieved in this QWIP.

The results of various QWIPs developed this program are summarized in Table 1.1, which lists the peak and cutoff wavelengths, responsivities, detectivities, and background limited performance temperatures for the QWIPs studied in this project. The background limited performance temperatures  $T_{BLIP}$  range from 45 K up to 100 K. The p-type tensile strained-layer InGaAs/InAlAs QWIP has the highest BLIP temperature with  $T_{BLIP} \leq 100 \text{ K}$ , while n-type unstrained InGaAs/InAlAs QWIP has the lowest BLIP temperature with  $T_{BLIP} \sim 45 \text{ K}$ . The dark current densities for some of the QWIPs studied and a standard GaAs/AlGaAs QWIP at  $T = 77 \text{ K}$  are shown in Fig. 1.2. The dark current densities for the n-type VT-QWIP and type-II QWIP were found to be about one order of magnitude lower than that of the standard GaAs/AlGaAs QWIP, whereas the dark current density of the n-type DM-QWIP was found to be about two orders of magnitude lower than that of the standard GaAs/AlGaAs QWIP due to the incorporation of the enlarged AlGaAs barrier layers in the DM-QWIP.

All QWIPs studied here have not been optimized with respect to the layer thickness, doping profile, growth conditions, and the number of quantum well period. Optimization of these QWIPs can further improve the quantum efficiency and reduce the dark current. In view of the advantages such as high growth uniformity, flexible spectral response tunability, and mature processing technologies for the III-V materials over the HgCdTe, large-area and high-quality GaAs QWIP imaging sensor arrays can be fabricated for a wide variety of applications in the atmospheric spectral window of 3-5  $\mu\text{m}$  and 8-14  $\mu\text{m}$  wavelength.

## APPENDIX A ENERGY DISPERSION EQUATION FOR SUPERLATTICE

By using the transfer matrix method, the energy dispersion equations for periodic structures such as multiple quantum wells and superlattices can be deduced [128]. It is assumed that each layer contains sufficient number of atomic sublayers (i.e. monolayers) so that the effective-mass model holds for the calculation. From the effective-mass model by using the effective mass envelope function approach, the solution of the conduction band envelope function for  $j$ -th region,  $\phi_j$ , can be obtained from

$$\phi_j'' + k_j^2 \phi_j = 0, \quad (\text{A.1})$$

where  $k_j$  is the wave propagation constant,  $k_j = \sqrt{\frac{2m_j^*(E-V_c)}{\hbar^2}}$ ,  $V_c$  conduction-band minimum energy referred to the valence-band maximum of the quantum well, and  $E$  the electron energy along the superlattice growth direction. When  $k_j$  is either real or imaginary, the equation gives either oscillatory or evanescent wave solution, respectively. For the one-band model and a flat-band condition, the functions of  $\phi_j$  and  $\phi_j'/m_j^*$  should be continuous across the heterointerfaces. These two continuous functions at the heterointerfaces can be expressed by a  $2 \times 1$  matrix, which is also called transfer vector,

$$\mathbf{S} = \begin{pmatrix} S_1 \\ S_2 \end{pmatrix} = \begin{pmatrix} \phi_j \\ \frac{\phi_j'}{m_j^*} \end{pmatrix} \quad (\text{A.2})$$

On the other hand, the wave conduction property through the multiple quantum wells or superlattice system can be also represented by the transmission line concepts with the transfer impedance  $Z_j = S_1/S_2$  and the characteristic impedance  $Z^* = m^*/k_j$ . The energy dispersion can be obtained by setting the total impedance equal to 0 or  $\infty$ .

For a superlattice with the basis  $L$ , the wave transfer equation is given by  $[S]_{z+L} = [T] \cdot [S]_z$ , where  $[T]$  is the transfer matrix (i.e., the transfer matrix of a superlattice is for one period of the superlattice). If one period of the superlattice consists of  $N'$  sublayers, then  $[T]$  is given by

$$\mathbf{T} = \begin{pmatrix} T_{11} & T_{12} \\ T_{21} & T_{22} \end{pmatrix} = \prod_{j=1}^{N'} \begin{pmatrix} \cos k_j L_j & Z_j^* \sin k_j L_j \\ -\frac{1}{Z_j^*} \sin k_j L_j & \cos k_j L_j \end{pmatrix}, \quad (\text{A.3})$$

where  $L_j$  is the thickness of a layer in one period of the superlattice. The dispersion equation for the system is readily found to be,

$$T_{11} + T_{22} = 2\cos k_z L, \quad (\text{A.4})$$

where  $k_z$  is the superlattice wave vector,  $L$  the period of the superlattice ( $=\sum_{j=1}^{N'} L_j$ ). The conduction band nonparabolicity, bias-dependent property, and coupling between X-band and  $\Gamma$ -band could be also included in the transfer matrix expression to give a complicated energy dispersion relation.

When an electric field  $F$  is applied on the superlattice, the conduction band  $V_c$  is tilted to be  $V_c(z) = V_c - eFz$ , and Eq. (A.1) and the transfer vector are changed. The transfer matrix elements  $T_{ij}$  are the linear combination of the Airy functions.

For the two-band and three-band models, the transfer vectors, wave vectors, transfer matrices, and dispersion relation are the same as the one-band results except that the effective mass  $m_j^*$  for  $j$ -th layer in the superlattice is replaced by,

$$m_j^* = \frac{m_o^*}{(1-\gamma)E_{go}} (E - V_{LHj}) \quad (\text{A.5})$$

for the two-band model (i.e., conduction and light-hole bands), and

$$m_j^* = \frac{m_o^*}{(1-\gamma)E_{go}} \frac{3E_{go} + 2\Delta_o}{E_{go} + \Delta_o} \frac{(E - V_{SOj})(E - V_{LHj})}{2(E - V_{SOj}) + (E - V_{LHj})} \quad (\text{A.6})$$

for the three-band model (i.e., conduction, light-hole, and split-off bands), where  $m_o^*$ ,  $E_{go}$ ,  $\gamma$ , and  $\Delta_o$  are the effective mass, energy bandgap, effective mass ratio (i.e.,  $m_o^*/m_o$ ,  $m_o$  free electron mass), and split-off energy for the quantum well, respectively.  $V_{LH}$  and  $V_{SO}$  are the light-hole band and split-off band maximum (referred to the quantum well valence band maximum), respectively. It is noticed that the effective masses of the electrons for both two-band and three-band models depend not only on the coupling effects among S-type conduction band and P-type valence bands, but also on their energy magnitude.

All above dispersion relations for the one-band, two-band, or three-band models are valid only for near  $\Gamma$ -point or X-point single valley quantum well/superlattice structures. However, in the multivalleys quantum well/superlattice structures such as  $\Gamma$ -X interaction (or coupling) in a type-II structure, the above simple envelope function approach breaks down since the coupling of their Bloch functions between the host materials cannot be neglected. Due to the lack of the translational symmetry at the interfaces in the  $\Gamma$ -X coupling superlattice,  $\Gamma$ -X valleys can couple with each other, and the electron states at the interfaces are a mixture of the zone-center  $\Gamma$  and

zone-edge X related bulk states. The wave function  $\psi$  is a mixed-symmetry form, and is written as the sum of the products of slowly varying envelope functions  $\phi_n$  and Bloch functions  $\phi_B$  for  $\Gamma$ -valley and X-valley,

$$\psi = (\phi_n \phi_B)_\Gamma + (\phi_n \phi_B)_X. \quad (\text{A.7})$$

On the other hand, the wave function  $\psi$  can be written in the vector notation,

$$\psi = \begin{pmatrix} \psi_\Gamma \\ \psi_X \end{pmatrix}. \quad (\text{A.8})$$

The elastic intervalley interactions are possible only between the  $\Gamma$  minimum and  $k_z$  direction of the X-minima due to the potential discontinuity in  $k_z$  direction of X-minima. The lateral  $k_x$  and  $k_y$  momenta in the X-minima do not play roles in the intervalley interaction (or mixing) because of their momentum conservation requirement in the quantum well/superlattice structure. The lateral interaction may be activated if the heterointerface roughness is taken into the consideration or the superlattice layers are grown on a tilted direction with respect to principal axes of ellipsoidal energy surface in X-valley. The transfer potential energy  $V_{\Gamma X}$  for the intervalley interaction can be expressed by [95],

$$V_{\Gamma X} = \begin{pmatrix} V_\Gamma & \alpha\delta(z) \\ \alpha\delta(z) & V_X \end{pmatrix} \quad (\text{A.9})$$

where diagonal terms  $V_\Gamma$  and  $V_X$  are the energy band offset potential for  $\Gamma$  and X valleys, respectively, and off-diagonal elements  $\alpha\delta(z)$  model the  $\Gamma$ -X coupling strength at the interfaces.  $\alpha$  is the coupling constant (typical value  $0.1 \sim 0.2$  eVÅ), and  $\delta(z)$  is the Dirac delta function. The effective mass Hamiltonian is,

$$H = \begin{bmatrix} -\frac{\hbar^2}{2} \frac{\partial}{\partial z} \frac{\partial}{m_\Gamma^* \partial z} & 0 \\ 0 & -\frac{\hbar^2}{2} \frac{\partial}{\partial z} \frac{\partial}{m_X^* \partial z} \end{bmatrix} + \begin{bmatrix} V_\Gamma & \alpha\delta(z) \\ \alpha\delta(z) & V_X \end{bmatrix}. \quad (\text{A.10})$$

By using the wave function connection rules across the interface, the coupled wave functions  $\psi$  can be obtained with using experimentally-determined coupling constant  $\alpha$ .

The dispersion relation for the coupling system can also be calculated by using the transfer matrix method. If the transfer vector notation is used in the  $\Gamma$  valley and X valley wave functions, then transfer vector  $[S_\Gamma]$  and  $[S_X]$  are expressed by,

$$S_\Gamma = \begin{pmatrix} \psi_\Gamma \\ \psi'_\Gamma \\ \frac{\psi'_\Gamma}{m_\Gamma^*} \end{pmatrix}; S_X = \begin{pmatrix} \psi_X \\ \psi'_X \\ \frac{\psi'_X}{m_X^*} \end{pmatrix}. \quad (\text{A.11})$$

The uncoupled elements  $[T_\Gamma]$  and  $[T_X]$  of the transfer matrices for  $\Gamma$ -X coupled quantum well/superlattice have the similar form as Eq. (A.3), whereas the coupled elements  $[T_{\Gamma X}]$  are,

$$T_{\Gamma X} = T_{X\Gamma} = \begin{pmatrix} 0 & 0 \\ \frac{2\alpha}{\hbar^2} & 0 \end{pmatrix}. \quad (\text{A.12})$$

The total transfer matrix becomes a  $4 \times 4$  matrix, and the overall transfer equation is written as,

$$\begin{bmatrix} S_\Gamma \\ S_X \end{bmatrix}_{z+L} = \begin{bmatrix} T_\Gamma & T_{\Gamma X} \\ T_{X\Gamma} & T_X \end{bmatrix} \cdot \begin{bmatrix} S_\Gamma \\ S_X \end{bmatrix}_z. \quad (\text{A.13})$$

The allowed minibands occur at the energies where the eigenvalues of  $[T]$  have absolute values equal to one. When the coupling interaction from light-hole band and split-off band becomes important in addition to the intervalley coupling, the uncoupled transfer elements  $[T_\Gamma]$  and  $[T_X]$  for the two-band or three-band model should be used, and then the  $4 \times 4$  transfer matrix can still give reasonable miniband structures.

## APPENDIX B OPTICAL MATRIX FOR STRAINED-LAYER SUPERLATTICE

The optical matrix elements  $|\hat{\epsilon} \cdot \mathbf{P}_{i,f}|$  can be obtained from the  $\mathbf{k} \cdot \mathbf{p}$  matrix elements, which have the same form as the  $\mathbf{k} \cdot \mathbf{p}$  matrix elements except that  $k_i k_j$  is replaced with  $k_i \epsilon_j + k_j \epsilon_i$  and multiplied by a constant factor  $m_o/\hbar$  [121]. The  $3 \times 3$  optical matrix elements are given as follows:

$$\frac{m_o}{\hbar} \begin{bmatrix} T_{HH} & T_{HL} & T_{HS} \\ T_{LH} & T_{LL} & T_{LS} \\ T_{SH} & T_{SL} & T_{SS} \end{bmatrix} \quad (\text{B.1})$$

where the  $T_{ij}$  are given by

$$T_{HH} = 2(A - B)\epsilon_z k_z + (2A + B)(\epsilon_x k_x + \epsilon_y k_y), \quad (\text{B.2})$$

$$T_{LL} = 2(A + B)\epsilon_z k_z + (2A - B)(\epsilon_x k_x + \epsilon_y k_y), \quad (\text{B.3})$$

$$T_{SS} = 2A(\epsilon_z k_z + \epsilon_x k_x + \epsilon_y k_y), \quad (\text{B.4})$$

$$\begin{aligned} T_{HL} = & j \frac{1}{\sqrt{3}} N(\epsilon_x \cos \eta - \epsilon_y \sin \eta) k_z - j \frac{1}{3} N \epsilon_z k_{||} \\ & - \sqrt{3} B(\epsilon_x k_x - \epsilon_y k_y) \cos \chi \\ & + \frac{1}{\sqrt{3}} N(\epsilon_x k_y + \epsilon_y k_x) \sin \chi, \end{aligned} \quad (\text{B.5})$$

$$\begin{aligned} T_{HS} = & \frac{1}{\sqrt{6}} N(-\epsilon_x \cos \eta + \epsilon_y \sin \eta) k_z + \frac{1}{6} N \epsilon_z k_{||} \\ & + j \sqrt{6} B(\epsilon_x k_x - \epsilon_y k_y) \cos \chi \\ & - \frac{2}{\sqrt{6}} N(\epsilon_x k_y + \epsilon_y k_x) \sin \chi, \end{aligned} \quad (\text{B.6})$$

$$\begin{aligned} T_{LS} = & \left[ j 2 \sqrt{2} B \epsilon_z + \frac{1}{\sqrt{2}} N \epsilon_x \cos(\chi - \eta) - \epsilon_y \sin(\chi - \eta) \right] k_z \\ & - j \sqrt{2} B(\epsilon_x k_x + \epsilon_y k_y) \\ & - \frac{1}{\sqrt{2}} N \epsilon_z k_{||} \cos(\chi - 2\eta), \end{aligned} \quad (\text{B.7})$$

$$T_{SH} = T_{HS}^*, \quad (\text{B.8})$$

$$T_{SL} = T_{LS}^*, \quad (\text{B.9})$$

$$T_{LH}^* = T_{HL}^*. \quad (\text{B.10})$$

Here A, B, N,  $\eta$ , and  $\chi$  are the inverse mass band parameters [121].

## REFERENCES

- [1] L. Esaki and R. Tsu, IBM J. Res. Dev. **14**, 61 (1970).
- [2] R. Tsu and L. Esaki, Appl. Phys. Lett. **22** 562, (1973).
- [3] L. Esaki and L. L. Chang, Phys. Rev. Lett. **33**, 495 (1974).
- [4] R. Dingle, W. Wiegmann, and C. H. Henry, Phys. Rev. Lett. **33**, 827 (1974).
- [5] E. O. Kane, J. Phys. Chem. Solids **1**, 249 (1957).
- [6] G. H. Dohler, R. Tus, and L. Esaki, Solid-State Commun. **17**, 317 (1975).
- [7] F. Capasso, K. Mohammed, A. Y. Cho, R. Hull, and A. Hutchinson, Appl. Phys. Lett. **47**, 420 (1985).
- [8] G. C. Osbourn, J. Appl. Phys. **53**, 1586 (1982).
- [9] L. C. West and S. J. Egash, Appl. Phys. Lett. **46** 1156 (1985).
- [10] B. F. Levine, K. K. Choi, C. G. Bethea, J. Walker, and R. J. Malik, Appl. Phys. Lett. **50**, 1092 (1987).
- [11] B. F. Levine, C. G. Bethea, G. Hasnain, V. O. Shen, E. Pelve, R. R. Abbott, and S. J. Hsieh, Appl. Phys. Lett. **56**, 851 (1990).
- [12] K. K. Choi, M. Dutta, P. G. Newman, M. -L. Sanders, and G. J. Iafrate, Appl. Phys. Lett. **57**, 1348 (1990).
- [13] L. S. Yu and S. S. Li, Appl. Phys. Lett. **59**, 1332 (1991).
- [14] L. J. Kozlowski, G. M. Williams, G. J. Sullivan, C. W. Farley, R. J. Andersson, J. Chen, D. T. Cheung, W. E. Tennant, and R. E. DeWames, IEEE Trans. ED-**38**, 1124 (1991).
- [15] T. S. Faska, J. W. Little, W. A. Beck, K. J. Ritter, A. C. Goldberg, and R. LeBlanc, in Innovative Long Wavelength Infrared Photodetector Workshop, JPL, Pasadena, CA, April 7-9, (1992).
- [16] C. S. Wu, C. P. Wen, R. N. Sato, M. Hu, C. W. Tu, J. Zhang, L. D. Flesner, Le Pham, and P. S. Nayer, IEEE Trans. ED-**39**, 234 1992.
- [17] G. Hasnain, B. F. Levine, D. L. Sivco, and A. Y. Cho, Appl. Phys. Lett. **56**, 770 (1990).
- [18] B. F. Levine, S. D. Gunapala, and R. F. Kopf, Appl. Phys. Lett. **58**, 1551 (1991).

- [19] J. S. Smith, L. C. Chiu, S. Margalit, A. Yariv, and A. Y. Cho, *J. Vac. Sci. Technol. B* **1**, 376 (1983).
- [20] D. D. Coon and R. P. G. Karunasiri, *Appl. Phys. Lett.* **33**, 495 (1984).
- [21] B. F. Levine, G. Hasnain, C. G. Bethea, and Naresh Chand, *Appl. Phys. Lett.* **54**, 2704 (1989).
- [22] A. Kastalsky, T. Duffield, S. J. Allen, and J. Harbison, *Appl. Phys. Lett.* **52**, 1320 (1988).
- [23] O. Byungsung, J. W. Choe, M. H. Francombe, K. M. S. V. Bandara, and D. D. Coon, *Appl. Phys. Lett.* **57**, 503 (1990).
- [24] J. M. Ziman, *Electrons and Phonons*, Oxford University Press, (1962).
- [25] J. R. Reitz, *Advances in Research Applications I*, in *Solid State Physics*, Academic Press, New York, (1955).
- [26] Sypryo Datta, *Quantum Phenomena*, Vol. 8 in *Modular Series on Solid State Devices*, Addison-Wesley, New York, (1989).
- [27] G. Bastard, *Phys. Rev. B*-**24**, 5693 (1981).
- [28] H. Sakaki, M. Tsuchiya, and J. Yoshino, *Appl. Phys. Lett.* **47**, 295 (1985).
- [29] Z. Chen, S. Pan, S. Feng, D. Cui, and G. Yang, *Infrared Phys.* **32**, 523 (1991).
- [30] A. K. Ghatak, K. Thyagarajan, and M. R. Shenoy, *IEEE, J. Quantum Electron.* **24**, 1524 (1988).
- [31] H. C. Liu, *J. Appl. Phys.* **73**, 3062 (1993).
- [32] A. Madhukar, T. C. Lee, M. Y. Yen, P. Chen, J. Y. Kim, S. V. Ghaisas, and P. G. Newman, *Appl. Phys. Lett.* **46**, 1148 (1985).
- [33] D. Calecki, J. F. Palmer, and A. Chomette, *J. Phys., C* **17**, 5017 (1984)
- [34] J. -W. Choe, O. Byungsung, K. M. S. V. Bandara, and D. D. Coon, *Appl. Phys. Lett.* **56**, 1679 (1990); W. L. Bloss, *J. Appl. Phys.* **66** (8), 3639 (1989).
- [35] K. M. S. V. Bardara and D. D. Coon, *Appl. Phys. Lett.* **53**, 1865 (1988).
- [36] S. J. Allen, Jr. and D. C. Tsui, *Solid-State Commun.* **20**, 425 (1976).
- [37] M. O. Manasreh, F. Szmulowicz, T. Vaughan, K. R. Evans, C. E. Stutz, and D. W. Fischer, *Phys. Rev. B***43**, 9996 (1991).
- [38] A. Raymond, J. L. Robert, and C. Bernard, *J. Phys. C***12**, 2289 (1979).
- [39] M. J. Kane, M. T. Emeny, N. Apsley, C. R. Whitehouse, and D. Lee, *Superlattices and Microstructures* **5**, 587 (1989).
- [40] A. Harwit and J. S. Harris, Jr., *Appl. Phys. Lett.* **50**, 685 (1987).
- [41] S. Y. Yuen, *Appl. Phys. Lett.* **43**, 813 (1983).

- [42] A. Seilmeier, H. J. Hubner, G. Abstreiter, G. Weiman, and W. Schlapp, Phys. Rev. Lett. **59**, 1345 (1987).
- [43] P. Yuh and K. L. Wang, Phys. Rev. B**37**, 1328 (1988).
- [44] Y. H. Wang, S. S. Li, and P. Ho, Appl. Phys. Lett. **62**, 621 (1993).
- [45] J. J. Sakurai, Advanced Quantum Mechanics, Addison-Wesley, New York, (1967).
- [46] F. Bassani and G. P. Parravicini, Electronic States and Optical Transitions in Solid, Pergamon, New York, (1975).
- [47] G. Hasnain, B. F. Levine, C. G. Bethea, R. A. Logan, J. Walker, and J. Malik, Appl. Phys. Lett. **54**, 2515 (1989).
- [48] S. D. Gunapala, B. F. Levine, and K. West, J. Appl. Phys. **69**, 6517 (1991).
- [49] G. D. Shen, D. X. Xu, M. Willander, and G. V. Hansson, Appl. Phys. Lett. **58**, 738 (1991).
- [50] S. S. Li, M. Y. Chuang, and L. S. Yu, Semicond. Sci. Technol. **8**, S406 (1993).
- [51] H. C. Liu, Appl. Phys. Lett. **60**, 1507 (1992); **61**, 2703 (1992).
- [52] W. A. Beck, Appl. Phys. Lett. **63**, 3589 (1993).
- [53] H. Nyquist, Phys. Rev. **32**, 110 (1928).
- [54] J. B. Johnson, Phys. Rev. **26**, 71 (1925).
- [55] W. Schottky, Phys. Rev. **28**, 74 (1926).
- [56] A. L. McWhorter, *1/f Noise and Related Surface Effects in Germanium*, Lincoln Lab. Rpt. No. 80, Boston (1955).
- [57] B. F. Levine, C. G. Bethea, G. Hasnain, J. Walker, and R. J. Malik, Appl. Phys. Lett. **53**, 296 (1988).
- [58] D. A. Scribner, M. R. Kruer, and J. M. Killiany, Proc. of the IEEE, **79**, 66 (1991).
- [59] G. Hasnain, B. F. Levine, S. Gunapala, and Naresh Chand, Appl. Phys. Lett. **57**, 605 (1990).
- [60] M. A. Kinch and A. Yariv, Appl. Phys. Lett. **55**, 2093 (1989).
- [61] R. B. Darling, IEEE J. Quantum Electron. **Q-22**, 1628, (1988).
- [62] A. S. Vebgurlekar, F. Capasso, A. L. Hutchinson, and W. T. Tsang, Appl. Phys. Lett. **56**, 262 (1990).
- [63] K. W. Goossen and S. A. Lyon, Appl. Phys. Lett., **53**, 1027 (1988).
- [64] H. Asai and Y. Kawamura, Appl. Phys. Lett. **56**, 746 (1990).
- [65] B. F. Levine, A. Y. Cho, J. Walker , R. J. Malik, D. A. Kleinman, and D. L. Sivco, Appl. Phys. Lett. **52**, 1481 (1988).
- [66] Larry. S. Yu, S. S. Li, Y. C. Kao, *Proc. International Electron Devices and Materials Symposium*, Nov.14 -16, Hsinchu, Taiwan, p. 468 (1990).

- [67] S. M. Sze, *High-Speed semiconductor Devices*, John Wiley & Sons, pp. 60 (1990).
- [68] K. K. Choi, B. F. Levine, R. J. Malik, J. Walker, and C.G. Bethea, Phys. Rev. B **35**, 4172 (1987).
- [69] B. F. Levine, J. Appl. Phys. **74**, R1, (1993).
- [70] J. D. Ralston, H. Schneider, D. F. Gallagher, K. K. Fuchs, P. Bittner, B. Dischler, and P. Koidl, J. Vac. Sci. Technol. B-**10**, 998 (1992).
- [71] Y. H. Wang, S. S. Li, and P. Ho, Appl. Phys. Lett. **62**, 93 (1993).
- [72] L. S. Yu, S. S. Li, and P. Ho, Appl. Phys. Lett. **59**, 2712 (1991).
- [73] L. S. Yu, Y. H. Wang, and S. S. Li, Appl. Phys. Lett. **60**, 992 (1992).
- [74] P. Dawson, B. A. Wilson, C. W. Tu, and R. C. Miller, Appl. Phys. Lett. **48**, 541 (1986).
- [75] B. F. Levine, R. J. Malik, J. Walker, K. K. Choi, C. G. Bethea, D. A. Kleinman, and J. M. Vandenberg, Appl. Phys. Lett. **50**, 273 (1987).
- [76] K. K. Choi, B. F. Levine, C. G. Bethea, J. Walker, and R. J. Malik, Appl. Phys. Lett. **50**, 1814; **52**, 1979 (1988).
- [77] E. R. Brown and S. J. Eglash, Phys. Rev. **41**, 7559 (1990).
- [78] P. Lefebvre, B. Gil, H. Mathieu, and R. Planel, Phys. Rev. **39**, 5550 (1989).
- [79] M. Dabbiacco, R. Cingolani, M. Ferrara, K. Ploog, and A. Fischer, Appl. Phys. Lett. **59**, 1497 (1991).
- [80] L. S. Yu, S. S. Li, and P. Ho, Electron. Lett. **28**, 1468 (1992).
- [81] J. Katz, Y. Zhang, and W. I. Wang, Appl. Phys. Lett. **61**, 1697 (1992).
- [82] P. Ho, P. A. Martin, L. S. Yu, Y. H. Wang, and S. S. Li, J. Vacuum. Science Technol. B-**11**, 935 (1992).
- [83] Y. C. Wang and S. S. Li, J. Appl. Phys. **74**, 2192 (1993).
- [84] J. Y. Andersson and L. Lundqvist, J. Appl. Phys. **71**, 3600 (1992).
- [85] R. P. G. Karunasiri, J. S. Park, and K. L. Wang, Appl. Phys. Lett. **59**, 2588 (1991).
- [86] R. People, J. C. Bean, C. J. Bethea, S. K. Sputz, and L. J. Peticolas, Appl. Phys. Lett. **61**, 1122 (1992).
- [87] M. Dabbiacco, R. Cingolani, M. Ferrara, L. Tapfer, A. Fischer, and K. Ploog, J. Appl. Phys. **72**, 1512 (1992).
- [88] L. I. Schiff, Quantum Mechanics, McGraw-Hill, New York, (1968).
- [89] E. Haga and H. Kimura, J. Phys. Soc. Jpn. **18**, 777 (1963).
- [90] F. Stern and W. E. Howard, Phys. Rev. **163**, 816 (1967).

- [91] C. L. Yang, D. S. Pan, and R. Somoano, *J. Appl. Phys.* **65**, 3253 (1989).
- [92] Y. Zhang, J. Katz, and W. I. Wang, *J. Vac. Sci. Technol.* **11B**, 1681 (1993).
- [93] M. Dutta, H. Shen, D. D. Smith, K. K. Choi, and P. G. Newman, *Surface Science*, **267**, 474 (1992).
- [94] D. Z. -Y. Ting and T. C. McGill, *J. Vac. Sci. Technol.* **B 10**, 1980 (1992).
- [95] H. C. Liu, *Appl. Phys. Lett.* **51**, 1019 (1987).
- [96] J. Feldmann, E. Gobel, and K. Ploog, *Appl. Phys. Lett.* **57**, 1520 (1990).
- [97] W. S. Fu, G. R. Olbright, J. F. Klem, and J. S. Harris Jr., *Appl. Phys. Lett.* **61**, 1661 (1992).
- [98] J. Y. Andersson, L. Lundqvist, and Z. F. Paska, *Appl. Phys. Lett.* **58**, 2264 (1991).
- [99] J. Y. Andersson, L. Lundqvist, and Z. F. Paska, *Appl. Phys. Lett.* **59**, 857 (1991).
- [100] K. W. Goossen and S. A. Lyon, *Appl. Phys. Lett.* **47**, 1257 (1985).
- [101] D. D. Coon, R. P. G. Karunasiri, and L. Z. Liu, *Appl. Phys. Lett.* **47**, 289 (1985).
- [102] F. Stern, *Phys. Rev. Lett.* **33**, 960 (1974)
- [103] C. -C. Chen, *IEEE Trans AP-18*, 660 (1970).
- [104] R. J. Baüerle, T. Elsaesser, and W. Kaiser, *Phys. Rev. B* **38**, 4307(1988).
- [105] C. C. Chen, *IEEE Trans. MTT-18*, 627 (1970).
- [106] Y. C. Wang and S. S. Li, *J. Appl. Phys.* **75**, 582 (1994).
- [107] B. F. Levine, S. D. Gunapala, J. M. Kuo, S. S. Pei, and S. Hui, *Appl. Phys. Lett.* **59**, 1864 (1991).
- [108] J. M. Kuo, S. S. Pei, S. Hui, S. D. Ganapala, and B. F. Levine, *J. Vac. Sci. Technol.* **B10**, 995, (1992).
- [109] J. Katz, Y. Zhang, and W. I. Wang, *Electron. Lett.* **28**, 932 (1992).
- [110] W. S. Hobson, A. Zussman, B. F. Levine, and J. deJong, *J. Appl. Phys.* **71**, 3642 (1992).
- [111] G. E. Bir and G. E. Pikus, *Symmetry and Strain-Induced Effects in Semiconductors*, J. Wiley, New York (1974).
- [112] J. W. Matthews and A. E. Blackeslee, *J. Cryst. Growth* **27**, 118 (1974); **29**, 273 (1975); **32**, 265 (1976).
- [113] G. C. Osbourn, *Phys. Rev. B-27*, 5126 (1983); *J. Vac. Sci. Technol.* **B-2**, 176 (1984), **A-3**, 826 (1985).
- [114] Landolt-Börnstein, *Numerical Data and Functional Relationships in Science and Technology*, ed. O. Madelung, Group III, **17a**, Springer-Verlag, Berlin (1982).
- [115] R. Hull, J. C. Bean, F. Cerdeira, A. T. Fiory, and J. M. Gibson, *Appl. Phys. Lett.* **48**, 56 (1986).

- [116] E. O. Kane, *Semiconductors and Semimetals*, ed. R. K. Willardson and A. C. Bear, Academic Press, **1**, 75 (1966).
- [117] F. H. Pollak, *Semiconductors and Semimetals*, ed. T. P. Pearsall, Academic Press, **32**, 17 (1990).
- [118] Y. C. Chang and R. B. James, *Phys. Rev. B*-**39**, 672 (1989).
- [119] P. Man and D. S. Pan, *Appl. Phys. Lett.* **61**, 2799 (1992).
- [120] S. H. Pan, H. Shen, Z. Hang, F. H. Pollak, W. Zhuang, Q. Xu, A. P. Roth, R. A. Masut, C. Lacelle, and D. Morris, *Phys. Rev. B*-**38**, 3375 (1988).
- [121] S. K. Chun, D. S. Pan, and K. L. Wang, *Phys. Rev. B*-**47**, 15638 (1993).
- [122] Y. H. Wang, S. S. Li, J. Chu, and P. Ho, *Appl. Phys. Lett.* **64**, 727 (1994).
- [123] H. Xie, J. Katz, and W. I. Wang, *Appl. Phys. Lett.* **59**, 3601 (1991).
- [124] H. Asai and Y. Kawamura, *Appl. Phys. Lett.* **56**, 746 (1990).
- [125] R. T. Kuroda and E. Garmire, *Infrared Phys.* **34**, 153 (1993).
- [126] K. Hirose, T. Mizutani, and K. Nishi, *J. Crystal Growth*, **81**, 130 (1987).
- [127] H. C. Liu, Z. R. Wasilewski, and M. Buchanan, *Appl. Phys. Lett.* **63**, 761 (1993).
- [128] P. Yuh and K. L. Wang, *Phys. Rev. B***38**, 13307 (1988).